A study of imbalanced quantum droplets

Thomas A Flynn

School of Mathematics, Statistics & Physics
Newcastle University
Newcastle upon Tyne
United Kingdom

May 2025

Acknowledgements

Before thanking those that have supported me throughout my PhD, I want to begin by thanking Mr Ward, Mr Smith and Mr Nelthorpe for sparking my interest in Maths. They demonstrate the impact that good teachers have on the lives of their students.

An enormous thank you goes to my supervisors Tom Billam and Nick Parker, whose patience I have pushed to new levels, but who have both been kind, funny and supportive throughout my research. Alongside Nick and Tom, I wish to thank my former supervisors Nick Keepfer and Luca Parisi, both of which offered significant time to me, including long chats about scientific computing. Similarly, I am not sure I would have had the confidence to begin a PhD if not for Tom Bland, who encouraged me throughout my Masters research work. I would also like to thank Kali Wilson, Simon Cornish, Tobias Franzen and Jack Segal, who have unknowingly convinced me that experimental Physics is magic.

Research is almost never conducted in isolation, and I have benefited from friendships and ample discussions with past and present members of Newcastle's Quantum group, including: Ryan Doran, Richard Tattersall, Julie Thomas, Sri Badariprasad, Henry Harper-Gardner, Kate Brown, Gary Liu, Peter Stasiak, Alex White, Sam Edmunds and of course (The Polish Geordie) Kuba Kopyciński. I am also indebted to those I have shared offices with, which includes: Sam Hartharn-Evans, Antoine Vauterin, Karthika Bhuvanendran, Federica Nardini, Rachadawan Darlai and Axa Lääperi, who had to tolerate me while trying to work. I would also like to thank James Murray, Nicola Hewitt, Lucia Asencio Martín, and the organisers of MathsAid: Vicky Hall and Dave McGeeney, and I am sure many others whose names currently escape me.

Looking to the future, I also want to extend a thanks to EPCC, particularly Mark Bull and James Richings, for giving me the opportunity to work at one of Europe's premier supercomputing centres, and hopefully not break anything. A huge thanks goes to Matt Linsley for giving me so much support, during both my undergraduate and postgraduate studies, such as arranging the resources for me to move to Edinburgh for my time at EPCC.

None of my academic studies would have been possible without the lifetime of encouragement from my Mam and Dad. Whether it has been coming to concerts, or being available for a chat on the phone, both of you have always been there for me.

Finally, I want to thank my partner Georgia. Gratitude does not cover the love and support you have given me over the years, even whilst completing your own PhD (which people always find more interesting than mine!). I look forward to seeing what the next portion of our life together brings, especially with our furry companion, Luna.

Abstract

Gases of ultracold atoms have proved to be a highly versatile platform for studying quantum physics due in part to their high controllability. One example of this control is the manipulation of interactions. A single-component Bose gas in free space is unstable to collapse under attractive contact interactions, whereas, in an attractive two-component Bose gas the collapse is arrested by the repulsion from quantum fluctuations, forming self-bound liquid droplets: quantum droplets. Quantum droplets are therefore a quantum fluid in which quantum fluctuations are not only present but integral. During formation quantum droplets preserve a constant density ratio such that the droplet can be approximately described by its total density rather than in terms of two independent component densities. This approximation, known as *density locking*, is powerful but limiting. Droplet experiments typically begin with a population imbalance during formation, meaning that imbalanced droplets may be the most prevalent. Motivated by a link with an experimental ^{174}YbCs mixture, which deviates from many of the assumptions built into the density-locked model, the primary focus of this thesis is: how are droplets modified by imbalances that break the assumptions of density locking?

This thesis begins by showing that, up to a saturation limit, free-space droplets can lower their energy through population imbalancing but correspondingly become less stably bound. By perturbing these imbalanced droplets, breathing modes are observed to have a complex parameter space of multiple, superimposed, decaying modes with time-dependent frequencies and decay rates.

All droplets are experimentally formed in harmonic traps, and so the free-space imbalanced results are extended to study how harmonic traps affect the structure and breathing modes of imbalanced droplets. Beyond the droplet formation, there is a crucial question around the stability of the imbalance during a release into free space. A key result of this thesis is that imbalances can be retained during either an instantaneous or linearly-ramped trap release.

Finally, the imbalanced droplet results above are applied to explore the ^{174}YbCs parameter space, by measuring droplet size, peak densities and lifetimes. A variety of dynamics are studied from droplet formation and excitations, to proposing potential experiments serving as a platform to study the non-equilibrium dynamics of droplets.

Contents

Chapter 1

Introduction

1.1 Quantum gases and many-body physics

Advances in the precise manipulation of ultracold atoms [1–3] led to a boom in both the experimental and theoretical study of quantum gases in the late 1990s–early 2000s. Quantum gases are highly controllable gases of ultracold atoms. Their controllability is in part due to refined techniques from atomic and optical physics that allow for control of, e.g., interatomic interactions and applied potentials. The cleanliness and precision of quantum gases has lead to them becoming a highly versatile platform for studying quantum many-body physics [4], and realising quantum simulators [5].

Advances in cooling techniques made it possible for experimentalists to achieve nanokelvin temperatures. Laser cooling is a primary cooling technique used in ultracold atoms in which irradiating an atomic cloud with laser light reduces the average motion, and hence temperature, of the atoms [6, 7]. The 'slowing' of atomic motion can be conceptualised by the schematic of laser cooling or slowing an atomic beam. Atoms absorb photons from a counter-propagating laser resulting in transitions and emissions that change the atomic momenta along an arbitrary axis. For an atomic cloud, laser cooling is typically achieved via an 'optical molasses' [8] which is produced in three-dimensions (3D) by six counter-propagating lasers, i.e., two opposing lasers along the x, y and z axes. The laser light has a small frequency detuning towards lower frequencies such that atoms absorbing photons opposing their direction see photons with frequency Doppler shifted on-resonance, and co-moving photons are Doppler shifted off-resonance. Thus, averaged out across the cloud, atoms dominantly absorb photons that counteract their motion, reducing the root-mean-square velocities of the atoms, i.e., reducing the overall temperature [8–10]. However, the temperatures achievable by laser cooling are limited to of order 100μK [11] and so, nanokelvin temperatures are predominantly achieved via evaporative cooling. Following laser cooling, the confinement of the cloud — typically a magnetic or optical trap — is reduced causing the most energetic atoms to be lost [12, 13]. This is analogous to the evaporative cooling of steam from a cup of tea, i.e., the most energetic molecules on the surface of the tea evaporate corresponding to a decrease in the average kinetic energy per

atom, or temperature.

Another useful property of quantum gases is the precise control of externally imposed potentials. In almost all quantum gas experiments, trapping potentials are placed on the atomic cloud to contain the gas [14]. There is some freedom in producing different trap structures from harmonic and box traps [15] to periodic traps. Optical lattices are created via counter-propagating lasers imposed on the cloud to generate periodic sinusoidal potentials [16]. As the atoms occupy the minima of these potentials, the system is analogous to the periodic lattice structures of solid states. The benefit of quantum gases in this field is again because of their controllability and cleanliness which cannot be achieved in typical condensed matter physics experiments due to issues such as defects [17]. Thus, the study of quantum gases in optical lattices led to breakthroughs such as the observation of the superfluid-Mott insulator transition [18] and individual atomic imaging via quantum gas microscopes [19]. Trapping potentials can also be used to vary dimensionality to study low-dimensional systems [20]. Quantum gases confined to one-dimension (1D) are unique as they possess exact analytic solutions such as the Lieb-Liniger model [21] in a single-component gas and the Tonks-Girardeau gas [22, 23] in the limit of infinitely repulsive interactions, which have also been experimentally realised [24, 25] (for a review of 1D bosonic gases see Ref. [26]). Beyond confinement, potentials have also been used to stir the atomic cloud via a 'laser spoon' [27–29], or in generating general potentials in 2D [30] using Digital Micromirror Devices (DMDs) [31].

In recent years, the role of ultracold atoms as quantum simulators has grown significantly [5, 32], with applications from the study of neutron stars [33, 34] through to acting as a 'universe in the lab' for studying cosmological phenomena [35–37]. However, the major revolution that originally propelled the field forward, was the observation of Bose-Einstein condensation in an ultracold cloud of bosons, for which Cornell, Weimann [38] and Ketterle [39] were awarded the 2001 Nobel Prize in physics [40, 41].

1.1.1 Bose-Einstein condensation

The observation of a Bose-Einstein Condensate (BEC) in 1995 confirmed the predictions of Bose [42] and Einstein [43, 44] from 1924. Bose-Einstein condensation is the macroscopic occupation of the lowest quantum state in a system of indistinguishable bosons [11, 45] resulting in a macroscopic matter wave. Below the critical temperature for Bose-Einstein condensation first-order correlations of the gas asymptote to a constant, in the limit of large distances, rather than decaying to zero; this property is typically referred to as off-diagonal long-ranged order [46–48]. Figure 1.1 shows velocity distributions in 2D of an ultracold cloud of bosons, with temperature decreasing left to right. In the left panel the gas is imaged above the BEC critical temperature and hence has a broad, thermal velocity distribution. With decreasing temperature a narrow velocity distribution can be seen with a near pure condensate shown in the right panel.

The coherent matter wave can be conceptualised by considering a dilute gas of bosons

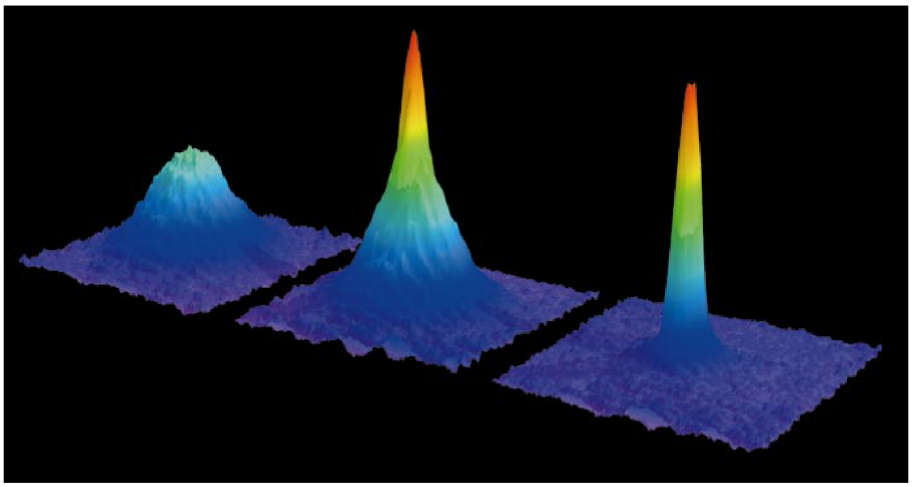

Figure 1.1: Early observation of a BEC observed via absorption imaging, with temperature decreasing left to right and an almost pure condensate given in the right-most panel. Reprinted figure with permission from Ref. [40]. Copyright (2002) by the American Physical Society.

at sufficiently high temperatures such that they can be modelled as highly-localised, 'billiard-ball'-like particles. As the gas is cooled, the wave-like nature of the bosons becomes more pronounced as the de Broglie matter wavelength is inversely proportional to the square root of the temperature, $\lambda_{dB} \propto 1/\sqrt{T}$. At lower temperatures, the increasing wavelength becomes comparable to the average inter-particle distance, such that the individual particle wavefunctions overlap one another and the microscopic quantum effects become macroscopic. All atoms reside in the condensate for a zero-temperature, non-interacting gas, whereas, for weak interactions some non-zero fraction of the atoms occupy low lying modes above the condensate, even at zero temperature.

BECs were first formed in clouds of ^{87}Rb [38], by the group of Cornell and Wieman, and ^{23}Na [39] by the group Ketterle. From this pioneering work came a plethora of experimental and theoretical works to study, e.g., superfluidity and non-linear physics. Bose-Einstein condensation and superfluidity were originally linked by Fritz London [49] and Laszlo Tisza [50] in low temperature Helium. The strong correlations and high densities of superfluid Helium make it difficult to model accurately, whereas dilute, weakly-interacting Bose gases can be explained by mean-field theories. Some key properties of superfluidity include: the absence of viscosity and dissipation, so long as the superfluid flow lies below the Landau critical velocity for the production of excitations [51]; and discretisation of circulation to individual singularities: quantum vortices. BECs have therefore allowed for the controllable creation and imaging of the vortices [52] and vortex lattices [53], a clear signature of superfluidity that has been widely studied in liquid Helium [54].

Vortex dynamics are crucial to understanding fluid flows. In classical fluids vortices can have arbitrary size and circulation, however, in superfluids the circulation of a vortex

is quantised, i.e., quantum vortices are uniform in size and circulation [1]. In 2D, quantum vortices are akin to point charges, whereas in 3D they are filamentary tubes. Owing to the cleanliness of ultracold atom experiments, quantum gases have become a versatile platform for studying fluid dynamics such as vortex dynamics [28, 53, 55–58] and quantum turbulence (for recent reviews see Refs. [59, 60]).

Vortices are not the only non-linear excitations that BECs can support; solitons are particle-like solitary waves that are present in many different fields [61], whose stability depends on the competition between interactions and dispersion from kinetic contributions. In quantum gases both bright [62] and dark [63] solitons have been observed. BECs can also exhibit collective excitations which are vital in understanding many-body systems. Collective excitations were observed in early BEC experiments [64, 65], along with other large-scale excitations of the cloud including sound propagation [66] and collapse dynamics [67, 68].

From the creation of the first BEC came a huge body of work studying different atomic species [69]. There are now a variety of elements that have been Bose condensed giving rise to, e.g., dipolar Bose gases which consist of atoms that have a relatively strong magnetic moment [70–73]. A close relative of bosonic quantum gases are ultracold Fermi gases. Advancements in cooling techniques led to the creation of degenerate Fermi gases [74–86], allowing for observation of the BCS-BEC (Bardeen-Cooper-Schrieffer-Bose-Einstein-Condensate) crossover [87–89] from superconductivity [90]. The BCS-BEC transition could only be observed due to advancements in controllability: namely, the control of interactions.

1.1.2 Interactions

The scattering theory of quantum mechanical particles is a large and complex field. Yet, many of the major complexities within scattering theory are reduced for bosonic quantum gases as they are typically dilute and weakly-interacting, thus collisions can be accurately described by s-wave scattering in terms of two-body only [11, 45]. By reducing the problem to s-wave scattering, the problem of describing collisions in many-body problems reduces to only zero angular momentum contributions. The utility of this is that collisions can be described by the characteristic length scale of s-wave scattering events: the scattering length, a. The ability to describe interactions by this single parameter has a major benefit to experiments in that a can be manipulated. Feshbach resonances allow for accurate tuning of a [91–93] from attractive ($a < 0$) to repulsive ($a > 0$) collisions (see Ref. [94] for a review of Feshbach resonances).

A schematic of a Feshbach resonance is given in Figure 1.2, showing two potentials that vary with atomic separation: the background potential known as the 'open' channel; and the closed channel, which can support bound states. In the case of two atoms interacting with an incident energy in the open channel (given by the green dashed line), a resonance

[1] Quantum vortices with higher circulation are unstable, limiting the so-called 'charge' to be ± 1.

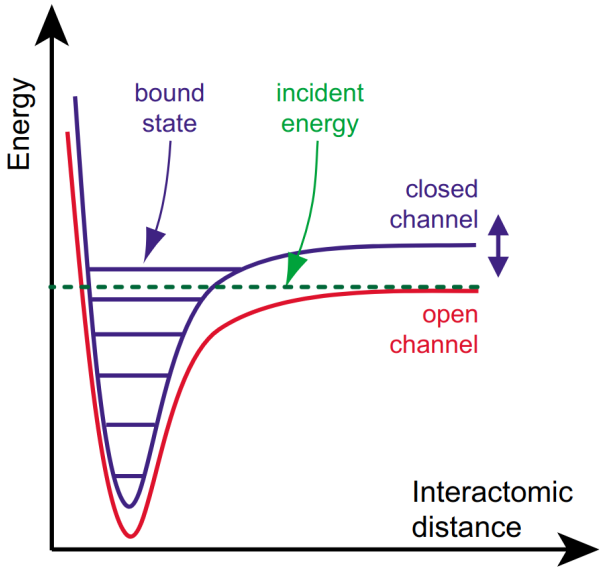

Figure 1.2: Schematic of a Feshbach resonance showing two potentials corresponding to an open and closed channel, with atoms interacting at the incident energy. Reprinted figure with permission from Ref. [4]. Copyright (2010) by the American Physical Society.

can be engineered in which this collision resonantly couples to a bound state in the closed channel. Feshbach resonances are a useful tool for experimentalists because this resonance can be tuned via an applied magnetic field allowing for the scattering length, a, to be varied significantly.

A simplified model of the Feshbach resonance is given by [95]

$$a(B) = a_{\mathrm{bg}}\left(1 - \frac{\Delta}{B - B_0}\right) \tag{1.1}$$

where B is the applied magnetic field, a_{bg} is the scattering length associated with the background potential or open channel, Δ describes the width of the resonance and B_0 is the position of the resonance 'pole' at which the scattering length diverges. Either side of the pole, the scattering length varies significantly and Equation (1.1) indicates that non-interacting gases can be engineered at $B = B_0 + \Delta$.

Experimentally, Feshbach resonances can often be identified as corresponding to a sudden increase in population loss [96]. The main mechanism for these losses are inelastic, three-body recombination events. Losses occur due to the metastability of atoms in the cloud and are typically caused by the formation of a lower energy configuration or molecular state during a collision, leading to a release of energy. For example, in the case of three-body losses the mechanism is the interaction of three atoms forming a two-atom molecular state and a free atom. The binding energy from the molecule is released causing heating of the condensate and, for typical energy scales, loss of atoms from the trap [4, 94]. Around the pole of a Feshbach resonance, these events are increased corresponding to pronounced dips in the population number that are indicative of a Feshbach resonance [96, 97]. Though quantum gases are many-body systems, Feshbach resonances are an

example of how quantum gases have been used to study few-body physics [98, 99]. For example, losses can be a useful fingerprint of few-body physics such as evidence of Efimov states [100], and higher-body bound states [101].

1.2 Quantum mixtures

Mixtures of distinguishable quantum gases exhibit further degrees of freedom and a richer parameter space than a single component gas. Spin or homonuclear mixtures — i.e., gases of the same atomic species and isotope, that are prepared in different hyperfine states of the ground state manifold — were the first two-component BECs to be experimentally produced [102]. The diversity of mixtures increased to include mixtures of different isotopes [103] and atomic species (heteronuclear mixtures) [104]. Heteronuclear mixtures extend the explorable systems further to Bose-Fermi mixtures [80, 105–107], and mass imbalances. Tunability of interactions through Feshbach resonances in mixtures was first observed in Bose-Fermi mixtures [108–110], and was later achieved in bosonic mixtures [111, 112].

Whilst early quantum gas experiments were composed of atoms with negligible magnetic dipole moment, gases with significant magnetic dipoles moments have gained a lot of interest due to their anisotropic, long-ranged interactions (see Ref. [113] for an earlier review of dipolar quantum gases, and Ref. [114] for a more recent review of dipolar experiments). Recently, dipolar bosonic mixtures have also been experimentally produced [115–117] leading to a very rich parameter space of both inter and intraspecies short-ranged and long-ranged interactions. Dipolar mixtures have been predicted to support novel ground states, which are discussed further in Section 1.3.

Mixtures with three or more components can be created in spinor BECs in which the atoms possess a spin degree of freedom [118]. A magnetic trap only retains atoms in a single spin state, whereas optical traps can confine atoms with arbitrary spin [118, 119]. A spin-n BEC has $2n + 1$ components — spin-1 (3 components) [120, 121], spin-2 (5 components) [121–123] and spin-3 (7 components) [124] have all been experimentally observed — leading to a variety of exotic ground states, excitations and dynamics (for reviews see Refs. [125, 126]). Though the variety of quantum mixtures continues to grow, this work is restricted to non-dipolar, two-component bosonic mixtures.

Both inter and intraspecies interactions can be tuned within bosonic mixtures, e.g., a significant repulsion between the two components can cause a transition from miscible to immiscible fluids [127, 128]. Figure 1.3 shows a mixture of two Rubidium isotopes (^{85}Rb and ^{87}Rb) with an immiscible mixture given in (a) and (b) and a miscible mixture give in (c) and (d). Miscible mixtures have led to studies of relative motion of the components as the fluids can be engineered to flow through one another [129–131]. The phase separation of fluids in the immiscible regime causes modifications of the fluid structures found in single-component Bose gases, e.g., infilling of one component changes the profile

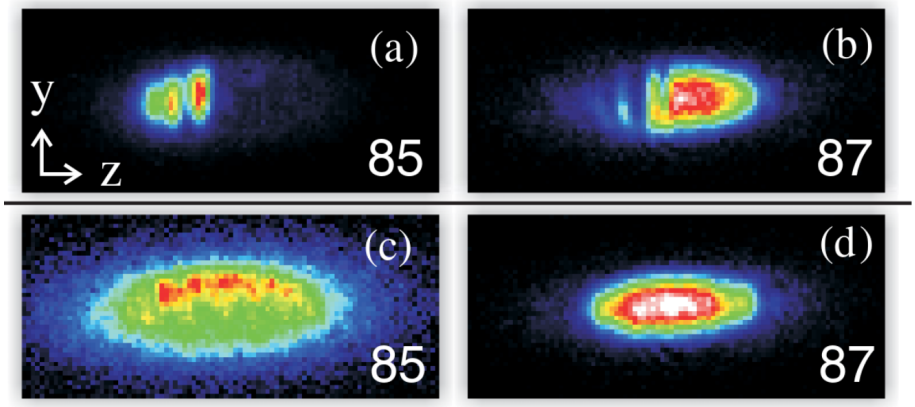

Figure 1.3: Absorption images of two mixtures of ^{85}Rb and ^{87}Rb isotopes where (a) and (b) are an immiscible mixture, whilst (c) and (d) are a miscible mixture. Reprinted figure with permission from Ref. [103]. Copyright (2008) by the American Physical Society.

of individual quantum vortices [132–135]. Furthermore the boundary formed between the fluids has lead to immiscible mixtures being used as a platform for studying multi-phase flows and fluid boundary instabilities such as the Rayleigh-Taylor [136–139] and Kelvin-Helmholtz instability [139–142].

Beyond varying interactions, there is also freedom in population numbers of the two components. This gives a spectrum from balanced mixtures to strongly imbalanced mixtures at the limit of few body impurities, i.e., the polaron regime, The study of both Bose [143, 144] and Fermi polarons [145–148] are clean and controllable systems with broader applications to the study of impurities coupled to a quantum bath. Quantum mixtures are therefore a natural extension of single-component Bose-condensed gases allowing for physics that go beyond that of single-component systems.

1.3 Quantum droplets

The stabilisation of a self-bound droplet in dilute gases was originally proposed for single-component Bose and Fermi gases with the addition of three-body effects [149, 150]. Ref. [149] proposed a mechanism in which attractive two-body interactions could be stabilised by repulsive three-body interactions, with the three-body interactions even dominating the two-body contributions. However, these droplets are yet to be experimentally observed, since one of the proposed systems is a tritium BEC [150, 151] which is suspected to have significant experimental challenges [152]. Thus without this three-body stabilisation mechanism, the stability of a single-component homogeneous Bose gas is governed by the two-body atomic interactions. A mean-field theory — which captures much of the physics of low-temperature, weakly-interacting, dilute gases [11, 45] — predicts that the gas is unstable to collapse for attractive interactions. Collapse dynamics have been demonstrated experimentally by using a Feshbach resonance to tune the interactions from repulsive to attractive [67, 68].

For a two-component system, the stability depends on both the inter and intraspecies contact interactions, which can all be tuned via Feshbach resonances [94]. For repulsive intraspecies interactions — to ensure stability of each individual component — and attractive interspecies interactions, mean-field theory once more predicts an unstable gas. However, this attractive collapse can be stabilised at high densities by quantum fluctuations [153] forming a self-bound quantum droplet. The inclusion of quantum fluctuations has inspired related work in so called Lee-Huang-Yang (LHY) fluids [154, 155], named for the correction describing quantum fluctuations to first-order. By tuning mean-field interactions between the components to vanish, the interactions of LHY fluids are described by quantum fluctuations alone [154, 155].

In free space quantum droplets exist in equilibrium with the vacuum and form a seemingly counter-intuitive dilute liquid-like state [153, 156]. This adds to the variety of properties that quantum gases can be used to investigate, as the majority of experiments are inherently within the gas phase, a property widely exploited in time-of-flight imaging [157]. Whereas quantum droplets open up the field to explore the properties of quantum liquids, such as surface tension [153, 158, 159] and incompressibility [160, 161], within controllable experimental conditions. For recent reviews of quantum droplets see Refs. [162, 163].

1.3.1 Dipolar quantum droplets

Quantum droplets have been experimentally observed in two systems: (i) dipolar gases of Dy [164–166] and Er [167]; (ii) homonuclear ^{39}K [161, 168–170] and heteronuclear, ^{41}K-^{87}Rb [171, 172] and ^{23}Na-^{87}Rb [173], two-component mixtures. Though the underlying mechanism for droplet formation is the stabilisation between attractive interactions and repulsive quantum fluctuations [153], the mean-field interactions of a dipolar Bose gas include both the two-body, short-ranged interactions of a non-dipolar gas, and anisotropic, long-ranged interactions resulting from strong atomic magnetic dipoles [113]. This anisotropy results in elongated droplet profiles [174–178], that differentiate dipolar droplets from non-dipolar, two-component droplets.

Beyond just single dipolar droplets, lattices of multiple droplets can be produced by confining the gas, e.g., the multiple droplets shown in Figure 1.4 that are confined along a waveguide. The density modulations which seed the multi-droplet state are caused by the production of rotons which are elementary excitations resulting from the long-ranged interactions [179, 180]. First predicted in superfluid Helium, rotons are associated with a minimum in the excitation spectrum [181]. The roton minimum can be manipulated by tuning the strength of dipolar interactions, and for strong dipole interactions the roton mode softens causing an unstable production of rotons, i.e., the roton instability [182–184]. However, the roton minimum occurs at an associated momentum [179] which defines the length scale of the droplet lattice. The softening of the roton mode is unstable to collapse in the mean-field theory but is stabilised via the effects of quantum fluctuations.

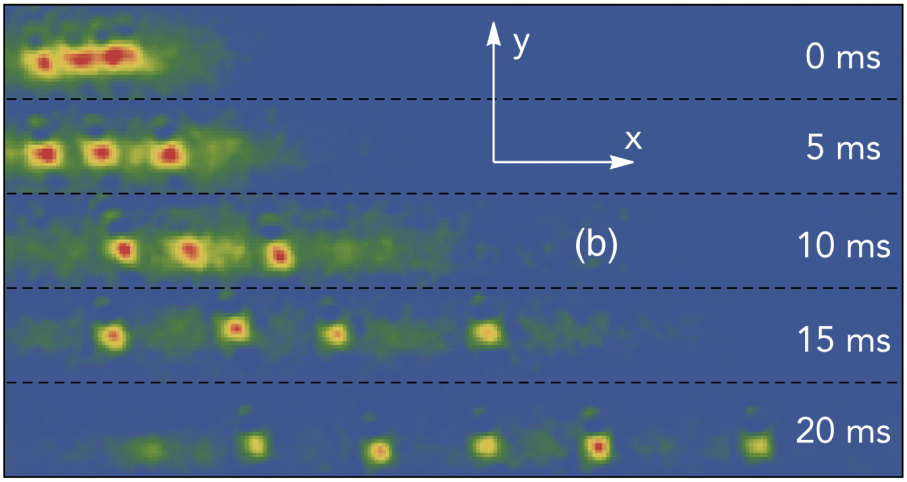

Figure 1.4: Experimental images of dipolar quantum droplets confined in a waveguide where red and blue correspond to high and low optical density. Multiple quantum droplets are formed in a waveguide, with tight confinement in y and z. Reprinted figure with permission from Ref. [165]. Copyright (2016) by the American Physical Society.

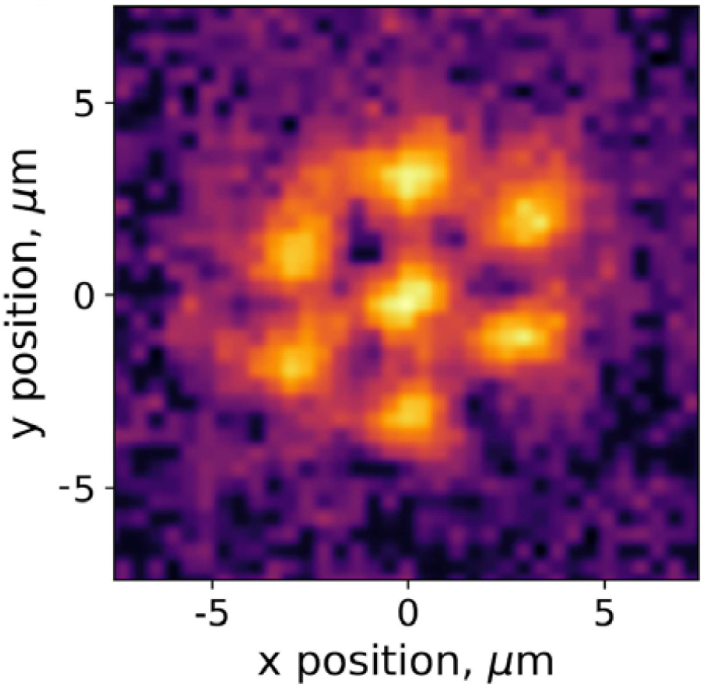

Figure 1.5: An in-situ image of a 2D supersolid. The high density, yellow areas are droplets, though the droplets have a non-zero gas density linking them, creating a hexagonal lattice of seven coherent droplets. Reprinted figure with permission from Ref. [185]. Copyright (2022) by the American Physical Society.

Though quantum droplets were predicted in non-dipolar mixtures, they were first observed in dipolar quantum gases [164–167], being followed up by the realisation of a related state, the supersolid. Quantum droplets in free space are independent objects. Supersolids bridge the gap between the unmodulated condensate and independent droplets because they exhibit high density droplets surrounded by a low density gas with a coherence between the droplets. This results in a superfluid-like phase, with a periodic lattice of droplets. The supersolid phase had been predicted many years earlier in the 1960s–70s

[186–188], for which Helium seemed the natural choice, however supersolidity in Helium has not yet been observed.

Supersolids and isolated-droplet arrays were initially observed in a quasi-1D geometry [189–191], though recently quasi-2D supersolids, with a hexagonal lattice of droplets have been reported [192]. A transition between quasi-1D and 2D was produced by varying the aspect ratio of the trap, leading from 1D linear arrays of droplets, to a middle regime of 'zig-zag' droplets, through to a hexagonal array [192–194] as shown by the in-situ image of a seven droplet hexagonal supersolid in Figure 1.5. Theoretical studies have also predicted that droplet arrays, both coherent and incoherent, may support exotic phases including: rotationally asymmetric lattices [195], 'honeycomb' [196, 197], 'labyrinth' and 'stripe-phase' supersolids [198, 199] that break spatial symmetries.

Noting the differences between dipolar and two-component quantum droplets is vital, as these droplets have very different structures and thus different physics. However, it is useful for the study of droplets to have these two platforms for comparing and contrasting the two related systems. Throughout this work, unless stated otherwise, the term 'quantum droplets' refers to non-dipolar, two-component quantum droplets.

1.3.2 Two-component quantum droplets

Two-component droplets were first experimentally observed using mixtures of ^{39}K hyperfine states in a quasi-2D geometry [168], confined along the z-axis, to compensate somewhat for gravity. Figure 1.6 shows the dynamical behaviour of the atomic cloud, following a release of the 2D radial traps. The top row of Figure 1.6 demonstrates that a mixture with dominantly repulsive interactions expands like a gas, whereas the attractive, single-component gas in the bottom row, collapses. It is only the combination of a mixture with attractive interactions that forms an object that is self-bound.

The first fully free-space mixture was likewise observed in a mass-balanced, ^{39}K spin mixture [169]. To observe the droplet in free space, Ref. [169] used a levitating potential by shining a red-detuned elliptical laser onto the cloud. Droplet lifetimes in ^{39}K mixtures are limited to only a few milliseconds due to high three-body losses. Evidence of this effect can be seen in the middle row of Figure 1.6 in which the droplet shrinks over time, and one way to overcome this is via heteronuclear droplets.

The first heteronuclear droplet was reported in a quasi-1D ^{41}K^{87}Rb mixture with lifetimes exceeding 28 milliseconds [171]. The most recent experimental mixture seeding droplets was ^{23}Na^{87}Rb which has lifetimes exceeding 15 milliseconds. For comparison lifetimes in the spin mixtures were limited to less than 10 milliseconds [168, 169]. Heteronuclear mixtures are one example of how inter-component asymmetries can be engineered within droplets. However, it is not just mass-imbalances that add asymmetries between components, intraspecies scattering lengths vary the internal interactions of each component leading to even richer systems.

Beyond experimental verification of droplet ground states, droplet dynamics have been

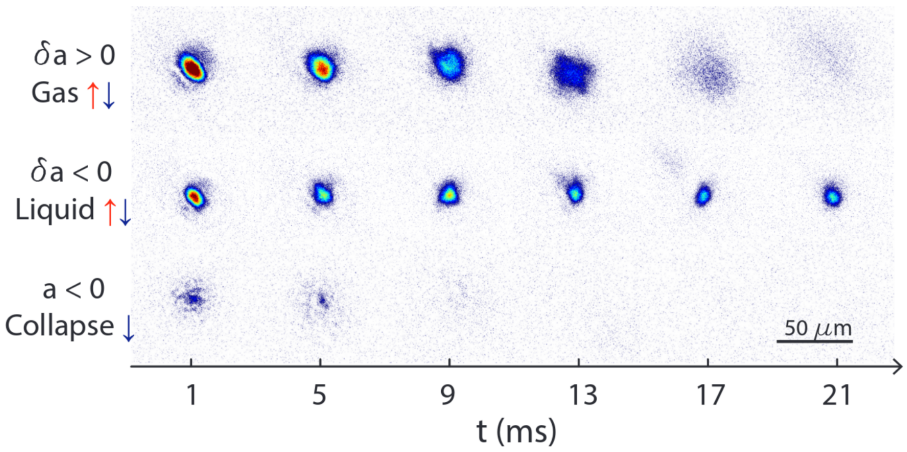

Figure 1.6: Tuning interactions and releasing a spin mixture of ^{39}K into free space. Top row: a repulsive mixture which expands in free space showing it is a gas. Middle row: an attractive mixture retaining a fixed volume in free space, i.e., a self-bound quantum droplet. Bottom row: an attractive single-component gas which collapses. From Ref. [168]. Reprinted with permission from AAAS.

studied with Ref. [161] reporting on droplet collisions in spin mixtures of ^{39}K. Within a harmonic trap the droplets are initially separated by a potential barrier. The potential barrier excludes each droplet from sitting in the trap centre, giving the droplets an initial potential energy. Removing this potential barrier causes the droplets to move towards one another, and the harmonic trap is linearly ramped off. Different ramp times correspond to different droplet velocities. Ref. [161] found a critical velocity, below which the droplets merge, and above which the droplets separate. The collisional behaviour is proposed as a method for contrasting between compressible and incompressible droplets. Other recent dynamics were reported by Ref. [172] in the ^{41}K^{87}Rb mixture, which ramped the intraspecies scattering length into the droplet regime and observed that certain droplets could form capillary instabilities, and fragment into multiple droplets acting as a quantum analogue to the Plateau-Rayleigh instability [200].

Droplets are not the only self-bound matter waves in attractive gases. Self-bound matter waves can be found in attractive gases confined by an optical waveguide in which the attraction is stabilised by dispersion. Ref. [170] studied the droplet-soliton transition by confining an attractive, two-component mixture to a waveguide. By mapping out the parameter space of this experimental setup Ref. [170] indicates that both solitons and quantum droplets can be formed and are either smoothly connected or bistable, depending on the parameter regime. By using a mass-balanced spin mixture, the populations of the two components can be varied by applying a radio-frequency pulse to the cloud, transitioning atoms from one spin state to the other, creating droplets in both population-balanced and imbalanced mixtures.

Though droplet experiments have made significant advances in recent years, there are still many theoretically predicted behaviours yet to be observed. For example, a defining property of three-dimensional (3D) two-component quantum droplets is self-evaporation [153]. In certain regimes of the droplet's phase diagram, excitations will

cause the droplet to shed atoms in order to relax to a lower energy state. This occurs when the energies of these excitations exceed $-\mu$, the particle emission threshold, where μ is the chemical potential of the droplet. Furthermore, one of the most significant evaporative regimes is of the lowest monopole mode — the breathing mode — which decays for a large proportion of the droplet's phase diagram [153, 201]. There is one regime in which all collective excitations are self-evaporated and thus these droplets are predicted to evaporate any excitation, even excitations from a thermal component [153]. Self-evaporation is a fascinating property which could lead to droplets that can lower their own temperature, and is not exhibited by dipolar quantum droplets [160], or for the breathing mode of a 1D two-component droplet [202]. Self-evaporation has not yet been experimentally observed, but it is crucial in understanding the dynamics of these objects.

Two-component quantum droplets can also be distinguished from single component dipolar droplets, in that they can be used to study spin properties. As previously discussed, collective modes have been a key physical property for studying excitations in quantum gases, but with mixtures an even richer landscape is recovered. For single component quantum gases, collective oscillations can only be excited within the density channel, whereas with two components, excitations can be initiated in both the density and spin channel, resulting in spin collective modes in which the two components oscillate out-of-phase [203, 204].

1.3.3 Dipolar mixtures

The recent experimental production of two-component dipolar BECs [115–117] has lead to various theoretical works studying how combining the properties of two-component gases with dipolar interactions manifests, from dipole-dependent miscibility [205] to spin roton modes [206]. As both single-component, dipolar and two-component, non-dipolar gases can support droplets, two-component dipolar gases can support droplets with several novel properties. Droplets can formed in dipolar mixtures through the interplay between interactions — both short and long-ranged — and quantum fluctuations, with Refs. [207, 208] reporting the first theoretical predictions of droplet states in dipolar mixtures. As single-component dipolar gases can form into droplets, two-component dipolar gases can form elongated, immiscible droplets which are distinct from two-component, non-dipolar droplets in which the gases must be miscible. This leads to both miscible and immiscible droplets that can support arbitrary population imbalance between the two components [207–209].

Dipolar mixtures can also form into supersolids, with Ref. [210] predicting that a one-component supersolid, stabilised with quantum fluctuations, can 'catalyse' density modulations in the other component. However, in the absence of quantum fluctuations, dipolar mixtures can still support supersolids with so-called 'alternating-domain supersolids' that are comprised of a lattice of droplets in quasi-1D that alternate between the two components [194, 211]. For certain parameter values, these droplets can be coherent

due to a low density background gas connecting them. Furthermore, as the alternating-domain supersolids are formed from a mechanism more akin to a miscible-immiscible transition, the densities are predicted to be much lower than single-component dipolar supersolids. Lower densities are more favourable to extended experimental lifetimes as three-body losses are suppressed [194, 211].

Whilst in one-component dipolar gases the roton mode plays a key role in stability, the two-component dipolar gas also exhibits a spin roton mode [206] leading to a spin Higgs mode in the alternating domain supersolid which are also predicted to have a rich excitation spectrum of three Goldstone modes in 1D along with optical and acoustic phonon modes [212]. Quasi-2D supersolids have been recently studied by Ref. [213] with a focus on the immiscible spin-stripe states which, as in the quasi-1D geometry, has a variety of density and spin excitations offering a further platform for studying spin systems, miscibility, supersolidity, and hydrodynamic properties.

Quantum droplets are therefore an active area of research that has experimental challenges but can open up quantum gases to the study of quantum liquids to explore, e.g., surface tension and incompressibility. This work benefits from an experimental link to an attractive, non-dipolar mixture that could add to the preexisting three, two-component droplet mixtures of ^{39}K [161, 168–170], ^{41}K^{87}Rb [171, 172] and ^{23}Na^{87}Rb [173].

1.4 CsYb mixture

This work has a link with an experimental mixture of Caesium (Cs) and Ytterbrium-174 (^{174}Yb), referred to here as the CsYb mixture, first cooled to dual Bose-Einstein condensation in Ref. [214]. The mixture of an alkali metal, Cs, and an alkaline-earth-like metal, Yb, poses experimental challenges, e.g., Cs is paramagnetic and Yb is diamagnetic, resulting from their different electronic structures, thus magnetic traps for both components cannot be used [215] and a single optical trap is challenging [214, 216]. However, due to the difference in atomic structure, species-specific traps can be engineered enabling greater control over the individual components than can be achieved in alkali mixtures [215, 217]. A further benefit of the CsYb mixture is the variety of Yb isotopes, allowing for the study of different mixtures such as repulsive and attractive bosonic mixtures, Bose-Fermi mixtures [214], and potentially ultracold molecules [218].

This work focuses on the ^{174}Yb isotope as the ^{174}Yb-Cs interspecies interactions are attractive, making it a candidate for droplet physics. The overall two-body interactions of the mixture are tuned by varying the Cs scattering length, a_{Cs}, which can be accurately controlled [220] with no effect on the scattering properties of Yb [214]. Ref. [219] reported the first dynamical results within the attractive CsYb mixture by studying centre-of-mass oscillations and collapse dynamics. The coupled centre-of-mass dynamics were studied with a_{Cs} large enough such that the two-body interactions were dominantly repulsive, i.e., in the gas phase. Further to these oscillations, Ref. [219] also probed the attractive

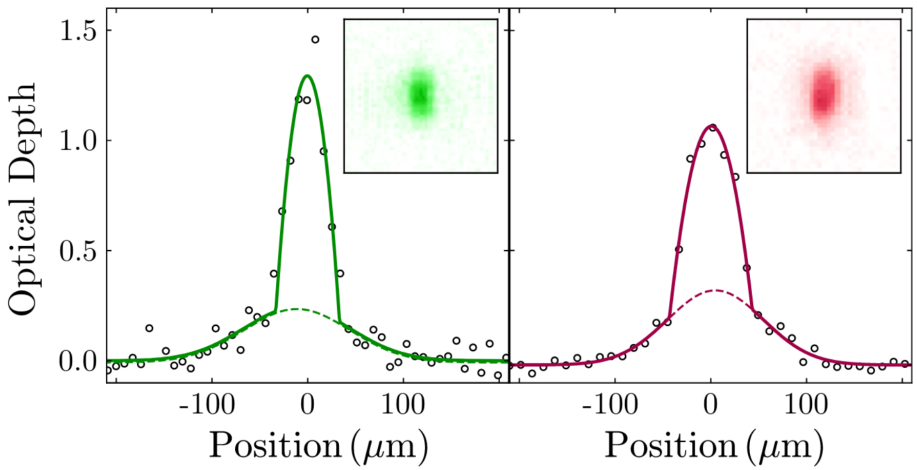

Figure 1.7: The CsYb, two-component BEC showing optical density cross sections through the condensate centre with the ^{174}Yb and Cs components given in the left and right panels, respectively. Experimental data is given by the individual points whilst the solid curves show a bimodal fitting corresponding to the condensate, and the dashed curves show a Gaussian fitting to the thermal component. Reprinted figure with permission from Ref. [219]. Copyright (2021) by the American Physical Society.

collapse regime by ramping a_{Cs} into the droplet regime and then out again over a finite time, and subsequently observing the final Cs population number. Entering this regime shows significant losses, indicative of attractive collapse dynamics [67, 68], though with no definitive evidence of droplet formation.

Caesium suffers from relatively large three-body losses [97] that can be exacerbated by the high densities of quantum droplets. Three-body losses are a limiting factor of droplet lifetimes [153] and so reduction of droplet densities will inevitably be a key consideration for the CsYb mixture. Condensate population numbers for each component are measured via bimodal fits to the optical density slices, observed through absorption imaging, given by the solid curves in Figure 1.7, whilst the thermal fraction is extracted via a Gaussian fit given by the dashed curves, demonstrating relatively large thermal fractions found in both components [214]. Due to the sympathetic cooling of Cs with Yb [214, 219], there is typically an Yb population imbalance with the fits in Figure 1.7 showing population numbers of $N_{\mathrm{Yb}} = 6 \times 10^4$ and $N_{\mathrm{Cs}} = 1.6 \times 10^4$, however, imbalances of up to $N_{\mathrm{Yb}} = [5, 7] \times 10^4$ and $N_{\mathrm{Cs}} = [4, 5] \times 10^3$ have been created [214]. Thus, the combination of high losses and small population numbers of the Cs component could be an issue for droplet formation, and thus one of the focuses of this work is to understand the constraints on this mixture and how these could be alleviated.

1.5 List of publications

The results presented in this thesis have yielded two publications:

[221] T. A. Flynn, L. Parisi, T. P. Billam, and N. G. Parker, "Quantum droplets in imbalanced atomic mixtures", Phys. Rev. Res. **5**, 033167 (2023) - This forms the

majority of the results presented in Chapter 3

[**222**] T. A. Flynn, N. A. Keepfer, N. G. Parker, and T. P. Billam, "Harmonically trapped imbalanced quantum droplets", Phys. Rev. Res. **6**, 013209 (2024) - This forms the majority of the results presented in Chapter 4

Other works via collaboration not presented within this thesis are:

[**223**] J. McMillan, T. A. Flynn, and R. Doran, "Predicting Bubble Fragmentation in Superfluids", Phys. Rev. Lett. **133**, 093403 (2024)

[**224**] N. Keepfer, T. Flynn, N. Parker, and T. Billam, "Supervortexnet: Reconstructing superfluid vortex filaments using deep learning" (2023), arXiv:2312.14815

1.6 Document outline

The overarching theme of this thesis is: how do imbalances modify two-component droplets? The main imbalances which can be considered are: population numbers, intraspecies scattering lengths, atomic masses and trapping potentials, and the motivation behind this is the CsYb mixture which possesses all of these imbalances. From an idealistic theory perspective, the simplest droplet to consider would have all of these properties balanced. This thesis principally explores the impact of population imbalances on droplet ground states and breathing modes, both in free space and within harmonic traps. Other imbalances such as scattering lengths and traps are likewise studied, predominantly in the context of the CsYb mixture.

The rest of this thesis is set out as:

Chapter 2 - presents the theoretical background of the models used to describe weakly-interacting mixtures, including the contributions of quantum fluctuations. The computational methods to solve these models are introduced and applied to review the physics of droplets presented in the seminal droplet work of Ref. [153].

Chapter 3 - studies the effect of population imbalances on the ground states and breathing of free-space droplets which display a rich parameter space of superimposed decaying modes. This chapter concludes by looking at population imbalances with the addition of intraspecies scattering length imbalances, which are more relevant to typical experimental mixtures.

Chapter 4 - builds from Chapter 3 to study population imbalances within traps, in which any unbound excess atoms are retained around the droplet. In the context of ground states and breathing modes, both trap frequencies and imbalance size are explored. The final results of this chapter focus on the stability of the imbalance under a trap release, both instantaneous and linearly-ramped, to answer the question of whether population imbalances can be retained in the transition from trapped to free space droplets.

Chapter 5 - focuses on the CsYb mixture to predict characteristics of CsYb droplets, including the application of results from Chapters 3 and 4. The principle observables are droplet sizes, densities and lifetimes. Following on from a discussion of the viability of droplets in the current CsYb experiment, this chapter proposes potential future experiments to study excitations and non-equilibrium of two-component droplets.

Chapter 6 - concludes the main results of this thesis and briefly discusses natural follow up questions that arise from this thesis leading to potential future work. This includes extending some of the results presented here and exploring potential future avenues for the experimental CsYb mixture.

Chapter 2

Theoretical Background

A mainstay of modelling Bose-condensed gases is mean-field Gross-Pitaevskii (GP) theory, in which the condensate is described by a classical field and quantum correlations are neglected. In addition to the typical repulsive interactions, this theory also accommodates attractive interactions, but for these it predicts collapse in free space, as observed experimentally by tuning from repulsive to attractive interactions [67, 68]. In the first work predicting the existence of quantum droplets, Ref. [153] proposes that attractive two-body interactions, paired with quantum fluctuations stabilises the collapse of a two-component bosonic mixture. This chapter presents the theoretical background necessary for modelling droplets, starting with microscopic derivations of the ground state energy of uniform, single and two-component Bose gases, including quantum corrections to the mean-field. Building from these uniform energy calculations non-uniform Bose gases can be described by the famed GP equation. To study ground states and dynamics, the GP equation must, in general, be solved numerically and so the computational techniques used throughout this thesis are presented here. Finally, these methods are put into practice to review well known results of quantum droplets, that were first introduced in the seminal paper of Petrov [153].

2.1 Bose gas ground state energy

The ground state energy of a homogeneous, weakly-interacting, dilute Bose gas at zero temperature is given by [225–227]

$$\frac{E_0}{V} = \frac{gn^2}{2}\left[1 + \frac{128}{15\sqrt{\pi}}\sqrt{na^3} + \dots\right], \tag{2.1}$$

where V is the system volume, n is the number density of the Bose gas and g is the effective interaction strength which relates to the scattering length a by

$$g = \frac{4\pi\hbar^2 a}{m},$$

where m is the atomic mass. The scattering length, a, characterises scattering events at low energy which is the dominant regime of two-body scattering events in ultracold, dilute gases. The first term of Equation (2.1) is described as the Mean-Field (MF) contribution whilst the second term is the Lee-Huang-Yang (LHY) correction. It should be noted that further corrections have been computed such as the beyond LHY correction, the so-called Wu-Hugenholtz-Pines-Sawada (WHPS) correction [228–230]. However, the WHPS correction is defined in terms of a coefficient that depends on the form of the interatomic interactions, whereas the LHY correction depends only on an expansion in terms of the gas parameter, na^3, i.e., no further information is required to compute the LHY correction.

Equation (2.1) shows the higher-order density dependence of the LHY correction, $\sim n^{5/2}$, relative to the MF contribution, $\sim n^2$. As ultracold experiments are within the dilute limit in which the gas parameter is assumed to be small, $na^3 \ll 1$, the LHY correction typically contributes very little to the system energy, though it has been measured in strongly-interacting Bose gases [231]. The derivation of the Bose gas ground state energy is a key result in the study of quantum many-body systems, especially given the simplicity of the expression which depends on only three parameters: the density, scattering length and atomic mass. This section works through the microscopic derivation of the single-component Bose gas ground state energy indicating the assumptions and approximations that are built into Equation (2.1).

2.1.1 Second quantisation

The system Hamiltonian in second-quantisation notation can be written as [45]

$$\hat{H} = \int \mathrm{d}\mathbf{r} \left[\frac{\hbar^2}{2m} \boldsymbol{\nabla}\hat{\Psi}^\dagger(\mathbf{r}) \boldsymbol{\nabla}\hat{\Psi}(\mathbf{r}) \right] + \frac{1}{2} \int \mathrm{d}\mathbf{r}\mathrm{d}\mathbf{r}' \left[\hat{\Psi}^\dagger(\mathbf{r}) \hat{\Psi}^\dagger(\mathbf{r}') \mathcal{V}(\mathbf{r}-\mathbf{r}') \hat{\Psi}(\mathbf{r}') \hat{\Psi}(\mathbf{r}) \right], \tag{2.2}$$

in which the Hamiltonian is expressed as $\hat{H} = \hat{H}_{\mathrm{ke}} + \hat{H}_{\mathrm{int}}$ with kinetic, $\hat{H}_{\mathrm{ke}}$, and interaction, $\hat{H}_{\mathrm{int}}$, contributions, where $\hat{\Psi}^\dagger(\mathbf{r})$ and $\hat{\Psi}(\mathbf{r})$ are the bosonic field operators and $\mathcal{V}$ is the two-body interaction potential. For a uniform gas it is convenient to express the bosonic field operators in a basis of single-particle states [11, 45],

$$\hat{\Psi}(\mathbf{r}) = \frac{1}{\sqrt{V}} \sum_{\mathbf{p}} \hat{a}_{\mathbf{p}} e^{i\mathbf{p}\cdot\mathbf{r}/\hbar},$$

and

$$\hat{\Psi}^\dagger(\mathbf{r}) = \frac{1}{\sqrt{V}} \sum_{\mathbf{p}} \hat{a}^\dagger_{\mathbf{p}} e^{-i\mathbf{p}\cdot\mathbf{r}/\hbar},$$

where $\hat{a}_{\mathbf{p}}$ and $\hat{a}^\dagger_{\mathbf{p}}$ are the bosonic annihilation and creation operators, respectively, of a particle with momentum $\mathbf{p}$. Substituting these plane-wave-like solutions into Equation (2.2)

gives

$$\hat{H} = \int \mathrm{d}\mathbf{r} \left\{ \frac{\hbar^2}{2m} \left[\left(-\frac{i}{\hbar}\mathbf{p} \right) \frac{1}{\sqrt{V}} \sum_{\mathbf{p}} \hat{a}^\dagger_{\mathbf{p}} e^{-i\mathbf{p}\cdot\mathbf{r}/\hbar} \right] \left[\left(\frac{i}{\hbar}\mathbf{p} \right) \frac{1}{\sqrt{V}} \sum_{\mathbf{p}} \hat{a}_{\mathbf{p}} e^{i\mathbf{p}\cdot\mathbf{r}/\hbar} \right] \right\}$$
$$+ \frac{1}{2} \int \mathrm{d}\mathbf{r}\mathrm{d}\mathbf{r}' \left[\left(\frac{1}{\sqrt{V}} \sum_{\mathbf{p}} \hat{a}^\dagger_{\mathbf{p}} e^{-i\mathbf{p}\cdot\mathbf{r}/\hbar} \right) \left(\frac{1}{\sqrt{V}} \sum_{\mathbf{p}} \hat{a}^\dagger_{\mathbf{p}} e^{-i\mathbf{p}\cdot\mathbf{r}'/\hbar} \right) \mathcal{V}(\mathbf{r}-\mathbf{r}') \right.$$
$$\left. \left(\frac{1}{\sqrt{V}} \sum_{\mathbf{p}} \hat{a}_{\mathbf{p}} e^{i\mathbf{p}\cdot\mathbf{r}'/\hbar} \right) \left(\frac{1}{\sqrt{V}} \sum_{\mathbf{p}} \hat{a}_{\mathbf{p}} e^{i\mathbf{p}\cdot\mathbf{r}/\hbar} \right) \right].$$

Kinetic energy

Considering the kinetic contributions first, the expression of $\hat{H}_{\mathrm{ke}}$ simplifies substantially to,

$$\begin{aligned} \hat{H}_{\mathrm{ke}} &= \frac{1}{V} \int \mathrm{d}\mathbf{r} \sum_{\mathbf{p}} \frac{p^2}{2m} \hat{a}^\dagger_{\mathbf{p}} \hat{a}_{\mathbf{p}} \\ &= \sum_{\mathbf{p}} \frac{p^2}{2m} \hat{a}^\dagger_{\mathbf{p}} \hat{a}_{\mathbf{p}}, \end{aligned}$$

in which $p^2 = \mathbf{p}\cdot\mathbf{p}$ and where, due to the lack of $\mathbf{r}$ dependence the identity, $\int \mathrm{d}\mathbf{r} = V$, is used.

Interaction energy

Next are the interaction contributions, $\hat{H}_{\mathrm{int}}$. A labelling is introduced for convenience: let $\mathbf{r_1}$ and $\mathbf{r_2}$ denote the positions of two interacting particles, with initial momenta $\mathbf{p_1}$ and $\mathbf{p_2}$ and final momenta $\mathbf{p_3}$ and $\mathbf{p_4}$, whose interaction is described by the potential $\mathcal{V}(\mathbf{r_1}-\mathbf{r_2})$. With this labelling the interaction Hamiltonian becomes

$$\begin{aligned} \hat{H}_{\mathrm{int}} &= \frac{1}{2} \int \mathrm{d}\mathbf{r_1}\, \mathrm{d}\mathbf{r_2} \left[\left(\frac{1}{\sqrt{V}} \sum_{\mathbf{p_3}} \hat{a}^\dagger_{\mathbf{p_3}} e^{-i\mathbf{p_3}\cdot\mathbf{r_1}/\hbar} \right) \left(\frac{1}{\sqrt{V}} \sum_{\mathbf{p_4}} \hat{a}^\dagger_{\mathbf{p_4}} e^{-i\mathbf{p_4}\cdot\mathbf{r_2}/\hbar} \right) \mathcal{V}(\mathbf{r_1}-\mathbf{r_2}) \right. \\ &\qquad \left. \left(\frac{1}{\sqrt{V}} \sum_{\mathbf{p_2}} \hat{a}_{\mathbf{p_2}} e^{i\mathbf{p_2}\cdot\mathbf{r_2}/\hbar} \right) \left(\frac{1}{\sqrt{V}} \sum_{\mathbf{p_1}} \hat{a}_{\mathbf{p_1}} e^{i\mathbf{p_1}\cdot\mathbf{r_1}/\hbar} \right) \right] \\ &= \frac{1}{2V^2} \int \mathrm{d}\mathbf{r_1}\, \mathrm{d}\mathbf{r_2} \left[\sum_{\{\mathbf{p_i}\}} \mathcal{V}(\mathbf{r_1}-\mathbf{r_2}) \hat{a}^\dagger_{\mathbf{p_3}} \hat{a}^\dagger_{\mathbf{p_4}} \hat{a}_{\mathbf{p_2}} \hat{a}_{\mathbf{p_1}} e^{-i(\mathbf{p_3}-\mathbf{p_1})\cdot\mathbf{r_1}/\hbar} e^{-i(\mathbf{p_4}-\mathbf{p_2})\cdot\mathbf{r_2}/\hbar} \right], \end{aligned}$$

where $\{\mathbf{p_i}\} = \{\mathbf{p_1}, \mathbf{p_2}, \mathbf{p_3}, \mathbf{p_4}\}$. Using conservation of linear momentum, $\mathbf{p_1}+\mathbf{p_2} = \mathbf{p_3}+\mathbf{p_4}$, the final momenta can be relabelled as $\mathbf{p_3} = \mathbf{p_1}+\mathbf{q}$ and $\mathbf{p_4} = \mathbf{p_2}-\mathbf{q}$, thus the interaction Hamiltonian becomes

$$\hat{H}_{\mathrm{int}} = \frac{1}{2V^2} \sum_{\mathbf{p_1},\mathbf{p_2},\mathbf{q}} \int \mathrm{d}\mathbf{r_1}\, \mathrm{d}\mathbf{r_2} \left[\mathcal{V}(\mathbf{r_1}-\mathbf{r_2}) e^{-i\mathbf{q}\cdot(\mathbf{r_1}-\mathbf{r_2})/\hbar} \right] \hat{a}^\dagger_{\mathbf{p_1}+\mathbf{q}} \hat{a}^\dagger_{\mathbf{p_2}-\mathbf{q}} \hat{a}_{\mathbf{p_2}} \hat{a}_{\mathbf{p_1}}.$$

Particle positions can instead be rewritten as $\mathbf{r}' = \mathbf{r_1}-\mathbf{r_2}$, thus the integral is expressed

as

$$\hat{H}_{\text{int}} = \frac{1}{2V^2} \sum_{\mathbf{p_1},\mathbf{p_2},\mathbf{q}} \int \mathrm{d}\mathbf{r}\, \mathrm{d}\mathbf{r}' \left[\mathcal{V}(\mathbf{r}')e^{-i\mathbf{q}\cdot\mathbf{r}'/\hbar}\right] \hat{a}^\dagger_{\mathbf{p_1}+\mathbf{q}} \hat{a}^\dagger_{\mathbf{p_2}-\mathbf{q}} \hat{a}_{\mathbf{p_2}} \hat{a}_{\mathbf{p_1}}.$$

Note that the interaction Hamiltonian has been written in terms of the Fourier transform of the interaction potential,

$$\mathcal{V}(\mathbf{q}) = \int \mathrm{d}\mathbf{r}'\, \mathcal{V}(\mathbf{r}')e^{-i\mathbf{q}\cdot\mathbf{r}'/\hbar},$$

thus, the interaction Hamiltonian is independent of $\mathbf{r}$ and so a factor of $V = \int \mathrm{d}\mathbf{r}$ is gained, giving,

$$\hat{H}_{\text{int}} = \frac{1}{2V} \sum_{\mathbf{p_1},\mathbf{p_2},\mathbf{q}} \mathcal{V}(\mathbf{q}) \hat{a}^\dagger_{\mathbf{p_1}+\mathbf{q}} \hat{a}^\dagger_{\mathbf{p_2}-\mathbf{q}} \hat{a}_{\mathbf{p_2}} \hat{a}_{\mathbf{p_1}}.$$

2.1.2 Bogoliubov approximation

Having now written the total system Hamiltonian in terms of momentum states as,

$$\hat{H} = \sum_{\mathbf{p}} \frac{p^2}{2m} \hat{a}^\dagger_{\mathbf{p}} \hat{a}_{\mathbf{p}} + \frac{1}{2V} \sum_{\mathbf{p_1},\mathbf{p_2},\mathbf{q}} \mathcal{V}(\mathbf{q}) \hat{a}^\dagger_{\mathbf{p_1}+\mathbf{q}} \hat{a}^\dagger_{\mathbf{p_2}-\mathbf{q}} \hat{a}_{\mathbf{p_2}} \hat{a}_{\mathbf{p_1}},$$

the system can be easily split up into different momentum contributions. The zero momentum state corresponds to the condensate, though even at zero-temperature there will still be some occupation of $\mathbf{p} \neq \mathbf{0}$ modes due to interactions.

Mean-Field

In the limit of large condensate occupation — i.e., in the regime of $N_0 \gg 1$, where N_0 is the population number of the zero momentum state — the zero momentum creation and annihilation operators can be replaced by the condensate number, $\hat{a}^\dagger_{\mathbf{0}} = \hat{a}_{\mathbf{0}} = \sqrt{N_0}$, an approximation first introduced by Bogoliubov [232]. In the case of a ground-state, non-interacting Bose gas at zero temperature, all bosons are condensed, however, the addition of weak interactions corresponds to a relatively small occupation of non-zero momentum modes, even at zero temperature [45]. Therefore a ground-state, weakly-interacting Bose gas at zero temperature can be roughly approximated by neglecting the small contributions from non-zero modes, i.e., total occupation of the zero momentum state, $N = N_0$. Hence, the MF ground state energy is given by

$$E_0 = \frac{gN_0^2}{2V}.$$

The true interaction potential between atoms is complicated and varies significantly with the interatomic distance, e.g., typically at small interatomic distances interactions are dominantly repulsive, but at larger distances interactions are weakly attractive [11, 45]. In the dilute, low-temperature limit, interactions between three or more atoms are extremely

rare, and so two-body interactions dominate. These interactions only contribute significantly in the small interatomic limit. Hence, rather than computing the interatomic potential explicitly, an effective interaction potential is introduced, in the form of a 'contact-interaction', $\mathcal{V}(\mathbf{r}) = \mathcal{V}_0\delta(\mathbf{r})$, with Fourier transform, $\mathcal{V}(\mathbf{q}) = \mathcal{V}_0$. Via the first-order Born approximation the interactive strength, $\mathcal{V}_0$, can be expressed as $\mathcal{V}_0 = g = 4\pi\hbar^2 a/m$. The MF energy density is therefore

$$\frac{E_{\mathrm{MF}}}{V} = \frac{gn^2}{2},$$

where the number density is defined as $n = N_0/V$.

The number density can be related to the so-called macroscopic wavefunction or order parameter of the gas, $n = |\Psi|^2$. Thus under a Local-Density Approximation (LDA) the non-uniform, MF energy can be written as [233]

$$E = \int \mathrm{d}\mathbf{r} \left[\frac{\hbar^2}{2m} |\boldsymbol{\nabla}\Psi|^2 + V_{\mathrm{ext}}|\Psi|^2 + \frac{g}{2}|\Psi|^4 \right],$$

where the first term is the kinetic energy, the second term describes an externally imposed potential V_{ext}, and the final term describes the two-body interactions. The First Green identity allows for the kinetic energy term to be rewritten as $|\boldsymbol{\nabla}\Psi|^2 = -\Psi^*\nabla^2\Psi$, and hence under the variational relationship [45]

$$i\hbar\frac{\partial\Psi}{\partial t} = \frac{\delta E}{\delta\Psi^*},$$

the energy functional can be minimised resulting in the famed Gross-Pitaevskii (GP) equation [234, 235]

$$i\hbar\frac{\partial\Psi}{\partial t} = \left[-\frac{\hbar^2}{2m}\nabla^2 + V_{\mathrm{ext}} + g|\Psi|^2 \right]\Psi. \tag{2.3}$$

There are inevitable questions about the LDA approach used here, i.e., how valid in general is this approach for non-uniform gases. This method results in the same GP equation as writing the field operator in the Heisenberg representation [45, 236]

$$i\hbar\frac{\partial\hat{\Psi}(\mathbf{r},t)}{\partial t} = \left[\hat{\Psi}(\mathbf{r},t), \hat{H}\right],$$

and then using similar arguments of replacing the field operator with a classical field, and the interaction potential with an effective interaction. The Heisenberg representation method is the more common and self-consistent approach for describing non-uniform, MF Bose gases [45, 236].

Beyond-Mean-Field

Beyond the MF approximation, non-zero momentum terms can be retained. However, one key assumption of the Bogoliubov approach used here is that the condensate mode

dominates, i.e., non-zero momentum interaction events are unlikely hence terms only up to quadratic order in non-zero momentum operators are retained in the interaction Hamiltonian,

$$\hat{H}_{\text{int}} = \frac{1}{2V}\left[\mathcal{V}(\mathbf{0})N_0^2 + N_0\sum_{\mathbf{p}\neq 0}\left(2\left[\mathcal{V}(\mathbf{0})+\mathcal{V}(\mathbf{p})\right]\hat{a}_{\mathbf{p}}^\dagger\hat{a}_{\mathbf{p}} + \mathcal{V}(\mathbf{p})\left[\hat{a}_{\mathbf{p}}^\dagger\hat{a}_{-\mathbf{p}}^\dagger + \hat{a}_{\mathbf{p}}\hat{a}_{-\mathbf{p}}\right]\right)\right]. \quad (2.4)$$

Details for this simplification can be found in Appendix A.1, but in brief: terms are neglected if they correspond to interactions between two non-zero momentum particles as these events are very rare in the dilute, weakly-interacting, zero-temperature regime.

Unlike in the MF approximation where the total number of atoms equals the condensate occupation, the total number of atoms including non-zero momentum particles can be expressed by the expectation value of the number operator [11]

$$N = N_0 + \sum_{\mathbf{p}\neq 0}\hat{a}_{\mathbf{p}}^\dagger\hat{a}_{\mathbf{p}}.$$

Recall that any terms beyond quadratic order in creation and annihilation operators are neglected, hence for the terms of Equation (2.4) that are linear in N_0, there is a simple replacement of $N_0 \approx N$. This is because otherwise these terms will be quartic in the creation and annihilation operators. However, for terms with N_0^2 dependence, the approximation $N_0^2 = \left(N - \sum_{\mathbf{p}\neq 0}\hat{a}_{\mathbf{p}}^\dagger\hat{a}_{\mathbf{p}}\right)^2 \approx N^2 - 2N\sum_{\mathbf{p}\neq 0}\hat{a}_{\mathbf{p}}^\dagger\hat{a}_{\mathbf{p}}$ is used, which gives

$$\begin{aligned}\hat{H}_{\text{int}} &= \frac{1}{2V}\Bigg[\mathcal{V}(\mathbf{0})N^2 - 2\mathcal{V}(\mathbf{0})N\sum_{\mathbf{p}\neq 0}\hat{a}_{\mathbf{p}}^\dagger\hat{a}_{\mathbf{p}} + N\sum_{\mathbf{p}\neq 0}\Big(2\left[\mathcal{V}(\mathbf{0})+\mathcal{V}(\mathbf{p})\right]\hat{a}_{\mathbf{p}}^\dagger\hat{a}_{\mathbf{p}} \\ &\qquad + \mathcal{V}(\mathbf{p})\left[\hat{a}_{\mathbf{p}}^\dagger\hat{a}_{-\mathbf{p}}^\dagger + \hat{a}_{\mathbf{p}}\hat{a}_{-\mathbf{p}}\right]\Big)\Bigg] \\ &= \frac{1}{2V}\left[\mathcal{V}(\mathbf{0})N^2 + N\sum_{\mathbf{p}\neq 0}\mathcal{V}(\mathbf{p})\left(2\hat{a}_{\mathbf{p}}^\dagger\hat{a}_{\mathbf{p}} + \hat{a}_{\mathbf{p}}^\dagger\hat{a}_{-\mathbf{p}}^\dagger + \hat{a}_{\mathbf{p}}\hat{a}_{-\mathbf{p}}\right)\right].\end{aligned}$$

Combining both the interaction and kinetic Hamiltonians yields

$$\hat{H} = \frac{\mathcal{V}(\mathbf{0})N^2}{2V} + \sum_{\mathbf{p}\neq 0}\left[\left(\varepsilon_p + \frac{\mathcal{V}(\mathbf{p})N}{V}\right)\hat{a}_{\mathbf{p}}^\dagger\hat{a}_{\mathbf{p}} + \frac{\mathcal{V}(\mathbf{p})N}{2V}\left(\hat{a}_{\mathbf{p}}^\dagger\hat{a}_{-\mathbf{p}}^\dagger + \hat{a}_{\mathbf{p}}\hat{a}_{-\mathbf{p}}\right)\right], \quad (2.5)$$

where $\varepsilon_p = p^2/2m$, is the dispersion relation of a free particle.

2.1.3 Bogoliubov transformation

The Bogoliubov transformation can be used to diagonalise Equation (2.5) [232], in which a new set of operators are introduced known as the Bogoliubov quasiparticle operators,

given by

$$\hat{\alpha}_{\mathbf{p}} = u_p \hat{a}_{\mathbf{p}} + v_p \hat{a}^{\dagger}_{-\mathbf{p}},$$
$$\hat{\alpha}^{\dagger}_{\mathbf{p}} = u_p \hat{a}^{\dagger}_{\mathbf{p}} + v_p \hat{a}_{-\mathbf{p}}.$$

The Bogoliubov quasiparticle operators likewise obey the bosonic commutation relations

$$\left[\hat{\alpha}_{\mathbf{p}}, \hat{\alpha}^{\dagger}_{\mathbf{p}'}\right] = \delta_{\mathbf{p},\mathbf{p}'},\ [\hat{\alpha}_{\mathbf{p}}, \hat{\alpha}_{\mathbf{p}'}] = 0, \text{ and, } \left[\hat{\alpha}^{\dagger}_{\mathbf{p}}, \hat{\alpha}^{\dagger}_{\mathbf{p}'}\right] = 0, \tag{2.6}$$

which result in the relationship,

$$u_p^2 - v_p^2 = 1, \forall \mathbf{p}. \tag{2.7}$$

The Bogoliubov operators can be equivalently written as

$$\hat{a}_{\mathbf{p}} = u_p \hat{\alpha}_{\mathbf{p}} - v_p \hat{\alpha}^{\dagger}_{-\mathbf{p}},$$
$$\hat{a}^{\dagger}_{\mathbf{p}} = u_p \hat{\alpha}^{\dagger}_{\mathbf{p}} - v_p \hat{\alpha}_{-\mathbf{p}}.$$

Substituting these expressions into Equation (2.5) gives

$$\begin{aligned}\hat{H} = \frac{\mathcal{V}(\mathbf{0})N^2}{2V} &+ \sum_{\mathbf{p}\neq 0}\left[\tilde{\varepsilon}_p v_p^2 - \frac{\mathcal{V}(\mathbf{p})N}{V} u_p v_p\right] \\ &+ \sum_{\mathbf{p}\neq 0}\left[\tilde{\varepsilon}_p\left(u_p^2 + v_p^2\right) - 2\frac{\mathcal{V}(\mathbf{p})N}{V} u_p v_p\right]\hat{\alpha}^{\dagger}_{\mathbf{p}}\hat{\alpha}_{\mathbf{p}} \\ &+ \sum_{\mathbf{p}\neq 0}\left[-\tilde{\varepsilon}_p u_p v_p + \frac{\mathcal{V}(\mathbf{p})N}{2V}\left(u_p^2 + v_p^2\right)\right]\left(\hat{\alpha}^{\dagger}_{\mathbf{p}}\hat{\alpha}^{\dagger}_{-\mathbf{p}} + \hat{\alpha}_{-\mathbf{p}}\hat{\alpha}_{\mathbf{p}}\right),\end{aligned}$$

where $\tilde{\varepsilon}_p = \varepsilon_p + \mathcal{V}(\mathbf{p})n$. Hence, the Hamiltonian can be written in the form

$$\hat{H} = E_0 + \sum_{\mathbf{p}\neq 0}\left[\tilde{\varepsilon}_p\left(u_p^2 + v_p^2\right) - 2\frac{\mathcal{V}(\mathbf{p})N}{V} u_p v_p\right]\hat{\alpha}^{\dagger}_{\mathbf{p}}\hat{\alpha}_{\mathbf{p}},$$

if

$$-\tilde{\varepsilon}_p u_p v_p + \frac{\mathcal{V}(\mathbf{p})n}{2}\left(u_p^2 + v_p^2\right) = 0.$$

With this condition and Equation (2.7), the Bogoliubov quasiparticle amplitudes are found to be

$$u_p^2 = \frac{1}{2}\left[\frac{\tilde{\varepsilon}_p}{\sqrt{\tilde{\varepsilon}_p^2 - \{\mathcal{V}(\mathbf{0})n\}^2}} + 1\right],$$
$$v_p^2 = \frac{1}{2}\left[\frac{\tilde{\varepsilon}_p}{\sqrt{\tilde{\varepsilon}_p^2 - \{\mathcal{V}(\mathbf{0})n\}^2}} - 1\right].$$

For details of finding the quasiparticle amplitudes see Appendix A.2. Substituting the definitions of u_p and v_p means the Hamiltonian can be written as

$$\hat{H} = E_0 + \sum_{\mathbf{p}\neq 0} E_p \hat{\alpha}_{\mathbf{p}}^\dagger \hat{\alpha}_{\mathbf{p}},$$

where E_p is

$$\begin{aligned} E_p &= \sqrt{\tilde{\varepsilon}_p^2 - [\mathcal{V}(\mathbf{p})n]^2} \\ &= \sqrt{\left(\frac{p^2}{2m}\right)^2 + \frac{\mathcal{V}(\mathbf{p})np^2}{m}}, \end{aligned} \tag{2.8}$$

which is the dispersion relation of the Bogoliubov quasiparticles or elementary excitations of the Bose gas [232]. The Bogoliubov dispersion relation or excitation spectrum, given in Figure 2.1, has two regimes: a linear phonon regime at small momentum, where $E_p \sim p$ (solid curve, inset); and a free-particle regime at large momentum, where $E_p \sim p^2$ (dashed curve). The transition between small and large momentum behaviour occurs at approximately the momentum associated with the healing length — indicated in Figure 2.1 as ξ^{-1} — which is defined as [11, 45]

$$\xi = \frac{\hbar}{\sqrt{mng}}.$$

The healing length can be considered the length scale at which the gas 'heals' to a boundary, i.e., the gas density at a hard-wall boundary must be zero and so the healing length defines the length scale at which the gas density decreases from the bulk or equilibrium density to zero. Below this 'healing momentum' the gas has a phonon or sound-like spectrum with speed of sound [11, 45]

$$c = \sqrt{\frac{ng}{m}},$$

whilst above, the spectrum is free-particle-like. Therefore, at lower momentum the system behaves collectively, rather than a system of free particles as at higher momentum. Equiv-

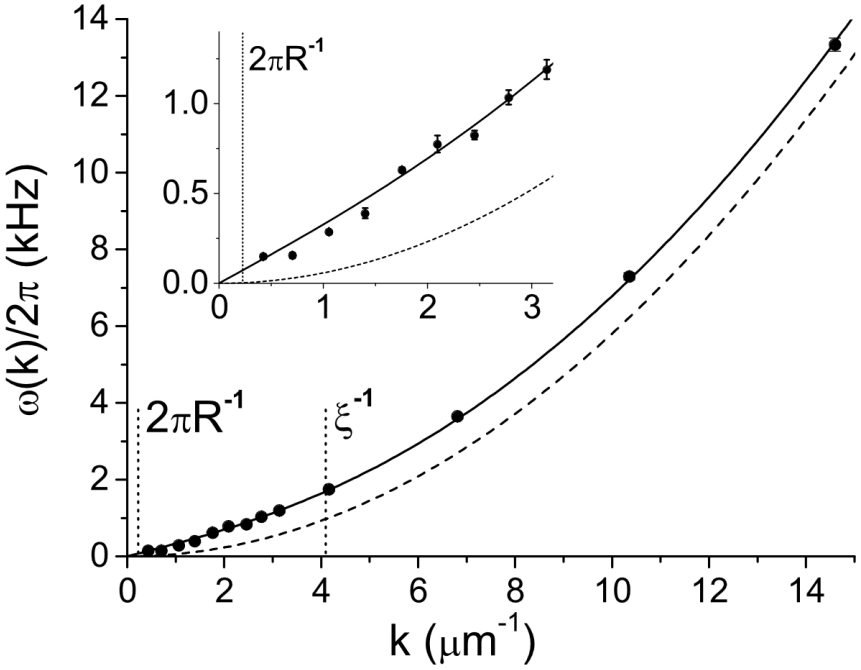

Figure 2.1: Excitation spectrum of a weakly-interaction, dilute gas of ^{87}Rb atoms. The black circles are experimental data with error bars (though these error bars are difficult to see in the main figure). The black curve is the Bogoliubov excitation spectrum given by Equation (2.8), whilst the dashed curve is the free-particle spectrum $E_p = \hbar^2 p^2/(2m)$. The inset shows the same data but focused onto the small momentum, phonon regime. Reprinted figure with permission from Ref. [237]. Copyright (2002) by the American Physical Society.

alently, by inverting from momentum space, the system behaves collectively at length scales larger than the healing length, in keeping with the notion of global coherence in Bose-Einstein condensates discussed in Chapter 1.

Having decomposed the Hamiltonian in terms of the ground state and the spectrum of quasiparticles, the ground state energy, E_0, takes the form

$$E_0 = \frac{\mathcal{V}(\mathbf{0})N^2}{2V} + \frac{1}{2}\sum_{\mathbf{p}\neq 0}\left(E_p - \tilde{\varepsilon}_p\right). \tag{2.9}$$

The lowest order Born approximation defines the zero momentum interaction potential as the effective interaction strength, $\mathcal{V}(\mathbf{0}) \approx g = 4\pi\hbar^2/m$. As shown above, this substitution is used to derive the MF ground state energy of a weakly-interacting Bose gas. Naively both $\mathcal{V}(\mathbf{p})$ and $\mathcal{V}(\mathbf{0})$ could be approximated by the effective interaction strength, g. However, unlike in the MF case the BMF ground state energy depends on a sum over momenta. Hence, simply replacing $\mathcal{V}(\mathbf{0})$ and $\mathcal{V}(\mathbf{p})$ by the lower order Born approximation causes Equation (2.9) to become UV divergent, demonstrating the significance of the interaction potential's momentum dependence.

2.1.4 Renormalisation

To eliminate the UV divergence in Equation (2.9) it is useful to return back to Equation (2.5),

$$\hat{H} = \frac{\mathcal{V}(\mathbf{0})N^2}{2V} + \sum_{\mathbf{p}\neq 0}\left[\tilde{\varepsilon}_p \hat{a}^\dagger_{\mathbf{p}}\hat{a}_{\mathbf{p}} + \frac{\mathcal{V}(\mathbf{p})N}{2V}\left(\hat{a}^\dagger_{\mathbf{p}}\hat{a}^\dagger_{-\mathbf{p}} + \hat{a}_{\mathbf{p}}\hat{a}_{-\mathbf{p}}\right)\right].$$

Beyond the lowest-order Born approximation, $\mathcal{V}(\mathbf{0}) = g$, the momentum interaction potential can be written as [45]

$$\mathcal{V}(\mathbf{0}) \approx g\left(1 + \frac{g}{V}\sum_{\mathbf{p}\neq 0}\frac{m}{p^2}\right).$$

The $1/p^2$ correction renormalises the UV divergence of Equation (2.9), and hence substituting this expression into Equation (2.5) gives

$$\begin{aligned}\hat{H} &= \frac{N^2}{2V}\left[g\left(1 + \frac{g}{V}\sum_{\mathbf{p}\neq 0}\frac{m}{p^2}\right)\right] + \sum_{\mathbf{p}\neq 0}\left[\tilde{\varepsilon}_p \hat{a}^\dagger_{\mathbf{p}}\hat{a}_{\mathbf{p}} + \frac{\mathcal{V}(\mathbf{p})N}{2V}\left(\hat{a}^\dagger_{\mathbf{p}}\hat{a}^\dagger_{-\mathbf{p}} + \hat{a}_{\mathbf{p}}\hat{a}_{-\mathbf{p}}\right)\right] \\ &= \frac{gN^2}{2V} + \sum_{\mathbf{p}\neq 0}\left[\tilde{\varepsilon}_p \hat{a}^\dagger_{\mathbf{p}}\hat{a}_{\mathbf{p}} + \frac{\mathcal{V}(\mathbf{p})N}{2V}\left(\hat{a}^\dagger_{\mathbf{p}}\hat{a}^\dagger_{-\mathbf{p}} + \hat{a}_{\mathbf{p}}\hat{a}_{-\mathbf{p}}\right) + \frac{mg^2nN}{2Vp^2}\right].\end{aligned}$$

This renormalised sum is convergent and so the interaction potential at arbitrary momentum can now be approximated by, $\mathcal{V}(\mathbf{p}) \approx g$, giving

$$\hat{H} = \frac{gN^2}{2V} + \sum_{\mathbf{p}\neq 0}\left[\tilde{\varepsilon}_p \hat{a}^\dagger_{\mathbf{p}}\hat{a}_{\mathbf{p}} + \frac{gN}{2V}\left(\hat{a}^\dagger_{\mathbf{p}}\hat{a}^\dagger_{-\mathbf{p}} + \hat{a}_{\mathbf{p}}\hat{a}_{-\mathbf{p}} + \frac{mgn}{p^2}\right)\right].$$

Proceeding through the Bogoliubov quasiparticle operator steps once more extends Equation (2.9) to

$$E_0 = \frac{gN^2}{2V} + \frac{1}{2}\sum_{\mathbf{p}\neq 0}\left[E_p - \tilde{\varepsilon}_p + \frac{(gn)^2 m}{p^2}\right],$$

or more explicitly, the LHY correction takes the form

$$E_{\mathrm{LHY}} = \frac{1}{2}\sum_{\mathbf{p}\neq 0}\left[\sqrt{\left(\frac{p^2}{2m}\right)^2 + \left(\frac{gn}{m}\right)p^2} - \frac{p^2}{2m} - gn + \frac{(gn)^2 m}{p^2}\right].$$

In the thermodynamic limit, the summation can be converted to an integral, $\sum_{\mathbf{p}\neq 0} \to V\int \mathrm{d}\mathbf{p}\,/(2\pi\hbar)^3$, i.e.,

$$E_{\mathrm{LHY}} = \frac{V}{2(2\pi\hbar)^3}\int \mathrm{d}\mathbf{p}\left[\sqrt{\left(\frac{p^2}{2m}\right)^2 + \left(\frac{gn}{m}\right)p^2} - \frac{p^2}{2m} - gn + \frac{(gn)^2 m}{p^2}\right].$$

Due the spherical symmetry of the system, the measure can be expressed in terms of the momentum magnitude only, $\int \mathrm{d}\mathbf{p} = 4\pi \int_0^\infty p^2 \,\mathrm{d}p$, resulting in

$$E_{\mathrm{LHY}} = \frac{(gn)^2 mV}{2\pi^2\hbar^3} \int \mathrm{d}p \left(\frac{\varepsilon_p}{gn}\right) \left[\sqrt{\left(\frac{\varepsilon_p}{gn}\right)^2 + 2\left(\frac{\varepsilon_p}{gn}\right)} - \left(\frac{\varepsilon_p}{gn}\right) - 1 + \frac{gn}{2\varepsilon_p}\right].$$

Let $x^2 = \varepsilon_p/gn$ which reduces the integral to

$$E_{\mathrm{LHY}} = 4gn^2V\sqrt{\frac{2na^3}{\pi}} \int_0^\infty \mathrm{d}x\, x^2 \left[\sqrt{x^4 + 2x^2} + x^2 - 1 + \frac{1}{2x^2}\right].$$

This integral can be computed analytically as $2^{7/2}/15$ — for details on the asymptotic method used here, see Appendix A.4 — therefore the ground state energy of a dilute, weakly-interacting Bose gas at zero-temperature, takes the form

$$\frac{E_0}{V} = \frac{gn^2}{2}\left[1 + \frac{128}{15\sqrt{\pi}}\sqrt{na^3}\right], \tag{2.10}$$

to first order. This calculation has considered a uniform Bose gas to derive the ground state energy and, as shown in Section 2.1.2, a LDA approximation can be used to build the uniform energy density into a non-uniform energy functional. However, other methods, such as the Heisenberg representation of the bosonic field operator, avoid the use of the LDA [45, 236], though the present author is not aware of these methods being used to include the LHY correction.

The mechanism for droplet formation is a balance between attractive interactions and repulsion from quantum fluctuations, here described to first order by the LHY correction. A natural question is to ask whether this stabilised attractive collapse can be realised in a single-component Bose gas. Equation (2.10) indicates that if interactions are tuned to be attractive, $a < 0$, the LHY correction becomes complex valued. In free-space the single-component Bose gas is therefore unstable to attractive collapse, however, stable attractive states can exist in the trapped Bose gas. Bright solitary waves are stabilised through the competition of attractive interactions and dispersion from kinetic contributions, with singular [62] and multiple (forming so-called 'soliton trains') [238] bright solitary waves observed in quasi-1D, and in more general 3D harmonic traps [239]. Therefore, The LHY correction of the single-component, non-dipolar Bose gas cannot stabilise attractive interactions in free space.

2.2 Two-component Bose gas ground state energy

As the LHY correction cannot stabilise an attractive non-dipolar gas, this work turns to two-component bosonic mixtures which, as shown by Petrov in the seminal work predicting droplets, offer one such platform in which attractive interactions can be stabilised in

free-space by quantum fluctuations [153]. Building from the single-component calculation of the Bose gas ground state energy, this section presents the equivalent calculation of the two-component MF and LHY contributions.

2.2.1 Second quantisation

Beginning with the system Hamiltonian expressed in second-quantisation notation,

$$\hat{H} = \int \mathrm{d}\mathbf{r} \sum_{\sigma} \left[\frac{\hbar^2}{2m} \boldsymbol{\nabla}\hat{\Psi}^\dagger_\sigma(\mathbf{r}) \boldsymbol{\nabla}\hat{\Psi}_\sigma(\mathbf{r}) - \mu_\sigma \hat{\Psi}^\dagger_\sigma(\mathbf{r}) \hat{\Psi}_\sigma(\mathbf{r}) \right] + \frac{1}{2} \int \mathrm{d}\mathbf{r}\, \mathrm{d}\mathbf{r}' \sum_{\sigma,\sigma'} \hat{\Psi}^\dagger_\sigma(\mathbf{r}) \hat{\Psi}^\dagger_{\sigma'}(\mathbf{r}') \mathcal{V}_{\sigma\sigma'}(\mathbf{r}-\mathbf{r}') \hat{\Psi}_\sigma(\mathbf{r}') \hat{\Psi}_{\sigma'}(\mathbf{r}),$$

where $\hat{\Psi}^\dagger_\sigma(\mathbf{r})$ and $\hat{\Psi}_\sigma(\mathbf{r})$, are the bosonic field operators for the σ component and $\mathcal{V}_{\sigma\sigma'}(\cdot)$ is the two-body interaction potential between the σ and σ' components, where σ can equal σ'. It should be noted that contrary to the single-component case, the two-component Hamiltonian follows the convention of Ref. [240] and includes the chemical potentials of the σth component, μ_σ, to fix conditions on the component densities. As in the single-component case, it is convenient for a uniform system to express the field operators as plane waves

$$\hat{\Psi}_\sigma(\mathbf{r}) = \frac{1}{\sqrt{V}} \sum_{\mathbf{p}} \hat{a}_{\sigma,\mathbf{p}} e^{i\mathbf{r}\cdot\mathbf{p}/\hbar},$$

and

$$\hat{\Psi}^\dagger_\sigma(\mathbf{r}) = \frac{1}{\sqrt{V}} \sum_{\mathbf{p}} \hat{a}^\dagger_{\sigma,\mathbf{p}} e^{-i\mathbf{r}\cdot\mathbf{p}/\hbar}.$$

The Hamiltonian is again built of kinetic and interaction contributions, $\hat{H} = \hat{H}_{\mathrm{ke}} + \hat{H}_{\mathrm{int}}$, where

$$\hat{H}_{\mathrm{ke}} = \sum_{\sigma,\mathbf{p}} \left(\frac{p^2}{2m_\sigma} - \mu_\sigma \right) \hat{a}^\dagger_{\sigma,\mathbf{p}} \hat{a}_{\sigma,\mathbf{p}},$$

and

$$\hat{H}_{\mathrm{int}} = \frac{1}{2V^2} \int \mathrm{d}\mathbf{r_1}\, \mathrm{d}\mathbf{r_2} \sum_{\substack{\sigma,\sigma',\\ \{\mathbf{p_i}\}}} \left[\mathcal{V}_{\sigma\sigma'}\left(\mathbf{r_1}-\mathbf{r_2}\right) \hat{a}^\dagger_{\sigma,\mathbf{p_3}} \hat{a}^\dagger_{\sigma',\mathbf{p_4}} \hat{a}_{\sigma,\mathbf{p_2}} \hat{a}_{\sigma',\mathbf{p_1}} \right],$$

in which $\{\mathbf{p_i}\} = \{\mathbf{p_1}, \mathbf{p_2}, \mathbf{p_3}, \mathbf{p_4}\}$. Under momentum conservation, the initial and final momenta of the collisional term can be expressed in terms of $\mathbf{p_3} = \mathbf{p_2} - \mathbf{q}$ and $\mathbf{p_4} = \mathbf{p_1} + \mathbf{q}$. This relabelling along with re-expressing the interaction potential by its Fourier transform, as in the single-component case, gives

$$\hat{H}_{\mathrm{int}} = \frac{1}{2V} \sum_{\substack{\sigma,\sigma',\\ \mathbf{p_1},\mathbf{p_2},\mathbf{q}}} \mathcal{V}_{\sigma\sigma'}(\mathbf{q}) \hat{a}^\dagger_{\sigma,\mathbf{p_2}-\mathbf{q}} \hat{a}^\dagger_{\sigma',\mathbf{p_1}+\mathbf{q}} \hat{a}_{\sigma,\mathbf{p_2}} \hat{a}_{\sigma',\mathbf{p_1}}. \tag{2.11}$$

Following the conventions of Ref. [240], the aim of diagonalising the two-component Bose Hamiltonian is to recover the ground state energy density which can be though of as

dividing Equation (2.11) by the volume, V, as $\hat{H} \to \hat{H}/V$. Furthermore, the methods for diagonalising the two-component Hamiltonian are largely the same as the single-component Hamiltonian except when splitting the system into zero and non-zero momentum states. In the single-component system the zero momentum operators are replaced by the condensate population number, $\hat{a}^\dagger_{\mathbf{p}} = \hat{a}_{\mathbf{p}} = \sqrt{N_0}$. However, from the conventions of Ref. [240], the two-component zero momentum operators are replaced by condensate densities, $\hat{a}^\dagger_{\sigma,\mathbf{0}} = \hat{a}_{\sigma,\mathbf{0}} = \sqrt{n_\sigma}$ where $n_\sigma = N_\sigma/V$, thus factors of the volume, V, can be absorbed into a relabelling of operators $\hat{a}^\dagger_{\sigma,\mathbf{p}} \to \sqrt{V}\hat{a}^\dagger_{\sigma,\mathbf{p}}$ and $\hat{a}_{\sigma,\mathbf{p}} \to \sqrt{V}\hat{a}_{\sigma,\mathbf{p}}$ giving

$$\hat{H} = \sum_{\sigma,\mathbf{p}} \left(\frac{p^2}{2m_\sigma} - \mu_\sigma \right) \hat{a}^\dagger_{\sigma,\mathbf{p}} \hat{a}_{\sigma,\mathbf{p}} + \frac{1}{2} \sum_{\substack{\sigma,\sigma', \\ \mathbf{p_1},\mathbf{p_2},\mathbf{q}}} \mathcal{V}_{\sigma\sigma'}(\mathbf{q}) \hat{a}^\dagger_{\sigma,\mathbf{p_2}-\mathbf{q}} \hat{a}^\dagger_{\sigma',\mathbf{p_1}+\mathbf{q}} \hat{a}_{\sigma,\mathbf{p_2}} \hat{a}_{\sigma',\mathbf{p_1}}. \tag{2.12}$$

2.2.2 Bogoliubov approximation

Having again expressed the system Hamiltonian as a sum over momentum states, Equation (2.12) can be split into zero and non-zero momentum contributions, by approximating the zero momentum operators as condensate number densities, $\hat{a}^\dagger_{\sigma,\mathbf{0}} = \hat{a}_{\sigma,\mathbf{0}} = \sqrt{n_\sigma}$, for each component. With this substitution — and by making similar collisional arguments as in the single-component case (for two-component collisional arguments see Appendix B.1) — the Hamiltonian can be written as

$$\begin{aligned} \hat{H} = H_0 + \sum_{\sigma,\mathbf{p}\neq 0} \left[\left(\frac{p^2}{2m_\sigma} - \mu_\sigma \right) + \sum_{\sigma'} \mathcal{V}_{\sigma\sigma'}(\mathbf{0}) n_{\sigma'} \right] \hat{a}^\dagger_{\sigma,\mathbf{p}} \hat{a}_{\sigma,\mathbf{p}} \\ + \frac{1}{2} \sum_{\substack{\sigma,\sigma' \\ \mathbf{p}\neq 0}} \mathcal{V}_{\sigma\sigma'}(\mathbf{p}) \left[2\hat{a}^\dagger_{\sigma,\mathbf{p}} \hat{a}_{\sigma',+} \hat{a}^\dagger_{\sigma,\mathbf{p}} \hat{a}^\dagger_{\sigma',-\mathbf{p}} + \hat{a}_{\sigma,\mathbf{p}} \hat{a}_{\sigma',-\mathbf{p}} \right], \end{aligned} \tag{2.13}$$

where the zero momentum contributions are given by

$$H_0 = -\sum_\sigma \mu_\sigma n_\sigma + \frac{1}{2} \sum_{\sigma,\sigma'} n_\sigma n_{\sigma'} \mathcal{V}_{\sigma\sigma'}(\mathbf{0}).$$

Using the commutation relation, $\hat{a}^\dagger_{\sigma,\mathbf{p}} \hat{a}_{\sigma',\mathbf{p}} = (\hat{a}^\dagger_{\sigma,\mathbf{p}} \hat{a}^\dagger_{\sigma',\mathbf{p}} + \hat{a}_{\sigma,\mathbf{p}} \hat{a}_{\sigma',\mathbf{p}} - \delta_{\sigma\sigma'})/2$, allows for the Hamiltonian to be written as

$$\hat{H} = H_0 - \frac{1}{2} \sum_{\sigma,\mathbf{p}\neq 0} \left[\left(\frac{p^2}{2m_\sigma} - \mu_\sigma n_\sigma \right) + \mathcal{V}_{\sigma\sigma}(\mathbf{p}) n_\sigma \right] + \frac{1}{2} \sum_{\mathbf{p}\neq 0} \left(\hat{a}^\dagger_{1,\mathbf{p}} \hat{a}^\dagger_{2,\mathbf{p}} \hat{a}_{1,-\mathbf{p}} \hat{a}_{2,-\mathbf{p}} \right) \mathcal{W} \begin{pmatrix} \hat{a}_{1,\mathbf{p}} \\ \hat{a}_{2,\mathbf{p}} \\ \hat{a}^\dagger_{1,-\mathbf{p}} \\ \hat{a}^\dagger_{2,-\mathbf{p}} \end{pmatrix}, \tag{2.14}$$

where

$$\mathcal{W} = \begin{pmatrix} \frac{p^2}{2m_1} + \mathcal{V}_{11}(\mathbf{p})n_1 & \mathcal{V}_{12}(\mathbf{p})\sqrt{n_2 n_1} & \mathcal{V}_{11}(\mathbf{p})n_1 & \mathcal{V}_{12}(\mathbf{p})\sqrt{n_1 n_2} \\ \mathcal{V}_{12}\sqrt{n_1 n_2} & \frac{p^2}{2m_2} + \mathcal{V}_{22}(\mathbf{p})n_2 & \mathcal{V}_{12}(\mathbf{p})\sqrt{n_2 n_1} & \mathcal{V}_{22}(\mathbf{p})n_2 \\ \mathcal{V}_{11}(\mathbf{p})n_1 & \mathcal{V}_{12}(\mathbf{p})\sqrt{n_1 n_2} & \frac{p^2}{2m_1} + \mathcal{V}_{11}(\mathbf{p})n_1 & \mathcal{V}_{12}(\mathbf{p})\sqrt{n_2 n_1} \\ \mathcal{V}_{12}(\mathbf{p})\sqrt{n_1 n_2} & \mathcal{V}_{22}(\mathbf{p})n_2 & \mathcal{V}_{12}(\mathbf{p})\sqrt{n_2 n_1} & \frac{p^2}{2m_2} + \mathcal{V}_{22}(\mathbf{p})n_2 \end{pmatrix}, \quad (2.15)$$

and for more details of this calculation see Appendix B.2. Note that Equation (2.15) has a similar form to the two-component Bogoliubov matrix [240],

$$\mathcal{B} = \begin{pmatrix} \frac{p^2}{2m_1} + \mathcal{V}_{11}(\mathbf{p})n_1 & \mathcal{V}_{12}(\mathbf{p})\sqrt{n_2 n_1} & \mathcal{V}_{11}(\mathbf{p})n_1 & \mathcal{V}_{12}(\mathbf{p})\sqrt{n_1 n_2} \\ \mathcal{V}_{12}\sqrt{n_1 n_2} & \frac{p^2}{2m_2} + \mathcal{V}_{22}(\mathbf{p})n_2 & \mathcal{V}_{12}(\mathbf{p})\sqrt{n_2 n_1} & \mathcal{V}_{22}(\mathbf{p})n_2 \\ -\mathcal{V}_{11}(\mathbf{p})n_1 & -\mathcal{V}_{12}(\mathbf{p})\sqrt{n_1 n_2} & -\left[\frac{p^2}{2m_1} + \mathcal{V}_{11}(\mathbf{p})n_1\right] & -\mathcal{V}_{12}(\mathbf{p})\sqrt{n_2 n_1} \\ -\mathcal{V}_{12}(\mathbf{p})\sqrt{n_1 n_2} & -\mathcal{V}_{22}(\mathbf{p})n_2 & -\mathcal{V}_{12}(\mathbf{p})\sqrt{n_2 n_1} & -\left[\frac{p^2}{2m_2} + \mathcal{V}_{22}(\mathbf{p})n_2\right] \end{pmatrix}, \quad (2.16)$$

which informs the Bogoliubov transformation to diagonalise this Hamiltonian.

2.2.3 Bogoliubov transformation

For this system, Ref. [240] defines the Bogoliubov transformation as

$$\begin{pmatrix} \hat{a}_{1,\mathbf{p}} \\ \hat{a}_{2,\mathbf{p}} \\ \hat{a}^\dagger_{1,-\mathbf{p}} \\ \hat{a}^\dagger_{2,-\mathbf{p}} \end{pmatrix} = \hat{S} \begin{pmatrix} \hat{\alpha}_{+,\mathbf{p}} \\ \hat{\alpha}_{-,\mathbf{p}} \\ \hat{\alpha}^\dagger_{+,-\mathbf{p}} \\ \hat{\alpha}^\dagger_{-,-\mathbf{p}\cdot} \end{pmatrix},$$

where $\hat{S}$ is a matrix defined such that [240]

$$\hat{S}^\dagger \mathcal{W} \hat{S} = \begin{pmatrix} E_{+,p} & 0 & 0 & 0 \\ 0 & E_{-,p} & 0 & 0 \\ 0 & 0 & E_{+,p} & 0 \\ 0 & 0 & 0 & E_{-,p} \end{pmatrix},$$

with Hermitian conjugate

$$\left(\hat{a}^\dagger_{1,\mathbf{p}} \hat{a}^\dagger_{2,\mathbf{p}} \hat{a}_{1,-\mathbf{p}} \hat{a}_{2,-\mathbf{p}}\right) = \left(\hat{\alpha}^\dagger_{+,\mathbf{p}} \hat{\alpha}^\dagger_{-,\mathbf{p}} \hat{\alpha}_{+,-\mathbf{p}} \hat{\alpha}_{-,-\mathbf{p}}\right) \hat{S}^\dagger,$$

and where

$$E_{\pm,p} = \sqrt{\frac{\omega_1^2(\mathbf{p}) + \omega_2^2(\mathbf{p})}{2} \pm \sqrt{\frac{\left[\omega_1^2(\mathbf{p}) - \omega_2^2(\mathbf{p})\right]^2}{4} + \frac{\mathcal{V}_{12}^2(\mathbf{p}) n_1 n_2 p^4}{m_1 m_2}}},$$

along with

$$\omega_\sigma(\mathbf{p}) = \sqrt{\frac{\mathcal{V}_{\sigma\sigma}(\mathbf{p})n_\sigma p^2}{m_\sigma} + \left(\frac{p^2}{2m_\sigma}\right)^2},$$

are the two-component quasiparticle dispersion relations. In the single-component gas the dispersion relation has one channel, whereas the two-component dispersion relations have two channels since $E_{\pm,p}$ and$-E_{\pm,p}$, are the eigenvalues of the Bogoliubov matrix given by Equation (2.16). Hence, under this transformation, Equation (2.14) becomes

$$\begin{aligned}
\hat{H} &= H_0 - \frac{1}{2}\sum_{\sigma\mathbf{p}\neq 0}\left[\left(\frac{p^2}{2m_\sigma} - \mu_\sigma n_\sigma\right) + \mathcal{V}_{\sigma\sigma}(\mathbf{p})n_\sigma\right] \\
&\quad + \frac{1}{2}\sum_{\mathbf{p}\neq 0}\left(\hat{\alpha}^\dagger_{+,\mathbf{p}}\hat{\alpha}^\dagger_{-,\mathbf{p}}\hat{\alpha}_{+,-\mathbf{p}}\hat{\alpha}_{-,-\mathbf{p}}\right)\begin{pmatrix} E_{+,p} & 0 & 0 & 0 \\ 0 & E_{-,p} & 0 & 0 \\ 0 & 0 & E_{+,p} & 0 \\ 0 & 0 & 0 & E_{-,p}\end{pmatrix}\begin{pmatrix}\hat{\alpha}_{+,\mathbf{p}} \\ \hat{\alpha}_{-,\mathbf{p}} \\ \hat{\alpha}^\dagger_{+,-\mathbf{p}} \\ \hat{\alpha}^\dagger_{-,-\mathbf{p}}\end{pmatrix} \\
&= H_0 - \frac{1}{2}\sum_{\sigma\mathbf{p}\neq 0}\left[\left(\frac{p^2}{2m_\sigma} - \mu_\sigma n_\sigma\right) + \mathcal{V}_{\sigma\sigma}(\mathbf{p})n_\sigma\right] \\
&\quad + \frac{1}{2}\left[E_{+,\mathbf{p}}\hat{\alpha}^\dagger_{+,\mathbf{p}}\hat{\alpha}_{+,\mathbf{p}} + E_{-,\mathbf{p}}\hat{\alpha}^\dagger_{-,\mathbf{p}}\hat{\alpha}_{-,\mathbf{p}} + E_{+,\mathbf{p}}\hat{\alpha}_{+,-\mathbf{p}}\hat{\alpha}^\dagger_{+,-\mathbf{p}} + E_{-,\mathbf{p}}\hat{\alpha}_{-,-\mathbf{p}}\hat{\alpha}^\dagger_{-,-\mathbf{p}}\right],
\end{aligned}$$

then via normal ordering $\hat{\alpha}_{+,-\mathbf{p}}\hat{\alpha}^\dagger_{+,-\mathbf{p}} = \hat{\alpha}^\dagger_{+,-\mathbf{p}}\hat{\alpha}^\dagger_{+,-\mathbf{p}}\hat{\alpha}_{+,-\mathbf{p}}+1$ and $\hat{\alpha}_{-,\mathbf{p}}\hat{\alpha}^\dagger_{-,-\mathbf{p}} = \hat{\alpha}^\dagger_{-,-\mathbf{p}}\hat{\alpha}_{-,-\mathbf{p}}+1$, and the symmetry relabelling, $-\mathbf{p}\to\mathbf{p}$, the Hamiltonian becomes

$$\hat{H} = H_0 + \frac{1}{2}\sum_{\mathbf{p}\neq 0}\left[\sum_{s=\pm}E_{s,\mathbf{p}} - \frac{1}{2}\sum_\sigma\left\{\frac{p^2}{2m_\sigma} + \mathcal{V}_{\sigma\sigma}(\mathbf{p})n_\sigma\right\}\right] + \sum_{s=\pm,\mathbf{p}\neq 0}E_{s,\mathbf{p}}\hat{\alpha}^\dagger_{s,\mathbf{p}}\hat{\alpha}_{s,\mathbf{p}},$$

finally resulting in the ground state energy

$$\frac{E_0}{V} = \frac{1}{2}\sum_{\sigma,\sigma'}\mathcal{V}_{\sigma\sigma'}(\mathbf{0})n_\sigma n_{\sigma'} + \frac{1}{2}\sum_{\mathbf{p}\neq 0}\left[\sum_{s=\pm}E_{s,\mathbf{p}} - \frac{1}{2}\sum_\sigma\left\{\frac{p^2}{2m_\sigma} + \mathcal{V}_{\sigma\sigma}(\mathbf{p})n_\sigma\right\}\right].$$

As with the single-component ground state energy, the final issue is to investigate how to express the interaction potentials in terms of effective interaction strengths, $g_{\sigma\sigma'}$.

2.2.4 Renormalisation via Born approximation

Simply replacing both zero and non-zero momentum interaction potentials with the lowest-order Born approximation

$$\mathcal{V}_{\sigma\sigma}(\mathbf{0}) \approx \mathcal{V}_{\sigma\sigma}(\mathbf{p}) \approx g_{\sigma\sigma} = \frac{4\pi a_{\sigma\sigma}\hbar^2}{m_\sigma}, \tag{2.17}$$

and

$$\mathcal{V}_{\sigma\sigma'}(\mathbf{0}) \approx \mathcal{V}_{\sigma\sigma'}(\mathbf{p}) \approx g_{\sigma\sigma'} = \frac{2\pi a_{\sigma\sigma}\hbar^2}{m_{\sigma\sigma'}}, \tag{2.18}$$

where $m_{\sigma\sigma'} = (m_\sigma + m_{\sigma'})/m_\sigma m_{\sigma'}$ is the reduced mass, leads once more to a UV divergence. The energy can once again be renormalised by using the first-order Born approximation for the two-component effective interaction strength [240],

$$g_{\sigma\sigma'} \approx \mathcal{V}_{\sigma\sigma'}(\mathbf{0}) - \sum_{\mathbf{p}\neq 0} \frac{2m_{\sigma\sigma'}\mathcal{V}^2_{\sigma\sigma'}(\mathbf{p})}{p^2},$$

allowing for the ground state energy to be written in the convergent form

$$\frac{E_0}{V} = \frac{E_{\mathrm{MF}}}{V} + \frac{1}{2}\sum_{\mathbf{p}\neq 0}\left[\sum_{s=\pm} E_{s,\mathbf{p}} - \frac{1}{2}\sum_{\sigma}\left\{\frac{p^2}{2m_\sigma} + \mathcal{V}_{\sigma\sigma}(\mathbf{p})n_\sigma\right\} + \sum_{\sigma,\sigma'}\frac{2m_{\sigma\sigma'}\mathcal{V}^2_{\sigma\sigma'}(\mathbf{p})n_\sigma n_{\sigma'}}{p^2}\right],$$

where the MF energy density is given by

$$\frac{E_{\mathrm{MF}}}{V} = \frac{1}{2}\sum_{\sigma,\sigma'} g_{\sigma\sigma'} n_\sigma n_{\sigma'}. \tag{2.19}$$

Having rewritten the ground state energy to be convergent, the final assumption is to again approximate the non-zero momentum interaction potential by the lowest-order Born approximation, $\mathcal{V}_{\sigma\sigma'}(\mathbf{p}) \approx g_{\sigma\sigma'}$, which gives

$$\frac{E_0}{V} = \frac{E_{\mathrm{MF}}}{V} + \frac{1}{2}\sum_{\mathbf{p}\neq 0}\left[\sum_{s=\pm} E_{s,\mathbf{p}} - \frac{1}{2}\sum_{\sigma}\left\{\frac{p^2}{2m_\sigma} + g_{\sigma\sigma} n_\sigma\right\} + \sum_{\sigma,\sigma'}\frac{2m_{\sigma\sigma'} g^2_{\sigma\sigma'} n_\sigma n_{\sigma'}}{p^2}\right].$$

The sum over momenta can again be replaced by a spherically symmetric integral, of the form, $\sum_{\mathbf{p}\neq\mathbf{0}} \to \int \mathrm{d}\mathbf{p}\,/(2\pi\hbar)^3 = \int \mathrm{d}p\, p^2/(2\pi\hbar)^3$, giving

$$\frac{E_{\mathrm{LHY}}}{V} = \frac{1}{2}\int \frac{\mathrm{d}p\, p^2}{(2\pi\hbar)^3}\left[E_{+,p} + E_{-,p} - \frac{p^2}{2m_r} - g_{11}n_1 - g_{22}n_2 + \frac{m_1 g^2_{11} n_1^2 + m_2 g^2_{22} n_2^2 + 4m_r g^2_{12} n_1 n_2}{p^2}\right],$$

then via the substitution $p \to (g_{11}n_1 m_1)^{1/2} k$, the integral can be expressed as

$$\frac{E_{\mathrm{LHY}}}{V} = \frac{8}{15\pi^2}\left(\frac{m_1}{\hbar^2}\right)^{3/2}(g_{11}n_1)^{5/2} f\left(\frac{m_2}{m_1}, \frac{g^2_{12}}{g_{11}g_{22}}, \frac{g_{22}n_2}{g_{11}n_1}\right), \tag{2.20}$$

where $f(\dots)$ is a function defined as [153, 241]

$$f(z,u,x) = \frac{15}{32}\int_0^\infty k^2 \mathcal{F}(k,z,u,x)\mathrm{d}k, \tag{2.21}$$

with

$$\begin{aligned}\mathcal{F}(k,z,u,x) = &\left\{\frac{1}{2}\left[k^2\left(1+\frac{x}{z}\right)+\frac{1}{4}k^4\left(1+\frac{1}{z^2}\right)\right]\right.\\ &\left.+\left[\frac{1}{4}\left[\left(k^2+\frac{1}{4}k^4\right)-\left(\frac{x}{z}k^2+\frac{1}{4z^2}\right)\right]^2+u\frac{x}{z}k^4\right]^{1/2}\right\}^{1/2}\\ &+\left\{\frac{1}{2}\left[k^2\left(1+\frac{x}{z}\right)+\frac{1}{4}k^4\left(1+\frac{1}{z^2}\right)\right]\right.\\ &\left.-\left[\frac{1}{4}\left[\left(k^2+\frac{1}{4}k^4\right)-\left(\frac{x}{z}k^2+\frac{1}{4z^2}\right)\right]^2+u\frac{x}{z}k^4\right]^{1/2}\right\}^{1/2}\\ &-\frac{1+z}{2z}k^2-(1+x)+\frac{1}{k^2}\left[1+x^2z+4ux\frac{z}{1+z}\right].\end{aligned} \tag{2.22}$$

defining $z = m_2/m_1$, $u = g_{12}^2/g_{11}g_{22}$ and $x = g_{22}n_2/g_{11}n_1$. For more details on the final rewriting of the momentum integral, see Appendix B.3.

In the case of a homonuclear mixture with $z = 1$, the momentum integral in Equation (2.21) can be computed analytically as [153]

$$f(1,u,x) = \frac{1}{4\sqrt{2}}\sum_{\pm}\left[1+x\pm\sqrt{(1-x)^2+4ux}\right]^{5/2}, \tag{2.23}$$

hence the ground state energy density can be expressed as

$$\frac{E_0}{V} = \frac{g_{11}n_1^2}{2}+\frac{g_{22}n_2^2}{2}+g_{12}n_1n_2+\frac{8}{15\pi^2}\left(c_+^5+c_-^5\right),$$

where c_+ and c_- are the density and spin sound velocities, respectively, given by [45]

$$c_\pm = \sqrt{\frac{g_{11}n_1+g_{22}n_2\pm\sqrt{(g_{11}n_1-g_{22}n_2)^2+4g_{12}^2n_1n_2}}{2}}.$$

Density and spin sound velocities correspond to in-phase and out-of-phase excitations, respectively, and this added excitation channel has led to recent experimental interest in spin dynamics [203, 242, 243] and speed of spin sound [244].

In the attractive case, the spin phonon mode has an imaginary contribution, as can be seen more clearly by considering the fully symmetric mixture with equal interactions, $g_{11} = g_{22} = g$, and densities, $n_1 = n_2 = n/2$. Thus the density and spin sound velocities can be written as [245]

$$c_\pm = \sqrt{\frac{(g\pm g_{12})n}{2m}},$$

i.e., with $g_{12} < 0$ the density phonon mode is imaginary. This work follows the method of Ref. [153] by neglecting the imaginary contribution as small, which Quantum Monte-Carlo (QMC) calculations have demonstrated is a relatively good approximation for small

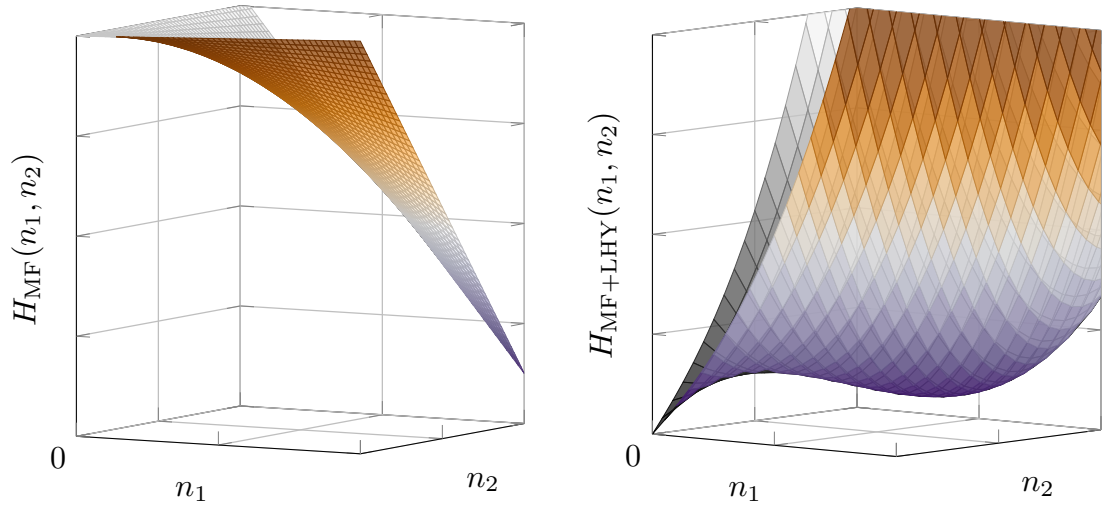

Figure 2.2: Schematic of the energy landscape in (n_1, n_2) space, with the $(n_1, n_2) = (0, 0)$ point labelled. Left - MF only contributions; (b) MF and LHY contributions.

attractive interactions [246]. Some theoretical works have managed to derive models for droplets that avoid the complex phonon mode. For example using a bosonic pairing theory [247, 248], which proposes a bosonic BEC-BCS (Bardeen-Cooper-Schrieffer) crossover [249] as found in fermionic systems [90, 250]. Other methods include adding higher-order quantum fluctuations [251, 252] to counter the imaginary contributions at the LHY level.

2.2.5 Two-component energy landscape

To explore the energy landscape of the attractive mixture, this section focuses on the homonuclear mixture due to the analytic form of its ground state energy. Even with the addition of the LHY correction, each component is still susceptible to MF attractive collapse internally, i.e., repulsive intraspecies interactions, $a_{ii} > 0$, are required for the stability of each component. With repulsive intraspecies interactions, the overall attraction is engineered via an interspecies interaction. MF interactions can be characterised by the parameter, $\delta g = g_{12} + \sqrt{g_{11} g_{22}}$, and in the regime $\delta g < 0$, the mixture is dominantly attractive.

The left panel of Figure 2.2 shows the energy landscape of the dominantly attractive MF mixture, given by

$$H_{\mathrm{MF}} = \frac{g_{11} n_1^2}{2} + \frac{g_{22} n_2^2}{2},$$

which is monotonically decreasing and possesses a global minimum at infinite n_1 and n_2 corresponding to the MF collapse. On the other hand, the right panel of Figure 2.2 shows the energy landscape including both MF and LHY contributions given by

$$H_{\mathrm{MF+LHY}} = H_{\mathrm{MF}} + \frac{8}{15\pi^2} \left(c_+^5 + c_-^5 \right).$$

With the addition of the LHY correction two minima appear: a global minimum at

$(n_1, n_2) = (0, 0)$, corresponding to the vacuum state; and a local minimum at finite (n_1, n_2). The existence of a minimum at finite (n_1, n_2) is the evidence of the liquid droplet as it indicates that the mixture stabilises, through no external influence, to a fixed density and hence a fixed volume. With repulsive MF interactions the mixture is gaseous and hence fills any confining volume. In free space a gas diffuses to zero density, whereas a liquid remains at a fixed volume for a given total atom number. Therefore a fixed volume and density in free space is a defining property of the formation of two-component quantum droplets.

Finally, the existence of this minimum can be probed further as it indicates an energetically favourable value of (n_1, n_2). Ref. [153] demonstrates that by minimising this energy landscape the fixed density ratio,

$$\frac{n_2}{n_1} = \sqrt{\frac{g_{11}}{g_{22}}},$$

is preserved. Under the stabilised attractive collapse, there is therefore an energetic favourability to maintain a constant ratio between the two-component densities, referred to here as 'density-balancing'.

Having established the two-component ground state energy, and the energy landscape under attractive interspecies interactions for the uniform mixture, the following sections will incorporate these results to model non-uniform mixtures.

2.3 Density-locked extended Gross-Pitaevskii equation

To construct a model of non-uniform mixtures, with the addition of the LHY correction, this section begins by building the two-component, non-uniform energy functional. Using the previously discussed density balancing, this section uses techniques established in Ref. [153] to express the mixture as an effective single component. Minimising this energy functional results in a single GP equation which, through dimensional arguments, reduces to the extended GP equation first derived in Ref. [153].

Section 2.1 explains how a LDA can be used to add the MF energy of a uniform gas, into the energy functional for a non-uniform gas by both including kinetic contributions, and expressing the gas density as related to the macroscopic wavefunction, $n = |\psi|^2$. This technique can likewise be used for defining the energy functional for a non-uniform mixture

$$E = \int \mathrm{d}^3\mathbf{r} \left[\frac{E_{\mathrm{KE}}}{V} + \frac{E_{\mathrm{MF}}}{V} + \frac{E_{\mathrm{LHY}}}{V} \right], \tag{2.24}$$

in which the kinetic energy density takes the form

$$\frac{E_{\mathrm{KE}}}{V} = \frac{\hbar^2}{2m_1}|\boldsymbol{\nabla}\Psi_1|^2 + \frac{\hbar^2}{2m_2}|\boldsymbol{\nabla}\Psi_2|^2, \tag{2.25}$$

where Ψ_1 and Ψ_2 are the macroscopic wavefunctions describing the two components of the mixture, related to the number densities by $n_i = |\Psi_i|^2$. The $|\boldsymbol{\nabla}\Psi_i|^2$ terms constitute the kinetic energy, whilst the MF and LHY contributions are defined by Equation (2.19) and Equation (2.20), respectively.

Density-balancing can be used to simplify the two-component energy functional, by assuming so-called 'density-locking' in which both wavefunctions are replaced by a rescaled single-component wavefunction, $\Psi_i = \sqrt{n_i^{(0)}}\phi$, i.e., neglecting any out-of-phase motion between the components [153, 203, 204]. This rescaling uses the dimensional equilibrium densities defined as [153]

$$n_1^{(0)} = \frac{25\pi}{1024}\frac{1}{f^2(m_2/m_1, 1, \sqrt{g_{22}/g_{11}})}\frac{1}{a_{11}^3}\frac{\delta g^2}{g_{11}g_{22}}, \tag{2.26}$$

which are likewise density balanced, $n_2^{(0)}/n_1^{(0)} = \sqrt{g_{11}/g_{22}}$, and are found by assuming the mixture is in equilibrium with the vacuum. There are two main assumptions for the equilibrium densities: (1) density-balancing, hence $x = (g_{22}n_2)/(g_{11}n_1) = \sqrt{g_{22}/g_{11}}$; (2) the MF interactions are critically attractive, $g_{12}^2 = g_{11}g_{22} \implies u = 1$, so as to remove any imaginary contribution resulting from complex phonon modes [153].

To begin density-locking the mixture, first let Ψ denote the wavefunction associated with the total density, $|\Psi|^2 = |\Psi_1|^2 + |\Psi_2|^2$. With density-balancing, $|\Psi_2|^2/|\Psi_1|^2 = \sqrt{g_{11}/g_{22}}$, each component wavefunction can be expressed in terms of the total-density wavefunction,

$$\Psi_1 = \left[\frac{\sqrt{g_{22}}}{\sqrt{g_{11}} + \sqrt{g_{22}}}\right]^{1/2}\Psi,$$

and

$$\Psi_2 = \left[\frac{\sqrt{g_{11}}}{\sqrt{g_{11}} + \sqrt{g_{22}}}\right]^{1/2}\Psi.$$

Starting with the two-component kinetic energy density, shown in Equation (2.25),

$$\begin{aligned}\frac{E_{\mathrm{KE}}}{V} &= \frac{\hbar^2}{2m_1}|\boldsymbol{\nabla}\Psi_1|^2 + \frac{\hbar^2}{2m_2}|\boldsymbol{\nabla}\Psi_1|^2 \\ &= \frac{\hbar^2}{2}\left[\frac{\sqrt{g_{11}}/m_2 + \sqrt{g_{22}}/m_1}{\sqrt{g_{11}} + \sqrt{g_{22}}}\right]|\boldsymbol{\nabla}\Psi|^2.\end{aligned}$$

Next, the MF energy contribution of the two-component system, takes the form

$$\frac{E_{\mathrm{MF}}}{V} = \frac{g_{11}}{2}|\Psi_1|^4 + \frac{g_{22}}{2}|\Psi_2|^4 g_{12}|\Psi_1|^2|\Psi_2|^2,$$

which again reduces to a single density,

$$\frac{E_{\mathrm{MF}}}{V} = \frac{\delta g\sqrt{g_{11}g_{22}}}{(\sqrt{g_{11}} + \sqrt{g_{22}})^2}|\Psi|^4.$$

The LHY correction can be simplified by first rearranging Equation (2.26)

$$f(m_2/m_1, 1, \sqrt{g_{22}/g_{11}}) = \left(\frac{25\pi}{1024} \frac{\delta g}{a_{11}^3 g_{11} g_{22} n_1^{(0)}} \right)^{1/2},$$

then substituting this into Equation (2.20) giving

$$\frac{E_{\mathrm{LHY}}}{V} = \frac{2}{3}\sqrt{\frac{g_{11}}{g_{22}}} \left(\frac{\delta g^2}{n_1^{(0)}} \right)^{1/2} n_1^{5/2}. \tag{2.27}$$

allowing for Equation (2.27) to be rewritten as

$$\frac{E_{\mathrm{LHY}}}{V} = \frac{2}{3}\sqrt{\frac{g_{11}}{g_{22}}} \left(\frac{\delta g^2}{n_1^{(0)}} \right)^{1/2} \left(\frac{\sqrt{g_{22}}}{\sqrt{g_{11}} + \sqrt{g_{22}}} \right)^{5/2} |\Psi|^5.$$

Thus, with all of the energy contributions expressed in terms of the 'total-density' wave-function the energy functional takes the form

$$\begin{aligned} E = \int \mathrm{d}^3\mathbf{r}\, \frac{\hbar^2}{2} \left[\frac{\sqrt{g_{11}}/m_2 + \sqrt{g_{22}}/m_1}{\sqrt{g_{11}} + \sqrt{g_{22}}} \right] |\boldsymbol{\nabla}\Psi|^2 + \frac{\delta g \sqrt{g_{11} g_{22}}}{(\sqrt{g_{11}} + \sqrt{g_{22}})^2} |\Psi|^4 \\ + \frac{2}{3}\sqrt{\frac{g_{11}}{g_{22}}} \left(\frac{\delta g^2}{n_1^{(0)}} \right)^{1/2} \left(\frac{\sqrt{g_{22}}}{\sqrt{g_{11}} + \sqrt{g_{22}}} \right)^{5/2} |\Psi|^5. \end{aligned}$$

The First Green identity again allows for the expression of the kinetic energy term to be rewritten as $|\Psi|^2 = -\Psi^* \nabla^2 \Psi$, hence using the variational approach [45]

$$i\hbar \frac{\partial \phi}{\partial t} = \frac{\delta E}{\delta \phi^*},$$

the energy functional can be minimised giving the dimensional, time-dependent, density-locked extended GP equation

$$\begin{aligned} i\hbar \frac{\partial \phi}{\partial t} = -\frac{\hbar^2}{2} \left[\frac{\sqrt{g_{11}}/m_2 + \sqrt{g_{22}}/m_1}{\sqrt{g_{11}} + \sqrt{g_{22}}} \right] \nabla^2 \Psi + \frac{2\delta g \sqrt{g_{11} g_{22}}}{(\sqrt{g_{11}} + \sqrt{g_{22}})^2} |\Psi|^2 \Psi \\ + \frac{5}{3}\sqrt{\frac{g_{11}}{g_{22}}} \left(\frac{\delta g^2}{n_1^{(0)}} \right)^{1/2} \left(\frac{g_{22}}{\sqrt{g_{11}} + \sqrt{g_{22}}} \right)^{5/2} |\Psi|^3 \Psi. \end{aligned} \tag{2.28}$$

From here this equation can be non-dimensionalised. By following from Ref. [153], time and length scales are defined as

$$\tau = \frac{3}{2}\hbar \frac{\sqrt{g_{11}} + \sqrt{g_{22}}}{|\delta g| \sqrt{g_{11}} n_1^{(0)}}, \qquad \xi = \hbar \sqrt{\frac{3}{2} \frac{\sqrt{g_{22}}/m_1 + \sqrt{g_{11}}/m_2}{|\delta g| \sqrt{g_{11}} n_1^{(0)}}},$$

which when substituted into Equation (2.28) give

$$i\frac{\partial\Psi}{\partial t} = \Bigg[-\frac{\nabla^2}{2} - 3\left(\frac{\sqrt{g_{22}}}{n_1^{(0)}(\sqrt{g_{11}}+\sqrt{g_{22}})}\right)|\Psi|^2 + \frac{5}{2}\left(\frac{\sqrt{g_{22}}}{n_1^{(0)}(\sqrt{g_{11}}+\sqrt{g_{22}})}\right)^{3/2}|\Psi|^3\Bigg]\Psi. \tag{2.29}$$

Finally, the 'total' wavefunction, Ψ, can be expressed in terms of the density-locked dimensionless wavefunction by using $\Psi_i = \sqrt{n_i^{(0)}}\phi$ [153]

$$\begin{aligned}|\Psi|^2 &= |\Psi_1|^1 + |\Psi_2|^2 \\ &= \left(n_1^{(0)} + n_2^{(0)}\right)|\phi|^2 \\ &= n_1^{(0)}\left(\frac{\sqrt{g_{11}}+\sqrt{g_{22}}}{\sqrt{g_{22}}}\right)|\phi|^2,\end{aligned}$$

with normalisation

$$\tilde{N} = \int |\phi|^2 \, \mathrm{d}^3\tilde{\mathbf{r}}\,, \tag{2.30}$$

where $\tilde{N}$ is an effective atom number and is the only parameter describing the density-locked mixture. Choosing the normalisation constant to be of the form

$$\tilde{N} = \left(\frac{\sqrt{g_{22}}}{n_1^{(0)}(\sqrt{g_{11}}+\sqrt{g_{22}})}\right)\frac{N}{\xi^3},$$

reduces Equation (2.29) to

$$i\frac{\partial\phi}{\partial t} = \left[-\frac{1}{2}\nabla^2 - 3|\phi|^2 + \frac{5}{2}|\phi|^3\right]\phi. \tag{2.31}$$

For typical experimental parameters used in Refs. [169, 171, 173], the length scale is of order $\sim [0.2, 2]\mu$m, whilst the time scale is of order $\sim [0.05, 3]$ms.

Though much of this work focuses on free-space droplets, all experiments form droplets within traps, and so there has been increasing interest in trapped quantum droplets [253], and droplets in reduced dimensions [254]. The energy density resulting from the addition of traps,

$$\frac{E_{\text{trap}}}{V} = V_1|\Psi_1|^2 + V_2|\Psi_2|^2,$$

can be included in the non-uniform energy functional given by Equation (2.24). Rewriting the trap energy density in terms of the 'total-density' wavefunction, Ψ, means the dimensional, density-locked energy is

$$\frac{E_{\text{trap}}}{V} = \frac{\left(V_1\sqrt{g_{22}} + V_2\sqrt{g_{11}}\right)}{\sqrt{g_{11}}+\sqrt{g_{22}}}|\Psi|^2,$$

hence by defining $V_1 = V_2 = V_{\text{ext}}$,

$$\frac{E_{\text{trap}}}{V} = V_{\text{ext}}|\Psi|^2.$$

In dimensionless units the trapping potentials are $V_{\text{ext}} = (m\xi^2/\tau^2)\tilde{V}$, i.e., the trapped, dimensionless, density-locked GP equation is given by

$$i\frac{\partial\phi}{\partial t} = \left[-\frac{1}{2}\nabla^2 + V - 3|\phi|^2 + \frac{5}{2}|\phi|^3\right]\phi,$$

where throughout this work, harmonic traps are the only potentials considered.

Two main benefits of the density-locked model are: 1. the two-component problem of modelling a mixture is simplified to a one-component problem by modelling the droplet's total density; 2. the parameter space is reduced to a single parameter, $\tilde{N}$, denoting droplet size. However, this model is quite restrictive. Firstly, typically in experimental mixtures there will not be population balance, $N_2/N_1 = \sqrt{g_{11}/g_{22}}$, during droplet formation particularly in heteronuclear mixtures [171, 173]. Hence, there are clear questions around the validity of population balancing in the density-locked approximation since droplets are known to support population imbalances [153] though studies into the effects of imbalances on ground states and dynamics are rarer. This is a crucial question in the context of the CsYb mixture which has an approximate order of magnitude difference in Yb population relative to Cs. Secondly, in general experimental mixtures may have large differences in the traps applied to each component (such as the CsYb mixture) and therefore by combining the trapping potential into a single potential acting on the total droplet density, any symmetry breaking between the components is neglected. Finally, there are subtleties that appear to be lost in the density-locked model such as mass and intraspecies scattering lengths imbalances, which are removed by assuming that both components are simply rescalings of one another. Nevertheless the density-locked model is robust and offers a simple and effective starting point for understanding droplet physics. To systematically study the effects of the various inter-component imbalances, GP equations are required in which each component is modelled explicitly.

2.4 Density-unlocked Gross-Pitaevkii equations

The previous section highlights the utility of the density-locked theory, in that the single component GP equation can be used to describe both homonuclear and heteronuclear mixtures, with only a single theoretical parameter. However, the heavy restrictions placed on the mixture make the model inflexible for mixtures with, e.g., population imbalances. Thus, this section derives density-unlocked GP equations to probe mixtures beyond the density lock.

Deviating from the density-locked system results in two distinct avenues: the equal mass coupled GP equations, and the unequal mass coupled GP equations. The unequal

mass GP equations are far more complex in their structure than the equivalent equal mass equations.

2.4.1 Heteronuclear mixture

To derive the coupled GP equations, the energy functional in Equation (2.24) can be minimised with respect to each wavefunction, Ψ_i, using the variational approach [45],

$$i\hbar\frac{\partial\Psi_1}{\partial t} = \frac{\delta E}{\delta\Psi_1^*}, \text{ and, } i\hbar\frac{\partial\Psi_2}{\partial t} = \frac{\delta E}{\delta\Psi_2^*}.$$

which gives the dimensional, coupled extended GP equations,

$$i\hbar\frac{\partial\Psi_1}{\partial t} = \Bigg[-\frac{\hbar^2}{2m_1}\nabla^2 + g_{11}|\Psi_1|^2 + g_{12}|\Psi_2|^2 + \frac{8}{15\pi^2}\left(\frac{m_1}{\hbar^2}\right)^{3/2} g_{11}^{5/2}\Bigg\{\frac{5}{2}f(x)|\Psi_1|^3 - \frac{g_{22}}{g_{11}}f'(x)|\Psi_1||\Psi_2|^2\Bigg\}\Bigg]\Psi_1,$$

$$i\hbar\frac{\partial\Psi_2}{\partial t} = \left[-\frac{\hbar^2}{2m_2}\nabla^2 + g_{22}|\Psi_2|^2 + g_{12}|\Psi_1|^2 + \frac{8}{15\pi^2}\left(\frac{m_1}{\hbar^2}\right)^{3/2} g_{11}^{3/2}g_{22}f'(x)|\Psi_1|^3\right]\Psi_2,$$

where the LHY function, $f(z,x)$, has been written in terms of $x = (g_{22}n_2)/(g_{11}n_1)$ only — though it still depends on $z = m_2/m_1$, this does not vary in time — simply for convenience. These equations can be non-dimensionalised giving

$$i\frac{\partial\Psi_1}{\partial t} = \left[-\frac{\gamma}{2}\nabla^2 + |\Psi_1|^2 + \eta|\Psi_2|^2 + \alpha\left(\frac{5}{2}f(x)|\Psi_1|^3 - \beta f'(x)|\Psi_1||\Psi_2|^2\right)\right]\Psi_1, \tag{2.32}$$

$$i\frac{\partial\Psi_2}{\partial t} = \left[-\frac{\gamma}{2z}\nabla^2 + \beta|\Psi_2|^2 + \eta\beta|\Psi_1|^2 + \alpha\beta^2 f'(x)|\Psi_1|^3\right]\Psi_2, \tag{2.33}$$

where

$$\eta = \frac{g_{12}}{\sqrt{g_{11}g_{22}}},$$

$$\gamma = \frac{\sqrt{g_{11}} + \sqrt{g_{22}}}{m_1(\sqrt{g_{11}}/m_2 + \sqrt{g_{22}}/m_1)},\ z = \frac{m_2}{m_1},$$

$$\alpha = \frac{8}{15\pi^2}\left[\frac{2}{3}\left(\frac{m_1}{\hbar^2}\right)^3\frac{g_{11}^{5/2}|\delta g|n_1^{(0)}}{(\sqrt{g_{11}} + \sqrt{g_{22}})}\right]^{1/2},\ \beta = \left(\frac{g_{22}}{g_{11}}\right)^{1/2},$$

with dimensional parameters

$$\xi = \hbar\sqrt{\frac{3}{2}\frac{\sqrt{g_{22}}/m_1 + \sqrt{g_{11}}/m_2}{|\delta g|\sqrt{g_{11}}n_1^{(0)}}}, \qquad \tau = \frac{3}{2}\hbar\frac{\sqrt{g_{11}} + \sqrt{g_{22}}}{|\delta g|\sqrt{g_{11}}n_1^{(0)}},$$

$$\rho_1 = \frac{2}{3}\frac{|\delta g|n_1^{(0)}}{\sqrt{g_{11}}(\sqrt{g_{11}} + \sqrt{g_{22}})}, \qquad \rho_2 = \frac{2}{3}\frac{|\delta g|n_1^{(0)}}{\sqrt{g_{22}}(\sqrt{g_{11}} + \sqrt{g_{22}})},$$

along with $x = \beta n_2/n_1$. These dimensional scalings include: length ($\mathbf{r} = \xi\tilde{\mathbf{r}}$), time ($t = \tau\tilde{t}$) and the two component wavefunctions ($\Psi_i = \rho_i^{1/2}\tilde{\Psi}_i$). Note that the parameters are defined in terms of the equilibrium density of the density-locked system, $n_1^{(0)}$.

2.4.2 Homonuclear mixture

Working through the coupled GP equations in the more general heteronuclear mixture does highlight the complexity of the LHY correction due to the LHY function given by Equation (2.21). Instead, for the homonuclear case, the LHY function takes the simpler form of Equation (2.23).

Variational energy minimisation relies on the derivatives,

$$\frac{\partial f}{\partial \Psi_1^*} = \frac{\partial x}{\partial \Psi_1^*}\frac{\partial f}{\partial x}, \; \frac{\partial f}{\partial \Psi_2^*} = \frac{\partial x}{\partial \Psi_2^*}\frac{\partial f}{\partial x}, \tag{2.34}$$

where $\partial f/\partial x$ is given by

$$\frac{\partial f}{\partial x} = \frac{5}{8\sqrt{2}}\sum_{\pm}\left\{\left(1 + x \pm \sqrt{(1-x)^2 + 4ux}\right)^{3/2}\left(1 \pm \frac{2(x-1)+4u}{2\sqrt{(1-x)^2+4ux}}\right)\right\}. \tag{2.35}$$

Further simplifications include again assuming that the interactions are at the critical point between attraction and repulsion (i.e. $g_{12}^2 = g_{11}g_{22}$) to avoid any complex contribution to the LHY term [153]. Thus, setting $u = 1$ gives

$$\frac{\partial f}{\partial x} = \frac{5}{2}(1+x)^{3/2}. \tag{2.36}$$

With Equation (2.36), this gives the two coupled, dimensional GP equations,

$$\begin{aligned}
i\hbar\frac{\partial \Psi_1}{\partial t} &= \left[-\frac{\hbar^2}{2m}\nabla^2 + g_{11}|\Psi_1|^2 + g_{12}|\Psi_2|^2 + \frac{4}{3\pi^2}\left(\frac{m}{\hbar^2}\right)^{3/2} g_{11}^{5/2}(1+x)^{3/2}|\Psi_1|^3\right]\Psi_1, \\
i\hbar\frac{\partial \Psi_2}{\partial t} &= \left[-\frac{\hbar^2}{2m}\nabla^2 + g_{22}|\Psi_2|^2 + g_{12}|\Psi_1|^2 + \frac{4}{3\pi^2}\left(\frac{m}{\hbar^2}\right)^{3/2} g_{11}^{3/2}g_{22}(1+x)^{3/2}|\Psi_1|^3\right]\Psi_2,
\end{aligned}$$

which, by substituting $x = g_{22}n_2/g_{11}n_1$, yields

$$\begin{aligned}
i\hbar\frac{\partial \Psi_1}{\partial t} &= \left[-\frac{\hbar^2}{2m}\nabla^2 + g_{11}|\Psi_1|^2 + g_{12}|\Psi_2|^2 + \frac{4}{3\pi^2}\left(\frac{m}{\hbar^2}\right)^{3/2} g_{11}\left(g_{11}|\Psi_1|^2 + g_{22}|\Psi_2|^2\right)^{3/2}\right]\Psi_1, \\
i\hbar\frac{\partial \Psi_2}{\partial t} &= \left[-\frac{\hbar^2}{2m}\nabla^2 + g_{22}|\Psi_2|^2 + g_{12}|\Psi_1|^2 + \frac{4}{3\pi^2}\left(\frac{m}{\hbar^2}\right)^{3/2} g_{22}\left(g_{11}|\Psi_1|^2 + g_{22}|\Psi_2|^2\right)^{3/2}\right]\Psi_2.
\end{aligned}$$

Finally, by use of dimensional arguments, it is possible to write the above coupled GP

equations in dimensionless form as

$$i\frac{\partial\Psi_1}{\partial t} = \left[-\frac{1}{2}\nabla^2 + |\Psi_1|^2 + \eta|\Psi_2|^2 + \alpha\left(|\Psi_1|^2 + \beta|\Psi_2|^2\right)^{3/2}\right]\Psi_1, \tag{2.37}$$

$$i\frac{\partial\Psi_2}{\partial t} = \left[-\frac{1}{2}\nabla^2 + \beta|\Psi_2|^2 + \eta\beta|\Psi_1|^2 + \alpha\beta^2\left(|\Psi_1|^2 + \beta|\Psi_2|^2\right)^{3/2}\right]\Psi_2. \tag{2.38}$$

where

$$\eta = \frac{a_{12}}{\sqrt{a_{11}a_{22}}},$$

$$\alpha = \frac{32}{3}\left[\frac{2}{3\pi}\frac{|\delta a|a_{11}^{5/2}n_1^{(0)}}{\sqrt{a_{11}}+\sqrt{a_{22}}}\right]^{1/2},\ \beta = \left(\frac{a_{22}}{a_{11}}\right)^{1/2},$$

with dimensional parameters

$$\xi = \sqrt{\frac{3}{8\pi}\frac{(\sqrt{a_{11}}+\sqrt{a_{22}})}{|\delta a|\sqrt{a_{11}}n_1^{(0)}}}, \qquad \tau = \frac{3m}{8\pi\hbar}\frac{(\sqrt{a_{11}}+\sqrt{a_{22}})}{|\delta a|\sqrt{a_{11}}n_1^{(0)}},$$

$$\rho_1 = \frac{2}{3}\frac{|\delta a|n_1^{(0)}}{\sqrt{a_{11}}(\sqrt{a_{11}}+\sqrt{a_{22}})}, \qquad \rho_2 = \frac{2}{3}\frac{|\delta a|n_1^{(0)}}{\sqrt{a_{22}}(\sqrt{a_{11}}+\sqrt{a_{22}})},$$

where $\delta a = a_{12} + \sqrt{a_{11}a_{22}}$ and by again scaling length ($\mathbf{r} = \xi\tilde{\mathbf{r}}$), time ($t = \tau\tilde{t}$) and the two component wavefunctions ($\Psi_i = \rho_i^{1/2}\tilde{\Psi}_i$).

The two most significant differences between the heteronuclear and homonuclear density-unlocked GP equations are: (1) the heteronuclear equations have unequal kinetic energy contributions; (2) the heteronuclear LHY correction does not simplify, as in homonuclear mixtures.

2.4.3 The Lee-Huang-Yang integral function

The integral form of the LHY function given in Equations (2.21) and (2.22) must be computed explicitly for heteronuclear mixtures. The integral can be difficult to numerically compute reliably as it is additively convergent; hence it can be susceptible to naive use of numerical techniques. Some of these difficulties can be somewhat mitigated by transforming the integral variable, $k = \tan(t)$, as introduced by Ref. [158] to aid numerical convergence.

The computational difficulties of evaluating the LHY integral are exacerbated further for density-unlocked mixtures. Consider the density-locked model in which the LHY integral only appears in defining the units, ξ and τ, and dimensionless parameter, $\tilde{N}$; for an individual simulation, the LHY integral need only be computed once to translate between the experimental parameters — i.e., $(a_{11}, a_{22}, a_{12}, m_1, m_2, N_1, N_2)$ — and the theoretical parameter, $\tilde{N}$. On the other hand in density-unlocked mixtures, density dependence is retained within the GP Hamiltonians as shown in Equation (2.33). Solving

Equation (2.33) in time is therefore very challenging because Equation (2.22) must be evaluated throughout the time-stepping procedure. Not only is this computationally expensive, but numerical evaluation of this integral can be volatile, and a robust solver of the GP equations should not have to rely on tuning the tolerance of numerical integral solvers.

It is therefore advisable to avoid the LHY integral and one proposed method to avoid this is presented in the supplementary material of Ref. [255], in which the momentum integrals of Equation (2.21) are rewritten, under the condition $z > 1$, as a combination of elliptic integrals

$$\begin{aligned} f(z,1,x) = &\left(-2-7xz+2z^2+x^2z^2\right)\frac{\sqrt{x+z}}{2\sqrt{z}\,(z^2-1)} \\ &+\left(-2-7xz+3z^2+3x^2z^2-7xz^3-2x^2z^4\right)\frac{E\left[\arcsin(1/z)|-xz\right]-E(-xz)}{2(z^2-1)^{3/2}} \\ &+\left(2+8xz-3z^2+6x^2z^2-2xz^3+x^2z^4\right)\frac{F\left[\arcsin(1/z)|-xz\right]-K(-xz)}{2(z^2-1)^{3/2}}, \end{aligned} \tag{2.39}$$

where $E(\phi|v)$ and $E(v)$ are the incomplete and complete elliptic integrals of the second kind, respectively, whilst $F(\phi|v)$ and $K(v)$ are the incomplete and complete elliptic integrals of the first kind, respectively. Writing the function in this way means that computation is far simpler as there are standard algorithms for the numerical evaluation of elliptic integrals.

By writing the LHY function in the form of Equation (2.39) it can be shown that, $f(z,u,x) = z^{3/2}x^{5/2}f(1/z,u,1/x)$, is an identity for the LHY function of inverse mass and density ratios — likewise shown in the supplementary materials of Ref. [255] — which means the dimensionless, unequal mass GP equations can be rewritten as [255]

$$\begin{aligned} i\frac{\partial\Psi_1}{\partial t} &= \left[-\frac{\gamma}{2}\nabla^2+|\Psi_1|^2+\eta|\Psi_2|^2+\alpha\beta^{3/2}z^{3/5}f'(\tilde{x})|\Psi_2|^3\right]\Psi_1, \\ i\frac{\partial\Psi_2}{\partial t} &= \left[-\frac{\gamma}{2z}\nabla^2+\beta|\Psi_2|^2+\eta\beta|\Psi_1|^2+\alpha\beta^{5/2}z^{3/5}\left(\frac{5}{2}\beta f(\tilde{x})|\Psi_2|^3-f'(\tilde{x})|\Psi_1|^2|\Psi_2|\right)\right]\Psi_2, \end{aligned} \tag{2.40}$$

where $\tilde{x} = 1/x$ for brevity. Writing the GP equations in this form aids solving for the mixture in the limit of $n_1 \to 0$ as otherwise the LHY function diverges for small n_1. This work therefore proposes the idea that the computational box could be divided into regions where: Equation (2.40) is evaluated for $n_1 \to 0$; Equation (2.33) is evaluated for $n_2 \to 0$; and finally, in the limit of $n_1, n_2 \to 0$, no LHY contribution needs to be calculated as it is negligible. However, though Equations (2.39) and (2.40) appear to avoid some complexities of modelling heteronuclear mixtures, a further issue arises.

Equation (2.40) is defined in terms of $f(1/z,u,1/x)$, and Equation (2.39) imposes the condition, $z > 1$. Thus, inverting the mass ratio implies that Equation (2.39) depends

on $\arcsin(z)$ which is undefined for $z > 1$, i.e., the inverted mass and density ratio GP equations in Equation (2.40) cannot be naively computed. There have been methods suggested to avoid this by swapping the component definitions in the limits of either $n_1 \to 0$ or $n_2 \to 0$ [255]. However, an effective expression for the heteronuclear LHY function has been proposed [241], and there are outstanding questions on the benefits of implementing either the more exact LHY definition, or simply relying on an approximation. The effective heteronuclear LHY corrections are discussed further in Section 5.3.

2.5 Density-locked Bogoliubov-de Gennes

Collective excitations have proven to be a useful tool in both the theoretical and experimental study of quantum gases (many early experimental studies are reviewed in Ref. [256]). The theory introduced by Bogoliubov offers a method for investigating small-amplitude excitations to weakly-interacting Bose gases [232]. The results of this theory [257] have shown excellent agreement with early experiments [64, 65, 258], including the experimental observation of the Bogoliubov dispersion relation [237] given in Figure 2.1.

To study the collective excitations of density-locked droplets described by Equation (2.31), a perturbation, $\delta\phi(\mathbf{r}, t)$, about the ground state wavefunction, $\phi_0(\mathbf{r}, t)$, is made. Substituting the perturbed ground state solution into Equation (2.31) and linearising the GP equation — i.e., rejecting terms of quadratic order in $\delta\phi$ and $\delta\phi^*$ — gives,

$$\begin{aligned} i\frac{\partial\delta\phi}{\partial t} &= -\frac{\nabla^2\delta\phi}{2} - 3\left[2|\phi_0|^2\delta\phi + \phi_0^2\delta\phi^*\right] + \frac{5}{2}\left[\frac{5}{2}|\phi_0|^3\delta\phi + \frac{3}{2}\phi_0^2|\phi_0|\delta\phi^*\right], \\ -i\frac{\partial\delta\phi^*}{\partial t} &= -\frac{\nabla^2\delta\phi^*}{2} - 3\left[2|\phi_0|^2\delta\phi^* + \phi_0^{*2}\delta\phi\right] + \frac{5}{2}\left[\frac{5}{2}|\phi_0|^3\delta\phi^* + \frac{3}{2}\phi_0^{*2}|\phi_0|\delta\phi\right], \end{aligned} \tag{2.41}$$

with further details of this calculation given in Appendix C. By writing the ground state wavefunction as $\phi_0(\mathbf{r}, t) = \sqrt{n(\mathbf{r})}e^{-i\mu t}$, the wavefunction perturbations can be written in the Bogoliubov form [232]

$$\begin{aligned} \delta\phi(\mathbf{r}, t) &= e^{-i\mu t}\left(u(\mathbf{r})e^{-i\omega t} - v^*(\mathbf{r})e^{i\omega t}\right), \\ \delta\phi^*(\mathbf{r}, t) &= e^{i\mu t}\left(u^*(\mathbf{r})e^{i\omega t} - v(\mathbf{r})e^{-i\omega t}\right), \end{aligned}$$

which substituted into Equation (2.41) gives

$$\begin{aligned} e^{-i\omega t}\left[(\mu+\omega)\,u\right] + e^{i\omega t}\left[(-\mu+\omega)\,v^*\right] = {} & e^{-i\omega t}\left(-\frac{\nabla^2 u}{2}\right) - e^{i\omega t}\left(-\frac{\nabla^2 v^*}{2}\right) \\ & - 3\left[e^{-i\omega t}\left(2|\phi_0|^2 u - \phi_0^2 v\right) + e^{i\omega t}\left(-2|\phi_0|^2 v^* + \phi_0^2 u^*\right)\right] \\ & + \frac{5}{2}\Bigg[e^{-i\omega t}\left(\frac{5}{2}|\phi_0|^3 u - \frac{3}{2}\phi_0^2|\phi_0| v\right) \\ & \quad + e^{i\omega t}\left(-\frac{5}{2}|\phi_0|^3 v^* + \frac{3}{2}\phi_0^2|\phi_0| u^*\right)\Bigg], \end{aligned}$$

and,

$$\begin{aligned} e^{-i\omega t}\left[(-\mu+\omega)\,v\right] + e^{i\omega t}\left[(\mu+\omega)\,u^*\right] = {} & e^{i\omega t}\left(-\frac{\nabla^2 u^*}{2}\right) - e^{-i\omega t}\left(-\frac{\nabla^2 v}{2}\right) \\ & - 3\left[e^{-i\omega t}\left(-2|\phi_0|^2 v + \phi_0^2 u\right) + e^{i\omega t}\left(2|\phi_0|^2 u^* - \phi_0^2 v^*\right)\right] \\ & + \frac{5}{2}\Bigg[e^{-i\omega t}\left(-\frac{5}{2}|\phi_0|^3 v + \frac{3}{2}\phi_0^2|\phi_0| u\right) \\ & \quad + e^{i\omega t}\left(\frac{5}{2}|\phi_0|^3 u^* - \frac{3}{2}\phi_0^2|\phi_0| v^*\right)\Bigg]. \end{aligned}$$

Equating terms in powers of $e^{-i\omega t}$ gives the Bogoliubov-de Gennes (BdG) equations which in matrix form are

$$\begin{pmatrix} -\frac{\nabla^2}{2} - 6\phi_0^2 + \frac{25}{4}\phi_0^3 - \mu & -\left[-3\phi_0^2 + \frac{15}{4}\phi_0^3\right] \\ -3\phi_0^2 + \frac{15}{4}\phi_0^3 & -\left[-\frac{\nabla^2}{2} - 6\phi_0^2 + \frac{25}{4}\phi_0^3 - \mu\right] \end{pmatrix} \begin{pmatrix} u \\ v \end{pmatrix} = \omega \begin{pmatrix} u \\ v \end{pmatrix}, \tag{2.42}$$

i.e., the BdG equations can be written as an eigenvalue problem in which the excitation frequencies, ω, and the associated quasiparticle wavefunctions, (u, v), are given by the eigenvalues and eigenvectors of the BdG matrix.

Much of this thesis studies spherically-symmetric droplets, i.e., solutions that vary with radius only, $\Psi_i(\mathbf{r}, t) \to \Psi_i(r, t)$. Spherically symmetric ground state wavefunctions can be used to probe collective modes with general angular momenta, l, by rewriting the quasiparticle wavefunctions as [45],

$$\begin{aligned} u(\mathbf{r}) &= u(r)Y_{lm}(\theta, \phi), \\ v(\mathbf{r}) &= v(r)Y_{lm}(\theta, \phi). \end{aligned}$$

where $Y_{lm}(\theta, \phi)$ are the spherical harmonics. This spherical form of the quasiparticle wavefunctions allows for the rewriting of the Laplacian via the identity

$$\nabla^2 Y_{lm}(\theta, \phi) = \frac{l(l+1)Y_{lm}(\theta, \phi)}{r^2},$$

giving

$$\nabla^2 u(\mathbf{r}) = u(r)\left[\frac{l(l+1)Y_{lm}(\theta,\phi)}{r^2}\right] + Y_{lm}(\theta,\phi)\left[\frac{2}{r}\frac{\partial u(r)}{\partial r} + \frac{\partial^2 u(r)}{\partial r^2}\right].$$

Hence, under this substitution there is a global factor of $Y_{lm}(\theta,\phi)$ in all elements of Equation (2.42) which can be cancelled through. Thus, the Hamiltonian on the diagonal of Equation (2.42) becomes

$$-\frac{1}{2}\left[\frac{2}{r}\frac{\partial}{\partial r} + \frac{\partial^2}{\partial r^2} + \frac{l(l+1)}{r^2}\right] - 6\phi_0^2 + \frac{25}{4}\phi_0^3 - \mu. \tag{2.43}$$

It is important here to make a distinction between the BdG analysis presented in this section, and the Bogoliubov approach discussed in Sections 2.1 and 2.2, as the similar naming conventions can be confused. The Bogoliubov methods in Sections 2.1 and 2.2 describe quantum mechanical Bogoliubov quasiparticle excitations to the Bose gas by examining the full system Hamiltonian. Then, calculating the zero point energy of these excitations allows for the construction of the extended GP equations via a LDA. On the other hand, the BdG analysis presented in this section uses linearised perturbations of the extended GP equations to study collective excitations of the droplet. However, in the case of a uniform Bose gas with contributions from contact interactions only, the BdG methods coincide with the same dispersion relation, Equation (2.8), as found via the quantum mechanical quasiparticle approach. Conversely, linearised perturbations of the extended GP equation will never directly correspond to the quantum quasiparticle calculations as it the sum of these quasiparticles that constitute the LHY term.

Having introduced the models, equations and methods for describing two-component quantum droplets, the next section of this chapter will introduce the numerical methods for solving these equations.

2.6 Computational techniques

The primary method of this work is to isolate ground state solutions of the GP equations, and study the dynamics of these solutions either through direct numerical simulation or via the BdG analysis discussed above.

2.6.1 Imaginary time

Stationary states of the GP equation can be found via a solution of the form $\phi(\mathbf{r},t) = \phi_0(\mathbf{r})e^{-i\mu t/\hbar}$ where μ is the chemical potential given by $\mu = \partial E/\partial N$. With this solution, the density-locked, extended GP equation takes the form of a time-independent non-linear Schrödinger equation,

$$\mu\phi_0 = \left[-\frac{1}{2}\nabla^2 - 3|\phi_0|^2 + \frac{5}{2}|\phi_0|^3\right]\phi_0.$$

Solving this equation results in the ground state, ϕ_0, of the system which is found here via imaginary-time propagation [259].

A time-dependent wavefunction, $\Psi(\mathbf{r}, t)$, can be written as a superposition of time-independent wavefunctions, $\psi_i(\mathbf{r})$, of the form,

$$\Psi(\mathbf{r}, t) = e^{-iE_0 t/\hbar}\psi_0(\mathbf{r}) + e^{-iE_1 t/\hbar}\psi_1(\mathbf{r}) + e^{-iE_2 t/\hbar}\psi_2(\mathbf{r}) + \ldots, \tag{2.44}$$

in which E_i is the energy of the ith state. The energies are ordered as $E_0 < E_1 < E_2 < \ldots$ such that the ground state energy, E_0, is smallest. Substituting $t \to -i\tau$, Equation (2.44) becomes a sum of negative exponentials which decay to zero for increasing τ. Due to the ordering of the energies, the 'least decayed' state is $\Psi \approx e^{-E_0\tau/\hbar}\psi_0(\mathbf{r})$, therefore imaginary time propagation converges to an approximate ground state of the system. Thus, under the imaginary time transformation Equation (2.31) becomes

$$\frac{\partial\phi}{\partial t} = -\left[-\frac{1}{2}\nabla^2 - 3|\phi|^2 + \frac{5}{2}|\phi|^3 - \mu\right]\phi, \tag{2.45}$$

i.e., the approximate form of a diffusion equation with constant diffusivity (equivalent to the heat equation), $\partial\phi/\partial t = \nu\nabla^2\phi$, for the field, ϕ.

Imaginary time propagation does not preserve the normalisation of the wavefunction [259]. Hence, at each time-step the wavefunction must be renormalised under the condition

$$\psi \to \psi\sqrt{\frac{N}{\int |\Psi|^2 \,\mathrm{d}^3\mathbf{r}}},$$

where N is the total number of atoms. Alongside the wavefunction renormalisation at each time step, the chemical potential is computed by the formula [45]

$$\mu = \int \mathrm{d}^3\mathbf{r}\, \phi^* H\phi = \int \mathrm{d}^3\mathbf{r}\, \phi^* \left[-\frac{1}{2}\nabla^2 - 3|\phi|^2 + \frac{5}{2}|\phi|^3\right]\phi, \tag{2.46}$$

which is included in the imaginary-time Hamiltonian as, $-\mu\phi$.

Imaginary time ends once 'adequate convergence' of some observable is reached. To isolate ground states, this work monitors: central density, total energy, and chemical potential convergence throughout imaginary time propagation, e.g., $\mu^{(n+1)} - \mu^{(n)} < 10^{-9}$. Following this convergence condition the approximate ground state wavefunction can then be propagated through real time, i.e., the original GP equations prior to the imaginary time transformation.

2.6.2 Spatial discretisation

Having introduced the basic algorithm for isolating ground states of the system, the following two sections introduce the spatial and temporal discretisations that define the numerical approximations used to solve the GP equations. Beginning with the spherically

symmetric geometry, the spatial discretisation defines a 'radial grid'

$$r = \Delta r \left[-\frac{1}{2}, \frac{1}{2}, \frac{3}{2}, \ldots, \left(N_r - \frac{1}{2} \right), \left(N_r + \frac{1}{2} \right) \right],$$

in which Δr is the spatial discretisation step, and N_r is the number of points within the spatial grid. The wavefunction, e.g., in the density-locked GP equation, ϕ, is therefore discretised across this grid, $\phi(r_i)$. The kinetic energy contribution to the GP Hamiltonian is defined on the grid using central finite difference methods

$$\begin{aligned} \nabla^2 \phi &= \frac{1}{r^2} \frac{\partial}{\partial r} \left(r^2 \frac{\partial \phi}{\partial r} \right) = \frac{2}{r} \frac{\partial \phi}{\partial r} + \frac{\partial^2 \phi}{\partial r^2} \\ &\approx \frac{2}{r} \left[\frac{\phi(r + \Delta r) - \phi(r - \Delta r)}{2 \Delta r} \right] + \left[\frac{\phi(r + \Delta r) - 2\phi(r) + \phi(r - \Delta r)}{\Delta r^2} \right]. \end{aligned} \tag{2.47}$$

The kinetic contribution shows why the radial grid is defined with a $\Delta r/2$ offset about the origin, because there is a discontinuity at $r = 0$ within the first-order derivative.

The centred finite difference approximations require the use of 'ghost points' at $r = -\Delta r/2$ and $r = N_r + \Delta r/2$ which are used to compute derivatives at the boundaries of the computational grid. These ghost points are subject to boundary conditions: Neumann boundary conditions ($\partial \phi / \partial r = 0$) are imposed at $r = 0$; and either Neumann or Dirichlet ($\phi = 0$) boundary conditions are imposed at $r = \Delta r N_r = L_r$. Neumann boundary conditions are approximated using a forward difference approximation

$$\frac{\partial \phi}{\partial r} \approx \frac{\phi(r + \Delta r) - \phi(r)}{\Delta r},$$

which at the origin sets $\phi(r = -\Delta r/2) = \phi(r = \Delta r/2)$.

The 3D grid is similarly defined as

$$\begin{aligned} x &= \Delta x \left[\left(-N_x - \frac{1}{2} \right), \left(-N_x + \frac{1}{2} \right), \ldots, -\frac{1}{2}, \frac{1}{2}, \ldots, \left(N_x - \frac{1}{2} \right), \left(N_x + \frac{1}{2} \right) \right], \\ y &= \Delta y \left[\left(-N_y - \frac{1}{2} \right), \left(-N_y + \frac{1}{2} \right), \ldots, -\frac{1}{2}, \frac{1}{2}, \ldots, \left(N_y - \frac{1}{2} \right), \left(N_y + \frac{1}{2} \right) \right], \\ z &= \Delta z \left[\left(-N_z - \frac{1}{2} \right), \left(-N_z + \frac{1}{2} \right), \ldots, -\frac{1}{2}, \frac{1}{2}, \ldots, \left(N_z - \frac{1}{2} \right), \left(N_z + \frac{1}{2} \right) \right], \end{aligned}$$

in which N_a and Δa are the number of grid points and the spatial grid discretisation, respectively, in the a-coordinate direction. The density-locked wavefunction is hence defined on this 3D grid, $\phi(x, y, z)$ i.e., as a 3D numerical array.

The kinetic contributions are therefore computed as

$$\begin{aligned}\nabla^2\phi &= \frac{\partial^2\phi}{\partial x^2} + \frac{\partial^2\phi}{\partial y^2} + \frac{\partial^2\phi}{\partial z^2} \\ &\approx \left[\frac{\phi(x+\Delta x,y,z) - 2\phi(x,y,z) + \phi(x-\Delta x,y,z)}{\Delta x^2}\right] \\ &+ \left[\frac{\phi(x,y+\Delta y,z) - 2\phi(x,y,z) + \phi(x,y-\Delta y,z)}{\Delta y^2}\right] \\ &+ \left[\frac{\phi(x,y,z+\Delta z) - 2\phi(x,y,z) + \phi(x,y,z-\Delta z)}{\Delta z^2}\right].\end{aligned}$$

Again boundary conditions are applied as either Neumann — using the same forward difference approximation as in the spherically symmetric case — or Dirichlet conditions.

2.6.3 Time discretisation

For both real and imaginary time propagation, time discretisation is implemented via the Runge-Kutta 4$^{\text{th}}$-order (RK4) method.

For the density-locked GP equation the imaginary-time propagation takes the form

$$\phi^{(n+1)} = \phi^{(n)} + \frac{1}{6}\left(k_1 + 2k_2 + 2k_3 + k_4\right),$$

where

$$\begin{aligned}k_1 &= -\Delta t\mathcal{H}[\phi] = -\Delta t\left[-\frac{\nabla^2}{2} - 3|\phi|^2 + \frac{5}{2}|\phi|^3\right]\phi, \\ k_2 &= -\Delta t\mathcal{H}\left[\phi + \frac{k_1}{2}\right] = -\Delta t\left[-\frac{\nabla^2}{2} - 3\left|\phi + \frac{k_1}{2}\right|^2 + \frac{5}{2}\left|\phi + \frac{k_1}{2}\right|^3\right]\left(\phi + \frac{k_1}{2}\right), \\ k_3 &= -\Delta t\mathcal{H}\left[\phi + \frac{k_2}{2}\right] = -\Delta t\left[-\frac{\nabla^2}{2} - 3\left|\phi + \frac{k_2}{2}\right|^2 + \frac{5}{2}\left|\phi + \frac{k_2}{2}\right|^3\right]\left(\phi + \frac{k_2}{2}\right), \\ k_4 &= -\Delta t\mathcal{H}\left[\phi + k_3\right] = -\Delta t\left[-\frac{\nabla^2}{2} - 3\left|\phi + k_3\right|^2 + \frac{5}{2}\left|\phi + k_3\right|^3\right]\left(\phi + k_3\right).\end{aligned} \tag{2.48}$$

Following imaginary-time propagation, the substitution $\Delta t \to i\Delta t$ can be made in the expressions of Equation (2.48) to give the real-time RK4 method.

For coupled GP equations, such as Equation (2.38), each $k_{i,j}$ — corresponding to the ith-step of the RK4 algorithm for the jth-component — of each equation need to be computed sequentially. Thus, defining

$$\begin{aligned}\mathcal{H}_1[\Psi_1,\Psi_2] &= \left[-\frac{1}{2}\nabla^2 + |\Psi_1|^2 + \eta|\Psi_2|^2 + \alpha\left(|\Psi_1|^2 + \beta|\Psi_2|^2\right)^{3/2}\right]\Psi_1, \\ \mathcal{H}_2[\Psi_1,\Psi_2] &= \left[-\frac{1}{2}\nabla^2 + \beta|\Psi_2|^2 + \eta\beta|\Psi_1|^2 + \alpha\beta^2\left(|\Psi_1|^2 + \beta|\Psi_2|^2\right)^{3/2}\right]\Psi_2,\end{aligned}$$

the implementation order of the algorithm is as follows:

$$\begin{aligned}
k_{1,1} &= \mathcal{H}_1\left[\Psi_1, \Psi_2\right], \\
k_{1,2} &= \mathcal{H}_2\left[\Psi_1, \Psi_2\right], \\
k_{2,1} &= \mathcal{H}_1\left[\Psi_1 + \frac{k_{1,1}}{2}, \Psi_2 + \frac{k_{1,2}}{2}\right], \\
k_{2,2} &= \mathcal{H}_2\left[\Psi_1 + \frac{k_{1,1}}{2}, \Psi_2 + \frac{k_{1,2}}{2}\right], \\
k_{3,1} &= \mathcal{H}_1\left[\Psi_1 + \frac{k_{2,1}}{2}, \Psi_2 + \frac{k_{2,2}}{2}\right], \\
k_{3,2} &= \mathcal{H}_2\left[\Psi_1 + \frac{k_{2,1}}{2}, \Psi_2 + \frac{k_{2,2}}{2}\right], \\
k_{4,1} &= \mathcal{H}_1\left[\Psi_1 + k_{3,1}, \Psi_2 + k_{3,2}\right], \\
k_{4,2} &= \mathcal{H}_2\left[\Psi_1 + k_{3,1}, \Psi_2 + k_{3,2}\right],
\end{aligned} \tag{2.49}$$

with the final time step of each GP equation taking the form

$$\begin{aligned}
\Psi_1^{(n+1)} &= \Psi_1^{(n)} + \frac{1}{6}\left(k_{1,1} + 2k_{2,1} + 2k_{3,1} + k_{4,1}\right), \\
\Psi_2^{(n+1)} &= \Psi_2^{(n)} + \frac{1}{6}\left(k_{1,2} + 2k_{2,2} + 2k_{3,2} + k_{4,2}\right),
\end{aligned}$$

and real-time propagation can be carried out via the substitution, $\Delta t \to i\Delta t$.

Finally, explicit time integration methods are stable if the discrete time step follows the Courant-Friedrich-Lewys (CFL) condition [260]. The imaginary time GP equation given in Equation (2.45) takes the approximate form of a diffusion equation, and so the CFL condition for the diffusion equation [259],

$$\frac{\Delta t}{\Delta r^2} < \frac{1}{4\nu}, \tag{2.50}$$

where $\nu = 1/2$ here, sets the time-step upper bound. Note that this work sets $\Delta t = 0.1\Delta r^2$, though in the 3D code there are three spatial coordinate discretisation, thus, the time step for the 3D code is defined as $\Delta t = 0.1\left[\min\left(\Delta x, \Delta y, \Delta z\right)\right]^2$.

2.6.4 Solving the Bogoliubov-de Gennes equations

The density-locked BdG equations given in Equation (2.42) are an eigenvalue problem, for which there are many numerical libraries [1]. In order to find the eigenvalues and eigenvectors of Equation (2.42) the 2×2 matrix must first be built and this is done by creating a submatrix for each of the four elements of the BdG matrix.

In a spherically symmetric geometry, the wavefunction is stored numerically as a 1D array. Hence, the off-diagonal elements of Equation (2.42) can be built as a diagonal

[1] The eigenvalue problem is solved here by the sparse.linalg.eigs function [261] from the SciPy library for Python [262]

matrix whose elements are the 1D array,

$$-3\phi_0^2 + \frac{15}{4}\phi_0^3 = \begin{pmatrix} -\phi_0^2\left(\frac{\Delta r}{2}\right) + \frac{15}{3}\phi_0^3\left(\frac{\Delta r}{2}\right) & & \\ & -\phi_0^2\left(\frac{3\Delta r}{2}\right) + \frac{15}{3}\phi_0^3\left(\frac{3\Delta r}{2}\right) & \\ & & \ddots \end{pmatrix}.$$

Likewise the non-derivative elements of the Hamiltonian given in the diagonal elements of Equation (2.42) are built this way. However, more care must be taken when building the Laplacian.

As discussed above, the Laplacian in the spherically symmetric geometry takes the form

$$\nabla^2 = \frac{2}{r}\frac{\partial}{\partial r} + \frac{\partial^2}{\partial r^2}.$$

The finite-difference approximations of the first and second order derivatives are defined by the stencil formula given in Equation (2.47). These finite difference stencils can instead by written in matrix form, and are here defined as,

$$\mathcal{D}_1 \coloneqq \frac{1}{2\Delta r}\begin{pmatrix} -1 & 1 & & & & & \\ -1 & 0 & 1 & & & & \\ & -1 & 0 & 1 & & & \\ & & \ddots & \ddots & \ddots & & \\ & & & -1 & 0 & 1 & \\ & & & & -1 & 0 & 1 \\ & & & & & -1 & 1 \end{pmatrix} \equiv \frac{\partial}{\partial r},$$

and,

$$\mathcal{D}_2 \coloneqq \frac{1}{\Delta r^2}\begin{pmatrix} -1 & 1 & & & & & \\ 1 & -2 & 1 & & & & \\ & 1 & -2 & 1 & & & \\ & & \ddots & \ddots & \ddots & & \\ & & & 1 & -2 & 1 & \\ & & & & 1 & -2 & 1 \\ & & & & & 1 & -1 \end{pmatrix} \equiv \frac{\partial^2}{\partial r^2}. \tag{2.51}$$

These matrices assume Neumann boundary conditions, $\partial\phi/\partial r = 0$. For example the central, finite-difference, first-order derivative at the $r = \Delta r/2$ boundary takes the form

$$\frac{\partial\phi}{\partial r} \approx \frac{\phi\left(\frac{3\Delta r}{2}\right) - \phi\left(\frac{-\Delta r}{2}\right)}{2\Delta r}.$$

As in Section 2.6.2, the forward difference approximation of the Neumann boundary condition is

$$\frac{\partial\phi}{\partial r} \approx \frac{\phi\left(\frac{\Delta r}{2}\right) - \phi\left(\frac{-\Delta r}{2}\right)}{\Delta r} = 0 \rightarrow \phi\left(\frac{\Delta r}{2}\right) \approx \phi\left(-\frac{\Delta r}{2}\right),$$

meaning that the first-order derivative at the $r = \Delta r/2$ boundary can be approximated as

$$\frac{\partial \phi}{\partial r} \approx \frac{\phi\left(\frac{3\Delta r}{2}\right) - \phi\left(\frac{\Delta r}{2}\right)}{2\Delta r}.$$

The same method is used for the boundary in the central finite-difference, second-order derivative which at the $r = \Delta r/2$ boundary can be approximated as

$$\frac{\partial^2 \phi}{\partial r^2} \approx \frac{\phi\left(\frac{3\Delta r}{2}\right) - \phi\left(\frac{\Delta r}{2}\right)}{\Delta r^2}.$$

These approximations can also be inverted to apply at the $r = L_r - \Delta r/2$ boundary, which therefore means that the so-called 'ghost points' at $r = -\Delta r/2$ and $r = L_r + \Delta r/2$ can be neglected.

For full 3D geometry, the 3D wavefunction array can be flattened into a 1D array and built along the diagonals of the submatrices of Equation (2.42) as in the spherically symmetric case. However, once again more care needs to be taken with the Laplacian, which is built by taking the second-order derivative operator, $\mathcal{D}_2$, in Equation (2.51), and computing

$$\nabla^2 = \mathbb{I}_{n_z} \otimes \mathbb{I}_{n_y} \otimes \mathcal{D}_{2,n_x} + \mathbb{I}_{n_z} \otimes \mathcal{D}_{2,n_y} \otimes \mathbb{I}_{n_x} + \mathcal{D}_{2,n_z} \otimes \mathbb{I}_{n_y} \otimes \mathbb{I}_{n_x},$$

where $\otimes$ denotes the Kronecker product, and $\mathbb{I}_{n_i}$ is the identity matrix with size given by the number of grid points in the i-axis. BdG analysis can be a computationally expensive technique for two main reasons. Firstly, to find accurate eigenvalues often highly resolved and converged ground states are required. Secondly, because of this reliance on accurate ground state solutions, large matrices are constructed which particularly in 3D are computationally expensive to solve. Hence, the BdG analysis presented in this work is limited to spherical symmetry.

Having built up the theoretical and numerical methods for modelling droplets, this chapter finishes by introducing some fundamental results of density-locked droplets first presented in Ref. [153]. These results include both the ground states and collective excitations of density-locked droplets.

2.7 Ground state density-locked droplets

The simplifications in reducing the seven-dimensional space of the two-component Bose mixture, $(a_{11}, a_{22}, a_{12}, m_1, m_2, N_1, N_2)$, to the effective one dimensional parameter space, $\tilde{N}$, of the density-locked GP equation given in Equation (2.31), is a remarkable reduction in complexity. A further reduction in complexity arises from the isotropic structure of two-component droplets.

As discussed in Chapter 1, dipolar droplets have an anisotropic density profile due to their anisotropic interactions, whereas two-component droplets have isotropic interac-

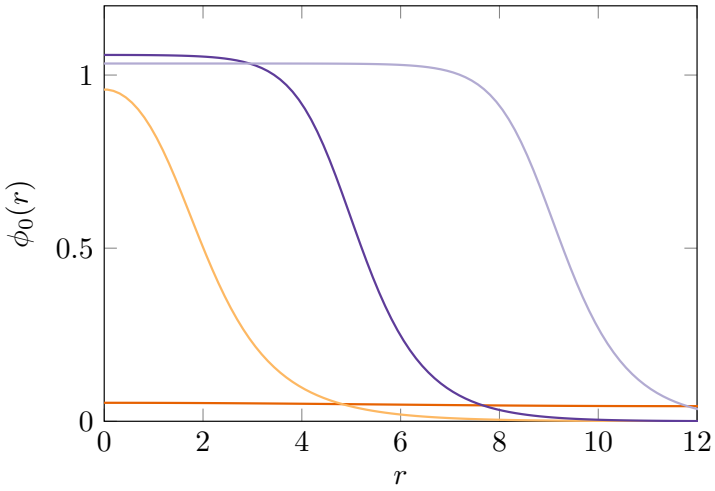

Figure 2.3: Ground state wavefunction profiles of quantum droplets, for $\tilde{N} = \{30, 500, 3000\}$ — given in light orange, dark purple and light purple, respectively — and of the unbound cloud for $\tilde{N} = 15$ — given in dark orange.

tions and therefore have a spherically symmetric density distribution in free space. This symmetry allows for free-space droplets to be described by a one-dimensional, spherically-symmetric wavefunction. Figure 2.3 shows spherically symmetric ground state wavefunctions of Equation (2.31), in which the wavefunctions vary with radius, r, only. Note that Figure 2.3 shows ground state wavefunctions rather than densities, to highlight the $\tilde{N} = 15$ case, since the ground state wavefunction is real-valued and thus $\phi(r) = \sqrt{n(r)}$.

At low atom numbers the droplet density is approximately Gaussian, as shown by the light orange curve. This profile is similar to that of a trapped, interacting Bose gas though the Gaussian-like droplet is self-bound in free space indicating the existence of a surface tension. Increasing the atom number leads to a central density saturation. This saturated central density corresponds to the 'top hat' or 'flat-top' density seen in both purple curves of Figure 2.3. Adding more atoms to the centrally saturated droplet in dark purple simply corresponds to an increasing droplet width. In the limit of $\tilde{N} \to \infty$, the bulk density saturated to $\phi_0 \to 1$ with $\mu \to -1/2$.

These density profiles are indicative of a liquid droplet; for example Figure 2.4 shows the density profile of a water droplet in free space — calculated numerically using smoothed particle hydrodynamics — in which there is a large constant bulk density and a rapid drop in density at the surface. A saturated bulk density corresponds to incompressibility, which in an extremely dilute system can initially seem counter intuitive. The incompressible, or flat-top density profile, regime is yet to be experimentally observed because, as discussed in Section 1.3, current droplet experiments are limited to the Gaussian-like regimes due to small atom numbers and high losses [168, 169, 173].

Below a critical atom number ($\tilde{N}_c \approx 18.65$) the kinetic energy of the gas overcomes any binding energy of the droplet leading to an unbound gas ground state [153] which can be seen by the dark orange line in Figure 2.3 for $\tilde{N} = 15$. The characteristic droplet profile and uniform condensate ground states force the use of Neumann boundary conditions, as

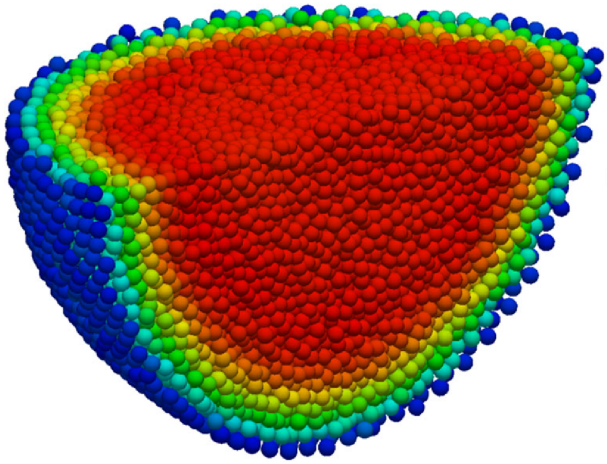

Figure 2.4: Density profile of a water droplet (with only a quarter of the droplet shown), calculated numerically using smoothed particle hydrodynamics. The highest and lowest density regions are shaded red and blue, respectively. Reprinted figure from Ref. [263] with permission from Springer Nature and Copyright Clearance Center.

the density is approximately constant at each boundary in both the droplet and uniform cases.

Having solved Equation (2.31) in a spherically symmetric geometry, these ground state solutions can be used to study the collective excitations of density-locked droplets via the BdG analysis presented in Section 2.5 as first introduced by Ref. [153]

2.8 Collective excitations of density-locked droplets

The collective excitations of quantum droplets have been extensively investigated, including: the BdG analysis of density-locked quantum droplets in the original work of Petrov [153], collective modes with and without trapping potentials [253], and deeper investigations of individual collective excitations, e.g., the breathing mode [201, 264] and spin dipole mode [204].

Figure 2.5(a) shows the lowest modes at angular momenta, $l = \{0, 2, 3, 4, 5, 6, 7\}$, obtained by solving Equation (2.42) using the numerical techniques presented in Section 2.6.4. Figure 2.5(a) excludes the dipole mode ($l = 1$), which is a centre-of-mass motion, hence $\omega_1 = 0$ in free space [153]. The bold orange curve spanning the whole domain is the particle-emission threshold, $-\mu$, computed from Equation (2.46); dark and light purple curves correspond to the $l = 0$ mode; and the $l = \{2, 3, 4, 5, 6, 7\}$ modes are shown by the thinner orange curves with increasing darkness corresponding to increasing l. By conceptualising the chemical potential, μ, as the energy cost of adding a particle to the system, the negative chemical potential of a droplet indicates that a droplet's total energy is lowered by having a higher population number. Hence, the particle-emission threshold, $-\mu$, gives an energy cut-off such that if an excitation exceeds this threshold, the droplet will 'self-evaporate', i.e., the excitation will be decayed by particle shedding such that the droplet settles to a lower energy state [153]. The decay of these modes highlights some of

the key differences between two-component droplets and the behaviour of trapped, single and two-component Bose gases. Typically the only decay mechanism for collective modes in a Bose-condensed gas is through interaction with a thermal component, i.e., higher temperatures correspond to higher damping rates [258].

All modes have decreasing frequency with increasing droplet size; a similar decrease in the lowest collective mode frequencies, with increasing atom number, has been found for Bose gases confined in axially symmetric traps [65, 265–267]. Furthermore, as the droplet size increases the higher l modes stabilise, except for the breathing mode which is stable for $\tilde{N} \gtrsim 933.7$. Note that Ref. [153] presents that the $l = 0$ mode is also stable in the range, $18.65 \lesssim \tilde{N} \lesssim 20.1$, not presented here. This therefore means that in the regime, $20.1 \lesssim \tilde{N} \lesssim 94.2$, all excitations exceed the particle-emission threshold, hence any excitation to the droplet leads to atom shedding. This is often referred to as self-evaporation and has been theorised as a regime which could lead to even lower temperatures because any finite-temperature component will excite the droplet corresponding to further evaporation such that the droplet cools further [153].

Simulating the collective modes dynamically can be achieved via the time-dependent, density-locked GP equation, in Equation (2.31). After finding the ground state solution via imaginary time a small perturbation can be made and the wavefunction is then evolved in real time. This is a technique used throughout Chapters 3 and 4, for previously unstudied systems, and so it is useful to first test the implementations of the time-dependent GP equations and BdG analysis to ensure that they match. Due to the restriction to spherical symmetry, the only mode which can be excited is the breathing mode.

To trigger a breathing mode in the droplet, a harmonic phase is imprinted on the ground state wavefunction, i.e., $e^{i\epsilon r^2}$ where ϵ takes a small value (here $\epsilon = 10^{-6}$) [45, 257]. To observe the oscillatory motion from the real time data, a measure of the droplet central density, $\bar{n}(t) = n(r = 0, t) - \langle n(r = 0)\rangle_t$, is used [shown in the insets of Figure 2.5(b) and (c)]. Thus to extract the breathing mode frequency, ω and decay rate, γ, the central density, $\bar{n}(t)$, is fitted to a damped sine wave

$$\bar{n} = Ae^{-\gamma t}\sin(\omega t + \varphi). \tag{2.52}$$

The breathing mode phase diagram is hence a function of $\tilde{N}$ only and thus the fitted breathing mode frequency, ω, is given by the dark purple dashed curve in Figure 2.5(a), which agrees with the BdG results.

Excitations above the particle-emission threshold result in unstable dynamics and the droplet responds by emitting atoms allowing the droplet to relax to a lower energy configuration. The excitation branches shown in Figure 2.5(a) are only shown in the stable region. Focusing on the breathing mode (given in purple), the dynamics are split into two regimes: self-evaporative and non-self-evaporative. Examples of these two regimes are given in Figure 2.5(b) and (c), respectively.

The points shown in Figure 2.5(b) and (c) are extracted by fitting the central density,

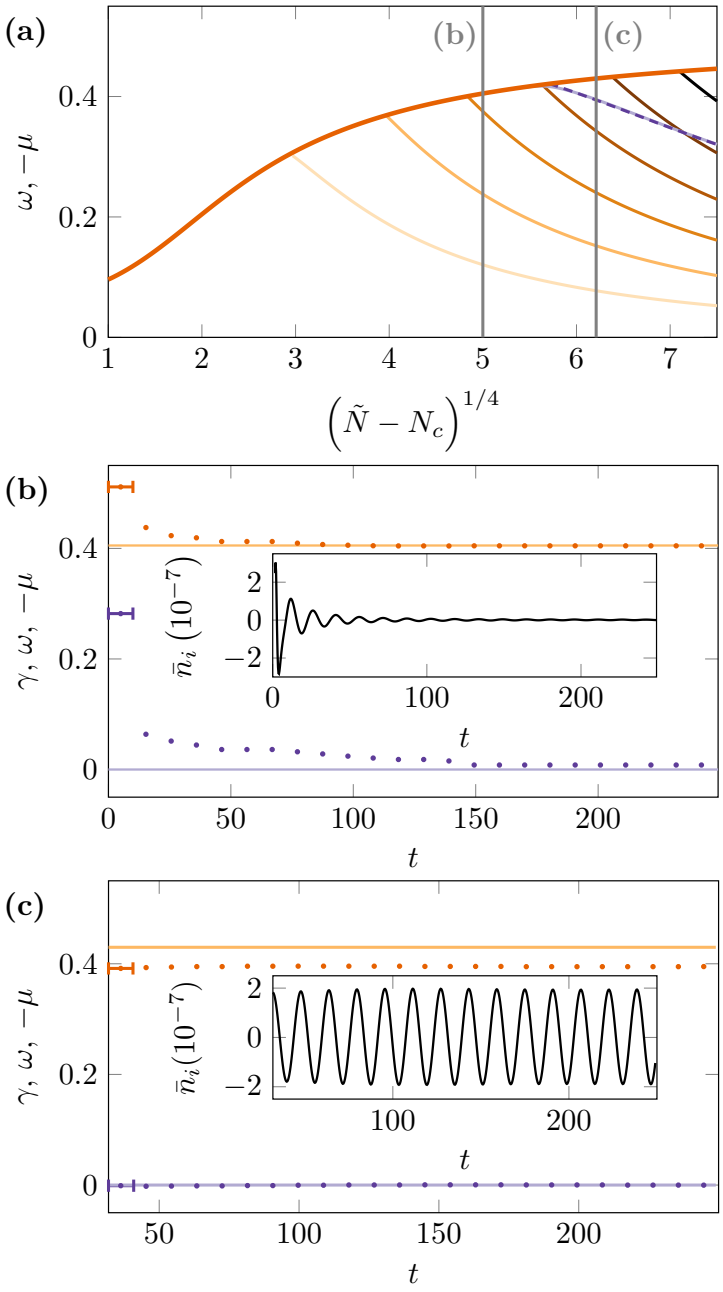

Figure 2.5: Collective excitations for spherically symmetric, density-locked quantum droplets as a function of droplet size, $\tilde{N}$. (a) The particle emission threshold, $-\mu$, (given by the bold orange curve) and mode frequencies of the $l = \{0, 2, 3, 4, 5, 6, 7\}$ modes of quantum droplets are given across a large range of a rescaled effective atom number $(\tilde{N} - N_c)^{1/4}$ (as presented in [153]). The $l = 0$ mode is given in purple where the dark, dashed purple curve is from fitting to dynamical simulations, and the light purple curve is from the BdG analysis. The $l = \{2, 3, 4, 5, 6, 7\}$ modes are given in orange with increasing l corresponding to increasingly darker shades. (b) Shows the fitted breathing mode frequency, ω, (orange points) and decay rate, γ, (purple points) dynamically in time for a droplet in the self-evaporative regime. The $\tilde{n}_i$ data is split into small ranges (an example time range is given by the bars around the first ω and γ points) and a damped sine curve is fitted. (c) Shows the equivalent analysis to (b) but for a droplet in the non-self-evaporative regime. In both (b) and (c) the orange and purple horizontal lines correspond to the particle emission threshold and zero decay rate, respectively.

$\bar{n}(t)$, to the damped sine wave in Equation (2.52), within small time intervals [given by the horizontal bars shown on the first points in Figure 2.5(b) and (c)]. The orange and purple points corresponding to the frequency, ω, and decay γ, respectively, whilst the horizontal orange and purple lines corresponds to the particle-emission threshold, μ, and zero decay rate, $\gamma = 0$, respectively. The central density oscillations in time are inset.

In Figure 2.5(b) the breathing mode frequency initially exceeds the particle emission threshold, with a corresponding high decay rate. The frequency then asymptotically decreases, converging to the particle emission threshold line, whilst the decay rate asymptotes towards zero. The idea behind this convergence to $-\mu$ was first presented in Ref. [264]. In the long-time limit, the particle emission is very slow, with particles emitted only at the energy of $-\mu$ which is negligible relative to the droplet energy. Contrast this with the non-self-evaporative regime, in which the breathing mode frequency is below the particle emission threshold, and hence the oscillations are stable as can be seen by the zero decay rate and constant frequency in Figure 2.5(c).

2.9 Discussion and conclusions

The ground state energy calculations of both the single and two-component Bose gases presented in this chapter show that quantum fluctuations can be described to first-order by the zero-point energy of the Bogoliubov quasiparticles. With the addition of quantum fluctuations attractive mixtures stabilise to form quantum droplets. A powerful model of two-component droplets is 'density-locking', in which the two component densities are simply rescalings of one another and the fundamental characteristic of a density-locked droplet is its size. The ability to describe the complexity of a two-component Bose by a single parameter is incredibly useful to understand the ground states and collective excitations of droplets, which offer a rich platform for studying stable and decaying excitations. However, alongside the simplicity of the density-locked model there are also restrictions. These restrictions are of particular concern for the CsYb mixture [214], such as population imbalances both in free space and within traps. To date there has been little work exploring the effects of population imbalanced droplets. Thus, building from the foundations of this chapter, Chapter 3 explores droplets with population imbalances in free space which is then extended to include trapped, imbalanced droplets in Chapter 4. Finally, Chapter 5 explores how the CsYb mixture is affected by these inter-component imbalances, and the resulting parameter space of interest experimentally.

Chapter 3

Quantum droplets in imbalanced atomic mixtures

A key result from the pioneering work of Petrov is the energetic favourability for the two component densities to maintain a fixed ratio $n_2/n_1 = \text{const.}$ [153] where n_i is the number density of the ith component. By pairing this assumption with negligible spin modes [153] — i.e., assuming only in-phase density oscillations — the mixture can be modelled via a single macroscopic wavefunction. The majority of the literature has focused on such balanced droplets, with theoretical studies of imbalanced systems limited to dipolar mixtures [207, 208] and 1D [268], confined to both a ring [269] and an optical lattice [270]. This chapter is a systematic study of the ground states and breathing modes of 3D spherical imbalanced quantum droplets in homonuclear mixtures. Adding atoms to one component of the mixture yields a lower energy configuration than the previous balanced droplet. This forms a droplet with a density imbalance in the core, and this imbalance can be increased up to a saturation limit at which any further atoms cannot bind to the droplet. By investigating imbalanced droplets in the free space limit, this chapter explores how the density profiles, chemical potentials and breathing mode dynamics of the droplet are modified by the presence of a population imbalance. This chapter begins by discussing imbalanced droplet ground states in Section 3.1 and then Section 3.2 explores propagating these states in time, subject to an initial perturbation, to analyse the droplet breathing modes. Beyond population imbalances, scattering length imbalances are discussed in Section 3.3. Finally the main results and potential future research avenues are discussed in Section 3.4.

3.1 Ground state density-unlocked droplets

To study imbalanced droplets, this chapter uses the density-unlocked GP equations derived in Section 2.4. Though the assumption of density-locking is neglected here, there are several assumptions made such as spherical symmetry and mass balance ($m_1 = m_2$). A density-unlocked, homonuclear mixture can be modelled by Equation (2.38), which

throughout this section and Section 3.2, reduces even further due to the assumption of balanced scattering lengths ($a_{11} = a_{22} \implies \beta = 1$). Thus, with this final assumption, the only differences between the components can arise from an imposed atom number imbalance of $N_1 = N_2 + \delta N_1$.

3.1.1 Flat-top droplet limit

A simplified ansatz for the density of large droplets, as used in Ref. [153], is a flat-top, step function in which kinetic energy contributions are neglected. The two-components of the imbalanced droplet are modelled as majority and minority components with $N + \delta N$ and N atoms, respectively. Substituting this ansatz into the two-component energy functional gives the equilibrium energy of the flat-top droplet,

$$E_{\text{eqbm}} = (2N + \delta N)\left[\frac{4\mathcal{A}^3}{27\mathcal{B}^2}\right],$$

as a function of imbalance, δN, where

$$\mathcal{A} = \left(1 + \frac{\delta N}{2N}\right) + (\eta - 1) + \frac{1-\eta}{2}\left(\frac{1}{1 + \frac{\delta N}{2N}}\right),$$

and

$$\mathcal{B} = \frac{4\sqrt{2}\alpha}{5}\left(1 + \frac{\delta N}{2N}\right)^{3/2},$$

and for further details see Appendix D, including a schematic of the ansatz. The results of this energy calculation are given in Figure 3.1 with the total equilibrium energy given in the main plot, and the inset showing the equilibrium energy per particle.

Firstly, the main plot of Figure 3.1 shows that there is a minimum at $\delta N \neq 0$ in the total energy, indicating the droplet can lower its energy by absorbing particles into one component. However, the equilibrium energy per particle given in the inset of Figure 3.1 exhibits a minimum at $\delta N = 0$ demonstrating that whilst the total energy of the droplet can be lowered by single-component absorption, there is a corresponding increase in the energy per particle resulting in a less stably bound droplet. Secondly, the Appendix D shows that the minimum in the equilibrium energy occurs at $\delta N/N = 2(\eta - 2) + [(\eta - 1)(4\eta - 14)]^{1/2}$. That is, the energy of the droplet decreases with imbalance up to this limit. The dependence of this quantity on the scattering lengths is consistent with the prediction of Ref. [153] at linear order [1]. For the parameters of Figure 3.1, $\delta n \approx 0.458$, as highlighted by the orange vertical line.

At this limit the droplet becomes saturated with the majority component. Hence if further majority component atoms are available, they cannot be absorbed into the droplet and in free space will be lost (as described in Ref. [153]). There are thus three

[1] Ref. [153] finds $\delta N/N \sim |\delta g|/g = -(1+\eta)/2$ for $|\delta g|/g \ll 1$; expanding our result in the same limit yields $\delta N/N \approx (1/3)|\delta g|/g$.

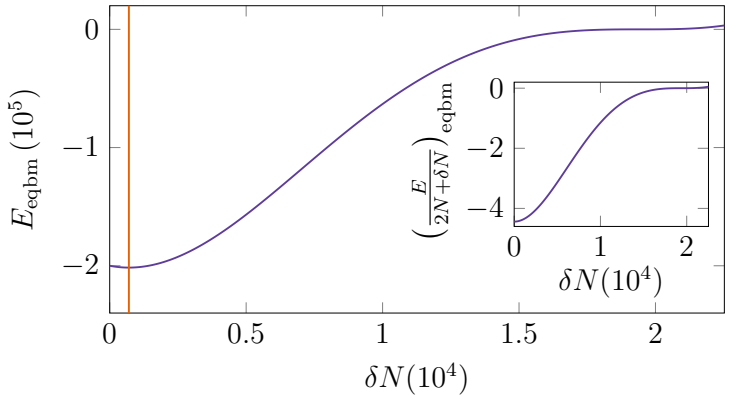

Figure 3.1: Energy of a flat-top density ansatz as a function of imbalance, δN, with parameters $N \approx 22524$, $\alpha \approx 0.0152$, $\beta = 1.0$ and $\eta = -1.2$. The equilibrium energy, E_{eqbm}, is shown in the main plot with the orange, vertical line indicating the location of the minimum at $\delta N \approx 703$. The inset shows the equilibrium energy per particle, $[E/(2N + \delta N)]_{\text{eqbm}}$, with the only minimum appearing at the origin.

droplet states: (1) balanced droplets; (2) bound, imbalanced droplets; and (3) saturated, imbalanced droplets (which can be immersed in a halo of unbound atoms if the mixture is trapped).

The decrease in energy of an imbalanced droplet is consistent with the predictions of Ref. [153] and stems from the basic argument that droplets always seek to lower their energy by absorbing atoms. For example, in the density-locked model, atoms can only be added to both components to ensure that $N_2/N_1 = \sqrt{g_{11}/g_{22}}$ is preserved, and by adding atoms to both components, a lower energy state is recovered. One way to conceptualise this is due to droplets having negative chemical potentials, meaning that it is always energetically favourable to absorb more particles into both components. However, the subtlety in the energy calculation given in Appendix D is that the energy of a droplet can also be lowered by absorbing particles into one component if there is an excess of this component available, up to the saturation limit discussed above.

By using the simple flat-top density ansatz, key insights are gained into effects of a population imbalance on the density structure and energy of a two-component droplet. However, for smaller droplet sizes kinetic energy cannot be neglected; thus, to extend this analysis to general, spherical droplets, the coupled GP equations are solved numerically.

3.1.2 Numerical solutions

To find ground state solutions, the coupled GP equations in Equation (2.38) are propagated numerically in imaginary time until the energy of the mixture is deemed adequately converged, via the 4^{th}-order Runge-Kutta method, with centred finite-difference methods for the spatial derivatives as discussed in Section 2.6. Neumann boundary conditions ($\partial\Psi_i/\partial r = 0$) are applied at the centre of the computational box as the density in the droplet core is approximately constant. The boundary at $r = L_r$, where L_r is the radial computational box size, has either Neumann or Dirichlet [$\Psi_i(r = L_r) = 0$] boundary

conditions, which are discussed further below with reference to Figure 3.2.

By enforcing the Dirichlet boundary condition at $r = L_r$, Figure 3.2(a), (b) and (c) show the three different ground state solutions (discussed above) by varying imbalance, δN_1. Figure 3.2(a) presents an example of a balanced droplet ($N_1 = N_2 \implies \delta N_1 = 0$) with an inset of the density difference $\delta n(r) = n_1(r) - n_2(r)$, showing that the two component densities are identical. By increasing the population imbalance to $\delta N_1 \approx 450$, as shown in Figure 3.2(b), the two component densities start to split within the droplet core, with both an increase and decrease in the majority and minority components' central densities, respectively. Hence, the two components are no longer identical but notably the density differences in the inset show that this imbalanced droplet has no unbound atoms around the droplet. This implies that this state is a bound, imbalanced droplet. Driving the imbalance higher to $\delta N_1 \approx 5631$, Figure 3.2(c) demonstrates a more pronounced density splitting within the droplet core, but crucially also exhibits a non-zero gas density outside of the droplet [highlighted in the inset of (c)]. This ground state hence corresponds to a saturated, imbalanced droplet at the centre of the box with an unbound gas cloud outside of the droplet core.

For a set droplet size — i.e., fixed α, η and N_2 — the only free parameter is δN_1 and

Figure 3.2 *(following page)*: Balanced and imbalanced ground state droplets, with fixed parameters: $N_2 \approx 22524$, $\alpha \approx 0.0152$, $\beta = 1.0$ and $\eta = -1.2$. (a), (b) and (c) Ground state density profiles of: a balanced droplet ($\delta N_1 = 0$); a bound, imbalanced droplet ($\delta N_1 \approx 450$); and a saturated, imbalanced droplet with an unbound halo of majority component atoms ($\delta N_1 \approx 5631$), respectively. The inset shows the difference in component densities, $\delta n(r)$. (d) The difference in central densities as a function of imbalanced majority component atoms, δN_1, with box size of $L_r = 128$. At $\delta N_1 = 0$ the system is balanced, with the leftmost vertical grey line corresponding to (a). Increasing δN_1 leads to an approximately linear increase in $\delta n(r = 0)$, there are however no atoms outside of the droplet as $n_1(r = 0.75L_r)$, a measure of density outside of the droplet, is zero. This regime corresponds to a bound, imbalanced droplet with the central vertical grey line corresponding to (b). The linear increase in $\delta n(r = 0)$ eventually plateaus to a regime in which the central densities in the droplet cannot be imbalanced further and the imbalanced droplet saturates with the density outside of the droplet increasing, resulting in a non-zero density of unbound atoms. The inset shows a measure of the difference in central densities in the limit of a saturated imbalanced droplet, $\delta n^{\text{sat}}(r = 0)$, as a function of droplet size given by the effective atom number $\tilde{N}$ in Equation (2.30), using the parameters for the $\delta N_1 = 0$ case. The orange, dashed, horizontal line corresponds to $\delta n \approx 0.458$ (from Figure 3.1), with the droplet size used in the main figure highlighted by the grey, vertical line. (e) Neumann boundary conditions are applied at both boundaries of the computational box, with $L_r = 1024$. The main plot shows the difference in central densities, recreating the results from (d), showing that the behaviour is not a function of the boundary conditions. It likewise demonstrates that the saturated droplet reaches a lower energy, $E[\Psi_1, \Psi_2]$, state than the balanced droplet. The inset shows an example imbalance of $\delta N_1 \approx 22524$, with varying box size L_r. In the limit of a large computational box any background gas will be effectively zero density, thus converging to a saturated droplet in free space.

(a)
(b)
(c)
(d)
(e)
$n_i(r)$
r
$\delta n(r)$
$\delta n(r=0)$
$\delta n^{\rm sat}(r=0)$
$\tilde{N}(10^3)$
$\delta N_1(10^3)$
$n_1(r=0.75L_r)(10^{-9})$
$1/L_r(10^{-2})$
$E[\Psi_1,\Psi_2]\,(10^4)$

thus Figure 3.2(d) shows two measures of the droplet ground states for varying δN_1. The two measures are the central density difference, $\delta n(r=0) = n_1(r=0) - n_2(r=0)$, and the majority component density, n_1, at a fixed radius outside of the droplet. The fixed radius is $r = 0.75L_r$, and is chosen to be relatively far from the droplet surface but not too close to $r = L_r$, to avoid the density drop resulting from the Dirichlet boundary condition. These measures are used to illustrate the transition between bound, imbalanced droplets, and saturated, imbalanced droplets. Figure 3.2(d) shows that for increasing δN_1 from zero, there is an immediate density splitting within the droplet corresponding to the approximately linear increase in $\delta n(r=0)$. It should be noted that in this regime, $n_1(r = 0.75L_r)$ stays fixed at zero, meaning that this relatively small δN_1 regime corresponds to bound, imbalanced droplets. However, increasing δN_1 further eventually leads to the formation of a shoulder in $\delta n(r=0)$ which is the saturation of the imbalanced droplet, i.e., the droplet is becoming saturated with majority component atoms. Beyond this shoulder $\delta n(r=0)$ then approaches a constant value [labelled here as $\delta n^{\text{sat}}(r=0)$]. Once in the saturated droplet regime, there is a corresponding increase in $n_1(r = 0.75L_r)$, indicating that the excess atoms reside outside of the droplet. The phase diagram in Figure 3.2(d) corresponds to the three ground state densities in (a), (b) and (c) given by the vertical grey lines. Furthermore, the inset of Figure 3.2(d) illustrates how the central density splitting of the saturated droplet varies with droplet size, given by $\tilde{N}$, the effective atom number of the balanced droplet in Equation (2.30) (from Ref. [153]). To vary droplet size, the fixed parameters are α and η, thus N_2 (and hence N_1) is varied for the different droplet sizes, with $\tilde{N}$ calculated for the balanced droplet ($\delta N_1 = 0$) parameters. The central density difference of the saturated droplet increases with droplet size and asymptotically approaches a constant value of $\delta n \approx 0.458$ [given by the orange, dashed, horizontal line in the inset of (d)] in the limit of a large, flat-top droplet as discussed in Section 3.1.1. Figure 3.2(c) and (d) show that in the limit of the saturated droplet, there exists the unbound gas. This chapter seeks to explore imbalanced droplets, in the absence of this unbound gas, to probe the physics of imbalancing the droplet in free space. Thus, rather than imposing a Dirichlet boundary condition at $r = L_r$, instead the same Neumann boundary condition used at $r = 0$, is used at $r = L_r$, also. This gives a numerical approximation to a free space system. Figure 3.2(e) uses equivalent parameters as in (d), with a slightly increased δN_1 range, and exhibits the same central density difference behaviour as with the Dirichlet boundary conditions at $r = L_r$. From this point on, Neumann boundary conditions are applied at both boundaries.

Figure 3.2(e) also shows the energy of the mixture which uses the dimensionless, homonuclear form of Equation (2.24), by defining $\tilde{E} = E/\epsilon$ where $\epsilon = [4/(3\pi^2\alpha)][\hbar^2/(m\xi^2)]$, in which tildes are subsequently neglected. The energy decreases with imbalance — as predicted by the analytic calculation presented in Appendix D— until again reaching the saturation limit. Note again that a saturated, imbalanced droplet cannot absorb further majority component atoms and thus the energy of the droplet does not vary with δN_1.

However, this is an effect of the large computational boxes used, in that the density of the unbound atoms is negligibly small such that once in this saturation limit the system is essentially identical with changing δN_1. In smaller computational boxes — or equivalently, exploring much larger imbalances — the density of the background gas becomes significant [e.g. Figure 3.2(c)], which is explored in the inset of (e). By fixing $\delta N_1 \approx 22524$, i.e., an imbalanced droplet in the saturation limit, the size of the computational box is varied. In small boxes, the density of the unbound gas is non-zero and thus has a significant, positive energy contribution. The existence of the background gas likewise modifies the internal structure of the droplet as can be seen by the increased value of $\delta n(r = 0)$. In the limit of large L_r (or equivalently small $1/L_r$) the energy contribution of the background approaches zero as the density of the gas approaches zero. Thus in the limit of a large box, all of the ground states converge to the saturated droplet in free space, as can be seen from the convergence of both the energy and $\delta n(r = 0)$ in the inset of Figure 3.2(e).

Further evidence of the energy saturation is given by the two component chemical potentials in Figure 3.3(a). For increasing δN_1 the majority component chemical potential (the dark orange curve) converges towards zero, implying there is no energetic favourability for the droplet to absorb more majority component atoms. Additionally, if more atoms of the minority component were made available to the droplet, then these atoms will likewise be absorbed into the droplet, reducing the energy of the droplet even further.

In summary, droplets will always seek to absorb atoms to reduce the system energy. If there is an imbalance of atoms away from $N_2/N_1 = \sqrt{g_{11}/g_{22}}$, the droplet will absorb more of the majority component but this reaches a limit in which the droplet is saturated with the majority component atoms. It should be noted that in the case of a non-zero density unbound gas, this limiting behaviour will be modified by the positive energy contribution of the majority component density tails, similar to submerged droplets observed in 1D imbalanced droplets [268, 269]. These results have been presented both from an analytic energy calculation, and from numerical simulations, the latter of which is to be used next to explore the dynamical stability of these imbalanced droplets across their parameter space.

3.2 Breathing modes of imbalanced droplets

Self-evaporation is a key property of 3D two-component quantum droplets [153]. Recalling that the density-locked droplet can be described by a single parameter, $\tilde{N}$, there are three main regimes of interest for the droplet collective modes: 1) all modes exceed the particle emission threshold and hence are evaporated ($\tilde{N} \lesssim 94.2$); 2) the monopole mode evaporates but other non-zero angular momentum modes are stable ($94.2 \lesssim \tilde{N} \lesssim 933.7$); 3) the monopole is stabilised ($\tilde{N} \gtrsim 933.7$) [153, 201]. This first phase is the principal argument behind the self-evaporative property of a two-component droplet, since a finite-temperature droplet is inherently excited by contributions from, for example, the non-

condensate components. Thus, these excitations are evaporated and the droplet relaxes to a lower energy configuration, akin to self-cooling [153].

Here the system is restricted to spherically symmetric droplets, meaning that the only observable mode is the breathing mode. The restriction of spherical symmetry is applied to reduce computational cost. This is due to particle shedding of self-evaporative droplets resulting in reflections from the computational box boundaries which become a substantial issue for long-time dynamics. To avoid this issue, very large box sizes — $L_r = 8192$, approximately 500 times the droplet sizes considered here — are used to observe the dynamics of the droplets without interference from reflected particles. If simulating a general 3D droplet, these box sizes would quickly become infeasible. Furthermore, as discussed in Section 3.1.2 large computational boxes are crucial to study imbalanced droplets in free space, i.e., to neglect the effects of unbound atoms. By excluding any non-zero angular momentum modes, the spherical symmetry yields two regimes: a decaying and a stable breathing mode, thus this section analyses the stability of breathing modes in the presence of an imbalance.

The breathing mode frequencies of the balanced, density-locked droplet are a function of the single parameter, $\tilde{N}$ [153]. However, for an imbalanced system, a further degree of freedom is introduced: the size of the imbalance. As shown in the previous section, the central density differences, chemical potentials and energies, as functions of imbalance, reach the saturation limit and any further imbalance has no significant effect on the internal structure of the droplet. In order to observe these collective modes, the ground state solutions found via imaginary time propagation, shown in Section 3.1, are then evolved in real time via Equation (2.38)). To trigger a breathing mode in the droplet, a harmonic phase is imprinted on the ground state wavefunction, i.e., $e^{i\epsilon r^2}$ where ϵ is small (here $\epsilon = 10^{-5}$) [45, 257]. This phase is always imprinted onto the minority component, though breathing modes are an in-phase oscillation so the subsequent dynamics are not dependent on this choice of component.

3.2.1 Self-evaporative regime

The first modes considered here are within the self-evaporative regime ($\tilde{N} \lesssim 933.7$). Breathing modes of spherical, balanced droplets have been extensively investigated [153, 201, 264]. Dynamically, within this regime, the droplet begins to oscillate at a frequency exceeding the particle emission threshold, $-\mu$, and rapidly decays with the decay rate asymptotically tending to zero and the oscillation frequency tending to the particle emission threshold [264]. The initial rapid decay is due to a high dissipation of energy through particle emission, though in the long-time limit this corresponds to limited particle emissions at the energy of the chemical potential. This asymptotically decaying behaviour is likewise recovered in the imbalanced case though with three modes instead of one due to the imbalance yielding two chemical potentials. Figure 3.3(a) describes the three distinct modes: the early-time, rapidly decaying mode, and two superimposed late-times modes.

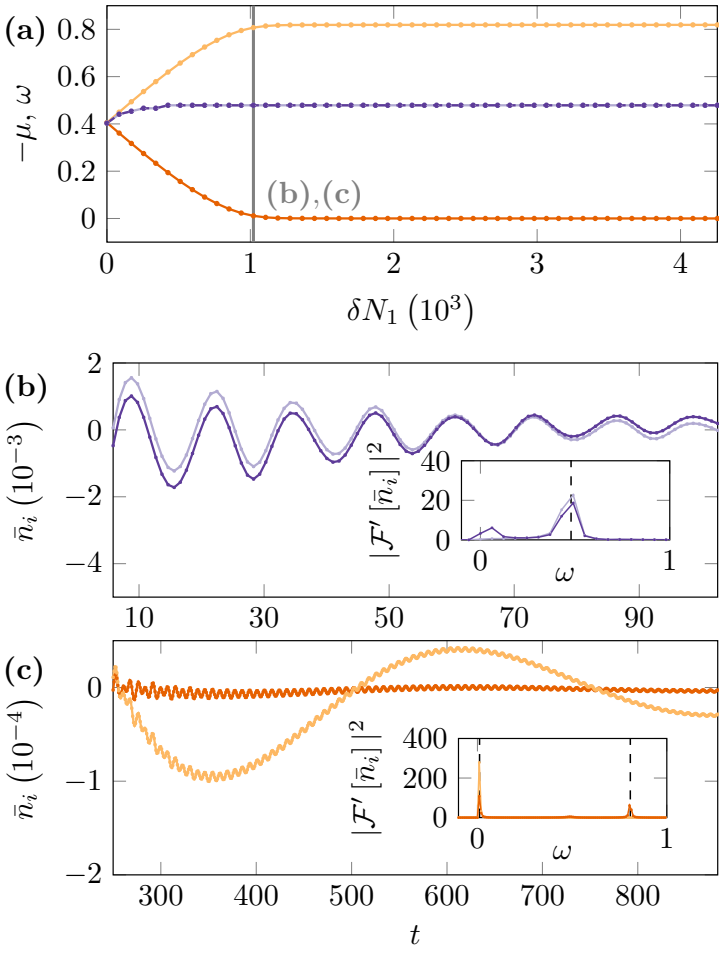

Figure 3.3: Chemical potentials and breathing modes as a function of majority component imbalance, δN_1, in the self-evaporative regime (equivalent to a balanced droplet, $N_1 = N_2$, with $\tilde{N} \approx 649$). (a) The chemical potentials (light orange — minority component, dark orange — majority component) and early-time breathing mode frequencies (light and dark purple dashed lines) as a function of imbalance. These results correspond to the range $0 \leq \delta N_1 \lesssim 4257$, $N_2 \approx 17027$, $\alpha \approx 0.00657$ and $\eta \approx -1.11$. At $\delta N_1 = 0$, the chemical potentials are equal but diverge as the imbalance is increased eventually reaching a saturation point where the chemical potential of the majority component is approximately zero. The minority component chemical potential likewise saturates, to an increased value. (b) A highlighted simulation of $\delta N_1 \approx 1447$ [corresponding to the bold vertical line in (a)] at early times, with an inset of the associated power spectrum. This indicates that at early times, there is a single rapidly decaying mode. (c) The same $\delta N_1 \approx 1447$ simulation at late times in which there is there is a superposition of two modes corresponding to the two chemical potentials, given by the vertical dashed lines in the inset power spectrum of (c).

The early-time mode — given by the purple dashed lines in Figure 3.3(a) representing the fitted equal frequencies of both components — varies marginally with imbalance, and can be considered the intrinsic droplet breathing mode. On the other hand, the late-time modes arise from the splitting of the chemical potentials which diverge with increasing imbalance before again reaching the saturated droplet [see orange lines in Figure 3.3(a)].

To visualise the single early mode and two late modes, Figure 3.3(b) and (c) represent a measure of the droplet central density, $\bar{n}_i(t) = n_i(r = 0, t) - \langle n_i(r = 0)\rangle_t$, with insets showing the associated power spectra $|\mathcal{F}'[\bar{n}_i]|^2$ in which $\mathcal{F}'[\cdot]$ denotes that the power spectrum is rescaled by the mean, and all negative frequencies are set to zero purely for data visualisation. The early-time mode is a high-amplitude, rapidly decaying mode that is given in Figure 3.3(b), with an inset of the associated power spectrum highlighting the frequency (vertical dashed line) corresponding to the purple dashed lines in Figure 3.3(a). As this mode decays, it is then replaced by the two late-time modes corresponding to the split chemical potentials. The late-time dynamics is thus a superposition of a higher and lower frequency mode, as can be seen in Figure 3.3(c), once more with the associated power spectra showing peaks at the two chemical potentials (given by the vertical dashed lines). It should be noted that evidence of these late-time modes can even be seen at early times, such as the shorter peak in the inset of Figure 3.3(b), which roughly corresponds to the chemical potential of the majority component.

In summary, at early times the droplet oscillates with an unstable, high-amplitude mode that decays rapidly due to energy dissipation from particle emission. In the long-time limit however, the particle emission is considerably reduced, with particles only emitted at energies of the two chemical potentials. Hence, these late-time modes decay at much slower rates than the initial mode. This is analogous to the density-locked mixture [264], in which the mode frequency asymptotically converges to the particle emission threshold, with a vanishing decay rate. Physically this vanishing decay rate is the result of late-time emitted particles of energy $\approx -\mu$, which thus have a negligible effect on the kinetic energy of the droplet. Equivalently, for an imbalanced droplet, there are now two chemical potentials which each have associated particle emission and hence associated residual long-lived breathing modes [264].

3.2.2 Non-self-evaporative regime

The second set of breathing modes are within the non-self-evaporative regime ($\tilde{N} \gtrsim 933.7$). For a balanced droplet in this regime the breathing mode frequency is lower than the particle emission threshold resulting in a stable oscillation [153, 264]. In the self-evaporative regime, the dynamics of the imbalanced droplet is highly reminiscent of the balanced case but with further modes corresponding to the split chemical potentials, whereas the non-self-evaporative region of the droplet phase has some greater subtleties.

Figure 3.4(a) shows that, as in the self-evaporative case, the chemical potentials diverge with increasing imbalance until reaching the saturated, imbalanced droplet. The dynamics

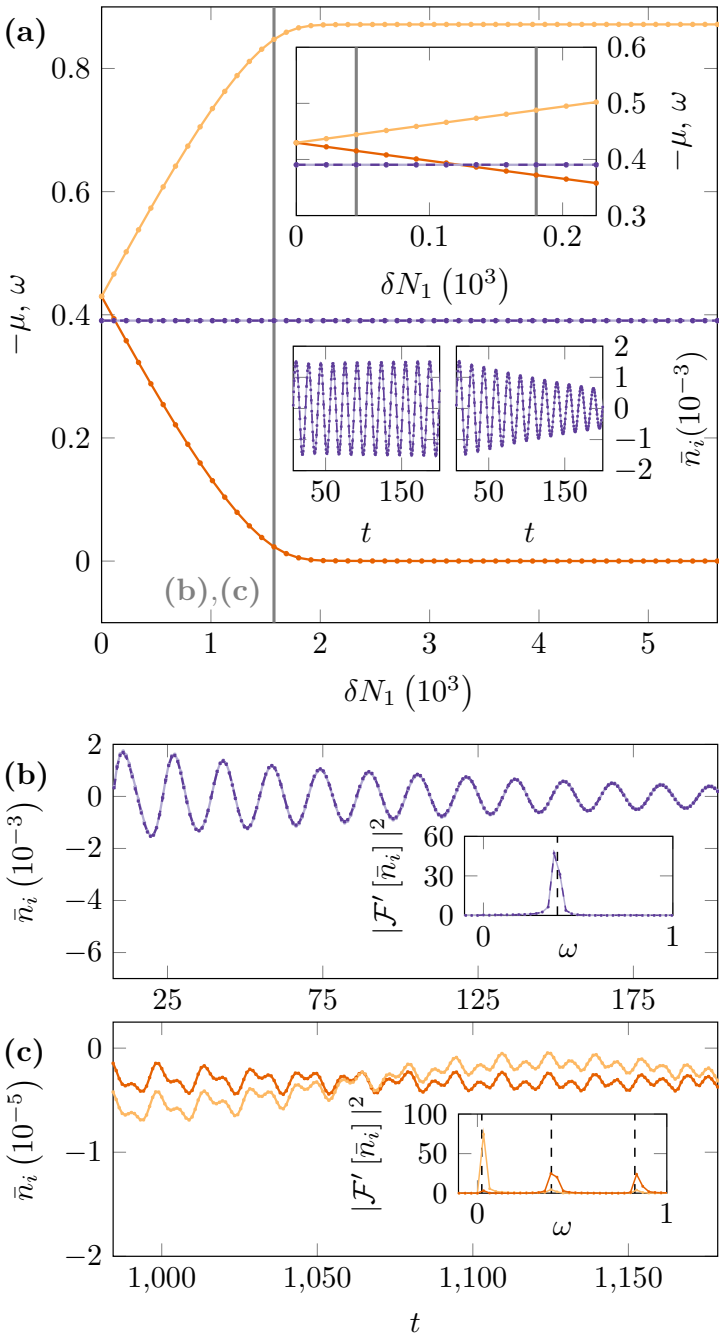

Figure 3.4: Chemical potentials and breathing modes as a function of majority component imbalance, δN_1, in the non-self-evaporative regime (equivalent to a balanced droplet, $N_1 = N_2$, with $\tilde{N} \approx 1502$), using the same parameters as in Figure 3.2 with $0 \leq \delta N_1 \lesssim 5631$. (a) The chemical potentials (light orange — minority component, dark orange — majority component) and early-time breathing mode frequencies (light and dark purple dashed lines) as a function of the imbalance. The top inset shows the majority component chemical potential crossing the breathing mode frequencies. This is shown in the lower insets in which the mode is either stable (left) or is decayed (right). (b) A highlighted simulation with $\delta N_1 \approx 1014$ [corresponding to the bold vertical line in (a)] at early times, with the associated power spectrum (inset). The early time dynamics are dominated by a single damped breathing mode. (c) The same $\delta N_1 \approx 1014$ simulation as in (b), at late times showing a superposition of three modes, with the lowest and highest energy modes corresponding to the majority and minority component chemical potentials, respectively. The third mode [the central peak in the inset of (c)] is the early-time mode, still decaying.

are again dominated by a high-amplitude mode in both components — given by the central purple dashed lines of Figure 3.4(a) — that is relatively constant with the changing imbalance. This mode can again be considered the intrinsic droplet breathing mode, as described in [253]. In the balanced case, the stability of the breathing mode for droplets of this size is due to the particle emission threshold exceeding the mode frequency. With increasing imbalance however, as the chemical potentials split, the majority component chemical potential [i.e., the lower chemical potential branch in Figure 3.4(a)] eventually crosses over the frequency of the stable high-amplitude mode, at which point this mode will begin to decay. This mode crossing implies that the imbalanced non-self-evaporative regime can instead be split into two regions: 1) a stable breathing mode; 2) a decaying breathing mode. This behaviour is highlighted in the upper inset of Figure 3.4(a), focusing on smaller imbalances. Decay of the high-amplitude, intrinsic mode occurs when the frequency exceeds the negative of the majority component chemical potential, validating the idea that stability of the mode is entirely dependent on the mode frequency exceeding the droplet's particle emission threshold. The lower left inset of Figure 3.4(a) shows that the mode is stable for an imbalance of $\delta N_1 \approx 45$ as the frequency lies beneath both chemical potentials. However, the lower right inset shows that this mode becomes unstable, for an imbalance of $\delta N_1 \approx 180$, and decays as the frequency exceeds one of the chemical potential branches. The critical imbalance between stability and instability of this mode is $\delta N_1 \approx 124$, for this specific droplet. Thus for a sufficiently small imbalance, it is possible to have an imbalanced droplet with a stable breathing mode.

Figure 3.4(b) and (c) focus on the early and late times of an unstable breathing mode in this regime. At early times, the initial high-amplitude mode dominates the system and oscillates at approximately the frequency of the balanced case. This is highlighted in the power spectrum shown in the inset of Figure 3.4(b) with the frequency given by the vertical dashed line. As found in the self-evaporative regime, the energy of the droplet is dissipated through atom shedding which then leads to the evaporation of the initial mode. The oscillations at late times — shown in Figure 3.4(c) — are instead dominated by two other modes, with frequencies corresponding to the chemical potentials of each component given by the two outer vertical dashed lines. There are still residual oscillations from the decaying initial mode which hence explains the interference seen in the oscillations of Figure 3.4(c) and the central peak shown in the power spectrum.

Thus, in both the self-evaporative and non-self-evaporative regimes, providing there is decay of the initial high-amplitude mode, there are two main regions of the dynamics: early times — where the dynamics is dominated principally by a high-amplitude, intrinsic mode that is related to the balanced droplet; and late times — where there is a superposition of two modes corresponding to each chemical potential. All of these modes are decaying but over different timescales due to the rate of atom shedding. The initial mode decays relatively rapidly due to a high dissipation of energy from the particle emission. However, at late times the particle emission is considerably reduced, with slower emission

of particles. This slower emission of particles, at energies of the two chemical potentials, is negligible relative to the droplet kinetic energy and hence the dynamics decay asymptotically [264].

Finally, it should be noted that the breathing modes of imbalanced droplets have a larger range of instability than balanced droplets, which have an unstable breathing mode in the self-evaporative regime only. This is consistent with the discussions in both Section 3.1 and the Appendix D, of how the energy, and energy per particle, varies with imbalance. The key point from these discussions is that increasing imbalance corresponds to an increasing energy per particle and thus a less stably bound droplet. Hence, it would be expected that a less stably bound object would be more susceptible to particle shedding when perturbed, as is shown in the main results of this section.

3.3 Imbalanced scattering lengths

Balanced scattering lengths, $\beta = \sqrt{a_{22}/a_{11}} = 1$, is an idealised assumption that is useful for theoretically studying droplets, but is not physically realistic for droplet experiments [168, 169]. Figure 3.5(a) shows a droplet with population balance, but an imbalance of intraspecies scattering lengths. In physical units this means imposing the condition of population balance, $N_2/N_1 = 1/\beta \rightarrow N_2 = N_1/\beta$, however when translated into the dimensionless units of Equation (2.38), the rescaled population balance condition reduces to, $N_2 = N_1$. Hence, as in the previous sections of this chapter, population imbalances of component-1 can be probed by $N_1 = N_2 + \delta N_1$. However, with the broken symmetry, $\beta \neq 1$, this is no longer trivially equivalent to imbalancing component-2. Instead, imbalances of each component are distinct.

Across the subfigures of Figure 3.5, the intraspecies scattering length imbalance is set at, $\beta = 2 \neq 1$, i.e., $a_{22} = 4a_{11}$, meaning that the internal interactions of component-2 can be considered 'more repulsive' than component-1. This difference in internal component interactions can be rationalised by the density profiles given in Figure 3.5(a). Component-1, given by the light purple curve has a higher internal density, i.e., the density profile is slightly squeezed relative to component-2, given by the dark purple curve. Equivalently, component-2 has a slightly broader density profile as a result of having more repulsive internal interactions.

A natural question is to ask how legitimate the density-locked approach is at modelling the $\beta \neq 1$ droplet. Rescaling the units of the density-locked wavefunction, ϕ, by

$$\Psi = \left[\frac{3}{2}\sqrt{\frac{\sqrt{a_{11}}\left(\sqrt{a_{11}}+\sqrt{a_{22}}\right)}{|\delta a|}}\right]\phi,$$

maps the density-locked and unlocked models onto the same density units and is given by the light orange curve in Figure 3.5(a). Information is lost in describing the $\beta \neq 1$ mixture via the density-locked model as the two component surfaces are different. The

two components are therefore not simply constant rescalings of one another, hence they cannot be mapped onto one density-locked density profile. This can be shown more concretely by mapping the density-locked approximation onto the coupled GP equations.

Beginning with the dimensional, time-independent, coupled GP equations,

$$\begin{aligned}\mu_1\Psi_1 &= \left[-\frac{\hbar^2}{2m}\nabla^2 + \frac{4\pi\hbar^2 a_{11}}{m}|\Psi_1|^2 + \frac{4\pi\hbar^2 a_{12}}{m}|\Psi_2|^2 + \frac{128\sqrt{\pi}\hbar^2 a_{11}}{3m}\left(a_{11}|\Psi_1|^2 + a_{22}|\Psi_2|^2\right)^{3/2}\right]\Psi_1,\\ \mu_2\Psi_2 &= \left[-\frac{\hbar^2}{2m}\nabla^2 + \frac{4\pi\hbar^2 a_{22}}{m}|\Psi_2|^2 + \frac{4\pi\hbar^2 a_{12}}{m}|\Psi_1|^2 + \frac{128\sqrt{\pi}\hbar^2 a_{22}}{3m}\left(a_{11}|\Psi_1|^2 + a_{22}|\Psi_2|^2\right)^{3/2}\right]\Psi_2,\end{aligned} \tag{3.1}$$

it is possible to rewrite these through the density-locking approach of Ref. [153], i.e., introduce a new macroscopic wavefunction, ϕ, such that $\phi = \sqrt{n_i^{(0)}}\Psi_i$, in which $n_i^{(0)}$ is the equilibrium density of the ith component given in Equation (2.26). The wavefunction rescaling yields a relationship between the two component wavefunctions, given by $\Psi_2 = \Psi_1\sqrt{n_2^{(0)}/n_1^{(0)}} = \Psi_1(a_{11}/a_{22})^{1/4}$. Thus, Equation (3.1) can be written in terms of one wavefunction only (chosen to be Ψ_1, without loss of generality) which gives,

$$\begin{aligned}\mu_1\Psi_1 &= \left[-\frac{\hbar^2}{2m}\nabla^2 + \frac{4\pi\hbar^2}{m}\delta a|\Psi_1|^2 + \frac{128\sqrt{\pi}\hbar^2 a_{11}}{3m}\left(a_{11} + \sqrt{a_{11}a_{22}}\right)^{3/2}|\Psi_1|^3\right]\Psi_1,\\ \mu_2\Psi_1 &= \left[-\frac{\hbar^2}{2m}\nabla^2 + \frac{4\pi\hbar^2}{m}\sqrt{\frac{a_{11}}{a_{22}}}\delta a|\Psi_1|^2 + \frac{128\sqrt{\pi}\hbar^2 a_{22}}{3m}\left(a_{11} + \sqrt{a_{11}a_{22}}\right)^{3/2}|\Psi_1|^3\right]\Psi_1.\end{aligned}$$

The two GP equations cannot be written as constant scalings of one another giving clear evidence of the symmetry breaking.

With this broken symmetry, the population imbalances of each component are no longer symmetric and thus can be probed independently. For example, Figure 3.5(b) shows a saturated imbalanced droplet in which $\delta N_1 \approx 3196$, i.e., the less internally repulsive component-1, has been made the majority component. This imbalance leads to an exaggerated central density splitting relative to Figure 3.2(c), as shown by the inset which also shows a small amount of majority component at the droplet surface. Contrasting Figure 3.5(b) with (c), in which an imbalance of $\delta N_2 \approx 3196$ has been added to the more internally repulsive component-2, there is a smaller change in $\delta n(r = 0)$ than for imbalancing component-1. A simple argument for this asymmetric imbalancing is that if one component is more internally repulsive, then the amount of atoms which can absorbed by this component will be fewer than the less repulsive component.

Figure 3.5(d) shows the central density differences for varying imbalance with the purple and orange curves corresponding to imbalancing component-1 and component-2, respectively. This highlights the disparity of the internal density imbalancing with component-1 supporting a considerably larger imbalance than component-2. The reason for this is given in the inset, i.e., imbalancing stops when the majority-component chemical potential saturates to approximately zero. Droplets possess negative chemical potentials indicating their ability to absorb more atoms. However, as discussed through-

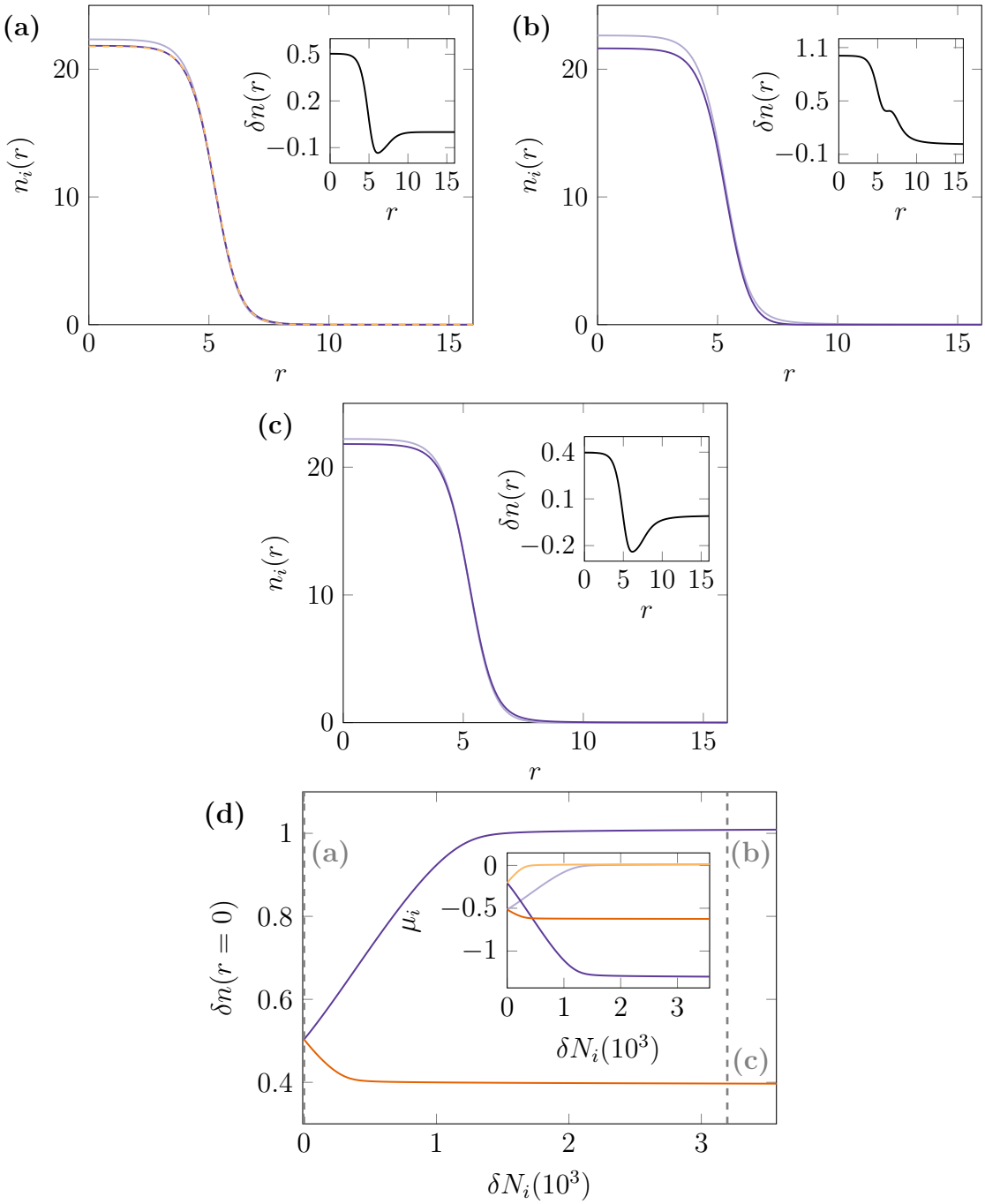

Figure 3.5: Balanced and imbalanced ground state droplets, with parameters: $N_1 = N_2 \approx 14269$, $\alpha \approx 0.00275$, $\beta = 2.0$ and $\eta = -1.114$. (a), (b) and (c): Ground state densities with $\delta N_i = 0$, $\delta N_1 \approx 3196$ and $\delta N_2 \approx 3196$, respectively. The 1st and 2nd components are represented by the light and dark purple curves, respectively, with the difference in component densities given by the inset. (d) Central density difference as a function of imbalance in the range $0 \leq \delta N_i \lesssim 3567$, in which purple and orange correspond to varying δN_1 and δN_2, respectively. The grey vertical lines highlight the regions of the parameter space that correspond to the density profiles in (a), (b) and (c), in which (b) lies on the purple curve and (c) lies on the orange curve. The inset shows the chemical potential splitting for changing imbalance. The light and dark orange curves correspond to the majority and minority components, respectively, for varying δN_2, whereas the light and dark purple correspond to the majority and minority components, respectively, for varying δN_1.

out the previous sections, this has a limit which is reached when the chemical potential saturates to zero indicating that there is no further decrease in energy by absorbing atoms. The dark and light orange curves of Figure 3.5(d)'s inset correspond to the minority and majority components, respectively, in the imbalancing component-2 case, whereas as the dark and light purple curves correspond to the minority and majority components, respectively, in the imbalancing component-1 case. At zero imbalance, the chemical potential of component-2 is larger and is hence closer to zero, hence if imbalancing this component, there is by definition a smaller δN_2 necessary to saturate the chemical potential to zero than if imbalancing component-1. Thus, the imbalance saturation is likewise asymmetric.

In previous sections imbalanced droplets were studied by imbalancing only one component without loss of generality as the components are entirely symmetric, whereas for $\beta \neq 1$ a population imbalance is not symmetric due to the bulk density imbalance, even at equal population numbers. However, the intraspecies scattering ratio, β, can in theory take any value creating a large parameter space, including the other parameters studied here of droplet and imbalance size (along with further parameters of trapping potentials and mass ratios). Hence, a broad study of β-values is not presented here, though mixtures of $\beta \neq 1$ will be revisited for the specific values pertaining to the CsYb mixture in Chapter 5.

In summary, the density-locking condition comes from the assumption of a homogeneous mixture used in Ref. [153], or equivalently, the flat-top droplet limit used in Section 3.1.1. In these cases, kinetic contributions can be neglected. However, as discussed in Section 2.2, a local density approximation is used to add the LHY contributions into the GP Hamiltonian. By adding in the kinetic contributions of the GP Hamiltonian, the symmetry breaking of the $\beta \neq 1$ mixture allows for different component surfaces. The difference in component surfaces is hence why the density-locked model cannot describe the $\beta \neq 1$ mixture, because with the addition of kinetic contributions the two components are not simple rescalings of one another.

3.4 Discussion and conclusions

This chapter has systematically investigated the spherical, free-space ground states and breathing modes of imbalanced droplets for varying droplet size and imbalance. Droplets can lower their energy by absorption of a symmetric number of atoms into each component, under the condition $N_2/N_1 = \sqrt{g_{11}/g_{22}}$. However, as has been investigated here, if there exists an asymmetric population of atoms available, the droplet will absorb the available atoms creating a majority and minority component. This modifies the core structure of the droplet by splitting the two central component densities, yielding a bound, imbalanced droplet. If further majority component atoms become available then the imbalanced droplet eventually saturates and any excess majority components will not bind to the droplet. To investigate the density profiles, chemical potentials and breathing

dynamics of these imbalanced droplets, without the external effects of the unbound gas, large computational boxes were used such that the background gas density is effectively zero.

In keeping with droplet experiments — and the CsYb mixture — this chapter has also studied the ground states of droplets with imbalanced intraspecies scattering lengths. All droplet experiments to date have an intraspecies scattering length imbalance, and this breaks a symmetry between the two components which cannot be explained by the density-locked model of Ref. [153]. In Sections 3.1 and 3.2, balanced droplets have identical components and so population imbalances in either component is equivalent; imbalanced intraspecies scattering lengths break this symmetry. The two components therefore can support different sizes of imbalance. For a mixture with a highly imbalanced scattering length ratio, it is possible that one of the components could support near zero imbalance whilst the other could be significantly imbalanced, hence emphasising the effects of imbalanced droplet cores shown throughout Sections 3.1 and 3.2.

One of the main experimental probes to justify the observation of a quantum droplet is measuring a constant width of the atomic cloud, after switching off all traps, to ensure the cloud is self-bound in free space [169, 171, 173]. Switching off the traps will cause any unbound gas to be lost, thus a key question of the next chapter is whether the imbalancing within the droplet could be retained. The observation of the three breathing mode frequencies could be experimentally achieved in homonuclear mixtures, for which the number of atoms in each component can be tuned by radio-frequency pulses on the cloud [170], and there have been recent experimental observations of imbalanced heteronuclear mixtures [243]. However these system will likewise be affected by three- and higher-body losses.

An immediate question raised by the results of this chapter is how does the application of trapping potentials effect imbalanced droplets. Isotropic harmonic traps could be applied to the spherically symmetric system considered here, to investigate the modification of both the ground states and breathing mode dynamics. The breathing mode dynamics of trapped, spherically symmetric droplets has been investigated in Ref. [253] and so there are natural extensions of these results for imbalanced droplets.

In the context of the highly imbalanced CsYb mixture it is increasingly important to understand how these mixtures can minimise their energy, from self-evaporating excitations to modifying their internal structure.

Chapter 4

Harmonically trapped imbalanced quantum droplets

Chapter 3 studied the ground states and breathing modes of imbalanced quantum droplets in free space, and showed that a droplet can lower its total energy by absorbing atoms into one of its components. The decrease in total energy corresponds to an increase in the energy per particle, indicating that imbalanced droplets are less stably bound, which is demonstrated further by the larger parameter space of unstable breathing modes. The primary focus of this chapter is to investigate how these imbalanced ground states and breathing modes are modified with the application of an isotropic harmonic trap. These investigations are motivated by the experimental feasibility of creating and probing harmonically trapped imbalanced quantum droplets. Additionally, this work explores the stability of these droplets when released into free space across a variety of timescales.

4.1 Imbalanced harmonic traps

Trapping potentials in cold atom experiments can be engineered into many different configurations such as the well-established harmonic potential [38, 39, 271] and the more recent box potentials to create near-homogeneous gases [15, 272]. Dimensionality can be varied from strongly 1D to symmetric 3D [20], and the control over dimensions has allowed cold atoms to become a versatile platform for studying low-dimensional physics [4, 26]. In mixtures the traps applied to each component are not typically the same [104, 214, 219, 273, 274], leading to asymmetric component densities.

This section probes the question: if the two components of a quantum droplet are typically tightly locked together, does trapping each component differently affect the droplet? This is of particular interest for this work as it is within the context of the CsYb experiment, which has highly anisotropic traps for each component, e.g., the Yb traps are prolate forming a quasi-1D gas, whilst the Cs traps are oblate giving an approximately quasi-2D gas [214]. However, beyond just the CsYb mixture, applying different traps to the two components of a quantum droplet has also been used in the other heteronuclear

droplet experiments in the ^{41}K-^{87}Rb mixture of Ref. [171] and the ^{23}Na-^{87}Rb mixture of Ref. [173].

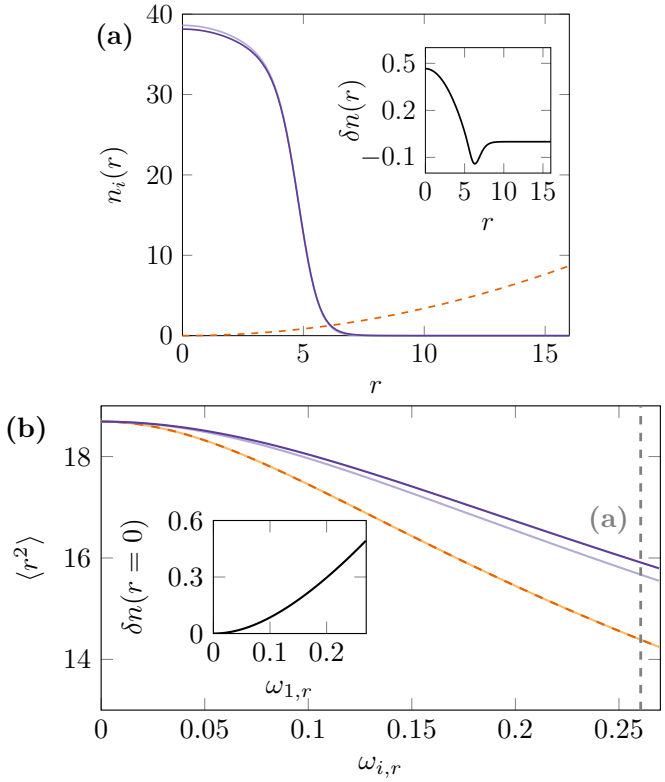

Figure 4.1: Imbalanced harmonic trap frequencies. (a) Example density profile in which a trap is applied to the light purple component whilst no trap is applied to the dark purple component, with the difference in densities inset. The orange, dashed curve shows the applied harmonic trap in units of energy. (b) A measure of droplet width varying across trap frequencies with the equally trapped components given in dark and light orange. The imbalanced trap cases are given in purple where the light purple is trapped and the dark purple is untrapped. The difference in central densities for the imbalanced trap case is given in the inset.

Figure 4.1(a) shows the ground state density of a balanced droplet in which the dark purple component is not trapped but the light purple component is trapped by the orange, dashed harmonic trap with frequency $\omega_1 \approx 0.261$. The inset shows the difference in component densities highlighting that there is a slight density splitting within the droplet core, with the confined component showing a higher central density and a corresponding density depletion at the surface.

How the density of a spherically-symmetric balanced droplet varies with harmonic trap frequency has been studied in Ref. [253]. The trap frequency can be considered low if there is no significant change from the free-space droplet density, whereas a higher frequency trap eventually leads to the flat-top density of large droplets being lost. Furthermore, in free space the negative chemical potential, $-\mu$, is described as the particle emission threshold of the droplet, however this description breaks down in a trap [253]. It can therefore be argued that in the trap-dominated regime the idea of a droplet begins to be less defined, as the notion of a droplet being 'self bound' whilst being strongly confined

is unclear. Note however that the high density of the droplet indicates that it can be considered a 'confined liquid' rather than a 'confined gas'. Ref. [253] approximates the transition to the trap-dominated regime as the point in which the potential energy at the droplet surface becomes comparable to the binding energy of the droplet, resulting in $\omega_r^{(c)} \sim (4\pi/3\tilde{N})^{1/3}$ where $\tilde{N}$ is the effective atom number of the density-locked model in Equation (2.30) [153]. Note that for all simulations presented in this chapter, $\omega_r^{(c)} \approx 0.186$. Hence, the trap frequency applied in Figure 4.1(a) can be considered in the trap-dominated regime and still the effect of the density splitting between the two components is small.

Exploring the parameter space of harmonic traps applied to component-1, Figure 4.1(b) shows a measure of the droplet width given by

$$\langle r^2 \rangle = \frac{\int \mathrm{d}^3\mathbf{r}\, \Psi_i^* r^2 \Psi_i}{\int \mathrm{d}^3\mathbf{r}\, |\Psi_i|^2}.$$

The equally trapped components have equal width (orange curves) as there is no symmetry breaking between the components. Contrast this to the imbalanced trapped components (purple curves) — where the trap is again applied to the light purple component — in which there is a marginal difference between the two-component widths. Applying a trap to only one component appears to correspond to slightly wider droplets, than if both components are trapped. However, the symmetry breaking of the imbalanced traps appears to be a small effect which is highlighted further by the central density splitting given in the inset of Figure 4.1(b). As discussed above, up to the order of harmonic trap frequencies considered here, the central density splitting in the case of imbalanced traps is small. The squeezing effect of the trapped component on to the untrapped component gives credence to the density-locked approach since the components are tightly bound together even with highly disparate traps.

In summary, applying different traps to the two components of a quantum droplet does modify the internal structure of the droplet. However, because the two components are bound together, the component experiencing a higher frequency trap tends to drag along the other component, up to a small difference between the two component densities. For the trap frequencies considered here, this density difference is deemed small enough such that only equal trap frequencies are considered throughout the rest of this chapter. Imbalanced trap frequencies will be revisited in Chapter 5 for the CsYb mixture.

4.2 Ground state trapped, imbalanced droplets

Having established that imbalanced traps do not significantly impact the density structure of droplets since the two components are tightly bound, the rest of this chapter studies population imbalances within trapped droplets and contrasts these findings both with balanced, trapped droplets [253] and free-space, imbalanced droplets from Chapter 3. The effects of harmonic traps on density-locked, spherically-symmetric droplets has been

extensively studied in Ref. [253]. The trap frequency can be considered low if there is no significant change from the free-space droplet density, whereas a higher frequency trap eventually leads to the flat-top density of large droplets being lost as shown by the purple curves in Figure 4.2(b).

To probe population imbalances, this chapter makes the same restrictions as Sections 3.1 and 3.2 by assuming equal masses and balanced intraspecies scattering lengths ($a_{11} = a_{22} \implies \beta = 1$). Therefore, the only possible difference between components is from an imposed population number imbalance of $N_1 = N_2 + \delta N_1$.

Figure 4.2(a) shows balanced (purple) and imbalanced (orange) droplet density profiles in a trap with frequency $\omega_r \approx 0.0442$. Figure 4.2(b) presents an example of the imbalanced atoms forming a significant gas density around the surface of the droplet in a trap with higher frequency $\omega_r \approx 0.353$. Figure 4.2(a) shows that the imbalanced and balanced droplets have comparable density profiles, whereas Figure 4.2(b) shows a more considerable deviation between the balanced and imbalanced droplets, in a higher frequency trap. The central density splitting becomes more pronounced in the higher frequency trap, showing a more suppressed minority-component central density.

The divergence of the two chemical potentials with increasing imbalance is a key observation of Chapter 3 [221]. For increasing trap frequency the chemical potential of a balanced droplet increases, eventually becoming positive as the density of the mixture significantly deviates from the free-space droplet density [253]. Figure 4.2(c) presents chemical potential data, defined by a 2D parameter space of imbalance and trap frequency $(\delta N_1, \omega_r)$, where $\omega_r \approx \{0.00441, 0.0662, 0.128, 0.190\}$, i.e., showing trap frequencies up to approximately $\omega_r^{(c)}$.

Figure 4.2(c) shows that the two-component chemical potentials of balanced droplets are equal and increase with trap frequency, in agreement with Ref. [253]. Beyond the balanced case, the lowest frequency trap ($\omega_r \approx 0.00441$) shows similar behaviour to the free-space chemical potentials presented in Chapter 3, in that the chemical potentials appear to reach a saturation limit, though there are effects from the unbound gas, such that these curves clearly deviate from the well defined saturation limit in free space. For the higher trap frequencies of $\omega_r \approx \{0.0663, 0.128, 0.190\}$, the two chemical potentials diverge with the majority component chemical potential becoming large and positive, whilst the minority component chemical potential becomes large and negative. The diverging chemical potentials represent a clear distinction between balanced and imbalanced trapped droplets, and an excerpt of the 2D parameter space is included in the inset of Figure 4.2(c), with the majority and minority chemical potentials plotted as orange and purple surfaces, respectively, demonstrating the chemical potentials diverging for increased trap strength and imbalance.

Adding harmonic traps to both balanced and imbalanced droplets causes the flat-topped density profile to eventually be lost with increasing trap frequency. One key difference between balanced and imbalanced droplets is that the trap causes any unbound

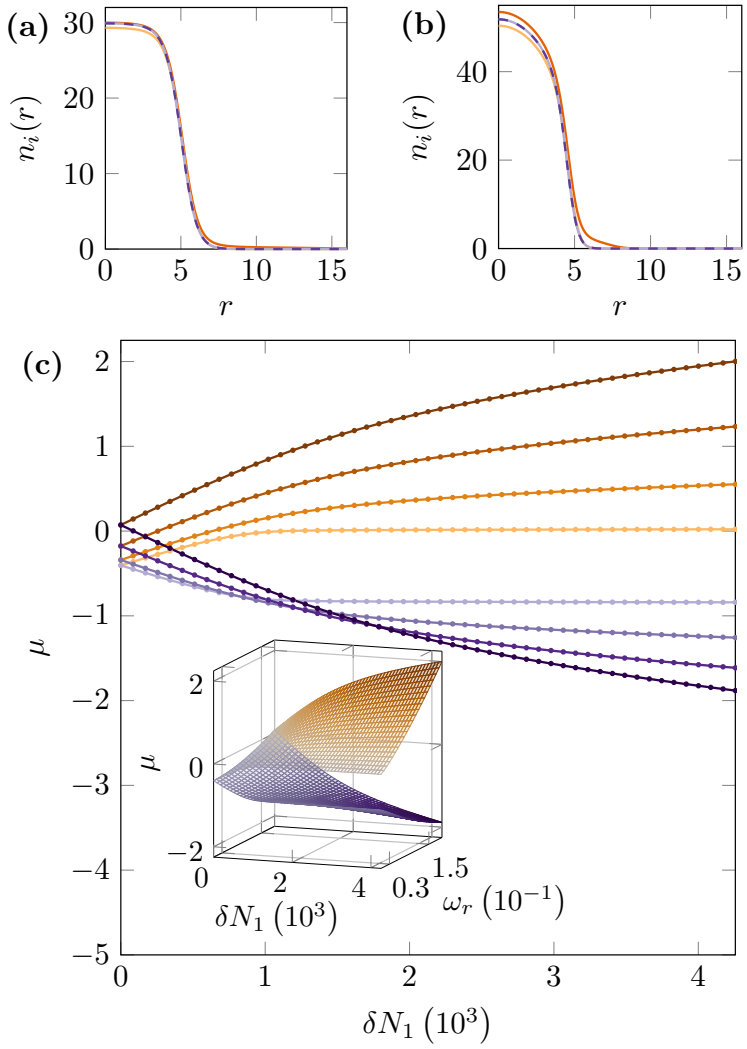

Figure 4.2: Balanced and imbalanced quantum droplets in isotropic harmonic traps (with, $N_2 \approx 17027$, $\alpha \approx 0.00657$ and $\eta \approx -1.11$). (a) Droplet ground state density profiles, of size $\tilde{N} \approx 649$ with balanced components, $\delta N_1 = 0$, (the light and dark purple dashed lines) and an imbalance of $\delta N_1 \approx 8513$ (majority component — dark orange, minority component — light orange), in a trap of frequency $\omega_r \approx 0.0442$. (b) Equivalent balanced and imbalanced droplet to (a), but with a trapping frequency of $\omega_r \approx 0.353$. (c) Majority (orange) and minority (purple) chemical potentials across the 2D parameter space of imbalance and trap frequency — i.e., $(\delta N_1, \omega_r)$ — for the fixed droplet size considered in (a) and (b), at trap frequencies of $\omega_r \approx \{0.00441, 0.0662, 0.128, 0.190\}$, with $0 \leq \delta N_1 \lesssim 4257$. The inset shows the surfaces for the majority (orange) and minority (purple) component chemical potentials across the 2D parameter space for which the curves in (c) are 1D slices of set ω_r values. Note that the two surfaces are equal at $\delta N_1 = 0$ imbalance, but diverge for increasing imbalance.

atoms to form a trapped gas at the droplet surface. For balanced droplets the chemical potential increases with trap frequency until eventually becoming positive. Whereas, for imbalanced droplets it is always possible for the minority component chemical potential to be made negative in isotropic harmonic traps by tuning the imbalance. One way to understand the effect that this squeezed external gas cloud has on the droplet is to analyse the breathing modes of imbalanced droplets, after reviewing the collective modes of density-locked, balanced droplets.

4.3 Breathing modes of trapped, imbalanced droplets

As explained in Chapter 3, the breathing modes of balanced droplets in free space have two regimes, self-evaporative and non-self-evaporative [153, 201]. In the self-evaporative regime the breathing mode is unstable because the mode frequency exceeds the particle emission threshold, $-\mu$. Hence, the droplet will emit atoms to lower its energy, corresponding to a decaying sinusoidal oscillation with a frequency that asymptotes to the particle emission threshold, $-\mu$. In the non-self-evaporative regime, the breathing mode frequency does not exceed the particle emission threshold therefore the mode is stable and non-decaying. Additionally, the frequency of the balanced droplet breathing mode varies with droplet size only [153].

Breathing modes in imbalanced droplets are instead dominated by unstable regions. For both self-evaporative and non-self-evaporative droplets, an imbalance implies an unstable, decaying breathing mode except for small imbalances in the non-self-evaporative regime [221]. The focus of this section is to investigate breathing modes in trapped, imbalanced droplets; i.e., what is the effect of the trap? Before this analysis though, it is important to understand how breathing modes and collective excitations of density-locked droplets are impacted by the addition of a trap.

4.3.1 Collective excitations of trapped, balanced droplets

The collective excitations of trapped, balanced droplets, using the density-locked approach, have been extensively studied in Ref. [253]. With the aim of studying the breathing mode of trapped, imbalanced droplets, this section reviews the collective excitations of trapped, balanced droplets by performing BdG analysis as in Section 2.8 with the addition of a harmonic trap.

A trapping potential can be added very simply to the BdG equations given in Equation (2.42),

$$\begin{pmatrix} -\frac{\nabla^2}{2} + V - 6\phi_0^2 + \frac{25}{4}\phi_0^3 - \mu & -\left[-3\phi_0^2 + \frac{15}{4}\phi_0^3\right] \\ -3\phi_0^2 + \frac{15}{4}\phi_0^3 & -\left[-\frac{\nabla^2}{2} + V - 6\phi_0^2 + \frac{25}{4}\phi_0^3 - \mu\right] \end{pmatrix} \begin{pmatrix} u \\ v \end{pmatrix} = \omega \begin{pmatrix} u \\ v \end{pmatrix}, \quad (4.1)$$

where V is here assumed to be a spherically symmetric harmonic trap, $V = \frac{1}{2}\omega_r^2 r^2$. Solutions of Equation (4.1) are given in Figure 4.3 with (a) and (b) corresponding to a lower, $\omega_r \approx 0.0309$, and higher, $\omega_r \approx 0.181$, frequency trap, respectively. The bold orange curve corresponds to $-\mu$ which in free space is referred to as the particle-emission threshold, however, as noted in Ref. [253] the notion of this threshold is not well defined within a trap. The $l = \{2, 3, 4, 5, 6, 7\}$ modes are given in orange with darker shades corresponding to higher l, and the monopole mode, $l = 0$, is given in purple.

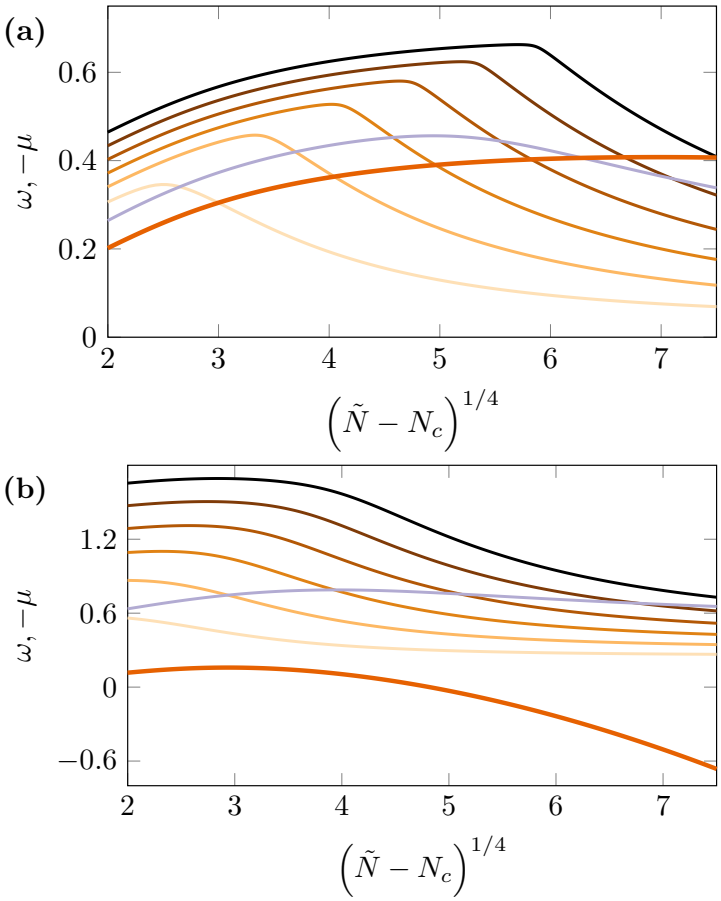

Figure 4.3: Collective excitation frequencies for varying droplet size. The bold, orange curve denotes $-\mu$; the $l = 0$ and $l = 2$ modes given by the light and dark purple curves, respectively; and, $l = \{2, 3, 4, 5, 6, 7\}$ modes given by orange curves with increasing darkness corresponding to increasing l. (a) The lower trap frequency, $\omega_r \approx 0.0309$, does not deviate significantly from the free-space mode landscape. (b) The higher trap frequency, $\omega_r \approx 0.181$, which shows much more significant deviations from the free-space excitations.

Contrasting Figure 4.3(a) with the free-space BdG analysis in Figure 2.5(a) shows qualitatively similar behaviour. For example, with increasing droplet size the mode frequencies all decrease however the excitation branches are all shifted up by the trap. Note that in Figure 2.5(a) the excitation branches are shown only below the particle-emission threshold, but since this threshold is not well defined in the trap, the excitation branches in Figure 4.3(a) are shown in their entirety. Figure 4.3(b) shows that the higher trap frequency leads to a larger deviation from the free-space system. For example, the mode frequencies are more significantly shifted up relative to the lower trap frequency, and

the chemical potential becomes positive at larger $\tilde{N}$. Likewise the large $\tilde{N}$ behaviour is modified by the trap. Ref. [253], shows that the mode frequencies in the trapped system asymptote to non-zero frequencies in the limit of large $\tilde{N}$ such as the $l = 2$ mode which approaches $\sqrt{2}\omega_r$. This agrees with the asymptotic limit of large $\tilde{N}$ for an interacting Bose gas, in which the mode frequency, ω_l, approaches the limit $\omega_l = \sqrt{l}\omega_r$ [257].

In the following sections, the focus will be on decaying breathing modes (i.e., excluding non-self-evaporative droplets that are either balanced or have sufficiently small imbalances). Therefore, to examine the decaying breathing modes of trapped, imbalanced droplets, the following sections will take one example droplet size, $\tilde{N} \approx 649$ (as in Figure 4.2). Different droplet sizes yield qualitatively the same behaviour, with only a difference in mode frequency. By fixing droplet size, the system is again reduced to a 2D parameter space in imbalance and trap frequency, $(\delta N_1, \omega_r)$. Therefore Figure 4.4 shows the $l = \{0, 1, 2, 3, 4, 5, 6, 7\}$ modes of the $\tilde{N} \approx 649$ droplet for varying trap frequency.

Ref. [253] describes the $l = 0$ and $l = 2$ modes as having a 'superlinear' dependence on ω_r, indicating that these modes are relatively insensitive to the trap frequency. For higher momenta, e.g., $l = \{5, 6, 7\}$, the excitation branches have an approximately linear dependence in ω_r at higher frequencies, but at low frequencies have a nonlinear ω_r dependence. Increasing angular momentum, l, can be intuited as the excitations becoming increasingly localised at the droplet surface. At weak trap frequencies the surface of the droplet density appears to be largely unchanged, though the bulk density changes from approximately uniform to non-uniform. Hence, it is consistent that if the density profile at the surface is relatively unchanged at low ω_r, then modes local to the surface will be relatively unchanged.

The only mode discussed here which is not presented in the free-space BdG analysis of Section 2.8 is the $l = 1$ or dipole mode. In free space this mode is zero valued [153]. However, by applying a trap the system will then obey the Kohn theorem which states that the dipole mode is equal to the trapping frequency [275].

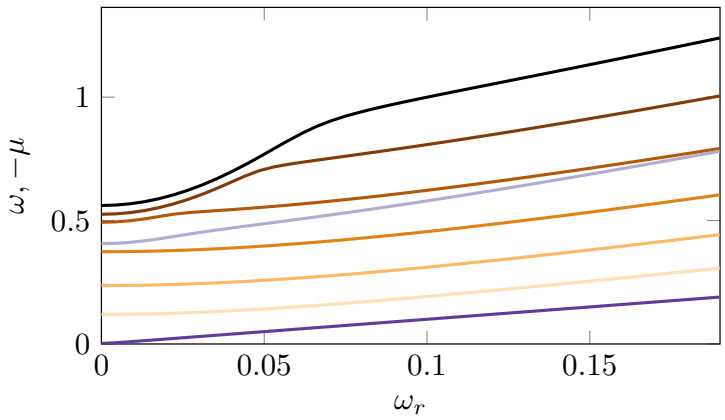

Figure 4.4: Collective of density-locked with, $\tilde{N} \approx 649$, for varying trap frequency. The $l = 0$ and $l = 1$ modes are given in light and dark purple, respectively, whilst the $l = \{2, 3, 4, 5, 6, 7\}$ modes are given in orange with increasing l corresponding to darker shades.

In summary, the mode frequencies are shifted up by the presence of the trap though all modes investigated here do not increase significantly in the range of frequencies considered here. The domain of frequencies used here are all within the regime at which the droplet is deemed 'weakly-trapped'. There have been investigations of droplets in tight confining traps [276], however, the notion of a self-bound droplet becomes ill-defined in this regime. The remainder of this section is split into two subsections to probe the 2D parameter space, $(\delta N_1, \omega_r)$: firstly, breathing modes are observed for varying trap strengths with small imbalances, of a similar magnitude to those in Figure 4.2(c); secondly, trap frequency is fixed allowing for breathing modes to be observed with imbalances much larger than those in Figure 4.2(c).

4.3.2 Varying trap frequency

Following from the BdG analysis above, the rest of this chapter will present dynamical results of the GP equation. The process is very much the same as in Sections 2.8 and 3.2, i.e., to initiate the breathing mode dynamics of trapped droplets, a perturbation is made by imprinting a harmonic potential of the form $e^{i\epsilon r^2}$, where ϵ is small (here $\epsilon = 10^{-5}$) onto the minority component ground state wavefunction [45, 257]. This perturbed ground state is then propagated in real time.

The upper panel of Figure 4.5(a) shows an example of a self-evaporative, balanced droplet in a trap of frequency $\omega_r \approx 0.00883$. The data shown is a measure of the droplet central density, $\bar{n}_i(t) = n_i(r = 0, t) - \langle n_i(r = 0)\rangle_t$, where $\langle \cdots \rangle_t$ represents time averaging. The droplet exhibits a decaying oscillation due to the emission of particles, causing the droplet to asymptotically relax to a lower energy state. However, the emitted particles are refocused by the trap back toward the droplet resulting in the short-lived, high-amplitude oscillations, which are the result of a recombination event between the droplet and the reabsorbed wavepacket. This then leads to the self-evaporation reoccurring at set intervals of approximately half the associated trap period of $T = 2\pi/\omega_r \approx 712 = 2 \times 356$ with $t = 356$ being the approximate time for the reinitialised decay in Figure 4.5(a).

The balanced droplet recombination can be thought of as 'clean', as there is little noise produced and the reinitialised oscillation is approximately equivalent to the initial oscillations. In the presence of an imbalance ($\delta N_1 \approx 4257$), given in the lower panel of Figure 4.5(a), the recombination events are not 'clean' as each separate repetition of decaying oscillation is not equivalent to the previous. The trapped, unbound atoms alter the recombination of the emitted particles. Eventually these recombination events will lead to significant noise and thus the remainder of the analysis presented here will focus on the dynamics prior to the first recombination event.

Figure 4.5(b), (c) and (d) show the same self-evaporative droplet given in Figure 4.5(a) with an imbalance of $\delta N_1 \approx 4257$, for three trap frequencies $\omega_r \approx \{0.00662, 0.0106, 0.0309\}$, with times shown only before the first recombination event. The data presented is the same measure of central density as in Figure 4.5(a), with insets of the associated power

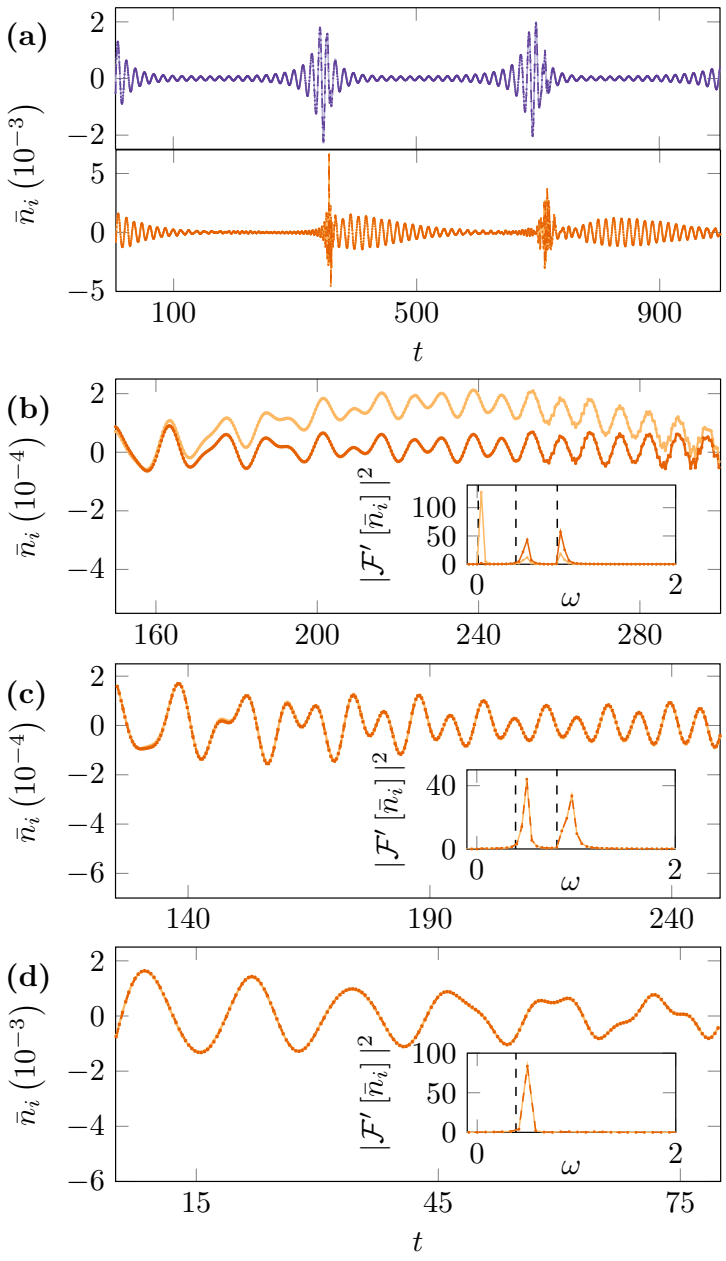

Figure 4.5: Breathing modes of trapped imbalanced droplets. (a) Droplet central densities in time for both a self-evaporative, balanced (upper) and imbalanced (lower) droplet (with imbalance $\delta N_1 \approx 4257$) in a trap with frequency $\omega_r \approx 0.00883$. The droplet is defined with the same parameters as in Figure 4.2. Note the recombination events that cause the self-evaporative dynamics to be reinitiated. (b) Droplet central density for the $\delta N_1 \approx 4257$ imbalanced droplet in the lower panel of (a), in a trap with $\omega_r \approx 0.00662$. The trap frequency is sufficiently low such that all three modes — i.e., the intrinsic mode, and the two modes corresponding to the two chemical potentials — can be observed before the first recombination event. (c) A higher trap frequency of $\omega_r \approx 0.0106$ showing that the shorter period between recombination events no longer allows for the long wavelength oscillation of the majority component. (d) An increased trap frequency of $\omega_r \approx 0.0309$. The recombination events occur within such short intervals that the dynamics are dominated by the intrinsic droplet breathing mode as there is not sufficient time for this mode to decay.

spectra $|\mathcal{F}'[\bar{n}_i]|^2$ in which $\mathcal{F}'[\cdot]$ denotes the power spectrum rescaled by the mean, and all negative frequencies are set to zero. The time periods are chosen to highlight the behaviour of the modes, largely after the decay of the initial mode, except for in Figure 4.5(d), discussed further below.

The breathing mode dynamics of an imbalanced droplet in a trap of frequency $\omega_r \approx 0.00662$ are given in Figure 4.5(b). These dynamics exhibit the three distinct modes of the equivalent free-space droplet (with the associated three peaks given in the inset power spectrum) [221]. The near-zero frequency peak in the power spectrum of the majority component corresponds to the free-space majority component chemical potential, and is the highest amplitude mode. The effect of this mode can be seen by the relative difference in oscillation between the two components in Figure 4.5(b). There is also the superposition of two other modes which are of comparable amplitude in both the majority and minority component, corresponding to the intrinsic droplet breathing mode (the central peak of the inset) — i.e., the initial, high amplitude mode — and the minority component chemical potential (the highest frequency mode in the inset).

Increasing the trap frequency applied to a balanced droplet corresponds to a relatively small increase in breathing mode frequency [253], and this effect appears to carry over to the trapped, imbalanced droplet. The inset power spectrum of Figure 4.5(b) includes the three free-space modes given by the vertical, dashed lines. All three of these modes have a frequency that is shifted up due to the trap, though this increase is small due to the relatively low trap frequency.

Figure 4.5(c) shows that if the trap frequency is increased, eventually the highest amplitude mode is lost. By increasing the trap frequency to $\omega \approx 0.0106$, the two component central densities oscillate in phase with one another, i.e., there is no long-wavelength oscillation between the two components as given in (b). The low frequency mode cannot oscillate within the reduced period between recombination events from the increased trap frequency.

Figure 4.5(d) shows the highest trap frequency, $\omega_r \approx 0.0309$, considered in this section. At this trap frequency, the period between recombination events is considerably shortened. Hence the time window in focus is dominated by the initial, high-amplitude mode of the droplet, shown by the single peak in the inset power spectrum. There are some interactions with other modes at the later times shown in Figure 4.5(d), but there is not sufficient time for the initial mode to decay.

No higher trap frequencies are studied here because the high recombination rate implies only the intrinsic mode is observable. Note too that this highest trapping frequency is still an order of magnitude smaller than $\omega_r^{(c)} \approx 0.188$.

In summary, there is a close relationship in the dynamics between imbalanced droplets in free-space and in harmonic traps. For low trap frequencies the three modes of the free-space, imbalanced droplet are visible. However, increasing the trap frequency leads to the loss of the majority component mode. Eventually for higher trap frequencies, the

oscillations are dominated by the intrinsic droplet mode, as there is not sufficient time between recombination events for the initial mode to decay, resulting in the loss of the minority component mode. The recombination events in higher frequency traps lead to dynamics rapidly dominated by excitations. Therefore, if the multiple breathing modes of trapped imbalanced droplets were to be experimentally observed, it is advised to use low trap frequencies, such that the initial intrinsic mode can sufficiently decay.

4.3.3 Varying imbalance

Having established how the breathing modes of imbalanced droplets vary with trap frequency, this section focuses on how these modes vary with increasing imbalance. To analyse the breathing modes as a function of imbalance, the weakest trap strength studied in Figure 4.5 is used, because all three imbalanced droplet modes are observable.

Figure 4.6(a) shows an example ground state density profile of a weakly-trapped, highly imbalanced droplet with the majority and minority components, shown in dark and light orange, respectively. The inset shows the density difference, $\delta n(r) = n_1(r) - n_2(r)$, between the majority and minority component. The density structure within the droplet core is comparable to the small imbalances shown in Figure 4.2(a). However, the key difference with highly imbalanced mixture is the large radius gas surrounding the droplet.

Figure 4.6(b) highlights two examples of breathing mode oscillations for droplets with high population imbalances. The upper panel shows a mixture with $\delta N_1 \approx 170267$, whilst the lower panel shows a mixture with $\delta N_1 \approx 16856418$. These population imbalances are so large due to the weak trap geometry used, i.e., to achieve significant gas densities in these low frequency traps, substantial imbalances are needed. The same measure of central density as used in Figure 4.5 is shown, prior to the first recombination event.

In both panels of Figure 4.6(b) there does not appear to be any out-of-phase oscillations between the two components from the majority-component chemical potential mode, as shown in Figure 4.5(b). The surrounding gas therefore seems to have frozen out this long-wavelength mode, similar to the higher frequency trap in Figure 4.5(c). The main difference between the upper and lower panels of Figure 4.6(b) is the lower decay rate of the initial, high-amplitude mode in the more imbalanced mixture. As shown in Figure 4.5(b), at later times the initial mode in the upper panel has decayed sufficiently such that the minority-component chemical potential mode is visible. By driving the imbalance even higher the decay rate of the initial rate is greatly reduced, such that minority-component chemical mode cannot be observed.

In Figure 4.6(c), the droplet central density is fitted to a decaying sinusoidal curve, of the form given in Equation (2.52) [1]. With increasing imbalance there is a corresponding decrease in the fitted decay rate, γ. This implies that a higher surrounding gas density resists the particle emission from the droplet. This could be of potential benefit to exper-

[1] Curve fitting is implemented by the optimize.curve_fit function [277] from the SciPy library for Python [262]

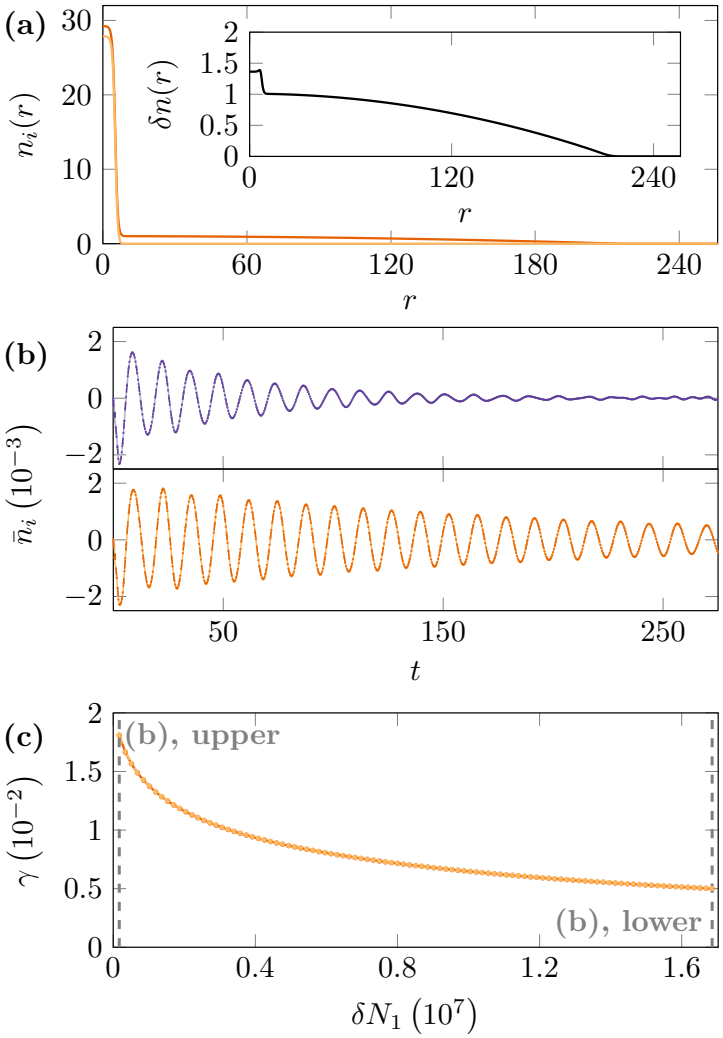

Figure 4.6: Ground states and breathing modes for high imbalances in a low frequency trap. (a) Example ground state density profile in a trap of frequency $\omega_r \approx 0.00662$, and an imbalance of $\delta N_1 \approx 16856418$. (b) Two examples of breathing modes with a smaller imbalance of $\delta N_1 \approx 170267$ in the upper panel, and a considerably larger imbalance of $\delta N_1 \approx 16856418$ in the lower panel. These example imbalances are highlighted in (c) by the vertical dashed lines. (c) Fitted decay rate to the initial droplet breathing mode, with varying size of imbalance.

iments as it implies that larger imbalances would give more time to observe the decaying breathing mode oscillations.

Beyond the observation of trapped imbalanced droplets, there are also questions to be asked of the experimental realisability of a free-space imbalanced droplet. For example, how stable is the imbalance under the transition from the trap — used to prepare the mixture — to the free-space droplet.

4.4 Release into free space

This section studies the dynamics of trapped, imbalanced droplets when released into free space. This is similar to a Time-Of-Flight (TOF) expansion, a method used in experiments in which trap potentials are switched off and the atomic cloud expands, often used for imaging. Imbalanced droplets are less stably bound than balanced droplets [221], thus the motivating question is whether it is possible to preserve the imbalance when released from a trap. This is a crucial question in the feasibility of experimentally creating a free-space, imbalanced droplet.

TOF expansion has been a widely used technique in quantum gas experiments [157] from the very first experimental observation of Bose-Einstein condensation [38, 39]. Typically, by removing the trap the resulting expansion increases the scale of defects, such as vortices, accounting for the low resolution of imaging apparatus [28, 53, 56]. Measurements of condensate density from TOF images can also be used to compute approximate temperatures and population numbers of the cloud [278, 279].

Whilst most quantum gas experiments are inherently in the gas phase, droplets are by definition self-bound, liquid states [153], and hence must retain an approximately fixed size when released into free space. This property is useful for experiments as evidence for the production of quantum droplets [168–171, 173, 243], though relatively high-resolution imaging is necessary.

The two observables used here to measure the dynamics resulting from the release into free-space, are: the population numbers contained within the droplet, and the central droplet density difference, $\delta n(r=0) = n_1(r=0) - n_2(r=0)$. The population numbers are used to measure the particle loss from each component, while the central density difference is used as a measure of how the droplet core evolves after being released from the trap. The population numbers of the droplet are computed by

$$N_i^{\mathrm{drop}}(t) = 4\pi \int_0^{R^{\mathrm{drop}}(t)} r^2 |\Psi_i(r,t)|^2 \mathrm{d}r,$$

in which $R^{\mathrm{drop}}(t)$ is defined as the radius at which the component density equals 0.1% of the maximum component density, giving an approximate droplet radius. The population numbers are extracted in time, and $R^{\mathrm{drop}}(t)$ is allowed to vary dynamically.

4.4.1 Instantaneous trap release

To simulate the release into free space, ground states are computed as in Section 4.2. The traps are then instantaneously turned off and the mixture is evolved in real time. The instant trap turn off can be quite a violent excitation of the droplet particularly with higher trap frequencies.

Figure 4.7(a) shows the population numbers of each component for two different initial trap frequencies: a lower frequency of $\omega_r \approx 0.0132$, given by the orange curves, and a

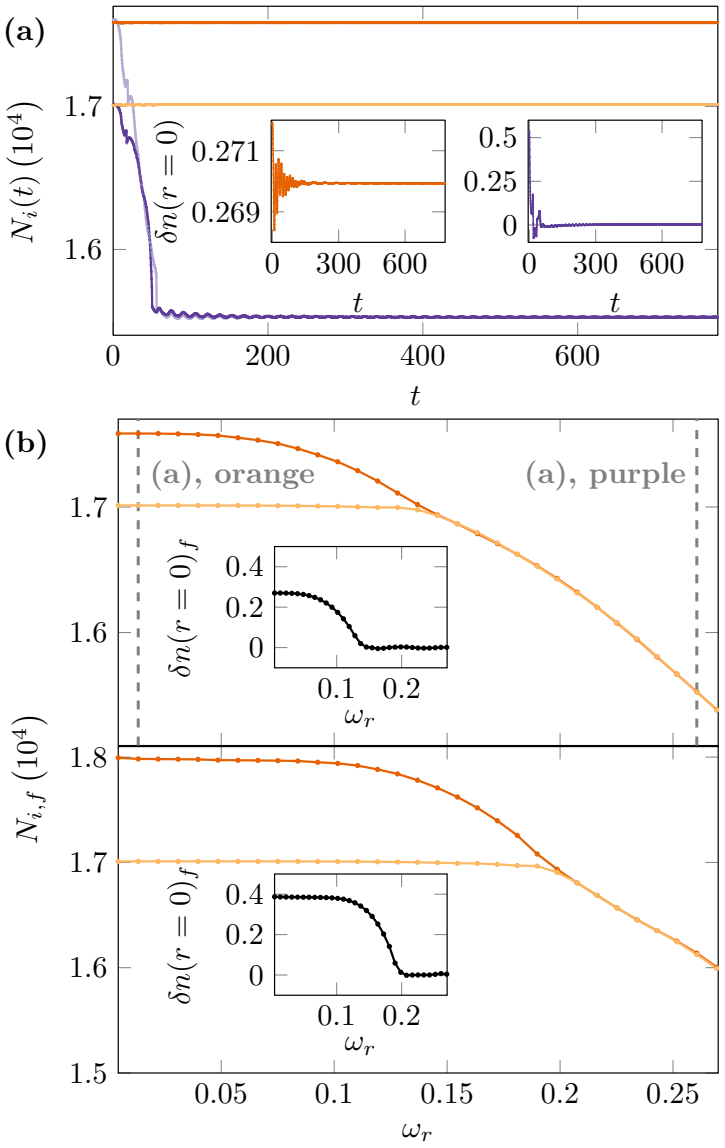

Figure 4.7: Dynamics of imbalanced droplets due to an instantaneous release into free space, with the same parameters as in Figures 4.2, 4.5 and 4.6. (a) Population numbers varying in time following the release into free space at $t = 0$. The bound, imbalanced droplet has an initial imbalance of $\delta N_1 \approx 596$. The orange curves correspond to an initial low frequency trap with $\omega_r \approx 0.0132$ (dark and light orange corresponding to majority and minority components, respectively), while the purple curves correspond to an initial high frequency trap, with $\omega_r \approx 0.261$ (light and dark purple corresponding to majority and minority components, respectively). The insets show the central density differences in time, with the left and right panels corresponding to the low and high frequency traps, respectively. These two example simulations are highlighted in the upper panel of (b) by the vertical, dashed lines. (b) The equilibrated population numbers and central density differences (inset) for varying initial trap frequencies, in the range $0.00442 \lesssim \omega_r \lesssim 0.269$. The upper panel corresponds to a bound, imbalanced droplet ($\delta N_1 \approx 596$) whilst the lower panel corresponds to a saturated, imbalanced droplet with an external unbound gas ($\delta N_1 \approx 4257$).

higher frequency of $\omega_r \approx 0.261$, given by the purple curves. The droplet size is the same as in Sections 4.2 and 4.3, and is within the bound, imbalanced regime ($\delta N_1 \approx 596$), i.e., there is no surrounding gas. The population numbers of both the minority (light orange) and majority (dark orange) components in the lower frequency trap remain relatively constant, as does the central density difference given in the left inset. Due to the arbitrary cut-off used, there are some small oscillations in the population numbers. In the higher frequency trap, both the majority (light purple) and minority (dark purple) components exhibit heavy initial losses before equilibrating to a population balance. Further evidence of this density balancing is given by the zero central density difference given in the right inset.

Figure 4.7(a) indicates that the equilibrated population numbers following the release into free space depend on the initial trap frequency. Figure 4.7(b) shows the trap frequency dependency of the late-time equilibrated population numbers, $N_{i,f}$. Presented are the majority (dark orange) and minority components (light orange) of a bound, imbalanced droplet (upper panel) and a saturated, imbalanced droplet surrounded by an unbound gas (lower panel), with the equilibrated central density difference, $\delta n(r=0)_f$, inset.

The upper panel of Figure 4.7(b) shows that the imbalance can be approximately conserved following the release from an initial low frequency trap, though the imbalance is lost at higher trap frequencies as demonstrated by the zero central density difference inset. Increasing the trap frequency further results in losses from both components. A larger imbalance of $\delta N_1 \approx 4257$ is given in the lower panel, showing that the transition to balanced droplets is suppressed to higher trap frequencies. For example the central density difference drops to zero for $\omega_r \approx 0.125$ in the upper panel but is shifted to $\omega_r \approx 0.2$ in the lower panel.

4.4.2 Ramping down trap

Having shown a population imbalance is lost when droplets are released instantaneously from a high frequency trap, it is natural to investigate whether the imbalance can be retained when gradually released from a high frequency trap. To do this the trap frequency is ramped down to zero in real time over a set time, t_{ramp}.

Figure 4.8(a) shows the population numbers in time of a droplet in a ramped-down trap of initial frequency $\omega_r \approx 0.261$. The trap frequency is ramped down by the relationship, $V_i = (1 - t/t_{\text{ramp}})V_i^{\text{init}}$, in which V_i^{init} is the initial trap profile. To compute the population numbers, the same method and radial cut-off as in Figure 4.7 are used. The dark and light orange curves correspond to the majority and minority components, respectively, under a ramp-down time of $t_{\text{ramp}} \approx 0.781$, which is fast relative to the trap period, $t_{\text{trap}} \approx 24.1$. Both components undergo heavy losses before equilibrating to balanced population numbers, and zero central density difference, comparable to the high frequency instantaneous trap release given by the purple curves in Figure 4.7(a). The dark and light purple curves correspond to the minority and majority components, respectively, under

a ramp-down time of $t_{\text{ramp}} \approx 38.3$, which is slow relative to the trap period, t_{trap}. There are some small losses primarily from the majority component; however, the imbalance is largely retained during these ramp-down dynamics. Furthermore, the central density difference of a trapped droplet is larger than that of a free space imbalanced droplet as highlighted in Figures 4.2(a) and (b). The left inset of Figure 4.8(a) shows that the central density difference initially decreases but stabilises at a non-zero value. Thus, the imbalance can be retained under the release from a high frequency trap, though the trap must be ramped down sufficiently slowly.

Figure 4.8(b) shows the ramp-down time, t_{ramp}, dependency of the final equilibrated population numbers and central density difference (inset). The upper panel considers a bound, imbalanced droplet showing that fast ramps result in balanced droplets that undergo losses from both components though slower ramps can retain some atoms in both components. Increasing the ramp-down time above $t_{\text{ramp}} \approx 8$ indicates that the original imbalance can be approximately retained. A saturated, imbalanced droplet with an unbound cloud is given in the lower panel of Figure 4.8(b) and likewise shows that fast ramps result in balanced droplets, whilst slower ramps yield a preservation of some imbalance. Note that the initial imbalance is not retained in the lower panel, because the unbound cloud will always be lost in free space, i.e., the resulting droplet is approximately a saturated, imbalanced droplet in free space.

To summarise, an imbalanced droplet prepared in a relatively low frequency trap can retain the majority of the initial imbalance after an instantaneous release into free space. With increasing trap frequency, the majority component will lose atoms until no imbalance is retained. The loss of imbalance can, in general, be suppressed by increasing the initial imbalance, lowering the initial trap frequency, or lengthening the ramp-down time. These results show that imbalanced droplets can be robust to a release into free space suggesting that free-space, imbalanced droplets are feasible using modern experimental techniques.

4.5 Discussion and conclusions

This chapter has investigated ground states, breathing modes and the release into free space of imbalanced droplets confined in isotropic harmonic traps. First, Section 4.1 studied how droplets are modified by unequal trapping of each component, by applying a harmonic trap to one component but leaving the other untrapped. Since the two components are bound together, increasing the trap frequency to one component leads to a squeezing effect on the untrapped component, i.e., up to a small deviation the two component densities behave according to the highest frequency trap. Hence, the system can be simplified by applying equal traps to both components.

Having reduced the problem to consider only equal component traps, Section 4.2 demonstrates that the trapping potential squeezes any unbound gas up to the droplet, forming a significant gas density at the droplet surface. The imbalance dependent diver-

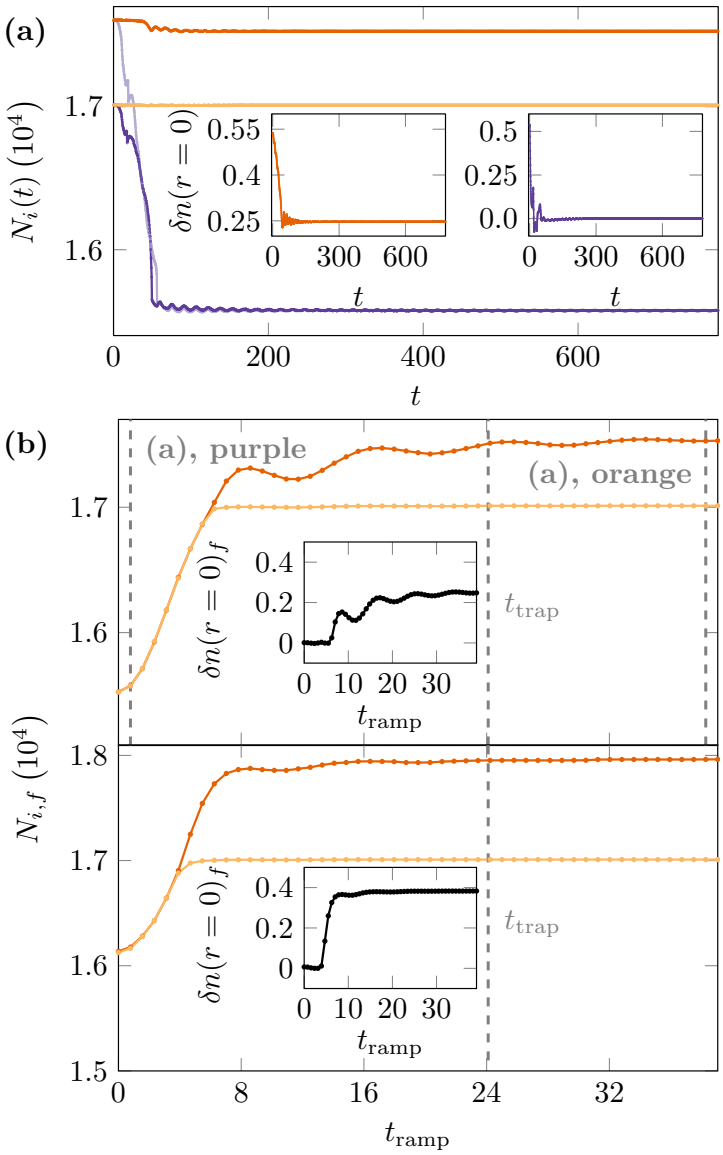

Figure 4.8: Dynamics of imbalanced droplets due to a ramped down trap potential, with the same parameters as in Figures 4.2, 4.5, 4.6 and 4.7. (a) Population numbers varying in time with the orange curves correspond to a relatively slow ramp-down of $t_{\text{ramp}} \approx 38.3$ (dark and light orange corresponding to majority and minority components, respectively), and purple colours corresponding to a relatively fast ramp-down of $t_{\text{ramp}} \approx 0.781$ (light and dark purple corresponding to majority and minority components, respectively). The insets show the central density differences in time, with the left and right panels corresponding to the slow and fast ramps, respectively. These two example simulations are highlighted in the upper panel of (b), by the vertical, dashed lines. (b) The equilibrated population numbers and central density differences (inset) for varying ramp-down times, t_{ramp}, in the range $0.0 \leq t_{\text{ramp}} \lesssim 39.1$. The upper panel corresponds to a bound, imbalanced droplet ($\delta N_1 \approx 596$) whilst the lower panel corresponds to a saturated, imbalanced droplet with an external unbound gas ($\delta N_1 \approx 4257$).

gence in the majority and minority component chemical potentials, increases further with higher trap frequencies.

Section 4.3 focused on the breathing modes of imbalanced droplets, and contrasted the trapped geometry with the free-space results of Ref. [221]. This section highlighted that the presence of a trap causes recombination events from reflected particles. For a free-space imbalanced droplet there are three mode frequencies [221]. These three modes can be observed in the trapped, imbalanced droplet though Section 4.3 shows that with increasing trap frequency these modes are lost. Similarly the decay rate of the imbalanced droplet breathing mode can be reduced by the presence of a significant majority-component gas.

The final results presented are the dynamics of releasing imbalanced droplets into free space given in Section 4.4. The results show primarily that with a low frequency initial trap, the droplet imbalance can be preserved under an instantaneous release, though higher trap frequencies lead to a loss of the imbalance. However, a droplet released from a higher frequency trap can preserve its imbalance if the trap is ramped down sufficiently slowly. This gives promise for the experimental realisation of free-space, imbalanced quantum droplets.

The stability of the imbalance under release from a trap may be significant in the experimental results of Refs. [161, 169], in which the mixture is prepared with $N_2/N_1 = 1 \neq \sqrt{a_{11}/a_{22}}$. These works assume that the droplet will dynamically balance, after the release into free space, to $N_2/N_1 = \sqrt{a_{11}/a_{22}}$. This could explain why the data points of N_1/N_2 in Fig.4(c) of Ref. [169] are shifted up from the balanced line of $N_2/N_1 = \sqrt{a_{11}/a_{22}}$, as component-1 is setup to be the majority component. Likewise, some of the results in Ref. [170] are speculated to be sensitive to imbalance. This chapter suggests that balanced droplets could be a special case, and that imbalanced droplets are more common.

The analysis of spherically symmetric ground states and breathing mode dynamics presented could be extended to explore heteronuclear mixtures. The different kinetic energy contributions of the two components may lead to novel physics, as adding an imbalance to either component is no longer symmetric. This is however a non-trivial extension due to the form of the two-component LHY correction of a heteronuclear mixture [153, 158].

The recombination events from the trap limit the time for observing collective modes. This restriction implies that smaller computational boxes could be used to probe collective modes in more general 3D simulations, allowing for observation of non-zero angular momentum modes such as dipole [204, 243] and quadrupole modes in both balanced and imbalanced droplets.

The potential of the CsYb mixture for probing droplet physics is exciting but the experiment uses highly anisotropic trap potentials with significant population number imbalances [214]. The next chapter begins to explore the parameter space of the CsYb mixture, to explore ground state CsYb droplets and contrast these results with the density-

locked results in Sections 2.7 and 2.8 and the imbalanced results of both this chapter and Chapter 3.

Chapter 5

A theoretical guide to CsYb droplet experiments

Ultracold atoms is a field in which there is significant communication between theorists and experimentalists and quantum droplets are yet another example of this collaboration. [161, 168, 169, 171, 264]. However, the previous chapters of this thesis have focused on idealised scenarios by ignoring, e.g., three-body losses and anisotropic harmonic traps, but also the reality that experiments do not begin with a clean ground state. Droplets are not immune to these restrictions, e.g., three-body losses have been shown to significantly limit the lifetimes of homonuclear droplets in ^{39}K spin mixtures to the order of several milliseconds, though heteronuclear mixtures have been shown to enhance lifetimes to tens of milliseconds [171, 173]. Likewise anisotropic traps have been used to form droplets in both quasi-2D [168] and quasi-1D geometries [170, 171]. Losses, anisotropies and excited initial states are all true of gaseous, ultracold atomic systems, although droplets also suffer from specific issues principally due to their small size. The combination of the small size and self-bound property of droplets means that imaging and manipulation pose challenges experimentally. In the context of previous droplet experiments, this work focuses on an experiment composed of an attractive mixture of Cs and ^{174}Yb, referred to here as the CsYb mixture [214, 219] which could support droplet formation.

This chapter begins by mapping out the CsYb parameter space, i.e., which parameters can be controlled and how does this relate to entering the droplet regime. Having mapped out the parameter space, ground state solutions of the density-unlocked GP equations are evaluated by measuring the approximate sizes and densities of CsYb droplets, in both free-space and within harmonic traps. Building from the results of Chapter 3, this chapter explores the effect of the large Yb imbalance on the droplet's structure. The sizes, densities and lifetimes of CsYb droplets are compared with other previously realised droplet mixtures, to understand the constraints on the current experiment and to propose potential changes which are more amenable to droplet production. Droplet formation is explored by quenching into the droplet regime to see if CsYb droplets can be created in the current experimental setup. Finally, two experimental procedures are proposed to

study excitations and non-equilibrium dynamics of droplets.

5.1 CsYb parameter space

Two-component mixtures have in general seven free parameters: three scattering lengths (a_{11}, a_{22} and a_{12}), two atomic masses (m_1 and m_2) and two species population numbers (N_1 and N_2). However, experimentally the atomic masses are fixed and there is some control over the population sizes (or population ratio). To enter the droplet regime, typically either the interspecies [171, 173] or intraspecies scattering lengths [168, 169] are significantly varied by tuning the applied magnetic field through a Feshbach resonance. Therefore, typically only one scattering length is varied though in principle multiple Feshbach resonances could be close together such that several scattering lengths vary notably with magnetic field.

For the CsYb mixture considered here, the fixed scattering lengths are $a_{22} = a_{\mathrm{Yb}} = 105a_0$ and $a_{12} = a_{\mathrm{CsYb}} = -75a_0$ [214], where a_0 is the Bohr radius. Furthermore, within this experimental apparatus previous CsYb experiments have had a high population imbalance of $N_{\mathrm{Yb}} = [5, 7] \times 10^4$ and $N_{\mathrm{Cs}} = [4, 5] \times 10^3$ [214], and hence as typical values of a_{Cs} correspond to the population balance condition being of order one ($N_{\mathrm{Cs}}/N_{\mathrm{Yb}} = \sqrt{g_{\mathrm{Yb}}/g_{\mathrm{Cs}}} \sim 1$), the mixture can be considered as having a 'surplus' of Yb atoms for droplet production. The Cs population number is therefore the limiting factor of droplet size and so to begin, the mixture can be considered balanced as a minimal case, reducing the system to a 2D parameter space of $(a_{\mathrm{Cs}}, N_{\mathrm{Cs}})$.

5.1.1 Density-locked CsYb phase diagram

By assuming the system to be density-balanced, the $(a_{\mathrm{Cs}}, N_{\mathrm{Cs}})$ parameter space can be explored via the density-locked model from Section 2.3. Firstly, Figure 5.1 shows the length, ξ, and time, τ, scales varying with the one free parameter, a_{Cs}, as these parameters are independent of N_{Cs}. As both the length and times scales vary with $\sim \delta g^{-1}$, they diverge for $\delta g = 0$ which here corresponds to $a_{\mathrm{Cs}} \approx 54.3a_0$. At lower a_{Cs} the length and time scales decrease rapidly, for example at $a_{\mathrm{Cs}} = 10a_0$ the healing length becomes $\xi \approx 0.0187\mu$m which has serious implications on the CsYb mixture since most experimental droplets have a width of only a few healing lengths. As discussed in Section 4.4, one key probe of droplets is to release them from any traps and observe that their size stays approximately fixed. This self-bound property means that the widely used 'Time-of-Flight' technique — which in the gaseous phase leads to an increase in relevant scales of the system — cannot be used and so droplet experiments rely on high resolution cameras. Such a small healing length could be of concern because to date the highest resolution imaging for a two-component droplet experiment has been on the order of $\sim 0.6\mu$m [173].

As shown in Section 2.3, the density-locked model maps all physical parameters to an effective atom number, $\tilde{N}$, corresponding to the droplet size. Ref. [153] indicates that

within this unit system, there are different droplet regimes:

- $\tilde{N}_c = \tilde{N} \approx 18.65$ - critical atom number for droplet formation, below which the droplet cannot form and the ground state is an unbound gas
- $\tilde{N}_m = \tilde{N} \approx 22.55$ - atom number for metastability, below which the droplet is metastable as it has positive energy
- $\tilde{N_{\rm SE}} = \tilde{N} \approx 94.2$ - self-evaporation transition, below which all collective excitations are unstable to decay

These three transition values are included in Figure 5.1(c), having been converted into the equivalent Cs population number, $N_{\rm Cs} = n_{\rm Cs}^{(0)}\xi^3\tilde{N}$, where $n_{\rm Cs}^{(0)}$ is the Cs equilibrium density. The critical transition, $\tilde{N}_c$, is given by the light purple curve which is close to the metastable transition, $\tilde{N}_m$, in dark purple. Likewise, the self-evaporative transition, $\tilde{N}_{\rm SE}$ is given in dark orange and can be thought of as defining the transition to 'small' droplets. As with the length and time scales, the transition values of $N_{\rm Cs}$, decrease quickly with $a_{\rm Cs}$, and therefore to assess which droplet regimes are achievable in the current experimental CsYb mixture, the dashed, light-orange line corresponds to the approximate maximum Cs population number, $N_{\rm Cs} = 5 \times 10^3$ [214]. Restrictions on the population of each component are not the result of physical limitations, but are the result of the experimental apparatus, and one aim of future generations of the CsYb experiment will be to increase the Cs population.

At $a_{\rm Cs} = 40a_0$ the droplet lies on approximately the critical formation curve, hence lower $a_{\rm Cs}$ is needed, however, as shown in Figure 5.1(a) there are drawbacks to probing values of $a_{\rm Cs}$ that are 'too small' as the droplet size becomes difficult to image. The range of $a_{\rm Cs} = [20, 30]a_0$ appears to be a balance between sufficiently many Cs atoms — as $a_{\rm Cs} = 30a_0$ lies on the self-evaporative curve — and healing lengths that are not far below current optical imaging resolution.

Having used the density-locked model to gain an understanding of the CsYb parameter space, a more accurate understanding of the ground states, densities and droplet sizes is required. As discussed throughout Chapters 2 and 3, the density-locked model is useful for reducing the parameter space of the system, however it is restrictive. For example, the density-locked GP equation assumes that the same traps are applied to each component, which for the CsYb mixture is not true and so the density-unlocked, heteronuclear GP equations are required, though as presented in Section 2.4.1 there are computational challenges with this approach.

5.1.2 Effective heteronuclear Gross-Pitaevskii equations

One major challenge of heteronuclear GP simulations is the complexity of the full LHY term, given in Section 2.4.3. The full heteronuclear LHY term has a number of computational challenges arising from the function $f(z, x)$. However, there is an approximate

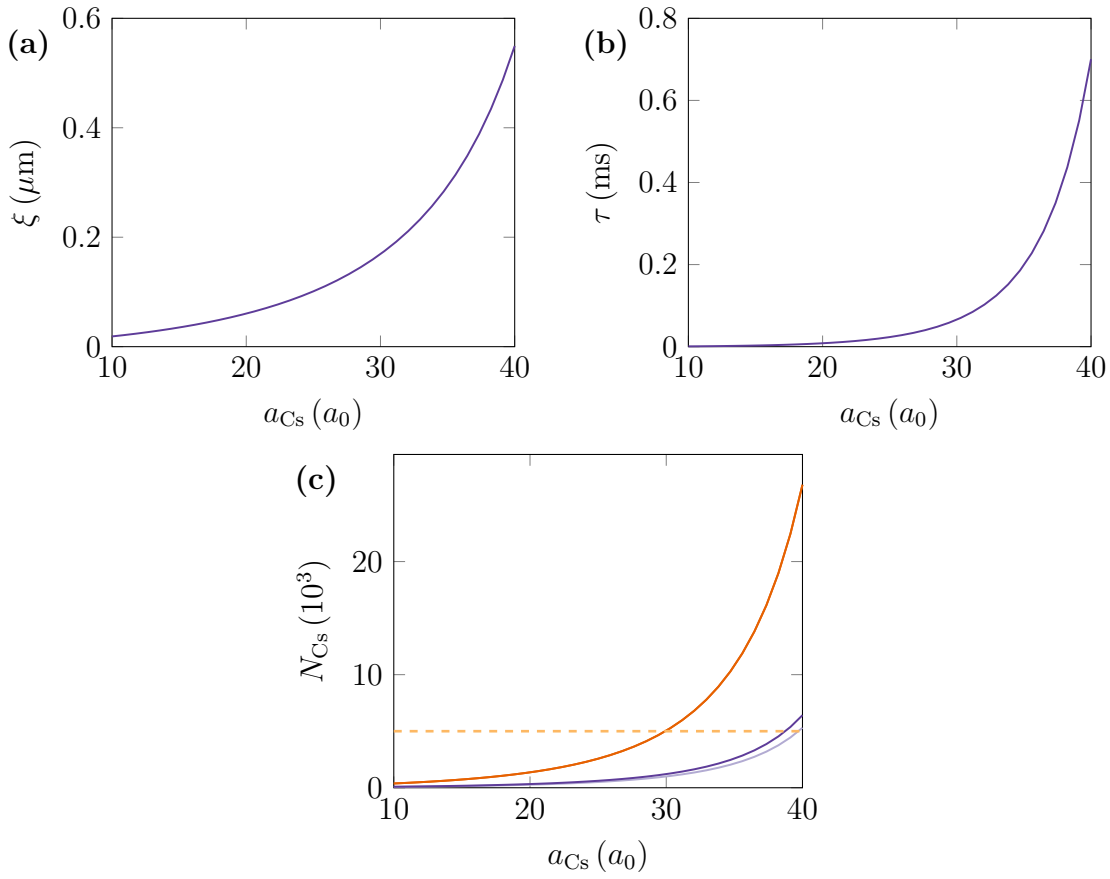

Figure 5.1: Density-locked dimensional parameters and critical atom numbers for varying a_{Cs}. (a) and (b) The healing length and time scale across a_{Cs} within the dominantly attractive regime. (c) Critical atom numbers for various density-locked droplet regimes, where light and dark purple corresponding to the critical and metastable droplet transitions, respectively, and the dark orange curve corresponds to the self-evaporative transition, i.e., below this curve all modes are self-evaporated. The dashed, light-orange line indicates the approximate highest population number of Cs, $N_{Cs} = 5 \times 10^3$, from previous experiments with this apparatus.

expression for the function, $f(z, x)$, given by [241],

$$f(z, x) = (1 + z^{3/5}x)^{5/2},$$

which is found by considering the asymptotic behaviour of the LHY function, whilst also being invariant under permutation of the two components. This effective expression significantly reduces the computational complexity of simulating a heteronuclear BMF mixture. It is necessary to check how much the approximation differs from the full heteronuclear LHY correction in order to have confidence in the validity and accuracy of the simulations.

Figure 5.2 compares the effective (purple) and full (orange) [from Equation (2.39)] forms of the function, $f(z, x)$, for the CsYb ($m_2/m_1 = 174/133$) and NaRb ($m_2/m_1 = 87/23$) mass ratios given by (a) and (b), respectively. The absolute percentage error between the effective and full function forms is inset. The maximum percentage difference for

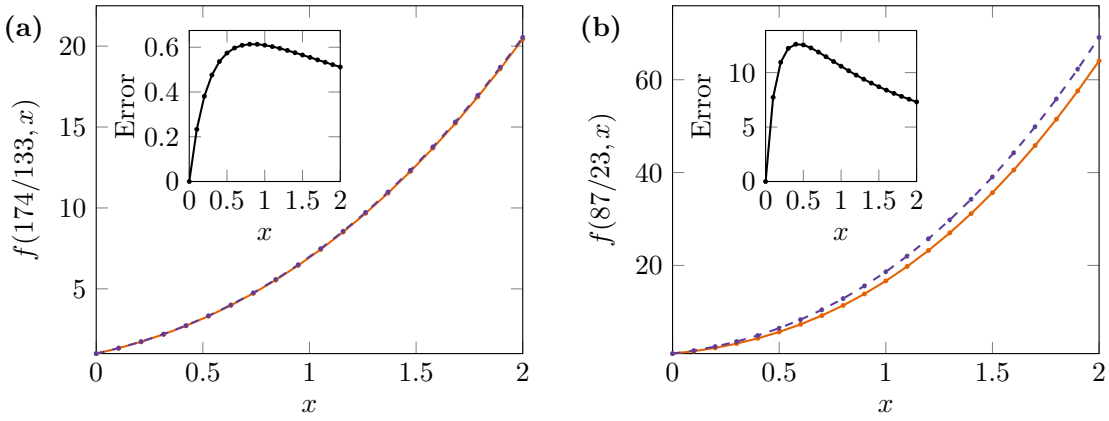

Figure 5.2: Comparison of effective (purple) and full (orange) heteronuclear LHY functions for varying $x = g_{22}n_2/g_{11}n_1$, with mass ratios: (a) CsYb ($m_2/m_1 = 174/133$); (b) NaRb ($m_2/m_1 = 87/23$). Absolute percentage error is given in the insets.

the CsYb mixture is $\sim 0.6\%$, which is relatively small compared to the $\sim 12\%$ of the NaRb mixture. The effective LHY correction appears to be a relatively good approximation for the CsYb mixture, especially since the BMF-GP model contains other assumptions, e.g., the removal of the complex contributions to the LHY correction. Substituting the effective LHY expression into the GP energy functional results in the effective, heteronuclear GP equations,

$$\begin{aligned} i\hbar\frac{\partial\Psi_1}{\partial t} =& \Bigg[-\frac{\hbar^2}{2m_1}\nabla^2 + g_{11}|\Psi_1|^2 + g_{12}|\Psi_2|^2 \\ &+ \frac{4}{3\pi^2}\left(\frac{m_1}{\hbar}\right)^{3/2} g_{11}\left(g_{11}|\Psi_1|^2 + \left(\frac{m_2}{m_1}\right)^{3/5} g_{22}|\Psi_2|^2\right)^{3/2}\Bigg]\Psi_1, \\ i\hbar\frac{\partial\Psi_2}{\partial t} =& \Bigg[-\frac{\hbar^2}{2m_2}\nabla^2 + g_{22}|\Psi_2|^2 + g_{12}|\Psi_1|^2 \\ &+ \frac{4}{3\pi^2}\left(\frac{m_1}{\hbar}\right)^{3/2}\left(\frac{m_2}{m_1}\right)^{3/5} g_{22}\left(g_{11}|\Psi_1|^2 + \left(\frac{m_2}{m_1}\right)^{3/5} g_{22}|\Psi_2|^2\right)^{3/2}\Bigg]\Psi_2. \end{aligned} \tag{5.1}$$

Using the same non-dimensionalisation of Equation (2.38) reduces Equation (5.1) to

$$\begin{aligned} i\frac{\partial\Psi_1}{\partial t} &= \left[-\frac{\gamma}{2}\nabla^2 + |\Psi_1|^2 + \eta|\Psi_2|^2 + \alpha\left(|\Psi_1|^2 + z^{3/5}\beta|\Psi_2|^2\right)^{3/2}\right]\Psi_1, \\ i\frac{\partial\Psi_2}{\partial t} &= \left[-\frac{\gamma}{2z}\nabla^2 + \beta|\Psi_2|^2 + \eta\beta|\Psi_1|^2 + \alpha z^{3/5}\beta^2\left(|\Psi_1|^2 + z^{3/5}\beta|\Psi_2|^2\right)^{3/2}\right]\Psi_2, \end{aligned} \tag{5.2}$$

i.e., the effective heteronuclear GP equations have a similar structure to the homonuclear GP equations in Equation (2.38). These GP equations are next solved via the computational techniques introduced in Section 2.6, to study ground state CsYb droplets.

5.2 CsYb droplets

Having established the relevant parameter space for the CsYb droplets by focusing on the balanced, density-locked GP model, this section studies ground state CsYb droplets. Using previous experimental works as a guide, this section begins by studying two main observables of spherical, free-space droplets: width and peak density.

Firstly, widths and densities of free-space, balanced CsYb droplets are calculated and compared with other droplet experiments. Due to the high Yb imbalance, a similar analysis as from Section 3.1 is used to observe the level of imbalance the CsYb droplet core can support. Secondly, the CsYb experiment applies highly anisotropic traps to each component and so more general 3D, trapped ground states are studied to measure how the anisotropy modifies the droplet density structure. Finally, ground state CsYb droplets are propagated in real time, with the addition of losses enabling the calculation of droplet lifetimes.

5.2.1 Free-space CsYb droplets

This section uses the density-unlocked GP equations in Equation (5.2). The aim is to explore the $(N_{\mathrm{Cs}}, a_{\mathrm{Cs}})$ parameter space by varying N_{Cs}, whilst also enforcing density-balancing, $N_{\mathrm{Yb}} = N_{\mathrm{Cs}}\sqrt{g_{\mathrm{Cs}}/g_{\mathrm{Yb}}}$, meaning that both N_{Cs} and N_{Yb} are varied.

By varying across the $(N_{\mathrm{Cs}}, a_{\mathrm{Cs}})$ parameter space, Figure 5.3 shows the width and peak density of the CsYb droplet. The droplet width or diameter is extracted by doubling the radius at which the droplet density is approximately 0.1% of the peak density. Figure 5.3(a) and (b) show the extracted widths of the Cs and Yb components, respectively, indicating a pronounced dependence on a_{Cs} whilst the N_{Cs} dependence appears much weaker. Reducing a_{Cs} means decreasing δg further, i.e., driving the overall MF interactions to be more attractive, and hence the droplet width decreases substantially with both the Cs and Yb widths on the order of 0.5μm, which would be very challenging to directly image.

Beyond just the problem of imaging submicron droplets, there is also the corresponding issue of high peak densities. Figure 5.3(c) and (d) show the peak densities of the Cs and Yb components, respectively, in units of atoms per cm^3. The first notable difference between (c) and (d) is that Cs has a significantly higher density than Yb, with some areas of the parameter space showing approximately four to five times higher Cs densities. This is a potentially concerning result as Cs suffers from high three-body losses [97]. At low a_{Cs} the droplet width decreases significantly which corresponds to higher peak densities, hence more evidence for why $a_{\mathrm{Cs}} = [10, 15]a_0$ should probably be avoided.

Contrasting the CsYb mixture with successful quantum droplet experiments, CsYb droplet widths at $a_{\mathrm{Cs}} = 30a_0$ are approximately $\sim 2\mu$m and these sizes are in keeping with ^{39}K spin mixtures [169] and heteronuclear ^{23}Na^{87}Rb mixtures [173]. However, the main issue is concerning the CsYb peak densities which are $\sim 10^3\times$ higher than the

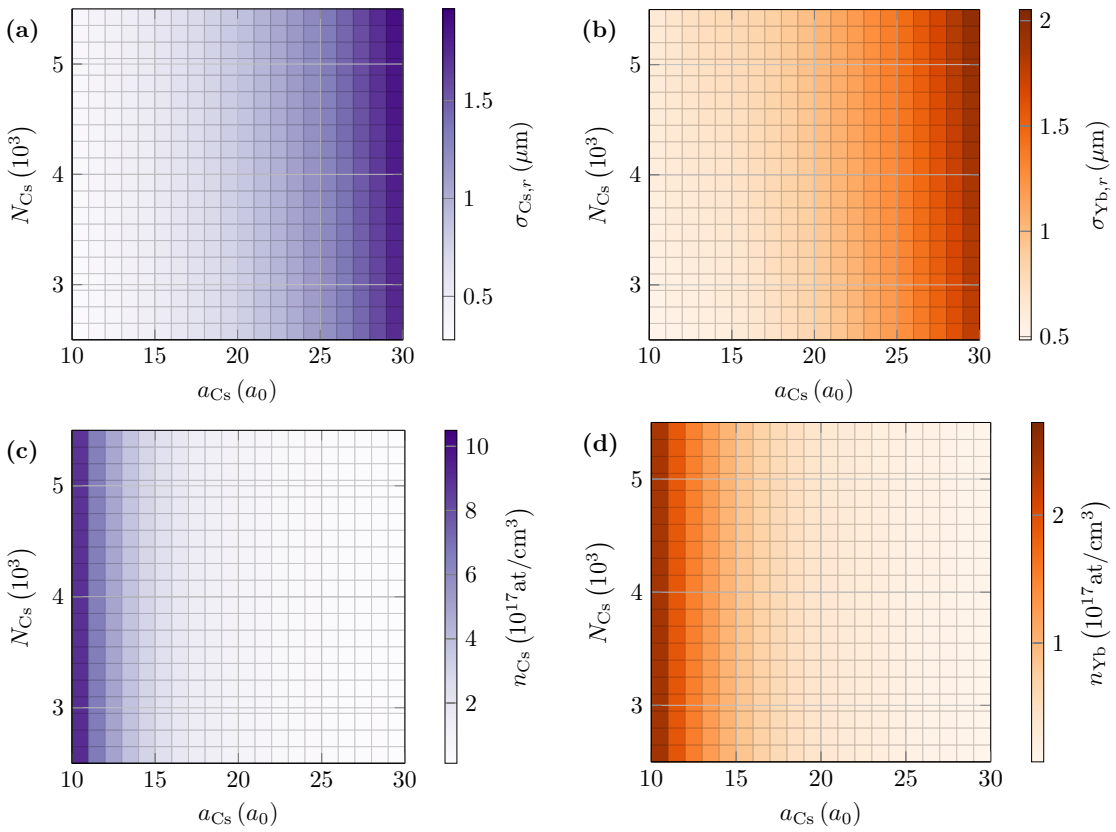

Figure 5.3: The $(N_{\mathrm{Cs}}, a_{\mathrm{Cs}})$ phase diagrams across $a_{\mathrm{Cs}} = [10, 30]a_0$ and $N_{\mathrm{Cs}} = [2.5, 5.5] \times 10^3$. (a) and (b) The width of the Cs and Yb component, respectively. (c) and (d) The peak density of the Cs and Yb, component, respectively.

$n \sim 1 \times 10^{14}\mathrm{at/cm}^6$ densities of the ^{39}K spin mixture presented in Ref. [168].

Having studied experimentally relevant observables of balanced CsYb droplets, there is still a crucial property of the CsYb mixture to be explored, namely, the large Yb imbalance. The rest of this section measures how spherical, free-space droplets are affected by varying the population imbalance, and contrasts these effects with discussions from Chapter 3. This analysis is similar to that presented in Section 3.1, therefore instead of using experimentally relevant units (μm, etc.), the following results are presented in the dimensionless units used throughout Chapters 3 and 4.

Figure 5.4(a) shows a population balanced, $N_{\mathrm{Yb}}/N_{\mathrm{Cs}} = \sqrt{g_{\mathrm{Cs}}/g_{\mathrm{Yb}}}$, ground state density profile corresponding to $N_{\mathrm{Cs}} = 5 \times 10^3$ in experimental units, in which $a_{\mathrm{Cs}} = 20a_0$ is set here as an example scattering length. Measurements at different a_{Cs} would be quantitatively different, but qualitatively similar. As in Figure 3.5(a), the population balancing in physical units corresponds to just $N_{\mathrm{Yb}} = N_{\mathrm{Cs}}$ in the dimensionless units introduced in Equation (2.33). Relative to the $\beta \neq 1$ results in Figure 3.5(a), there is a more pronounced density splitting. The scattering length imbalance is more pronounced here, $\sqrt{a_{22}/a_{11}} = \sqrt{a_{\mathrm{Yb}}/a_{\mathrm{Cs}}} \approx 2.291$, than in the homonuclear case presented in Figure 3.5. However Figure 5.4 also exhibits a mass imbalance, i.e., the central density splitting now depends on the intraspecies scattering length and mass ratios, $\beta = \sqrt{g_{22}/g_{11}} = \sqrt{g_{\mathrm{Yb}}/g_{\mathrm{Cs}}} = \sqrt{a_{\mathrm{Yb}}m_{\mathrm{Cs}}/a_{\mathrm{Cs}}m_{\mathrm{Yb}}} \approx 2.003$. Section 3.3 demonstrates that

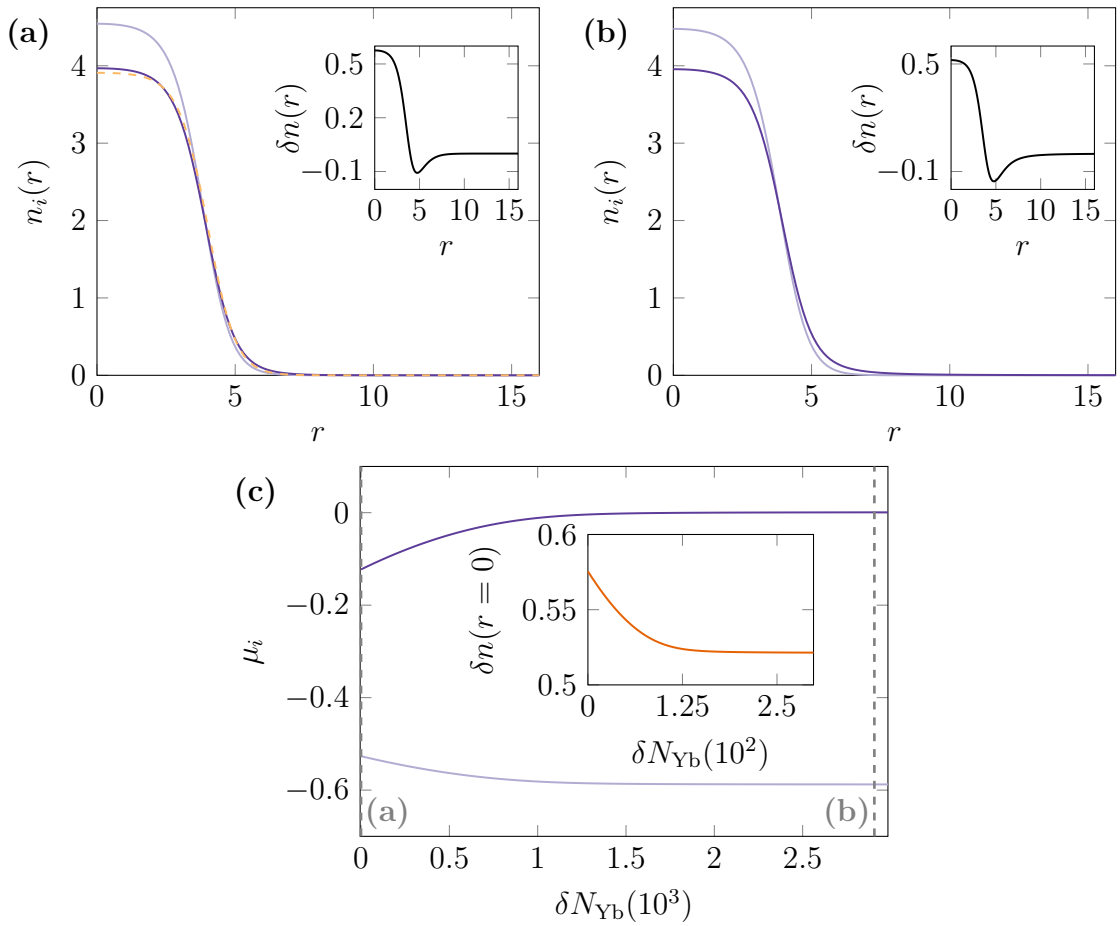

Figure 5.4: Free-space CsYb droplets, with light and dark purple corresponding to Cs and Yb, respectively, where $\alpha \approx 0.0285$, $z \approx 1.308$, $\gamma \approx 1.085$, $\beta \approx 2.003$, $\eta \approx -1.651$ and $N_1 \approx 1193$ correspond to $N_{\mathrm{Cs}} = 5 \times 10^3$ at $a_{\mathrm{Cs}} = 20a_0$ in experimental units, with population balance $N_{\mathrm{Yb}} = 2496$. (a) Balanced CsYb droplet with density difference inset, compared with density-locked prediction given by the orange, dashed curve. (b) CsYb saturated with Yb atoms, i.e., $\delta N_1 \approx 291$ (or $\delta N_1 = 608$ in experimental units) with density difference again inset. (c) Chemical potentials and central density difference (inset) for varying number of Yb atoms.

an imbalance of the intraspecies scattering lengths corresponds to a symmetry breaking such that even with balanced populations, the two-component densities are not equivalent. However, for the droplets shown in Figure 5.4, intraspecies scattering lengths and masses are imbalanced, i.e., there is both an imbalancing of the interaction strengths, $\beta = \sqrt{g_{22}/g_{11}} \neq 1$, and the kinetic contributions to the GP Hamiltonians in Equation (5.1).

Refs. [214, 219] indicate that the CsYb mixture is heavily Yb imbalanced, and so Figure 5.4(b) shows a droplet saturated with the Yb component. The saturated, imbalanced droplets shown in Chapter 3 can exhibit a much larger central density splitting than the CsYb droplet in Figure 5.4(b) which has a density profile almost unchanged from the balanced case. The density difference inset shows a slight decrease in central density splitting and a greater Yb density at the droplet surface.

By varying across the Yb imbalance, Figure 5.4(c) shows that the chemical potentials

at zero imbalance are substantially split relative to Figure 3.5(d). The Yb chemical potential is close to zero, $\mu_{\mathrm{Yb}} \approx -0.123$, and so the Yb component cannot absorb many atoms before the chemical potential approaches zero, the necessary criterion for imbalance saturation. The inset shows how small the central density splitting varies with Yb imbalance, compared to saturation limits shown in Chapter 3. In experimental units the maximum imbalance considered in Figure 5.4(c) is, $\delta N_{\mathrm{Yb}} = 10000 \implies N_{\mathrm{Yb}} = 12496$, which is significantly into the saturated regime but is also small relative to the experimental value of $N_{\mathrm{Yb}} \approx [50000, 75000]$ used in the CsYb mixture [214, 219]. However, as stated in Ref. [214] the quantity of Yb atoms can be controlled via the control of the loading of the Cs Magneto-Optical-Trap (MOT).

In summary, in the current experimental setup free-space droplets can only be formed for values of a_{Cs} that correspond to extremely dense droplets. This high density is in part a result of their small size, but these sizes are comparable to previous droplet experiments. Beyond balanced populations, the CsYb mixture cannot support a substantial imbalance in the droplet core, hence with the addition of traps the droplet can be almost approximated as a balanced droplet surrounded by a large Yb unbound gas.

5.2.2 Trapped CsYb droplets

The CsYb mixture is trapped by a set of anisotropic harmonic traps with frequencies, $(\omega_x, \omega_y, \omega_z)_{\mathrm{Yb}} = 2\pi\,(10, 120, 80)\,\mathrm{Hz}$ and $(\omega_x, \omega_y, \omega_z)_{\mathrm{Cs}} = 2\pi\,(40, 70, 260)\,\mathrm{Hz}$, i.e., the Yb trap is more 1D with less confinement along x, whilst the Cs trap is more 2D as it is tightly trapped in z [214, 219]. Whilst the numerical schemes used throughout this thesis are introduced in Section 2.6, throughout the remainder of this section and Section 5.3, a different numerical method is used to solve Equation (5.1). This chapter uses an adaptive Runge-Kutta-4(5) method using XMDS2 [280], which retains physical dimensions and works with rescaled units: length scale - microns (μm); time scale - milliseconds (ms); and, energy scale - nanoKelvin multiplied by Boltzmann's constant, k_B, (k_BnK).

Figure 5.5 shows the ground state density of an anisotropically-trapped CsYb droplet, with (a) and (b) showing the Cs (purple) and Yb (orange) components, respectively. Note that even with the application of anisotropic traps, the density profile of the droplet is almost entirely isotropic. This is further highlighted by the x, y and z-slices given in Figure 5.5(c), which likewise show the largely isotropic density structure. The reason for the isotropic density distribution is because the droplet is very small relative to the trap confinement.

Though the effect of the trap appears small Figure 5.6 demonstrates how both the droplet width (in x, y, and z) and peak density varies with a_{Cs} within the anisotropic traps. Figure 5.6(a), (b) and (c) show the widths in x, y and z, extracted again by doubling the radius at which the density reaches 0.1% of the peak density. The dark orange and purple data corresponds to the trapped Yb and Cs components, respectively, with the light orange and purple corresponding to the free-space components. Across

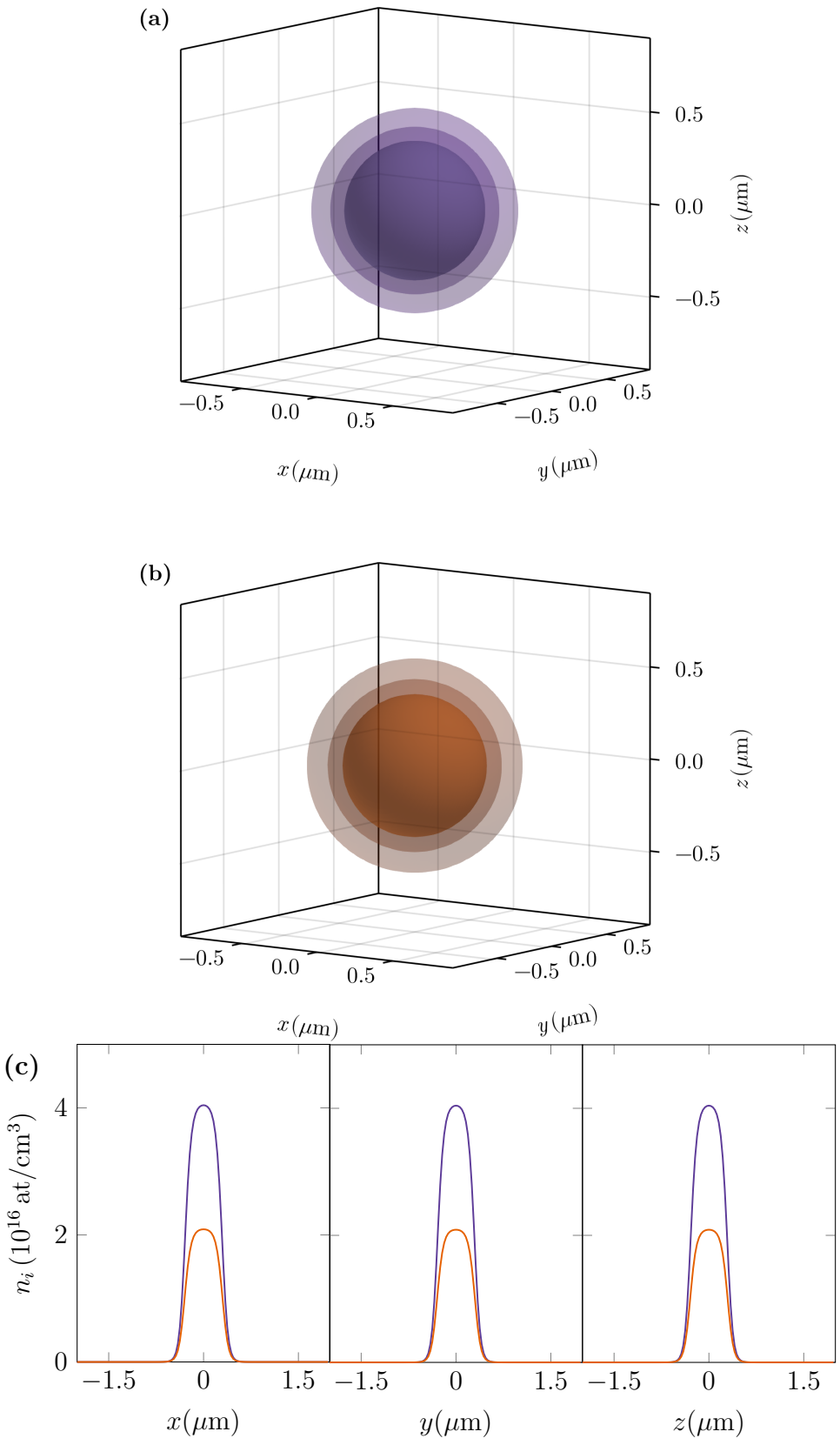

Figure 5.5: Ground state densities of trapped, balanced CsYb droplet, with $a_{\mathrm{Cs}} = 25a_0$, $N_{\mathrm{Cs}} = 5{\times}10^3$, and $N_{\mathrm{Yb}} \approx 2791$. (a) and (b) The Cs (purple) and Yb (orange) components, respectively, with isosurfaces given at $\{0.5, 5, 25\}$ % of each component's peak density. (c) 1D slices — where, again, purple and orange correspond to Cs and Yb, respectively — along, x, y and z, i.e., the x-slice is taken at $(y, z) = (0, 0)$.

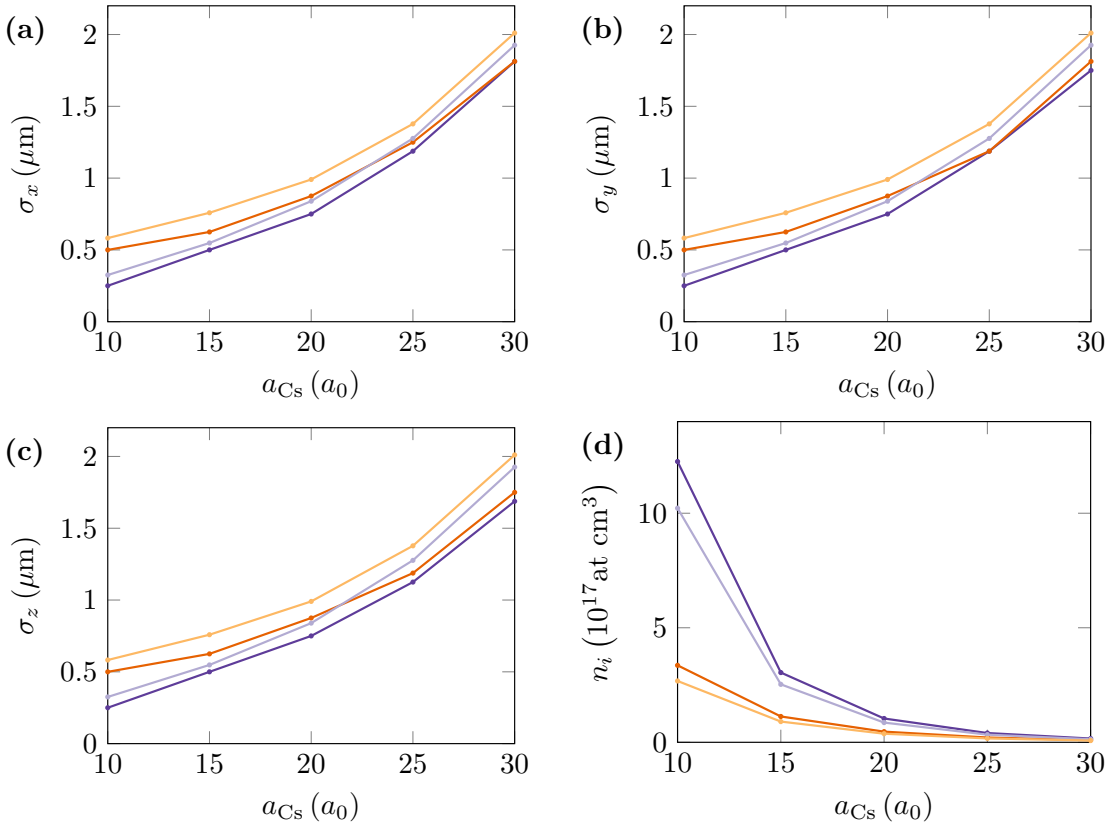

Figure 5.6: Droplet width, σ_i, along (x, y, z), and peak density, where dark purple and orange correspond to the 3D, trapped Cs and Yb components, respectively, whilst light purple and orange correspond to the spherical, free-space Cs and Yb components, respectively. Populations are balanced to $N_{\mathrm{Cs}} = 5 \times 10^3$ via $N_{\mathrm{Yb}} = N_{\mathrm{Cs}}\sqrt{g_{\mathrm{Cs}}/g_{\mathrm{Yb}}}$. (a), (b) and (c) Droplet widths in x, y and z, respectively, for varying a_{Cs}. (d) Peak density for varying a_{Cs}.

the three axes there is a 'squeezing' effect from the traps, however, these differences are relatively small. There is evidence that for larger a_{Cs} the droplet is larger and hence 'sees' more of the trap leading to slightly more pronounced deviations from the free-space droplet, particularly in the tighter trapped y and z directions, however these affects are still relatively minor. Alongside the differences in droplet width, the peak density is also increased by the squeezing of the trap, though the density is still within the same order of magnitude.

Figure 5.4 demonstrated that the CsYb mixture cannot support a large Yb imbalance in the droplet core, in part due to the large intraspecies scattering length imbalance necessary to enter the droplet regime. The implication of this property is that imbalancing the CsYb droplet in a trap approximately corresponds to the density-balanced CsYb droplet surrounded by a large unbound gas. Figure 5.7(a) and (b) show the Cs (purple) and Yb (orange) components, respectively, with a large, experimentally relevant, Yb imbalance [214, 219]. The small scale of the droplet is highlighted in Figure 5.7(b) in which the Yb component bound to the droplet is of order $\sim 1\mu$m whilst the gas has a size of $\sim 20\mu$m, in the x direction. However, as discussed throughout Chapters 3 and 4,

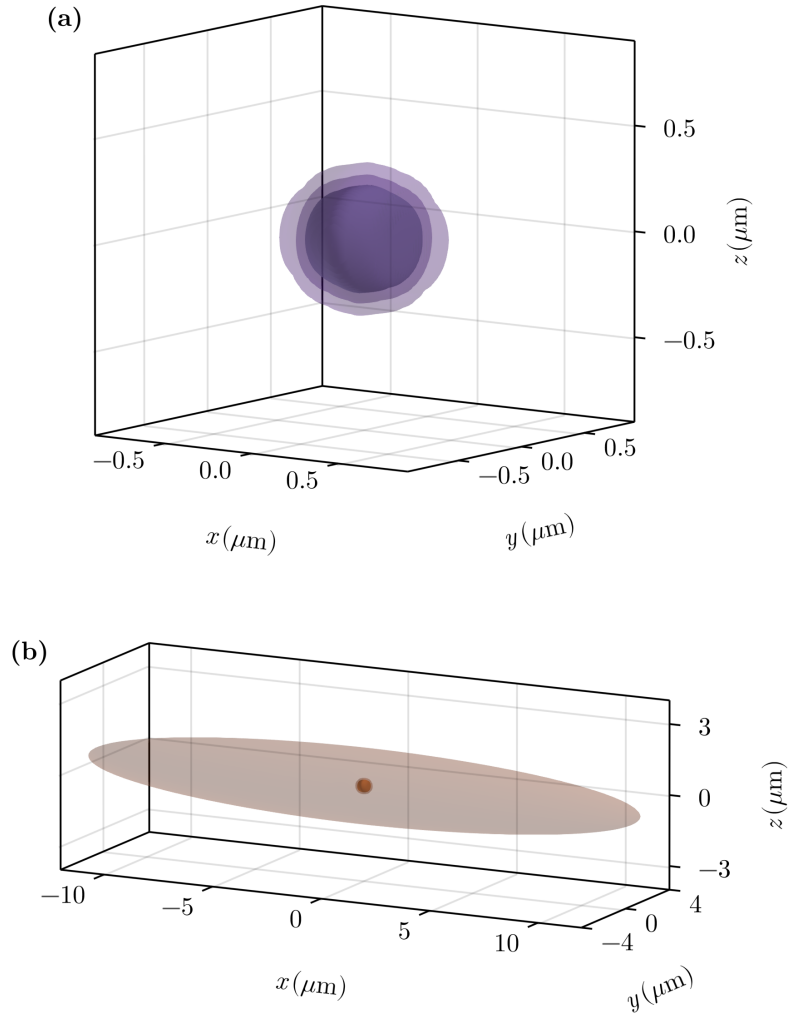

Figure 5.7: Ground state densities of imbalanced CsYb at $a_{\mathrm{Cs}} = 20a_0$, where (a) and (b) correspond to the Cs (purple) and Yb (orange) components, respectively. With $N_{\mathrm{Cs}} = 5 \times 10^3$ and $N_{\mathrm{Yb}} = 5 \times 10^4$, there is an imbalance of $\delta N_{\mathrm{Yb}} \approx 47504$. Isosurfaces are given at $\{0.5, 5, 25\}$ % of each component's peak density.

the imbalance only significantly modifies the droplet behaviour, if the droplet core is imbalanced. Therefore, whilst the unbound Yb gas may influence some of the dynamics, such as the atom shedding and mode dissipation shown in Section 4.3, the droplet is relatively population balanced.

Droplet sizes, both free-space and harmonically trapped, are comparable to some previous droplet experiments though probing deep into the attractive regime, $a_{\mathrm{Cs}} \sim 10a_0$ corresponds to very small, dense droplets that would be both difficult to image and would be rapidly destroyed by three-body losses. The CsYb droplets do appear to be approximately three orders of magnitude more dense than other droplet experiments in ^{39}K spin mixtures, and so the next section predicts how losses will affect CsYb lifetimes and how these compare with known droplet experiments.

Table 5.1: Three-body loss rates, K_3, and approximate lifetimes, t_{life}, of all experimental droplet mixtures to date. For some experiments the loss rates of both components are listed (e.g., ^{23}Na^{87}Rb), however in experiments that have one dominant loss channel, only this loss rate is listed.

Experiment	Component	K_3 (cm^6/s)	t_{life}(ms)
Ref. [168]	^{39}K $\lvert F=1, m_F=0\rangle$	7.5×10^{-28}	25
Ref. [169]	^{39}K $\lvert F=1, m_F=0\rangle$	9.0×10^{-28}	8
Ref. [169]	^{39}K $\lvert F=1, m_F=-1\rangle$	1.0×10^{-29}	8
Ref. [171]	^{41}K (K-Rb-Rb channel)	7.0×10^{-29}	28
Ref. [173]	^{87}Rb	7.2×10^{-30}	7
Ref. [173]	^{23}Na	1.1×10^{-30}	7

5.2.3 CsYb droplet lifetimes

Three-body losses are common to all quantum gases [96, 97, 281–284], not just droplets, and are the result of inelastic three-body collisions. The high density of a quantum droplet relative to a gaseous atomic cloud leads to considerably higher three-body losses, i.e., the population of one or both components is depleted in time until the critical population number for droplet formation is crossed and the droplet transitions to a gas. This is also of concern within the CsYb mixture particularly due to the relatively high peak densities shown in Figure 5.6(d) as this issue is most critical at low values of a_{Cs}, whilst more favourable peak densities are found closer to the droplet-gas transition $a_{\text{Cs}} \approx 54.3a_0$. This section looks briefly at the loss rates and lifetimes of CsYb droplets, to compare with other experimental droplets.

Three-body losses can be added as a 'sink' term to the dimensional Cs Hamiltonian, $-\left(i\hbar K^{(\text{C})}_{3,\text{Cs}}/2\right)|\Psi_{\text{Cs}}|^4$, where $K^{(\text{C})}_{3,\text{Cs}}$ is the three-body loss coefficient for the Cs condensate. The three-body loss coefficient used here matches that of Ref. [219], $K_{3,\text{Cs}} = 1.8\times10^{-27}\text{cm}^6/\text{s}$, in keeping with Refs. [100, 216], where $K_{3,\text{Cs}}$ is the Cs loss rate in the thermal gas, and is a factor of 3! higher than the condensate loss rate, $K^{(\text{C})}_{3,\text{Cs}}$ [285, 286]. Comparing the Cs three-body loss rates with the loss rates of other droplet mixtures in Table 5.1 shows that the Cs loss rate is at least one order of magnitude higher than other experiments. However, Ref. [100] demonstrates that the three-body loss rate of Cs can lie within the range $8.2\times10^{-29}\text{cm}^6/\text{s} \lesssim K_{3,\text{Cs}} \lesssim 1.3\times10^{-27}\text{cm}^6/\text{s}$, indicating that the lower bound of the Cs loss rate is closer to the loss rates in Table 5.1. Hence, with the combination of the relatively high Cs three-body losses and the peak densities found in Figures 5.3 and 5.6, the CsYb droplet lifetimes in the current experimental setup are predicted to be very short.

Table 5.2 shows lifetimes, t_{life}, in ms for $a_{\text{Cs}} \in \{10, 15, 20, 25, 30\}a_0$. These lifetimes are calculated by propagating a ground state droplet in real time, with the addition of three-body losses, until the Cs population number drops below the minimum atom number set by $\tilde{N} \approx 18.65$ as given in Figure 5.3(c). Shorter lifetimes are found for decreasing a_{Cs} since, as shown in Figures 5.3 and 5.6, a lower a_{Cs} corresponds to a less internally

Table 5.2: CsYb droplet lifetimes for varying a_{Cs}, with initial $N_{\mathrm{Cs}} = 5 \times 10^3$ in a balanced mixture, $N_{\mathrm{Yb}} = N_{\mathrm{Cs}}\sqrt{g_{\mathrm{Cs}}/g_{\mathrm{Yb}}}$.

$a_{\mathrm{Cs}}\,(a_0)$	t_{life} (ms)
10	0.00472
15	0.0177
20	0.0365
25	0.0811
30	0.1950

repulsive Cs component and hence a higher peak density. Comparing the predicted CsYb lifetimes with the experimental lifetimes shown in Table 5.1 shows a stark difference as the CsYb lifetimes are almost two to three orders of magnitude shorter. Hence, Table 5.2 seems to indicate that, in the current setup, the CsYb mixture cannot viably produce droplets, because even if the system could be initialised in the droplet regime, the losses are so significant that the droplet will transition to a gas very rapidly.

One future aim of the experimental CsYb mixture is therefore to reduce peak densities for which there are two methods discussed here. Firstly, reducing the system to 1D by tuning the applied traps has been theoretically shown to reduce the equilibrium density, somewhat suppressing the effects of three-body losses [287]. The region of the two-component parameter space corresponding droplets is also increased by reducing to 1D [254, 288, 289]. The issue here with 1D droplets is that the stabilisation mechanism is reversed, i.e., weakly-repulsive MF interactions, $\delta g > 0$, stabilise weakly-attractive quantum fluctuations [254]. Secondly, the peak densities can also be reduced by preparing the mixture with higher a_{Cs}, close to the $\delta g = 0$ transition. The equilibrium densities given in Equation (2.26) scale as $n^{(0)} \sim |\delta g|^2$ and hence lifetimes scale as $t_{\mathrm{life}} \sim |\delta g|^{-4}$ [153]. However, as noted in Figure 5.1 the critical atom number diverges towards $\delta g < 0$, i.e., small, negative δg gives favourable peak densities, but the population number needed for the droplet to form is very large, well beyond the current upper bound, $N_{\mathrm{Cs}} = 5 \times 10^3$. One way to remedy this is by reducing dimensionality to 2D in which the droplet transition occurs for the range $g_{12} < 0$ rather than $\delta g < 0$ [254] implying that larger a_{Cs} can be used to form droplets, mitigating the three-body losses. Ref. [289] demonstrates that droplets can therefore be formed with dominantly attractive, repulsive and no MF interaction at all, akin to the argument of Ref. [254] that a gas in 3D may become a droplet in 2D. Alternatively, if the population number of the Cs component could be increased then again higher a_{Cs} could be used to form droplets.

Having briefly discussed the dramatic effect three-body losses have on CsYb droplet lifetimes the next sections investigate dynamical processes of entering the droplet regime by ramping or 'quenching' the Cs scattering length into the droplet regime. This is to study how the losses impact the droplet formation, e.g., can enough Cs atoms be retained during the quench to even produce a droplet. These results build on some of the results from Ref. [219], and ask the question of whether the experimental results of Ref. [219]

already suggest signatures of CsYb droplets and BMF effects more generally.

5.3 Beyond-mean-field quench dynamics

The first dynamical results from the attractive CsYb mixture are reported in Ref. [219] in which one of the experimental procedures is a dynamical collapse induced by ramping the Cs scattering length, a_{Cs}, to different values, $a_{\mathrm{Cs}}^{(\mathrm{jump})}$, probing the MF collapse regime. The dynamical collapse analysis carried out in Ref. [219] quenches a_{Cs} and allows the system to evolve. The Cs cloud suffers from high three-body losses which deplete the Cs condensate. The final condensate number of the Cs cloud, N_{Cs}, is extracted following the quench procedure. The results from this experiment are given by the purple points in Figure 5.9 and are compared to MF-GP simulations given by the dark orange points. The MF-GP simulations are carried out up to $a_{\mathrm{Cs}} \approx 54.3a_0$ which is the approximate MF-mixture collapse (given by the rightmost vertical dashed line in Figure 5.9). For values of $a_{\mathrm{Cs}} \lesssim 54.3a_0$, the MF theory predicts collapse, and hence MF-GP simulations are not stable. This section extends these results by comparing the experimental data in Figure 5.9 to BMF-GP simulations.

5.3.1 Scattering length quench

Beginning with the ground state gas given in Figure 5.8, the experimental protocol of the dynamical collapse from Ref. [219] is: (1) hold $a_{\mathrm{Cs}} = 147a_0$ for 5ms; (2) linearly ramp for 10ms to $a_{\mathrm{Cs}} = a_{\mathrm{Cs}}^{(\mathrm{jump})}$; (3) hold at $a_{\mathrm{Cs}} = a_{\mathrm{Cs}}^{(\mathrm{jump})}$ for 30ms; (4) linearly ramp for 10ms back to $a_{\mathrm{Cs}} = 147a_0$; (5) Final hold at $a_{\mathrm{Cs}} = 147a_0$ for 1ms. Once again, a three-body loss term is added to the Cs Hamiltonian, $-\left(i\hbar K_{3,\mathrm{Cs}}^{(\mathrm{C})}/2\right)|\Psi_{\mathrm{Cs}}|^4$, where $K_{3,\mathrm{Cs}}^{(\mathrm{C})}$ is the three-body loss coefficient for the Cs condensate. By including this loss term, the Cs population number is dynamically depleted throughout the simulation. The final Cs population numbers using MF-GP (dark orange) and BMF-GP (light orange) simulations are given in Figure 5.9.

The BMF-GP simulations show greater agreement with the experimental data given by the purple points, demonstrating that there are significant BMF contributions to the mixture. However, as a result of this experimental protocol, there are significant excitations to the cloud. Furthermore, the final Cs population number, N_{Cs}, is relatively low for the production of droplets. This implies that either very small droplets could be produced, or droplets may not be formed due to a combination of small condensate numbers and high excitations to the cloud. Hence, the excitations and low population numbers imply that, though BMF corrections impact the dynamics, Figure 5.9 is not sufficient evidence for droplet formation. For example, Figure 5.10(c) shows the Cs and Yb components in dark and light purple, respectively, following the 10ms ramp to $a_{\mathrm{Cs}} = 20a_0$ only, in which no distinctive droplet profile can be seen but significant density fluctuations buffet both components. Hence, ramping to scattering lengths in the attractive regime leads to a high reduction of the Cs condensate, and therefore raises questions about the ability to form

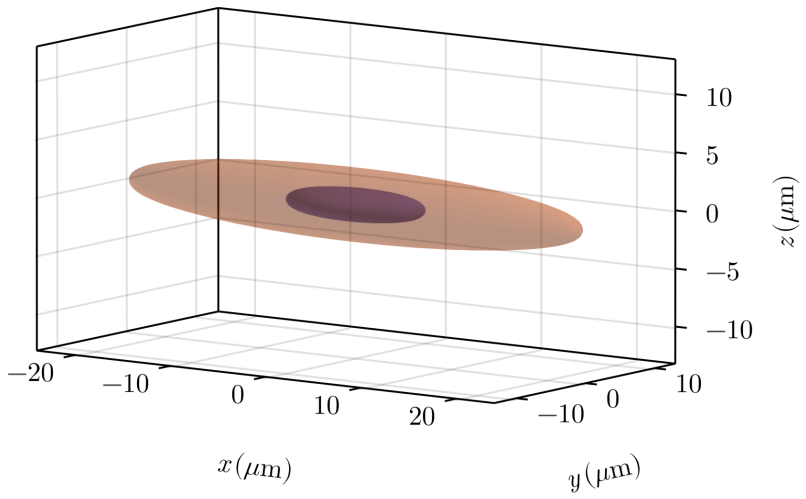

Figure 5.8: Ground state of the CsYb gas, where $a_{\mathrm{Cs}} = 147a_0$, with smaller purple component corresponding to Cs ($N_{\mathrm{Cs}} = 4\times10^3$), and the larger orange component corresponding to Yb ($N_{\mathrm{Yb}} = 5 \times 10^4$). The isosurfaces are plotted at 10% of the peak, central density.

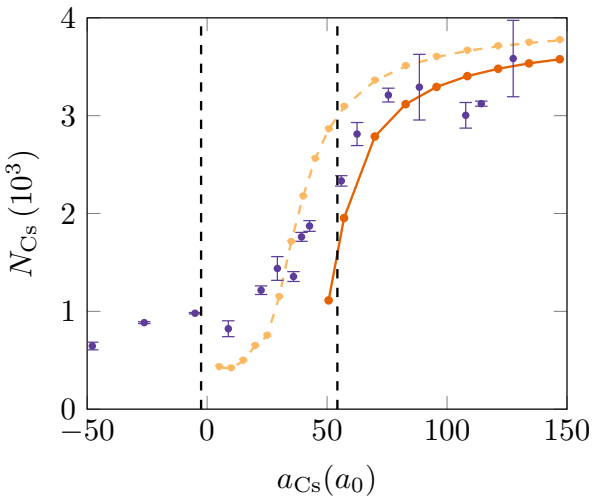

Figure 5.9: The final extracted Cs condensate number, N_{Cs}, for varying quenched a_{Cs}. Experimental data are given with error bars by the purple points, with MF-GP and BMF-GP simulations given by the dark and light orange points, respectively. The MF-mixture collapse is given by the rightmost vertical dashed line, whilst the single-component Cs MF-collapse is given by the leftmost vertical dashed line.

droplets.

5.3.2 Varying ramp protocols

Though Figure 5.9 shows signs of BMF physics but no overall evidence of droplet formation, a question emerges: could this experimental protocol be modified to give more favourable conditions for droplet formation? The experimental protocol is relatively fixed without an enormous degree of flexibility in population numbers. However, one variable of interest is the scattering length ramp time, which this section explores to see whether

there are ways of ramping into the droplet regime whilst retaining more Cs atoms.

From the quench simulations given in Figure 5.9 it is apparent that due to the low number of Cs atoms, the focus for droplet formation should be on relatively low values of a_{Cs}. However, at values of a_{Cs} that are 'too close' to $a_{\mathrm{Cs}} = 0$ the simulations become very prone to a collapse instability, e.g., numerical instabilities have been observed here at around $a_{\mathrm{Cs}} = 10a_0$. This highly attractive regime also leads to dense, short-lived droplets as shown throughout Section 5.2. Thus, the two values in focus here are $a_{\mathrm{Cs}} = 20a_0$ and $25a_0$, in keeping with values studied throughout Section 5.2.

The previous protocol of ramping from $a_{\mathrm{Cs}} = 147a_0$ to the desired $a_{\mathrm{Cs}}^{(\mathrm{jump})}$ in 10ms is understood to be one of the shortest ramp times possible within the current experimental setup. The density profiles following the 10ms ramps, such as Figure 5.10(c), indicate that both components become highly excited as there is no source of dissipation, hence this explores whether longer ramp times can mitigate the production of these significant density fluctuations. Ramp times of $\{10, 15, 20, 25\}$ms for both $a_{\mathrm{Cs}} = 20a_0$ and $25a_0$, are studied here.

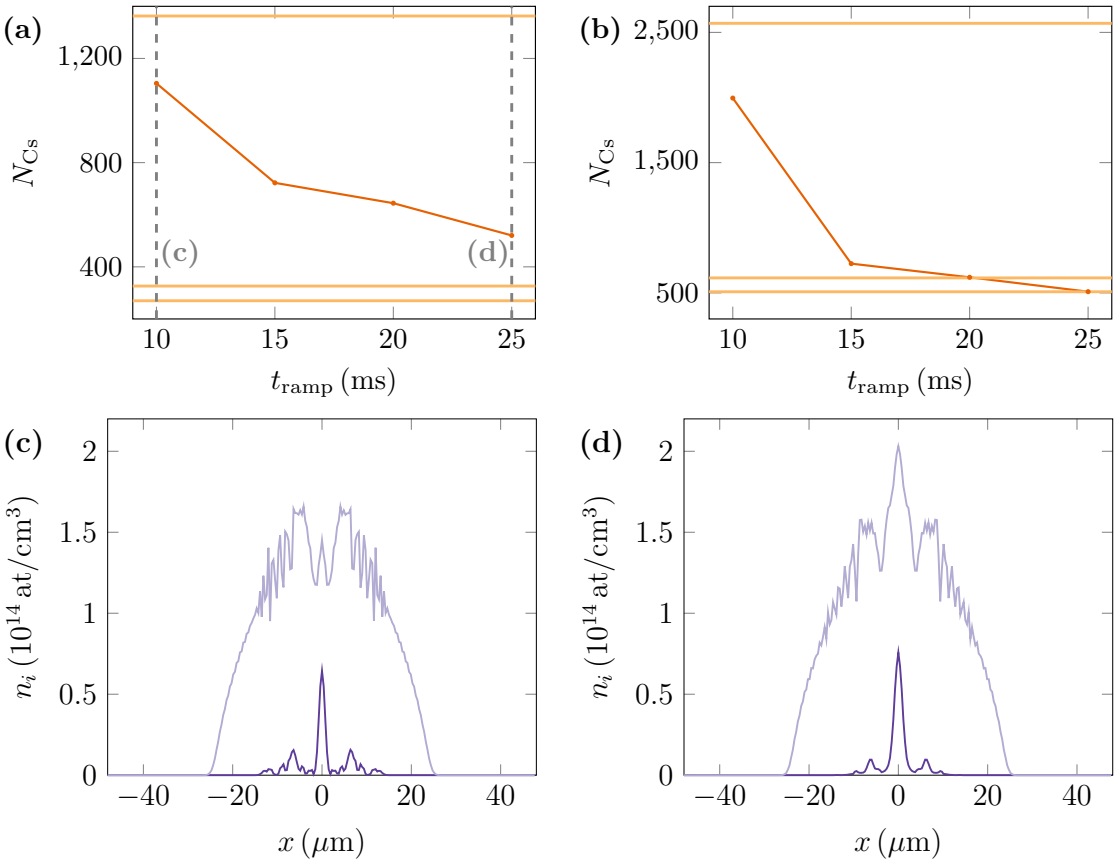

Figure 5.10: Ramping down a_{Cs} into the droplet regime. (a) and (b) Final Cs condensate number for different ramp times down to $a_{\mathrm{Cs}} = 20a_0$ and $a_{\mathrm{Cs}} = 25a_0$. The three horizontal, light orange lines show transition to non-self-evaporative droplets (top), metastable droplets (middle), and critical droplet formation (bottom). (c) and (d) 1D density slices along the long axis [here the x-axis at $(y, z) = (0, 0)$] for ramping down to $a_{\mathrm{Cs}} = 20a_0$ for 10ms and 25ms, respectively. The Cs and Yb densities given by the dark and light purple curves, respectively.

As discussed in Chapter 2, the single-component model of droplets proposed in Ref. [153] reduces the key experimental parameters (a_{11}, a_{22}, a_{12}, m_1, m_2, N_1, N_2) to a single effective atom number, $\tilde{N}$. This single parameter can be used to characterise the approximate droplet size for a given number of Cs atoms, though it is less accurate than the more general density-unlocked model [as shown in Figure 5.4(a)]. This section uses the three transition values of $\tilde{N}$ used in Section 5.1.1: $\tilde{N} = \tilde{N}_{\text{crit}} \approx 18.65$ - the minimum droplet size; $\tilde{N} = \tilde{N}_{\text{meta}} \approx 22.55$ - metastability transition; and $\tilde{N}_{\text{SE}} \approx 94.2$ - self-evaporative transition.

Figure 5.10(a) and (b) show the remaining Cs condensate atoms following a ramp of length t_{ramp} to $a_{\text{Cs}} = 20a_0$ and $a_{\text{Cs}} = 25a_0$, respectively. In the $a_{\text{Cs}} = 20a_0$ case all ramps result in population numbers within the self-evaporative regime. Whereas, for $a_{\text{Cs}} = 25a_0$, only $t_{\text{ramp}} = 10$ms and 15ms yield droplets that are above the metastable transition. Across Figure 5.10(a) and (b) no droplets are formed above the self-evaporative regime, raising questions about the effect of the high density fluctuations and excitations. When a droplet is self-evaporative, all excitations are dissipated, i.e., atoms are shed from the droplet into the surrounding system which could be a further cause of noise. In the droplet regime, three-body losses in the Cs component will increase causing a release of Yb atoms to preserve an approximate population balance. Thus, pairing losses with the self-evaporation property could lead to significant excitations and atom shedding, focused around the trap centre.

Figure 5.10(c) and (d) show two example $a_{\text{Cs}} = 20a_0$ simulations for the 10ms and 25ms ramp, indicating that the system suffers from excitations and large density fluctuations without a very distinguishable 'droplet' profile in the Cs component. Both ramps lead to these large significant excitations and potentially very small droplets, far from the flat-top density profiles that are characteristic of droplets but are yet to be experimentally observed. Recall too that the Cs condensate number in Figure 5.10 is extracted instantaneously when the linear ramp reaches the target value of a_{Cs}, and thus any further time evolution would lead to further reduction of the Cs population number.

To conclude, fast ramps are better for retaining atoms but the starting atom numbers are already very small and thus lead to very small droplets which could be hard to detect and short-lived. These results compound evidence for the Cs population number being the limiting parameter, thus even though quick ramp times may generate large density fluctuations, it seems as though the priority should be to retain as large a proportion of N_{Cs} as is possible. With the next generation of experiments there is a hope more Yb atoms will be available in the science chamber which, via sympathetic cooling [80, 102, 106, 107, 290–294], could result in a larger initial Cs population number.

5.4 Future experiments

Dynamics are of crucial interest in droplet physics and have garnered much attention in theory from collective modes [202, 204, 253, 295–297] to vortices [276, 298–307], but experimentally significant challenges remain. Droplet experiments are limited by three-body losses as droplets have significantly higher densities than ultracold gases. In most droplet experiments, the only time-dependent behaviour reported is the dynamical population loss and droplet size [168, 169, 171, 173]. The only experiment to have studied dynamics beyond this is the droplet collisions experiment of Ref. [161]. With results in heteronuclear droplets demonstrating longer lifetimes [171, 173], this section proposes some dynamics that future experiments may be able to study.

Owing to their isotropic interactions, spherically symmetric droplets are a natural starting point for two-component droplets in free space. The reduction in computational cost of simplifying the 3D system to an effective 1D system has allowed for investigation of long-time dynamics of systems that rely on large computational boxes as shown in Chapters 3 and 4. However, the following sections study 3D, non-equilbirium dynamics where the assumption of spherical symmetry breaks down.

5.4.1 Ramping trap centres

Droplets are typically formed in experiments by preparing the mixture in a trap and varying the applied magnetic field to alter the inter or intraspecies scattering length via a Feshbach resonance. As shown in Section 5.3, linearly ramping the scattering length creates significant density fluctuations and hence high losses. This section introduces the idea of gradually overlapping two attractive gases such that the gases eventually equilibrate to form a droplet. Beyond just being a proposed method for droplet formation, this potential experiment is also of interest as it highlights the transition from gas to liquid in a unique way. When separate the two components are gases; the liquid droplet only exists when the two components overlap, and as shown by the assumptions of the density-locked model, the two components are tightly bound together. Hence, trapping each component offers a method for studying how the two-components interact and allows for some control over the individual component dynamics, since as shown by Ref. [204] out-of-phase droplet dynamics are typically high energy.

To initialise the system as two separate gases, the mixture is configured with potentials

$$V_{\pm} = \frac{1}{2}\left[\omega_x \left(x \pm x_0(t)\right)^2 + \omega_y y^2 + \omega_z z^2\right],$$

where $x_0(t = 0) = 16$, with component-1 and component-2 trapped by V_+ and V_-, respectively. The initial configuration of the system is given in the top panel of Figure 5.11, in which density isosurfaces are shown at 10% of the peak density. The trap positions are changed by linearly ramping to $x_0 = 0$; once the traps fully overlap both are instantaneously switched off. After a small change in the trap separation, the two components

make contact and due to the interspecies attraction rush together as shown by the second frame of Figure 5.11. This rushing together is highlighted in Figure 5.12 which shows the average x position of each component computed as

$$\langle x \rangle = \frac{\int \mathrm{d}^3\mathbf{r}\, \Psi_i^* x \Psi_i}{\int \mathrm{d}^3\mathbf{r} |\Psi_i|^2},$$

with $\langle x \rangle$ for component 1 and 2 given by the dark orange and purple curves of Figure 5.12, respectively. The light orange and purple lines show the linearly ramped trap centres, and the vertical dashed, grey line shows the time at which the trap centres are switched off. At early times the components move at a slower rate than the trap centres, until the components make contact and they rush together moving at a much higher rate than the linear ramp. At approximately $t = 30$, the coming together of the components is slowed as the component traps are still relatively far apart, i.e., the fluids are rushing together towards $x = 0$ but this is counteracted by the potential energy of the trap in which each component should sit in the trap minimum. This can be seen by the third panel of Figure 5.11 in which a large proportion of each components has condensed to form a droplet but there is still a significant unbound gas either side of the droplet core.

At small trap separations, the majority of the two gases are condensed into the droplet; however, as there is no dissipation in the zero-temperature GP equations, high momentum excitations surround the droplet and are focused by the trap, shown by the fourth panel of Figure 5.11. Following the trap release the droplet in the final frame of Figure 5.11 appears to shed these high momentum excitations, though lower momentum surface modes remain. Due to the finite size of the computational box, there will always be residual excitations reflected from the boundaries. After the trap release the average x-position in Figure 5.12 continues to vary, and this effect is because the significant excitations during the droplet formation have averaged out to give an overall trajectory to the droplet. Though this process suggests a different way of producing droplets than the typical way of tuning the scattering length of overlapping gases, the dynamics of this trap ramping procedure is similar to a counterflow between the two fluids.

Counterflows have long been studied in superfluids, beginning with thermal counterflows in liquid Helium experiments generated by a heated wire [308–311]. More recently, superfluid counterflows have been studied theoretically within quantum gases, in particular two-component Bose-Bose [312, 313] and Bose-Fermi [314] mixtures, and multi-component spinor gases [315]. For experiments, these controllable systems allow for the study of counterflow instabilities in various dimensions. For example, in a quasi-1D geometry, the counterflow leads to a large production of solitons [130, 131, 312], likewise 2D solitons eventually decay due to the snake instability [55, 316–318] producing vortex pairs [312], whereas in 3D, theoretical studies have shown the instability produces vortex rings [313], resulting in a turbulent quantum fluid.

An example of some of the non-equilibrium dynamics are given in Figure 5.13 which

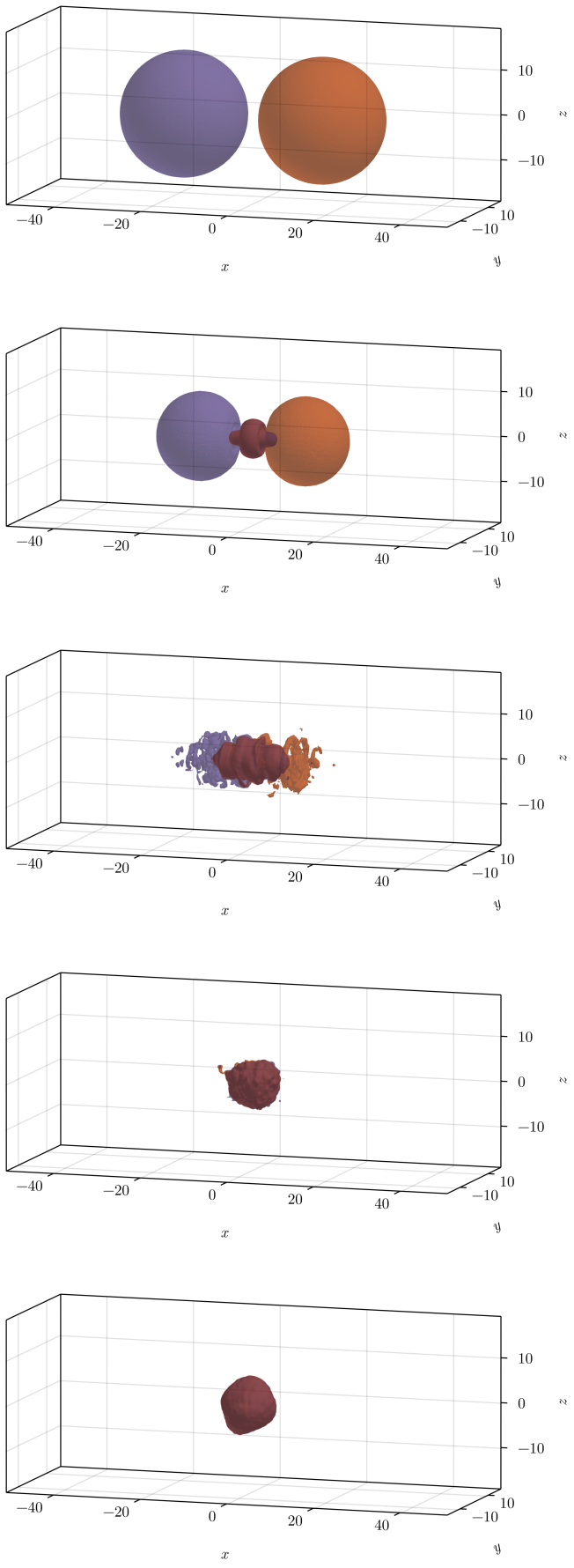

Figure 5.11: Density isosurfaces for both components, at 10% of the maximum density, ramping together trap centres at times $t = \{0.246, 32.387, 67.379, 126.995, 160.691\}$ from the top panel to the bottom.

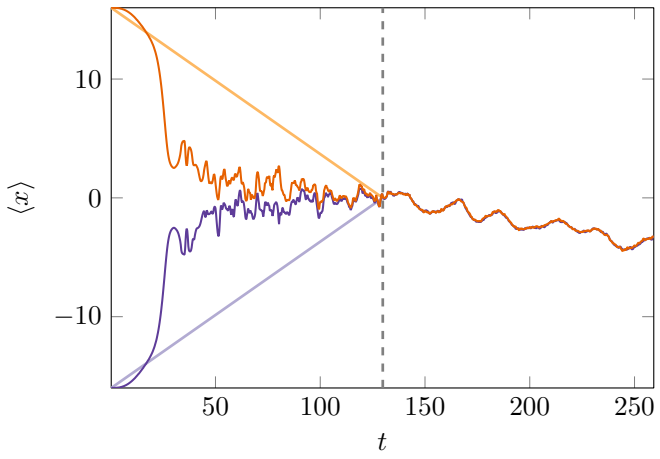

Figure 5.12: Average x-position, $\langle x \rangle$, for component 1 and 2 given by the dark orange and purple curves, respectively. The linear ramp of the trap centres is given by light orange and purple lines, whilst the vertical, grey line corresponds to the instantaneous trap switch off.

shows a slice in the xy-plane ($z = 0$). The top two panels of Figure 5.13 show the density deviations from the ground state of components 1 (top) and 2 (bottom), whilst the bottom two panels show the phases of each component. Close to $x = 0$, the top panels of Figure 5.13 show two small density depletions which in the phase correspond to two singularities surrounded by a 2π phase winding indicative of a vortex dipole in 2D, however, as this is just within the xy-plane, this dipole corresponds to a vortex ring in 3D.

The droplet counterflow problem therefore appears to be a platform for studying a variety of interesting dynamics. For example, the problem could be studied in lower dimensions creating solitons and vortex dipoles. Similarly, the creation and decay of non-linear waves and vortex rings could be studied by extracting the energy spectra and vortex line-length decay, as the formation of the high-density droplet core appears to dissipate these excitations. Dissipation is always a point of interest in two-component droplet physics, and likewise these attractive counterflows may be influenced by the size of the final droplet state, i.e., what is the effect on the creation and dissipation of these excitations of being in either the self-evaporative or non-self-evaporative regime

In summary, initialising the scattering lengths within the droplet regime and gradually bringing together the two isolated gases is another potential method for droplet formation. The dynamics of this process is also of interest as it is akin to a counterflow problem, and results in a large production of non-linear waves and vortex rings. This method is suggested here as a potential future study for the CsYb experiment, since in Ref. [219] it is shown that dynamics have been explored within the gaseous CsYb mixture by shifting the Cs component in z, out of the Yb plane to generate oscillations. Hence, by initialising the Cs component vertically above the Yb component and linearly ramping these traps together, a similar process as discussed here may be observed. Further theoretical analysis of this experiment would be needed such as adding the effects of three-body losses to see

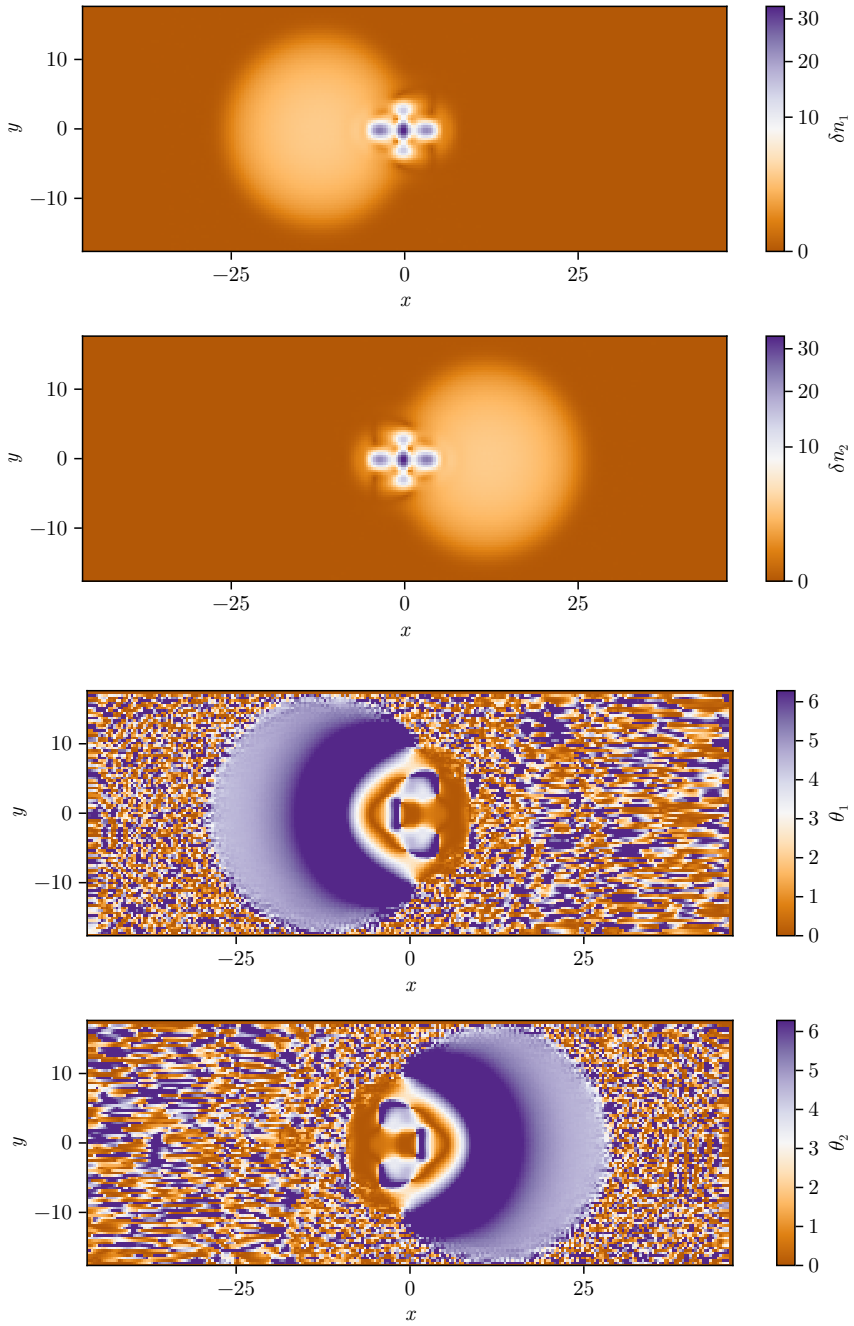

Figure 5.13: Slices in the xy-plane of density (top, two panels) and phase (bottom, two panels), at time $t \approx 32.387$. The densities shown are the deviations from the ground state, i.e., $\delta n_i = n_i - n_i^{(\mathrm{gs})}$, where $n_i^{(\mathrm{gs})}$ is the ground state density. The density deviations are shown on a square root scale, to emphasise low and high density regions. The phase has a bounded domain $\theta_i \in [0, 2\pi)$.

whether this method is a more efficient way of producing droplets, or how the anisotropic traps affect the dynamics.

5.4.2 Driving surface modes

Collective modes have been a mainstay in the study of quantum gases, but are yet to be experimentally observed in quantum droplets. Thus experimental measurements of collective modes and the droplet dispersion relation are crucial for the study of droplet physics. This section discusses the idea of driving surface modes by oscillating the applied trap.

To drive the surface mode resonance, the trap frequency oscillates in the x-direction by

$$V_i = \frac{1}{2}\left[\{1+\varepsilon\sin(\omega_d t)\}^2\,\omega_x^2 x^2 + \omega_y y^2 + \omega_z z^2\right],$$

in which $\varepsilon = 0.01$ here. For an example of surface mode resonances, this section again fixes the droplet size to be $\tilde{N} \approx 649$, as used throughout Chapter 4; similarly only isotropic traps are considered here with $\omega_{x,y,z} \approx 0.181$, so that the BdG analysis presented in Figure 4.3(b) is relevant and hence the mode frequencies are known.

The left-hand column of Figure 5.14 shows density isosurfaces at 10% of the maximum density for driving the quadrupole mode, $\omega_d \approx 0.3$, on resonance. The right-hand column of Figure 5.14 shows a 2D slice in the $z = 0$ plane of deviations from the ground state density, $\delta n_1 = n_1 - n_1^{(\mathrm{gs})}$, for component-1 only though both components oscillate in-phase and so this is identical to component-2. At early times, given in the upper two rows, the droplet oscillates between an oblate density in the yz-plane and an prolate density distribution along the x-axis. For example in the top row, the oscillations along x and y are out-of-phase in the 2D plane, but as the droplet expands in y (given by the purple regime) there is also an expansion along the z-axis shown by the isosurface. Therefore, oscillations along the y and z axes are in-phase but have a phase offset of π with the oscillations along the x-axis, indicative of a quadrupole mode. However, driving this resonance further leads to the excitation of further non-linear modes shown at later times in the bottom two roles of Figure 5.14, in which more exotic surface oscillations can be seen. In particular the xy-slices two a variety of surface and bulk excitations.

By oscillating the trap frequency in x at distinct frequencies, two surface modes can be excited: the breathing mode, $l = 0$, and quadrupole mode, $l = 2$, whose associated energies in time are given by the dark orange and purple curves in Figure 5.15. The $l = 0$ and $l = 2$ modes are driven by $\omega_d = 0.76$ and $\omega_d = 0.3$, respectively, whilst a reference 'off-resonance' simulation is given by the light purple curve in Figure 5.15 driving at $\omega_d = 0.5$. Before propagating the ground state in real time, 1% of Gaussian noise is added to both wavefunctions to break the symmetry of the two components. This noise will by definition contain contributions which are shorter wavelength than the computational grid resolution and is the cause of the initial drop in energy seen in all three energy curves in Figure 5.15.

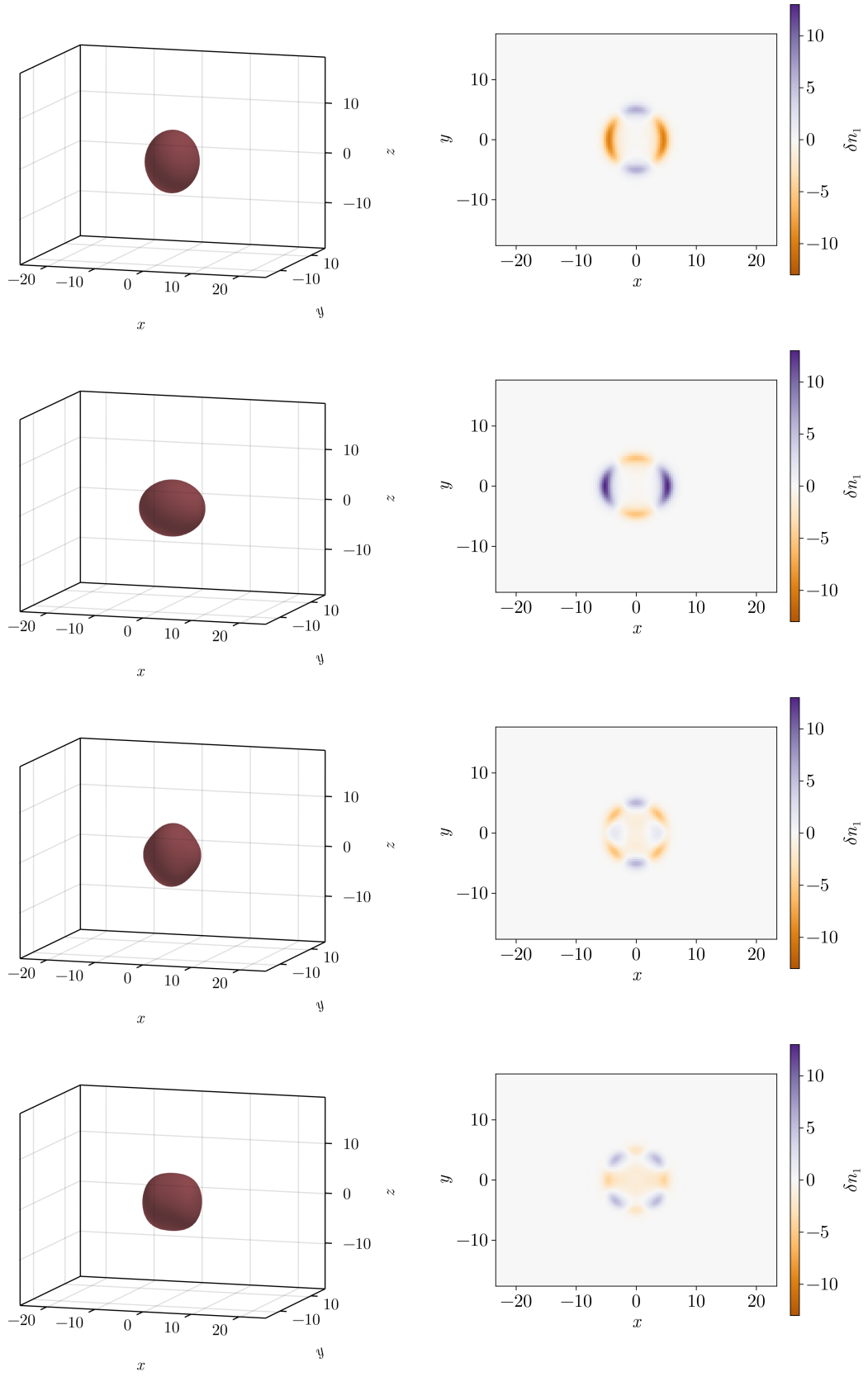

Figure 5.14: Density isosurfaces at 10% of peak density in the light column and xy-slices of the density deviations $\delta n_1 = n_1 - n_1^{(\mathrm{gs})}$, for component-1, whilst driving the quadrupole mode, $\omega_d = 0.36$, at $t \approx \{180.131, 191.147, 602.627, 609.107\}$.

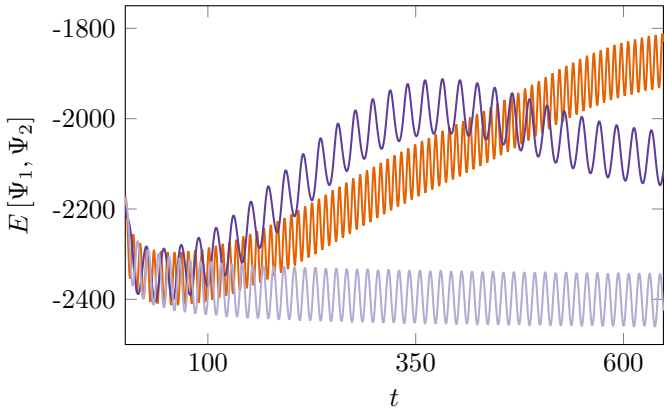

Figure 5.15: Energy in time for driving the quadrupole ($\omega_d \approx 0.3$) and breathing mode ($\omega_d \approx 0.76$), on resonance in dark purple and orange respectively, compared to an off-resonance driving ($\omega_d \approx 0.5$) in light purple.

For $l \notin \{0, 2\}$ this work finds that these modes cannot be excited by simply oscillating the trap frequency, but could be exciting by oscillating an applied potential of the form of the associated spherical harmonic, $Y_{lm}(\theta, \phi)$, which are degenerate in m. Experimentally driving a potential in the form of a spherical harmonic is not realistic, but the $l = \{0, 2\}$ dynamics could be triggered either by oscillating the trap, as shown here, or by oscillating the scattering length [319–321].

Finally, whilst this section has explored driving individual surface modes, future work could include measuring the full dispersion relation of the droplet. One method for this would be Bragg spectroscopy [322] which has been used in cold atom physics for a number of years [323], both theoretically [324–326] and experimentally to explore excitations of Bose-condensed gases [237, 327–329], with a review of these early experiments given in Ref. [330]. Two-photon Bragg spectroscopy works by shining two beams onto the cloud giving an overall momentum of $\hbar k$, in which the momentum can be tuned via the angle between the beams. Having worked through the BdG analysis in Chapter 2, the quasiparticle frequencies and wavefunctions can be used to build the dynamic structure factor, resulting in the full droplet dispersion relation as shown for a dipolar Bose gas in Ref. [331]. Bragg spectroscopy could be used as indirect evidence for a droplet, e.g., the CsYb droplets appear to be very small which could prove difficult for current imaging apparatus. Therefore by instead measuring the droplet excitation spectrum, and validating against theoretical predictions, existence of the droplet can be evidenced without a direct image.

5.5 Discussion and conclusions

By exploring the CsYb parameter space, this chapter has shown that there are complications in creating droplets with the current experimental setup. Pairing high three-body losses with small and hence dense droplets, leads to droplets that are small and difficult to observe, with extremely small lifetimes (less than 1ms). The high peak densities

could be somewhat mitigated by reducing to 2D in which the droplet can be formed for parameters more amenable to lower densities. Beyond just the size and lifetimes of the droplets, this chapter also explored whether droplets can even be formed in the first place by simulating linear ramps into the droplet regime. However, due to the three-body losses and large density fluctuations produced by the quench, no current evidence for droplets can be found from previous CsYb experiments. Looking to the future, this chapter has proposed some experimental procedures to explore the excitations and non-equilibrium dynamics of droplets with a view to measure the droplet excitation spectrum, potentially offering a method to indirectly evidence the CsYb droplet.

This work suggests that the successful production of CsYb droplets may be aided by: increasing the initial Cs population number via sympathetic cooling; reducing the dimensionality down to 2D in order to increase the parameter space that supports droplets; and, finally, finer control over a_{Cs} near the droplet transition to reduce the peak densities as much as possible to create larger, less dense and hence longer-lived droplets.

Chapter 6

Conclusion and future work

6.1 Conclusion

The focus of this thesis has been imbalances within two-component, quantum droplets. Studying imbalances is motivated by a link to an attractive experimental CsYb mixture that exhibits imbalances of: populations, trapping potentials, intraspecies scattering lengths and atomic masses.

To model quantum droplets this thesis has worked in the zero-temperature limit, using the Beyond-Mean-Field (BMF) Gross-Pitaevskii (GP) theory which includes contributions from two-body interactions and quantum fluctuations, described to first order by the zero-point energy of Bogoliubov quasiparticles. As droplets tend to preserve a constant density ratio during formation, a common approximation is to model the mixture by a single component. A natural question is how robust is this single-component model under inter-component imbalances or broken symmetries.

Firstly, population imbalances can be supported within the droplet core leading to a decrease in total energy but a gain in the energy per particle, i.e., imbalanced droplets are less stably bound. The imbalance can be supported up to a saturation limit associated with the majority component chemical potential reaching zero. Beyond this limit any further atoms are unbound and are either lost in free space, or are retained as a surrounding gas within a trap. The dynamics studied here are principally breathing modes and, as imbalanced droplets are less stably bound, there is an increased parameter space of unstable decaying modes. The time dependent behaviour of these modes is split into early and late time dynamics with early times dominated by an initial breathing mode frequency, followed by a superposition of two late time modes corresponding to the chemical potentials of each component.

Within a harmonic trap, the breathing mode dynamics are limited in time since any decaying mode sheds atoms which are then refocused by the trap back toward the droplet. The subsequent absorption of these refocused atoms reinitialises the decaying mode; however, with an imbalance this reabsorption causes significant density fluctuations making it difficult to observe longer time dynamics. Thus, for increasing trap frequencies the time

between recombination events decreases and so observing each of the three modes of an imbalanced droplet becomes impossible. At fixed trap frequency but varying imbalance, the higher the unbound gas density, the lower the decay rate, i.e., the unbound atoms appear to resist the atom shedding from the droplet.

As droplets are formed in traps, and predominantly are initialised with a population imbalance, this thesis studied whether the imbalance can be retained under a release into free space. In brief, imbalances can be retained so long as the release does not cause significant excitation of the droplet. This can be achieved by an instantaneous release from a relatively low frequency trap; higher frequency traps can also be used so as long as they are slowly ramped off. Therefore, if imbalances can be retained, and most droplets are formed from imbalanced gases, then imbalanced droplets may be most common in realistic experiments.

Secondly, imbalanced harmonic traps were studied by taking the limiting case of trapping one component in an isotropic, harmonic trap whilst the other component remains untrapped. Due to the strong binding between the components, the trapped component tends to 'drag' the other component with it, i.e., squeezing the untrapped component such that, up to a small correction, both components behave as if they are trapped.

Thirdly, imbalanced intraspecies scattering lengths were found to not be accurately described by the single-component model as this approach loses information on the density profile of each component. In this case, even with balanced populations, the density profile of each component is distinct; they are hence not simply constant rescalings of one another and therefore cannot be described by a single-component model. In the case of significant imbalanced scattering lengths, as in the CsYb mixture, the more internally repulsive component cannot support a large imbalance. In the CsYb droplet, there is a large Yb imbalance; however, because Yb is the more repulsive component the droplets can be roughly approximated as a balanced droplet surrounded by an unbound Yb gas.

Fourthly, mass imbalances were considered in the context of the CsYb mixture, though as the mass ratio of CsYb is close to one, the heteronuclear LHY correction can be approximated quite accurately by a functional form similar to that of homonuclear mixtures. The production of droplets in the CsYb mixture appears to be significantly limited by the current Cs population number. The low Cs population number implies that droplets can only be produced for low a_{Cs} which corresponds to the droplets being small, relative to other droplet experiments, and hence approximately three orders of magnitude denser. The traps have little effect on the CsYb droplets as the droplets are so small, although there is a slight increase in peak densities. Lifetimes are predicted, via the addition of Cs three-body losses, to be considerably shorter than comparable experiments with other alkalis due to the high peak densities combined with the considerable Cs loss rate.

In spite of the limited lifetimes, this thesis also explored current methods of droplet production by comparing to a previous experimental protocol of ramping a_{Cs} into the droplet regime, and out again, then observing the final Cs population number. This

thesis found that the BMF-GP approach showed better agreement than the typical MF-GP theory, though with no evidence of droplet formation. Droplet formation appears to be suppressed due to losses and excitations. Hence, this thesis concludes that the focus of the CsYb experiment should be to suppress densities. To do this, this thesis suggests reducing the dimensionality to 2D, expanding the parameter space that can support droplets allowing for higher a_{Cs} to form droplets and hence reducing the densities.

Finally, with an aim of increasing the viability of CsYb droplets, this thesis finishes by proposing experimental procedures to probe non-equilibrium dynamics and excitations of droplets. Rather than ramping scattering lengths into the droplet regime, this thesis proposes a system that is initialised as two separate but attractive gases that are gradually overlapped. This results in a production of non-linear waves and vortices, but also appears to be a viable way to produce droplets. Furthermore, surface excitations can be excited by resonantly driving the external trapping potential, though this could also be achieved by driving a_{Cs}.

6.2 Future work

This section discusses some potential future avenues of work, which are largely split into two main categories: further general theoretical studies of imbalances, and studies specific to modelling the CsYb mixture.

6.2.1 Two-component Bogoliubov-de Gennes

Chapter 3 demonstrated that population imbalances modify collective modes, such as increasing the regime of mode decay but also shifting the breathing mode frequency as shown in Figure 3.3(a). The imbalance dependence of collective mode frequencies could be significantly extended by solving the two-component BdG equations, given in Appendix E. Thus, the mode landscape can be mapped out across the 2D parameter space of droplet size and imbalance. This could explain why the breathing mode frequency for the non-self-evaporative droplet in Section 3.2 does not vary with imbalance, whilst the self-evaporative breathing mode frequency increases slightly with imbalance.

Two-component BdG could allow for a greater understanding of spin modes, which are high energy within balanced droplets, though are yet to be studied in imbalanced droplets. By including also intraspecies scattering length imbalances, even larger population imbalances can be engineered. Hence, it is possible that by driving the population imbalances higher, spin modes may be accessible at lower energies. This would also link to the droplet resonances discussed in Section 5.4.2, potentially allowing for resonant driving of spin modes.

In keeping with the context of systematic studies of imbalances, a related future body of work would be to focus on mass imbalances. As shown in Section 5.1.2, the effective heteronuclear LHY correction is a relatively good approximation for the CsYb mixture

since the mass ratio, $m_2/m_1 = 174/133$, is closer to one than the ^{41}K^{87}Rb and ^{23}Na^{87}Rb mixture. For example, Figure 5.2 finds that the maximum difference between the approximate and exact heteronuclear corrections for the ^{23}Na^{87}Rb mixture is approximately 12%. It would therefore be useful to solve for the full LHY correction in the heteronuclear GP equations to compare to the effective LHY correction particularly for ground states and collective excitations via BdG analysis. However, as noted Section 2.4.3 the full LHY correction is difficult to solve for as it depends on the density ratio, $n_2(\mathbf{r})/n_1(\mathbf{r})$, and so care needs to be taken for divergent limits such as, $n_1(\mathbf{r}) \to 0$.

These works would build on the results of Chapters 3 and 4 to explore how collective excitation frequencies are changed by imbalancing populations, intraspecies scattering lengths and masses.

6.2.2 Quasi-two-dimensional CsYb droplets

Chapter 5 demonstrated that droplets formed in the current CsYb would be small, dense and therefore short lived, relative to all current droplet experiments. Chapter 5 also proposed that one way to remedy some of these issues is by reducing to 2D, or quasi-2D, to suppress the droplet peak densities. Hence, a natural body of work following this prediction is to map out the droplet sizes and densities across the $(N_{\mathrm{Cs}}, a_{\mathrm{Cs}})$ parameter space, as produced in Section 5.2, but confined in the quasi-2D geometry. Once the parameter space of ground state quasi-2D CsYb droplets is mapped out, it is vital to measure the predicted lifetimes by again performing real-time dynamical simulations with the addition of three-body losses. These simulations will verify whether a reduction in dimensionality can decrease the densities and hence increase the lifetimes of CsYb droplets.

If there is evidence of longer lived droplets, then it would be beneficial to perform simulations of the a_{Cs} ramping protocols shown in Section 5.3. The results of Figure 5.10 appear to suggest that faster ramp times are more ideal but this is because the limiting behaviour of 3D droplet formation is the Cs population number. However, if this is less of a concern in quasi-2D then it is possible that slower ramps may mitigate some of the density fluctuations given in Figure 5.10.

Finally, after the analysis of the quasi-2D CsYb parameter space and formation dynamics, a further study would involve computing the CsYb droplet excitation spectrum. Building from the two-component BdG analysis discussed above, one avenue of work would be to solve the two-component BdG equations for the quasi-2D CsYb droplets. The eigenfunctions and eigenvalues of the BdG equations can be used to build the dynamic structure factor. These theoretical calculations of excitation spectrum can then be compared with experimental observations from two-photon Bragg spectroscopy as has been carried out in elongated dipolar gases [331] and in single dipolar droplets [332].

Appendix A

Lee-Huang-Yang derivation details

A.1 Interactions between zero and nonzero momentum particles

To simplify the interaction Hamiltonian several interaction cases need to be considered, listed here.

1. All particles in zero momentum state, $\mathbf{p_1} = \mathbf{p_2} = \mathbf{p_3} = \mathbf{p_4} = 0$, contribute $N_0^2 g/2V$ to the Hamiltonian. Momentum is also conserved by interaction of creation-creation and annihilation-annihilation of $\mathbf{p}$ and $-\mathbf{p}$ particles.

2. Contributions from two condensate operators have four different combinations:

   - {1,3}: $\frac{1}{2V}\sum_{\mathbf{p}\neq 0}\mathcal{V}(\mathbf{q})\sqrt{N_0}\hat{a}^\dagger_{\mathbf{p_4}}\hat{a}_{\mathbf{p_2}}\sqrt{N_0} = \frac{N_0}{2V}\sum_{\mathbf{p}\neq 0}\mathcal{V}(\mathbf{0})\hat{a}^\dagger_{\mathbf{p_2}-\mathbf{q}}\hat{a}_{\mathbf{p_2}}$
   - {1,4}: $\frac{1}{2V}\sum_{\mathbf{p}\neq 0}\mathcal{V}(\mathbf{q})\hat{a}^\dagger_{\mathbf{p_3}}\sqrt{N_0}\hat{a}_{\mathbf{p_2}}\sqrt{N_0} = \frac{N_0}{2V}\sum_{\mathbf{p}\neq 0}\mathcal{V}(\mathbf{q})\hat{a}^\dagger_{\mathbf{p_1}+\mathbf{q}}\hat{a}_{\mathbf{p_2}}$
   - {2,3}: $\frac{1}{2V}\sum_{\mathbf{p}\neq 0}\mathcal{V}(\mathbf{q})\sqrt{N_0}\hat{a}^\dagger_{\mathbf{p_4}}\sqrt{N_0}\hat{a}_{\mathbf{p_1}} = \frac{N_0}{2V}\sum_{\mathbf{p}\neq 0}\mathcal{V}(\mathbf{q})\hat{a}^\dagger_{\mathbf{p_2}-\mathbf{q}}\hat{a}_{\mathbf{p_1}}$
   - {2,4}: $\frac{1}{2V}\sum_{\mathbf{p}\neq 0}\mathcal{V}(\mathbf{q})\hat{a}^\dagger_{\mathbf{p_3}}\sqrt{N_0}\sqrt{N_0}\hat{a}_{\mathbf{p_1}} = \frac{N_0}{2V}\sum_{\mathbf{p}\neq 0}\mathcal{V}(\mathbf{0})\hat{a}^\dagger_{\mathbf{p_1}-\mathbf{q}}\hat{a}_{\mathbf{p_1}}$

   This therefore results in two contributions of the form $\frac{N_0}{2V}\sum_{\mathbf{p}\neq 0}\mathcal{V}(\mathbf{0})\hat{a}^\dagger_{\mathbf{p}}\hat{a}_{\mathbf{p}}$ and two contributions of the form $\frac{N_0}{2V}\sum_{\mathbf{p}\neq 0}\mathcal{V}(\mathbf{p})\hat{a}^\dagger_{\mathbf{p}}\hat{a}_{\mathbf{p}}$.

3. It is possible to have terms with 1 or 3 non-condensate operators but these will result in unpaired creation and annihilation operators which have zero expectation.

4. Then, likewise, reject terms with 4 non-condensate operators due to the assumption that $N_0 \gg 1$ and so will have negligible contributions.

A.2 Finding u_p and v_p

With the condition $u_p^2 - v_p^2 = 1$, define $u_p = \cosh\phi_p$ and $v_p = \sinh\phi_p$. Thus,

$$-\tilde{\varepsilon}_p\left[\cosh\phi_p \sinh\phi_p\right] + \frac{gn}{2}\left[\cosh^2\phi_p + \sinh^2\phi_p\right] = 0,$$

which via the double-angle formulae $\cosh 2\beta = \cosh^2\beta + \sinh^2\beta$ and $\sinh 2\beta = 2\cosh\beta\sinh\beta$ yields

$$-\frac{\tilde{\varepsilon}_p}{2}\sinh 2\phi_p + \frac{gn}{2}\cosh 2\phi_p = 0,$$

resulting in

$$\coth 2\phi_p = \frac{\tilde{\varepsilon}_p}{gn},$$

Next, using $\cosh^2 2\phi_p - \sinh^2 2\phi_p = 1$ and dividing by a factor of $\sinh^2 2\phi_p$ gives

$$\begin{aligned}
\coth^2 2\phi_p - 1 &= \operatorname{csch}^2 2\phi_p \\
&= \frac{1}{\sinh^2 2\phi_p} \\
&= \frac{1}{4\cosh^2\phi_p \sinh^2\phi_p} \\
&= \frac{1}{4u_p^2 v_p^2},
\end{aligned}$$

thus

$$\begin{aligned}
\frac{1}{\coth^2 2\phi_p - 1} &= 4u_p^2 v_p^2 \\
&= 4\left(1 + v_p^2\right) v_p^2 \\
&= 4\left(v_p^4 + v_p^2\right) \\
&= 4\left[\left(v_p^2 + \frac{1}{2}\right)^2 - \frac{1}{4}\right].
\end{aligned}$$

This allows v_p to be isolated

$$\begin{aligned}
v_p^2 &= \frac{1}{2}\left[\frac{\coth^2 2\phi_p}{\coth^2 2\phi_p - 1} + 1\right]^{1/2} - \frac{1}{2} \\
&= \frac{1}{2}\left[\frac{\coth^2 2\phi_p}{\coth^2 2\phi_p - 1}\right]^{1/2} - \frac{1}{2} \\
&= \frac{1}{2}\frac{\coth 2\phi_p}{\sqrt{\coth^2 2\phi_p - 1}} - \frac{1}{2} \\
&= \frac{1}{2}\left[\frac{\tilde{\varepsilon}_p/\mathcal{V}(\mathbf{p})n}{\sqrt{(\tilde{\varepsilon}_p/\mathcal{V}(\mathbf{p})n)^2 - 1}} - 1\right] \\
&= \frac{1}{2}\left[\frac{\tilde{\varepsilon}_p}{\sqrt{\tilde{\varepsilon}_p^2 - (\mathcal{V}(\mathbf{p})n)^2}} - 1\right],
\end{aligned}$$

and therefore by $u_p^2 - v_p^2 = 1$ results in

$$u_p^2 = \frac{1}{2}\left[\frac{\tilde{\varepsilon}_p}{\sqrt{\tilde{\varepsilon}_p^2 - (\mathcal{V}(\mathbf{p})n)^2}} + 1\right].$$

A.3 Bogoliubov transformation details

Substituting these expressions into Equation (2.5) gives

$$\begin{aligned}\hat{H} = \frac{\mathcal{V}(\mathbf{0})N^2}{2V} + \sum_{\mathbf{p}\neq 0}\Bigg\{ &\left(\varepsilon_p + \frac{\mathcal{V}(\mathbf{p})N}{V}\right)\left[u_p\hat{\alpha}_{\mathbf{p}}^\dagger - v_p\hat{\alpha}_{-\mathbf{p}}\right]\left[u_p\hat{\alpha}_{\mathbf{p}} - v_p\hat{\alpha}_{-\mathbf{p}}^\dagger\right] \\ &+\frac{\mathcal{V}(\mathbf{p})N}{2V}\Bigg(\left[u_p\hat{\alpha}_{\mathbf{p}}^\dagger - v_p\hat{\alpha}_{-\mathbf{p}}\right]\left[u_{-p}\hat{\alpha}_{-\mathbf{p}}^\dagger - v_{-p}\hat{\alpha}_{\mathbf{p}}\right] \\ &+\left[u_p\hat{\alpha}_{\mathbf{p}} - v_p\hat{\alpha}_{-\mathbf{p}}^\dagger\right]\left[u_{-p}\hat{\alpha}_{-\mathbf{p}}^\dagger - v_{-p}\hat{\alpha}_{\mathbf{p}}^\dagger\right]\Bigg)\Bigg\},\end{aligned}$$

which using $u_p = u_{-p}$ and $v_p = v_{-p}$ results in

$$\begin{aligned}\hat{H} = \frac{\mathcal{V}(\mathbf{0})N^2}{2V} + \sum_{\mathbf{p}\neq 0}\Bigg\{ &\left(\varepsilon_p + \frac{\mathcal{V}(\mathbf{p})N}{V}\right)\left[u_p^2\hat{\alpha}_{\mathbf{p}}^\dagger\hat{\alpha}_{\mathbf{p}} + v_p^2\hat{\alpha}_{-\mathbf{p}}\hat{\alpha}_{-\mathbf{p}}^\dagger - u_pv_p\left(\hat{\alpha}_{\mathbf{p}}^\dagger\hat{\alpha}_{-\mathbf{p}}^\dagger + \hat{\alpha}_{-\mathbf{p}}\hat{\alpha}_{\mathbf{p}}\right)\right] \\ &+\frac{\mathcal{V}(\mathbf{p})N}{2V}\Big[u_p^2\hat{\alpha}_{\mathbf{p}}^\dagger\hat{\alpha}_{-\mathbf{p}}^\dagger + v_p^2\hat{\alpha}_{-\mathbf{p}}\hat{\alpha}_{\mathbf{p}} - u_pv_p\left(\hat{\alpha}_{\mathbf{p}}^\dagger\hat{\alpha}_{\mathbf{p}} + \hat{\alpha}_{-\mathbf{p}}\hat{\alpha}_{\mathbf{p}}\right) \\ &+u_p^2\hat{\alpha}_{\mathbf{p}}\hat{\alpha}_{-\mathbf{p}} + v_p^2\hat{\alpha}_{\mathbf{p}}^\dagger\hat{\alpha}_{\mathbf{p}}^\dagger - u_pv_p\left(\hat{\alpha}_{\mathbf{p}}\hat{\alpha}_{\mathbf{p}}^\dagger + \hat{\alpha}_{-\mathbf{p}}^\dagger\hat{\alpha}_{-\mathbf{p}}\right)\Big]\Bigg\}.\end{aligned}$$

The bosonic commutation relations in Equation (2.6) define normal ordering as $\hat{\alpha}_{\mathbf{p}}\hat{\alpha}_{\mathbf{p}}^\dagger = 1 + \hat{\alpha}_{\mathbf{p}}^\dagger\hat{\alpha}_{\mathbf{p}}$, thus the Hamiltonian becomes

$$\begin{aligned}\hat{H} = \frac{\mathcal{V}(\mathbf{0})N^2}{2V} + \sum_{\mathbf{p}\neq 0}\Bigg\{ &\tilde{\varepsilon}_pu_p^2\hat{\alpha}_{\mathbf{p}}^\dagger\hat{\alpha}_{\mathbf{p}} + \tilde{\varepsilon}_pv_p^2 + \tilde{\varepsilon}_pv_p^2\hat{\alpha}_{-\mathbf{p}}^\dagger\hat{\alpha}_{-\mathbf{p}} - \tilde{\varepsilon}_pu_pv_p\hat{\alpha}_{\mathbf{p}}^\dagger\hat{\alpha}_{-\mathbf{p}}^\dagger - \tilde{\varepsilon}_pu_pv_p\hat{\alpha}_{-\mathbf{p}}\hat{\alpha}_{\mathbf{p}} \\ &+\frac{\mathcal{V}(\mathbf{p})N}{2V}\Big[u_p^2\hat{\alpha}_{\mathbf{p}}^\dagger\hat{\alpha}_{-\mathbf{p}}^\dagger + v_p^2\hat{\alpha}_{-\mathbf{p}}\hat{\alpha}_{\mathbf{p}} - u_pv_p\hat{\alpha}_{\mathbf{p}}^\dagger\hat{\alpha}_{\mathbf{p}} - u_pv_p - u_pv_p\hat{\alpha}_{-\mathbf{p}}^\dagger\hat{\alpha}_{-\mathbf{p}} \\ &+u_p^2\hat{\alpha}_{\mathbf{p}}\hat{\alpha}_{-\mathbf{p}} + v_p^2\hat{\alpha}_{-\mathbf{p}}^\dagger\hat{\alpha}_{\mathbf{p}}^\dagger - u_pv_p - u_pv_p\hat{\alpha}_{\mathbf{p}}^\dagger\hat{\alpha}_{\mathbf{p}} - u_pv_p - u_pv_p\hat{\alpha}_{-\mathbf{p}}^\dagger\hat{\alpha}_{-\mathbf{p}}\Big]\Bigg\},\end{aligned}$$

where $\tilde{\varepsilon}_p = \varepsilon_p + \mathcal{V}(\mathbf{p})N/V$. By symmetry, $\hat{\alpha}^\dagger_{-\mathbf{p}}\hat{\alpha}_{-\mathbf{p}} = \hat{\alpha}^\dagger_{\mathbf{p}}\hat{\alpha}_{\mathbf{p}}$, and collecting together like terms, the Hamiltonian simplifies to,

$$\begin{aligned}\hat{H} = \frac{\mathcal{V}(\mathbf{0})N^2}{2V} &+ \sum_{\mathbf{p}\neq 0}\left[\tilde{\varepsilon}_p v_p^2 - \frac{\mathcal{V}(\mathbf{p})N}{V}u_p v_p\right] \\ &+ \sum_{\mathbf{p}\neq 0}\left[\tilde{\varepsilon}_p\left(u_p^2+v_p^2\right) - 2\frac{\mathcal{V}(\mathbf{p})N}{V}u_p v_p\right]\hat{\alpha}^\dagger_{\mathbf{p}}\hat{\alpha}_{\mathbf{p}} \\ &+ \sum_{\mathbf{p}\neq 0}\left[-\tilde{\varepsilon}_p u_p v_p + \frac{\mathcal{V}(\mathbf{p})N}{2V}\left(u_p^2+v_p^2\right)\right]\left(\hat{\alpha}^\dagger_{\mathbf{p}}\hat{\alpha}^\dagger_{-\mathbf{p}} + \hat{\alpha}_{-\mathbf{p}}\hat{\alpha}_{\mathbf{p}}\right).\end{aligned}$$

A.4 Final integral

Beginning with the integral

$$I = \int_0^\infty \mathrm{d}x\, x^2\left(\sqrt{x^4+2x^2} - x^2 - 1 + \frac{1}{2x^2}\right),$$

which can be written as

$$\begin{aligned}I &= \int_0^\infty \mathrm{d}x\, x^2\sqrt{x^4+2x^2} + \int_0^\infty \mathrm{d}x\left(-x^4 - x^2 + \frac{1}{2}\right) \\ &= I_1 + \frac{1}{30}\left[-6x^5 - 10x^3 + 15x\right]_0^\infty,\end{aligned}$$

where $I_1 = \int_0^\infty \mathrm{d}x\left(x^2\sqrt{x^4+2x^2}\right)$. The integral I_1 can likewise be computed via the substitution $u = x^2 + 2$, which results in

$$\begin{aligned}I_1 &= \frac{1}{2}\int_0^\infty \mathrm{d}u\,\sqrt{u}(u-2) \\ &= \frac{1}{3}\left(\frac{3u}{5} - 2\right)u^{3/2} \\ &= \frac{1}{15}(3x^2-4)(x^2+2)^{3/2}.\end{aligned}$$

Thus, the total integral, I, is given by

$$I = \frac{1}{30}\left[2(x^2+2)^{3/2}(3x^2-4) - 6x^5 - 10x^3 + 15x\right]_0^\infty.$$

It is not clear how the upper limit of this function converges, however in the limit of large x an expansion of the form,

$$\begin{aligned}(x^2+2)^{3/2} &= (x^2+2)(x^2+2)^{1/2} \\ &= x(x^2+2)\left(1+\frac{2}{x^2}\right)^{1/2} \\ &= (x^3+2x)\left[1+\frac{1}{x^2}-\frac{1}{2x^4}+\frac{1}{2x^6}+\mathcal{O}\left(\frac{1}{x^8}\right)\right] \\ &= x^3+3x+\frac{3}{2x}-\frac{1}{2x^3}+\frac{1}{x^5}+\mathcal{O}\left(\frac{1}{x^7}\right),\end{aligned}$$

can be used. With some foresight this approximation can be cut to lower powers of $1/x$, i.e.,

$$\begin{aligned}2(x^2+2)^{3/2}(3x^2-4) &= 2\left[x^3+3x+\frac{3}{2x}+\mathcal{O}\left(\frac{1}{x^3}\right)\right](3x^2-4) \\ &= 6x^5+10x^3-15x+\mathcal{O}\left(\frac{1}{x}\right).\end{aligned}$$

Thus, in the limit of large x, there are no contributions to the integral, I, giving contributions only for $x=0$,

$$I=\frac{2^{7/2}}{15}.$$

Appendix B

Two-component Lee-Huang-Yang derivation details

B.1 Interactions between zero and nonzero momentum particles

To simplify the interaction Hamiltonian several interaction cases need to be considered, listed here.

1. All particles in zero momentum state, $\mathbf{p_1} = \mathbf{p_2} = \mathbf{p_3} = \mathbf{p_4} = 0$, contribute $\frac{1}{2}\sum_{\sigma\sigma'}\mathcal{V}_{\sigma\sigma'}(\mathbf{0})n_\sigma n_{\sigma'}$ to the Hamiltonian. Momentum is also conserved by interaction of creation-creation and annihilation-annihilation of $\mathbf{p}$ and $-\mathbf{p}$ particles.

2. Contributions from two condensate operators have four different combinations:

   - {1,3}: $\frac{1}{2}\sum_{\{\mathbf{p_i}\}\neq\mathbf{0}}\mathcal{V}_{\sigma\sigma'}(\mathbf{q})\sqrt{n_\sigma}\hat{a}^\dagger_{\mathbf{p_4}}\hat{a}_{\mathbf{p_2}}\sqrt{n_{\sigma'}} = \frac{1}{2}\sum_{\{\mathbf{p_i}\}\neq\mathbf{0}}\mathcal{V}_{\sigma\sigma'}(\mathbf{q})\sqrt{n_\sigma n_{\sigma'}}\hat{a}^\dagger_{\mathbf{p_1}+\mathbf{q}}\hat{a}_{\mathbf{p_2}}$
   - {1,4}: $\frac{1}{2}\sum_{\{\mathbf{p_i}\}\neq\mathbf{0}}\mathcal{V}_{\sigma\sigma'}(\mathbf{q})\hat{a}^\dagger_{\sigma,\mathbf{p_3}}\sqrt{n_{\sigma'}}\hat{a}_{\sigma,\mathbf{p_2}}\sqrt{n_{\sigma'}} = \frac{1}{2}\sum_{\{\mathbf{p_i}\}\neq\mathbf{0}}\mathcal{V}_{\sigma\sigma'}(\mathbf{0})n_{\sigma'}\hat{a}^\dagger_{\sigma,\mathbf{p_2}-\mathbf{q}}\hat{a}_{\sigma,\mathbf{p_2}}$
   - {2,3}: $\frac{1}{2}\sum_{\{\mathbf{p}\}\neq\mathbf{0}}\mathcal{V}_{\sigma\sigma'}(\mathbf{q})\sqrt{n_\sigma}\hat{a}^\dagger_{\sigma',\mathbf{p_4}}\sqrt{n_\sigma}\hat{a}_{\sigma',\mathbf{p_1}} = \frac{1}{2}\sum_{\{\mathbf{p_i}\}\neq\mathbf{0}}\mathcal{V}_{\sigma\sigma'}(\mathbf{0})n_\sigma\hat{a}^\dagger_{\sigma',\mathbf{p_1}+\mathbf{q}}\hat{a}_{\sigma',\mathbf{p_1}}$
   - {2,4}: $\frac{1}{2}\sum_{\{\mathbf{p_i}\}\neq\mathbf{0}}\mathcal{V}_{\sigma\sigma'}(\mathbf{q})\hat{a}^\dagger_{\sigma,\mathbf{p_3}}\sqrt{n_{\sigma'}}\sqrt{n_\sigma}\hat{a}_{\sigma',\mathbf{p_1}} = \frac{1}{2}\sum_{\{\mathbf{p_i}\}\neq\mathbf{0}}\mathcal{V}_{\sigma\sigma'}(\mathbf{q})\sqrt{n_\sigma n_{\sigma'}}\hat{a}^\dagger_{\sigma,\mathbf{p_2}-\mathbf{q}}\hat{a}_{\sigma',\mathbf{p_1}}$

   This therefore results in two contributions of the form $\frac{1}{2}\sum_{\mathbf{p}\neq 0}\mathcal{V}_{\sigma\sigma'}(\mathbf{0})n_\sigma\hat{a}^\dagger_{\sigma,\mathbf{p}}\hat{a}_{\sigma,\mathbf{p}}$ and two contributions of the form $\frac{1}{2}\sum_{\mathbf{p}\neq 0}\mathcal{V}_{\sigma\sigma'}(\mathbf{p})\sqrt{n_\sigma n_{\sigma'}}\hat{a}^\dagger_{\sigma,\mathbf{p}}\hat{a}_{\sigma',\mathbf{p}}$.

3. Consistent with the single-component derivation, terms with 1 or 3 non-condensate operators have zero expectation.

4. As with the single-component derivation, the Bogoliubov approximation allows for neglecting higher-order corrections, i.e., the assumption that condensate occupation is large means that corrections beyond quadratic order in operators are negligible. For more information see Ref. [153].

B.2 Matrix form of the Hamiltonian

Substituting $\hat{a}^\dagger_{\sigma,\mathbf{p}}\hat{a}_{\sigma',\mathbf{p}} = (\hat{a}^\dagger_{\sigma,\mathbf{p}}\hat{a}^\dagger_{\sigma',\mathbf{p}} + \hat{a}_{\sigma,\mathbf{p}}\hat{a}_{\sigma',\mathbf{p}} - \delta_{\sigma\sigma'})/2$ into Equation (2.13) gives

$$\begin{aligned}
\hat{H} = H_0 &+ \sum_{\mathbf{p}\neq 0}\left[\frac{p^2}{2m_1} - \mu_1 + \mathcal{V}_{11}(\mathbf{0})n_1 + \mathcal{V}_{12}(\mathbf{0})n_2\right]\hat{a}^\dagger_{1,\mathbf{p}}\hat{a}_{1,\mathbf{p}} \\
&+ \sum_{\mathbf{p}\neq\mathbf{0}}\left[\frac{p^2}{2m_2} - \mu_2 + \mathcal{V}_{22}(\mathbf{0})n_2 + \mathcal{V}_{12}(\mathbf{0})n_1\right]\hat{a}^\dagger_{2,\mathbf{p}}\hat{a}_{2,\mathbf{p}} \\
&+ \frac{1}{2}\sum_{\mathbf{p}\neq\mathbf{0}}\Bigg[\mathcal{V}_{11}(\mathbf{p})\left\{\hat{a}^\dagger_{1,\mathbf{p}}\hat{a}_{1,\mathbf{p}} + \hat{a}_{1,\mathbf{p}}\hat{a}^\dagger_{1,\mathbf{p}} - \delta_{11} + \hat{a}^\dagger_{1,\mathbf{p}}\hat{a}^\dagger_{1,-\mathbf{p}} + \hat{a}_{1,\mathbf{p}}\hat{a}_{1,-\mathbf{p}}\right\}n_1 \\
&\qquad + \mathcal{V}_{12}(\mathbf{p})\left\{\hat{a}^\dagger_{1,\mathbf{p}}\hat{a}_{2,\mathbf{p}} + \hat{a}_{1,\mathbf{p}}\hat{a}^\dagger_{2,\mathbf{p}} - \delta_{12} + \hat{a}^\dagger_{1,\mathbf{p}}\hat{a}^\dagger_{2,-\mathbf{p}} + \hat{a}_{1,\mathbf{p}}\hat{a}_{2,-\mathbf{p}}\right\}\sqrt{n_1 n_2} \\
&\qquad + \mathcal{V}_{21}(\mathbf{p})\left\{\hat{a}^\dagger_{2,\mathbf{p}}\hat{a}_{1,\mathbf{p}} + \hat{a}_{2,\mathbf{p}}\hat{a}^\dagger_{1,\mathbf{p}} - \delta_{21} + \hat{a}^\dagger_{2,\mathbf{p}}\hat{a}^\dagger_{1,-\mathbf{p}} + \hat{a}_{2,\mathbf{p}}\hat{a}_{1,-\mathbf{p}}\right\}\sqrt{n_2 n_2} \\
&\qquad + \mathcal{V}_{22}(\mathbf{p})\left\{\hat{a}^\dagger_{2,\mathbf{p}}\hat{a}_{2,\mathbf{p}} + \hat{a}_{2,\mathbf{p}}\hat{a}^\dagger_{2,\mathbf{p}} - \delta_{22} + \hat{a}^\dagger_{2,\mathbf{p}}\hat{a}^\dagger_{2,-\mathbf{p}} + \hat{a}_{2,\mathbf{p}}\hat{a}_{2,-\mathbf{p}}\right\}n_2\Bigg],
\end{aligned}$$

Recalling that the Kronecker delta has the property of $\delta_{11} = \delta_{22} = 1$ and $\delta_{12} = \delta_{21} = 0$ and using the conditions

$$\begin{aligned}
\mu_1 &= \mathcal{V}_{11}(\mathbf{0})n_1 + \mathcal{V}_{12}(\mathbf{0})n_2, \\
\mu_2 &= \mathcal{V}_{22}(\mathbf{0})n_2 + \mathcal{V}_{12}(\mathbf{0})n_1,
\end{aligned}$$

gives

$$\begin{aligned}
\hat{H} = H_0 &+ \sum_{\mathbf{p}\neq\mathbf{0}}\left[\frac{p^2}{2m_1}\hat{a}^\dagger_{1,\mathbf{p}}\hat{a}_{1,\mathbf{p}} + \frac{p^2}{2m_2}\hat{a}^\dagger_{2,\mathbf{p}}\hat{a}_{2,\mathbf{p}} - \frac{\mathcal{V}_{11}(\mathbf{p})n_1 + \mathcal{V}_{22}(\mathbf{p})n_2}{2}\right] \\
&+ \frac{1}{2}\sum_{\mathbf{p}\neq\mathbf{0}}\Bigg[\mathcal{V}_{11}(\mathbf{p})\left\{\hat{a}^\dagger_{1,\mathbf{p}}\hat{a}_{1,\mathbf{p}} + \hat{a}_{1,\mathbf{p}}\hat{a}^\dagger_{1,\mathbf{p}} + \hat{a}^\dagger_{1,\mathbf{p}}\hat{a}^\dagger_{1,-\mathbf{p}} + \hat{a}_{1,\mathbf{p}}\hat{a}_{1,-\mathbf{p}}\right\}n_1 \\
&\qquad + \mathcal{V}_{12}(\mathbf{p})\left\{\hat{a}^\dagger_{1,\mathbf{p}}\hat{a}_{2,\mathbf{p}} + \hat{a}_{1,\mathbf{p}}\hat{a}^\dagger_{2,\mathbf{p}} + \hat{a}^\dagger_{1,\mathbf{p}}\hat{a}^\dagger_{2,-\mathbf{p}} + \hat{a}_{1,\mathbf{p}}\hat{a}_{2,-\mathbf{p}}\right\}\sqrt{n_1 n_2} \\
&\qquad + \mathcal{V}_{21}(\mathbf{p})\left\{\hat{a}^\dagger_{2,\mathbf{p}}\hat{a}_{1,\mathbf{p}} + \hat{a}_{2,\mathbf{p}}\hat{a}^\dagger_{1,\mathbf{p}} + \hat{a}^\dagger_{2,\mathbf{p}}\hat{a}^\dagger_{1,-\mathbf{p}} + \hat{a}_{2,\mathbf{p}}\hat{a}_{1,-\mathbf{p}}\right\}\sqrt{n_2 n_2} \\
&\qquad + \mathcal{V}_{22}(\mathbf{p})\left\{\hat{a}^\dagger_{2,\mathbf{p}}\hat{a}_{2,\mathbf{p}} + \hat{a}_{2,\mathbf{p}}\hat{a}^\dagger_{2,\mathbf{p}} + \hat{a}^\dagger_{2,\mathbf{p}}\hat{a}^\dagger_{2,-\mathbf{p}} + \hat{a}_{2,\mathbf{p}}\hat{a}_{2,-\mathbf{p}}\right\}n_2\Bigg].
\end{aligned}$$

Next, consider the matrix form of the Hamiltonian

$$\begin{aligned}
&\frac{1}{2}\sum_{\mathbf{p}\neq 0}\left(\hat{a}^\dagger_{1,\mathbf{p}}\hat{a}^\dagger_{2,\mathbf{p}}\hat{a}_{1,-\mathbf{p}}\hat{a}_{2,-\mathbf{p}}\right)\mathcal{W}\begin{pmatrix}\hat{a}_{1,\mathbf{p}}\\ \hat{a}_{2,\mathbf{p}}\\ \hat{a}^\dagger_{1,-\mathbf{p}}\\ \hat{a}^\dagger_{2,-\mathbf{p}}\end{pmatrix}\\
&=\frac{1}{2}\sum_{\mathbf{p}\neq\mathbf{0}}\Bigg[\frac{p^2}{m_1}\hat{a}^\dagger_{1,\mathbf{p}}\hat{a}_{1,\mathbf{p}}+\frac{p^2}{m_2}\hat{a}^\dagger_{2,\mathbf{p}}\hat{a}_{2,\mathbf{p}}+\frac{p^2}{2m_1}+\frac{p^2}{2m_2}\\
&\quad+\mathcal{V}_{11}(\mathbf{p})\left\{\hat{a}^\dagger_{1,\mathbf{p}}\hat{a}_{1,\mathbf{p}}+\hat{a}_{1,\mathbf{p}}\hat{a}^\dagger_{1,\mathbf{p}}+\hat{a}^\dagger_{1,\mathbf{p}}\hat{a}^\dagger_{1,-\mathbf{p}}+\hat{a}_{1,\mathbf{p}}\hat{a}_{1,-\mathbf{p}}\right\}n_1\\
&\quad+\mathcal{V}_{12}(\mathbf{p})\left\{\hat{a}^\dagger_{1,\mathbf{p}}\hat{a}_{2,\mathbf{p}}+\hat{a}_{1,\mathbf{p}}\hat{a}^\dagger_{2,\mathbf{p}}+\hat{a}^\dagger_{1,\mathbf{p}}\hat{a}^\dagger_{2,-\mathbf{p}}+\hat{a}_{1,\mathbf{p}}\hat{a}_{2,-\mathbf{p}}\right\}\sqrt{n_1n_2}\\
&\quad+\mathcal{V}_{21}(\mathbf{p})\left\{\hat{a}^\dagger_{2,\mathbf{p}}\hat{a}_{1,\mathbf{p}}+\hat{a}_{2,\mathbf{p}}\hat{a}^\dagger_{1,\mathbf{p}}+\hat{a}^\dagger_{2,\mathbf{p}}\hat{a}^\dagger_{1,-\mathbf{p}}+\hat{a}_{2,\mathbf{p}}\hat{a}_{1,-\mathbf{p}}\right\}\sqrt{n_2n_2}\\
&\quad+\mathcal{V}_{22}(\mathbf{p})\left\{\hat{a}^\dagger_{2,\mathbf{p}}\hat{a}_{2,\mathbf{p}}+\hat{a}_{2,\mathbf{p}}\hat{a}^\dagger_{2,\mathbf{p}}+\hat{a}^\dagger_{2,\mathbf{p}}\hat{a}^\dagger_{2,-\mathbf{p}}+\hat{a}_{2,\mathbf{p}}\hat{a}_{2,-\mathbf{p}}\right\}n_2\Bigg],
\end{aligned}$$

in which the symmetries $\mathcal{V}_{12}(\mathbf{p})=\mathcal{V}_{21}(\mathbf{p})$ and $\hat{a}^\dagger_{\sigma,-\mathbf{p}}\hat{a}_{\sigma,-\mathbf{p}}=\hat{a}^\dagger_{\sigma,\mathbf{p}}\hat{a}_{\sigma,\mathbf{p}}$, and normal ordering have been used. Thus, by comparison Equation (2.13) can be written as

$$\hat{H}=H_0-\frac{1}{2}\sum_{\sigma,\mathbf{p}\neq 0}\left[\frac{p^2}{2m_\sigma}+\mathcal{V}_{\sigma\sigma}(\mathbf{p})n_\sigma\right]+\frac{1}{2}\sum_{\mathbf{p}\neq 0}\left(\hat{a}^\dagger_{1,\mathbf{p}}\hat{a}^\dagger_{2,\mathbf{p}}\hat{a}_{1,-\mathbf{p}}\hat{a}_{2,-\mathbf{p}}\right)\mathcal{W}\begin{pmatrix}\hat{a}_{1,\mathbf{p}}\\ \hat{a}_{2,\mathbf{p}}\\ \hat{a}^\dagger_{1,-\mathbf{p}}\\ \hat{a}^\dagger_{2,-\mathbf{p}}\end{pmatrix}.$$

B.3 Final integral

Beginning with integral

$$\frac{E_{\mathrm{LHY}}}{V}=\frac{1}{2}\int\frac{\mathrm{d}^3\mathbf{p}}{(2\pi\hbar)^3}\left[E_{+,p}+E_{-,p}-\frac{p^2}{2m_r}-g_{11}n_1-g_{22}n_2+\frac{m_1g_{11}^2n_1^2+m_2g_{22}^2n_2^2+4m_rg_{12}^2n_1n_2}{p^2}\right],$$

the measure can therefore be rewritten $\mathrm{d}^3\mathbf{p}\to 4\pi p^2\,\mathrm{d}p$ giving

$$\frac{E_{\mathrm{LHY}}}{V}=\frac{8}{15\pi^2}\frac{1}{\hbar^3}\frac{15}{32}\int\mathrm{d}p\,p^2\left[E_{+,p}+E_{-,p}-\frac{p^2}{2m_r}-g_{11}n_1-g_{22}n_2+\frac{m_1g_{11}^2n_1^2+m_2g_{22}^2n_2^2+4m_rg_{12}^2n_1n_2}{p^2}\right],$$

then with the substitution $p\to(g_{11}n_1m_1)^{1/2}k$ and taking out a factor of $(g_{11}n_1)^{5/2}m_1^{3/2}$ gives

$$\begin{aligned}
\frac{E_{\mathrm{LHY}}}{V}=\frac{8}{15\pi^2}\left(\frac{m_1}{\hbar^2}\right)^{3/2}(g_{11}n_1)^{5/2}\frac{15}{32}\int\mathrm{d}p\,p^2\Bigg[&\frac{E_{+,p}+E_{-,p}}{g_{11}n_1}-\frac{m_1k^2}{2m_r}-1-\frac{g_{22}n_2}{g_{11}n_1}\\
&+\frac{m_1g_{11}^2n_1^2+m_2g_{22}^2n_2^2+4m_rg_{12}^2n_1n_2}{(g_{11}^2n_1^2m_1)\,k^2}\Bigg].
\end{aligned}$$

Finally, by tidying up it is found that the integral can be written in terms of $z = m_2/m_1$, $x = g_{22}n_2/g_{11}n_1$ and $u = g_{12}^2/g_{11}g_{22}$ as shown in Equation (2.22).

Appendix C

Density-locked Gross Pitaevskii equation linearisation

Beginning with the density-locked GP equation

$$i\frac{\partial\phi}{\partial t} = \left[-\frac{\nabla^2}{2} - 3|\phi|^2 + \frac{5}{2}|\phi|^3\right]\phi,$$

the wavefunction, $\phi(\mathbf{r},t)$, can be expressed as a perturbed ground state, $\phi(\mathbf{r},t) = \phi_0(\mathbf{r},t) + \delta\phi(\mathbf{r},t)$, giving

$$\begin{aligned} i\frac{\partial\phi_0}{\partial t} + i\frac{\partial\delta\phi}{\partial t} = &-\frac{\nabla^2\phi_0}{2} - \frac{\nabla^2\delta\phi}{2} - 3\left[|\phi_0|^2 + \phi_0\delta\phi^* + \phi_0^*\delta\phi + |\delta\phi|^2\right](\phi_0 + \delta\phi) \\ &+ \frac{5}{2}\left[|\phi_0|^2 + \phi_0\delta\phi^* + \phi_0^*\delta\phi + |\delta\phi|^2\right]^{3/2}(\phi_0 + \delta\phi)\,. \end{aligned}$$

Terms of quadratic order in $\delta\phi$ must be neglected, thus

$$\begin{aligned} i\frac{\partial\phi_0}{\partial t} + i\frac{\partial\delta\phi}{\partial t} = &-\frac{\nabla^2\phi_0}{2} - \frac{\nabla^2\delta\phi}{2} - 3\left[|\phi_0|^2\phi_0 + 2|\phi_0|^2\delta\phi + \phi_0^2\delta\phi^*\right] \\ &+ \frac{5}{2}\left[|\phi_0|^2 + \phi_0\delta\phi^* + \phi_0^*\delta\phi\right]^{3/2}(\phi_0 + \delta\phi)\,. \end{aligned}$$

Focusing on the LHY contribution

$$\begin{aligned} H_{\mathrm{LHY}} &= \frac{5}{2}|\phi_0|^3\left[1 + \left(\frac{\delta\phi}{\phi_0}\right)^* + \left(\frac{\delta\phi}{\phi_0}\right)\right]^{3/2}(\phi_0 + \delta\phi) \\ &\approx \frac{5}{2}|\phi_0|^3\left[1 + \frac{3}{2}\left(\frac{\delta\phi}{\phi_0}\right)^* + \frac{3}{2}\left(\frac{\delta\phi}{\phi_0}\right)\right](\phi_0 + \delta\phi) \\ &\approx \frac{5}{2}|\phi_0|^3\phi_0 + \frac{5}{2}|\phi_0|^3\delta\phi + \frac{15}{4}\phi_0^{5/2}\left(\phi_0^*\right)^{1/2}\delta\phi^* + \frac{15}{4}\phi_0^{3/2}\left(\phi_0^*\right)^{1/2}|\delta\phi|^2 \\ &+ \frac{15}{4}\phi_0^{3/2}\left(\phi_0^*\right)^{3/2}\delta\phi + \frac{15}{4}\phi_0^{1/2}\left(\phi_0^*\right)^{3/2}\delta\phi^2, \end{aligned}$$

and again neglecting terms of quadratic order in $\delta\phi$ gives

$$H_{\mathrm{LHY}} \approx \frac{5}{2}|\phi_0|^3\phi_0 + \frac{25}{4}|\phi_0|^3\delta\phi + \frac{15}{4}\phi_0^2|\phi_0|\delta\phi^*.$$

The ground state wavefunction, $\phi_0(\mathbf{r},t)$, is a solution of the density-locked GP equation

$$i\frac{\partial\phi_0}{\partial t} = \left[-\frac{\nabla^2}{2} - 3|\phi_0|^2 + \frac{5}{2}|\phi_0|^3\right]\phi_0,$$

thus the linearised density-locked GP equation is

$$i\frac{\partial\delta\phi}{\partial t} = -\frac{\nabla^2\delta\phi}{2} - 3\left[2|\phi_0|^2\delta\phi + \phi_0^2\delta\phi^*\right] + \frac{5}{2}\left[\frac{5}{2}|\phi_0|^3\delta\phi + \frac{3}{2}\phi_0^2|\phi_0|\delta\phi^*\right],$$

and, equivalently,

$$i\frac{\partial\delta\phi^*}{\partial t} = -\frac{\nabla^2\delta\phi^*}{2} - 3\left[2|\phi_0|^2\delta\phi^* + (\phi_0^*)^2\,\delta\phi\right] + \frac{5}{2}\left[\frac{5}{2}|\phi_0|^3\delta\phi^* + \frac{3}{2}\,(\phi_0^*)^2\,|\phi_0|\delta\phi\right].$$

Appendix D

Density difference of imbalanced, infinite droplets

The density profile of a droplet in the limit of large $\tilde{N}$ approaches a flat-top, step function, i.e., a constant density in the droplet core and a steep drop to zero density at the surface [153]. This approximate form is a useful model for infinite sized droplets as it allows for kinetic energy contributions to be neglected. Figure D.1 shows a schematic of the step function model of a large imbalanced droplet, used in this derivation. The minority component is modelled as having volume $V = \frac{4}{3}\pi R^3$, whilst the majority component has volume $V + \delta V = \frac{4}{3}\pi(R + \delta R)^3$. The step functions hence correspond to the central densities n and $n + \delta n$ for the minority and majority components, respectively, with the two components normalised to N and $N + \delta N$ in which $\delta N \geq 0$, imposing the population imbalance.

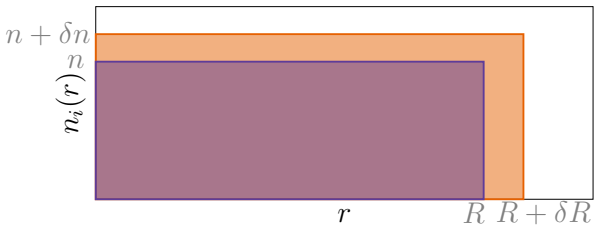

Figure D.1: Flat-top density profiles as an ansatz for each component of an imbalanced droplet. The orange component is the higher-density, majority component and the purple component is the lower-density, minority component.

The dimensionless form of the energy functional given in Equation (2.24), with $\beta \equiv \sqrt{a_{22}/a_{11}} = 1$, can be written in terms of these constant imbalanced densities giving,

$$E = \int \mathrm{d}^3\mathbf{r} \left[\frac{(n+\delta n)^2}{2} + \frac{n^2}{2} + \eta(n+\delta n)n + \frac{2}{5}\alpha\left(2n+\delta n\right)^{5/2} \right]. \tag{D.1}$$

The schematic in Figure D.1 states nothing about the sign of δR, i.e., the volume of the majority component, $V + \delta V$, can be larger or smaller than the minority component volume, V. However, it can be shown that the only physical system is that where $\delta V = 0$,

which is demonstrated in the following calculation.

Beginning with the $\delta V > 0$ case, Equation (D.1) can be written in terms of the component volumes and population numbers as,

$$E = \frac{(N+\delta N)^2}{2(V+\delta V)} + \frac{N^2}{2V} + \eta\frac{N(N+\delta N)}{V+\delta V} + \frac{2}{5}\alpha\left\{V\left[\frac{N+\delta N}{V+\delta V} + \frac{N}{V}\right]^{5/2} + \delta V\left[\frac{N+\delta N}{V+\delta V}\right]^{5/2}\right\}.$$

To analyse how the energy of this model varies with δV, the energy above can be minimised with respect to the difference in component volumes, giving,

$$\begin{aligned}\frac{\partial E}{\partial(\delta V)} = &-\frac{(N+\delta N)^2}{2(V+\delta V)^2} - \eta\frac{N(N+\delta N)}{(V+\delta V)^2} \\ &+ \frac{2}{5}\alpha\left\{-\frac{5}{2}\frac{V(N+\delta N)}{(V+\delta V)^2}\left[\frac{N+\delta N}{V+\delta V} + \frac{N}{V}\right]^{3/2}\right. \\ &\left.+ \left[\frac{N+\delta N}{V+\delta V}\right]^{5/2} - \frac{5}{2}\delta V\frac{(N+\delta N)^{5/2}}{(V+\delta V)^{7/2}}\right\}.\end{aligned}$$

Taking the limit of $\delta V \to 0^+$ reduces to,

$$\begin{aligned}\left.\frac{\partial E}{\partial(\delta V)}\right|_{\delta V\to 0^+} = &-\frac{(N+\delta N)^2}{2V^2} - \eta\frac{N(N+\delta N)}{V^2} \\ &+ \alpha\left\{-\frac{(N+\delta N)}{V}\left[\frac{2N+\delta N}{V}\right]^{3/2}\right. \\ &\left.+ \frac{2}{5}\left[\frac{N+\delta N}{V}\right]^{5/2}\right\},\end{aligned}$$

which can be written in the form,

$$\left.\frac{\partial E}{\partial(\delta V)}\right|_{\delta V\to 0^+} = -\frac{N+\delta N}{2V^2}\left[(1+2\eta)N + \delta N\right] + \mathcal{O}(\alpha).$$

Recall from Chapter 2 that $\delta a = a_{12} + \sqrt{a_{11}a_{22}}$, and that defining $\delta a < 0$ implies dominantly attractive interactions, which can be written as $\eta < -1$ in the dimensionless parameters used here. Thus, with δN small, the mean-field terms becomes dominantly positive whilst the LHY contributions are small due to $\alpha \ll 1$. Hence, the limit of $\delta V \to 0^+$ yields, $\partial E/\partial(\delta V) \geq 0$.

The next case to check is $\delta V < 0$, for which Equation (D.1) takes the form,

$$E = \frac{(N+\delta N)^2}{2(V+\delta V)} + \frac{N^2}{2V} + \eta\frac{N(N+\delta N)}{V} + \frac{2}{5}\alpha\left\{(V+\delta V)\left[\frac{N+\delta N}{V+\delta V} + \frac{N}{V}\right]^{5/2} - \delta V\left[\frac{N}{V}\right]^{5/2}\right\}.$$

This expression is again minimised with respect to the difference in component volumes,

$$\frac{\partial E}{\partial(\delta V)} = -\frac{(N+\delta N)^2}{2(V+\delta V)^2} + \frac{2}{5}\alpha\Bigg\{\left[\frac{N+\delta N}{V+\delta V}+\frac{N}{V}\right]^{5/2} - \frac{5}{2}\frac{(N+\delta N)}{V+\delta V}\left[\frac{N+\delta N}{V+\delta V}+\frac{N}{V}\right]^{3/2} - \left(\frac{N}{V}\right)^{5/2}\Bigg\}.$$

Taking the limit of $\delta V \to 0^-$ yields,

$$\left.\frac{\partial E}{\partial(\delta V)}\right|_{\delta V\to 0^-} = -\frac{(N+\delta N)^2}{2V^2} + \alpha\Bigg\{\frac{2}{5}\left[\frac{2N+\delta N}{V}\right]^{5/2} - \frac{N+\delta N}{V}\left[\frac{2N+\delta N}{V}\right]^{3/2} - \frac{2}{5}\left(\frac{N}{V}\right)^{5/2}\Bigg\},$$

which can be written in the form,

$$\left.\frac{\partial E}{\partial(\delta V)}\right|_{\delta V\to 0^-} = -\frac{(N+\delta N)^2}{2V} + \mathcal{O}(\alpha).$$

Hence, the limit of $\delta V \to 0^-$ results in, $\partial E/\partial(\delta V) \leq 0$. Thus, the conditions

$$\left.\frac{\partial E}{\partial(\delta V)}\right|_{\delta V\to 0^+} \geq 0, \text{ and, } \left.\frac{\partial E}{\partial(\delta V)}\right|_{\delta V\to 0^-} \leq 0,$$

imply that $\delta V = 0$ is either a smooth minimum or a cusp. This is physically realistic in the limit of large droplets, as this implies that the radii of the two components are equal, i.e., no single-component atoms reside outside of the droplet core. However, in the finite droplet limit this is not the case as kinetic energy contributions cannot be neglected, as is highlighted in the ground state profiles in Figure 3.2 (b) and (c). The imbalanced droplet hence appears to slowly approach the flat-top density profile, relative to the rate at which the large, balanced droplet approaches the flat-top density limit.

Taking the case of $\delta V = 0$, the energy can be written as,

$$\frac{E}{2N} = \frac{(N+\delta N)^2}{4NV} + \frac{N}{4V} + \eta\frac{N+\delta N}{2V} + \frac{2}{5}\alpha\left[\frac{V}{2N}\left(\frac{2N+\delta N}{V}\right)^{5/2}\right].$$

A factor of $(1+\delta N/2N)$ can be factored out of this expression, allowing for the above equation to be written in powers of (N/V),

$$\frac{E}{2N} = \left(1+\frac{\delta N}{2N}\right)\left[\mathcal{A}\left(\frac{N}{V}\right) + \mathcal{B}\left(\frac{N}{V}\right)^{3/2}\right],$$

where

$$\mathcal{A} = \left(1+\frac{\delta N}{2N}\right) + (\eta-1) + \frac{1-\eta}{2}\left(\frac{1}{1+\frac{\delta N}{2N}}\right),$$

and

$$\mathcal{B} = \frac{4\sqrt{2}\alpha}{5}\left(1+\frac{\delta N}{2N}\right)^{3/2}.$$

Chapter 2 discusses the key property that droplets exist in equilibrium with the vacuum, i.e., they have zero pressure, $\partial E/\partial V = 0$. With N constant, this expression for the zero pressure droplet can be rewritten as $\partial(E/2N)/\partial(N/V) = 0$, yielding,

$$\left(\frac{N}{V}\right)^{1/2} = -\frac{2\mathcal{A}}{3\mathcal{B}} \implies n = \left(\frac{N}{V}\right) = \frac{4\mathcal{A}^2}{9\mathcal{B}^2},$$

giving an expression for the equilibrium density. This results in the equilibrium energy, given by,

$$E_{\text{eqbm}} = (2N+\delta N)\left[\frac{4\mathcal{A}^3}{27\mathcal{B}^2}\right], \tag{D.2}$$

or equivalently as the equilibrium energy per particle,

$$\left(\frac{E}{2N+\delta N}\right)_{\text{eqbm}} = \frac{4\mathcal{A}^3}{27\mathcal{B}^2}. \tag{D.3}$$

For fixed α, η and N, Equations D.2 and D.3 are plotted as functions of δN in Figure 3.1. The main plot in Figure 3.1 shows Equation (D.2) varying with δN. By differentiating Equation (D.2), the minimum is located at

$$\frac{\delta N}{N} = 2(\eta-2) + [(\eta-1)(4\eta-14)]^{1/2}.$$

For the parameters of Figure 3.1 the minimum is at $\delta N \approx 703$, which using the expression,

$$\delta n = \frac{\delta N}{N}\left(\frac{4\mathcal{A}^2}{9\mathcal{B}^2}\right),$$

corresponds to $\delta n \approx 0.458$, i.e., the orange, dashed, horizontal line in the inset of Figure 3.2(d).

Appendix E

Two-component, beyond-mean-field Bogoliubov-de Gennes equations

E.1 Density-unlocked Gross Pitaevskii equation linearisation

The dimensionless, effective, heteronuclear GP equations are

$$
\begin{aligned}
i\frac{\partial \Psi_1}{\partial t} &= \left[-\frac{\gamma}{2}\nabla^2 + |\Psi_1|^2 + \eta|\Psi_2|^2 + \alpha\left(|\Psi_1|^2 + z^{3/5}\beta|\Psi_2|^2\right)^{3/2}\right]\Psi_1, \\
i\frac{\partial \Psi_2}{\partial t} &= \left[-\frac{\gamma}{2z}\nabla^2 + \beta|\Psi_2|^2 + \eta\beta|\Psi_1|^2 + \alpha z^{3/5}\beta^2\left(|\Psi_1|^2 + z^{3/5}\beta|\Psi_2|^2\right)^{3/2}\right]\Psi_2,
\end{aligned}
$$

reducing to the homonuclear GP equations under $\gamma, z \to 1$. The wavefunctions, $\Psi_i(\mathbf{r}, t)$, can be expressed as a perturbed ground state, $\Psi_i(\mathbf{r}, t) = \Psi_{i,0}(\mathbf{r}, t) + \delta\Psi_i(\mathbf{r}, t)$, giving

$$
\begin{aligned}
i\frac{\partial \Psi_{1,0}}{\partial t} + i\frac{\partial \delta\Psi_1}{\partial t} &= -\frac{\gamma\nabla^2\Psi_{1,0}}{2} - \frac{\gamma\nabla^2\delta\Psi_1}{2} \\
&\quad + \left(|\Psi_{1,0}|^2 + \Psi_{1,0}\delta\Psi_1^* + \delta\Psi_1\Psi_{1,0}^* + |\delta\Psi_1|^2\right)(\Psi_{1,0} + \delta\Psi_1) \\
&\quad + \eta\left(|\Psi_{2,0}|^2 + \Psi_{2,0}\delta\Psi_2^* + \delta\Psi_2\Psi_{2,0}^* + |\delta\Psi_2|^2\right)(\Psi_{1,0} + \delta\Psi_1) \\
&\quad + \alpha\Big[\left(|\Psi_{1,0}|^2 + \Psi_{1,0}\delta\Psi_1^* + \delta\Psi_1\Psi_{1,0}^* + |\delta\Psi_1|^2\right) \\
&\qquad + z^{3/5}\beta\left(|\Psi_{2,0}|^2 + \Psi_{2,0}\delta\Psi_2^* + \delta\Psi_2\Psi_{2,0}^* + |\delta\Psi_2|^2\right)\Big]^{3/2}(\Psi_{1,0} + \delta\Psi_1),
\end{aligned}
$$

$$
\begin{aligned}
i\frac{\partial \Psi_{2,0}}{\partial t} + i\frac{\partial \delta\Psi_2}{\partial t} &= -\frac{\gamma\nabla^2\Psi_{2,0}}{22} - \frac{\gamma\nabla^2\delta\Psi_2}{2z} \\
&\quad + \beta\left(|\Psi_{2,0}|^2 + \Psi_{2,0}\delta\Psi_2^* + \delta\Psi_2\Psi_{2,0}^* + |\delta\Psi_2|^2\right)(\Psi_{2,0} + \delta\Psi_2) \\
&\quad + \eta\beta\left(|\Psi_{1,0}|^2 + \Psi_{1,0}\delta\Psi_1^* + \delta\Psi_1\Psi_{1,0}^* + |\delta\Psi_1|^2\right)(\Psi_{2,0} + \delta\Psi_2) \\
&\quad + \alpha z^{3/5}\beta^2\Big[\left(|\Psi_{1,0}|^2 + \Psi_{1,0}\delta\Psi_1^* + \delta\Psi_1\Psi_{1,0}^* + |\delta\Psi_1|^2\right) \\
&\qquad + z^{3/5}\beta\left(|\Psi_{2,0}|^2 + \Psi_{2,0}\delta\Psi_2^* + \delta\Psi_2\Psi_{2,0}^* + |\delta\Psi_2|^2\right)\Big]^{3/2}(\Psi_{2,0} + \delta\Psi_2).
\end{aligned}
$$

The perturbation, $\delta\Psi_i$, is assumed to be small hence terms of quadratic order in $\delta\Psi_i$ are neglected

$$\begin{aligned} i\frac{\partial\Psi_{1,0}}{\partial t}+i\frac{\partial\delta\Psi_1}{\partial t} &= -\frac{\gamma\nabla^2\Psi_{1,0}}{2}-\frac{\gamma\nabla^2\delta\Psi_1}{2} \\ &\quad+\left(|\Psi_{1,0}|^2\Psi_{1,0}+2|\Psi_{1,0}|^2\delta\Psi_1+\Psi_{1,0}^2\delta\Psi_1^*\right) \\ &\quad+\eta\left(|\Psi_{2,0}|^2\Psi_{1,0}+|\Psi_{2,0}|^2\delta\Psi_1+\Psi_{1,0}\Psi_{2,0}^*\delta\Psi_2+\Psi_{1,0}\Psi_{2,0}\delta\Psi_2^*\right) \\ &\quad+H_{1,\mathrm{LHY}}(\Psi_{1,0}+\delta\Psi_1), \end{aligned}$$

$$\begin{aligned} i\frac{\partial\Psi_{2,0}}{\partial t}+i\frac{\partial\delta\Psi_2}{\partial t} &= -\frac{\gamma\nabla^2\Psi_{2,0}}{22}-\frac{\gamma\nabla^2\delta\Psi_2}{2z} \\ &\quad+\beta\left(|\Psi_{2,0}|^2\Psi_{2,0}+2|\Psi_{2,0}|^2\delta\Psi_2+\Psi_{2,0}^2\delta\Psi_2^*\right) \\ &\quad+\eta\beta\left(|\Psi_{1,0}|^2\Psi_{2,0}+|\Psi_{1,0}|^2\delta\Psi_2+\Psi_{2,0}\Psi_{1,0}^*\delta\Psi_1+\Psi_{1,0}\Psi_{2,0}\delta\Psi_1^*\right) \\ &\quad+H_{2,\mathrm{LHY}}(\Psi_{2,0}+\delta\Psi_2). \end{aligned}$$

Focusing on the BMF contributions

$$\begin{aligned} H_{1,\mathrm{LHY}} &= \alpha\Bigg\{|\Psi_{1,0}|^2\left[1+\left(\frac{\delta\Psi_1}{\Psi_{1,0}}\right)^*+\left(\frac{\delta\Psi_1}{\Psi_{1,0}}\right)\right]+z^{3/5}\beta|\Psi_{2,0}|^2\left[1+\left(\frac{\delta\Psi_2}{\Psi_{2,0}}\right)^*+\left(\frac{\delta\Psi_2}{\Psi_{2,0}}\right)\right]\Bigg\}^{3/2} \\ &= \alpha\left(|\Psi_{1,0}|^2+z^{3/5}\beta|\Psi_{2,0}|^2\right)^{3/2}\Bigg\{\frac{|\Psi_{1,0}|^2}{|\Psi_{1,0}|^2+z^{3/5}\beta|\Psi_{2,0}|^2}\left[1+\left(\frac{\delta\Psi_1}{\Psi_{1,0}}\right)^*+\left(\frac{\delta\Psi_1}{\Psi_{1,0}}\right)\right] \\ &\qquad+\frac{z^{3/5}\beta|\Psi_{2,0}|^2}{|\Psi_{1,0}|^2+z^{3/5}\beta|\Psi_{2,0}|^2}\left[1+\left(\frac{\delta\Psi_2}{\Psi_{2,0}}\right)^*+\left(\frac{\delta\Psi_2}{\Psi_{2,0}}\right)\right]\Bigg\}^{3/2} \\ &= \alpha\left(|\Psi_{1,0}|^2+z^{3/5}\beta|\Psi_{2,0}|^2\right)^{3/2}\left\{1+\frac{\Lambda}{|\Psi_{1,0}|^2+z^{3/5}\beta|\Psi_{2,0}|^2}\right\}^{3/2}, \end{aligned}$$

where

$$\Lambda=|\Psi_{1,0}|^2\left[\left(\frac{\delta\Psi_1}{\Psi_{1,0}}\right)^*+\left(\frac{\delta\Psi_1}{\Psi_{1,0}}\right)\right]+z^{3/5}\beta|\Psi_{2,0}|^2\left[\left(\frac{\delta\Psi_2}{\Psi_{2,0}}\right)^*+\left(\frac{\delta\Psi_2}{\Psi_{2,0}}\right)\right].$$

As $\Lambda/\left(|\Psi_{1,0}|^2+z^{3/5}\beta|\Psi_{2,0}|^2\right)$ is small, and terms of quadratic order in $\delta\Psi_i$ are neglected, the LHY contributions become

$$\begin{aligned} H_{1,\mathrm{LHY}}(\Psi_{1,0}+\delta\Psi_1) &\approx \alpha\left(|\Psi_{1,0}|^2+z^{3/5}\beta|\Psi_{2,0}|^2\right)^{3/2}\left\{1+\frac{3}{2}\frac{\Lambda}{|\Psi_{1,0}|^2+z^{3/5}\beta|\Psi_{2,0}|^2}\right\}(\Psi_{1,0}+\delta\Psi_1) \\ &= \alpha\left(|\Psi_{1,0}|^2+z^{3/5}\beta|\Psi_{2,0}|^2\right)^{1/2}\Bigg\{\left(|\Psi_{1,0}|^2+z^{3/5}\beta|\Psi_{2,0}|^2\right)\Psi_{1,0} \\ &\qquad+\frac{3}{2}\big(\Psi_{1,0}^2\delta\Psi_1^*+|\Psi_{1,0}|^2\delta\Psi_1 \\ &\qquad+z^{3/5}\beta\left[\Psi_{1,0}\Psi_{2,0}\delta\Psi_2^*+\Psi_{1,0}\Psi_{2,0}^*\delta\Psi_2\right]\big) \\ &\qquad+\left(|\Psi_{1,0}|^2+z^{3/5}\beta|\Psi_{2,0}|^2\right)\delta\Psi_1\Bigg\}. \end{aligned}$$

By symmetry, the same linearisation can be performed for component-2 giving

$$\begin{aligned}H_{2,\mathrm{LHY}}(\Psi_{2,0}+\delta\Psi_2) = \alpha z^{3/5}\beta^2\left(|\Psi_{1,0}|^2+z^{3/5}\beta|\Psi_{2,0}|^2\right)^{1/2}\Big\{&\left(|\Psi_{1,0}|^2+z^{3/5}\beta|\Psi_{2,0}|^2\right)\Psi_{2,0}\\&+\frac{3}{2}\big(\Psi_{1,0}^*\Psi_{2,0}\delta\Psi_1+\Psi_{1,0}\Psi_{2,0}\delta\Psi_1^*\\&+z^{3/5}\beta\left[|\Psi_{2,0}|^2\delta\Psi_2+\Psi_{2,0}^2\delta\Psi_2^*\right]\big)\\&+\left(|\Psi_{1,0}|^2+z^{3/5}\beta|\Psi_{2,0}|^2\right)\delta\Psi_2\Big\}.\end{aligned}$$

Note that both ground state wavefunctions are solutions of

$$\begin{aligned}i\frac{\partial\Psi_{1,0}}{\partial t} &= \left[-\frac{\gamma}{2}\nabla^2+|\Psi_{1,0}|^2+\eta|\Psi_{2,0}|^2+\alpha\left(|\Psi_{1,0}|^2+z^{3/5}\beta|\Psi_{2,0}|^2\right)^{3/2}\right]\Psi_{1,0},\\ i\frac{\partial\Psi_{2,0}}{\partial t} &= \left[-\frac{\gamma}{2z}\nabla^2+\beta|\Psi_{2,0}|^2+\eta\beta|\Psi_{1,0}|^2+\alpha z^{3/5}\beta^2\left(|\Psi_{1,0}|^2+z^{3/5}\beta|\Psi_{2,0}|^2\right)^{3/2}\right]\Psi_{2,0},\end{aligned}$$

which, along with recalling that by symmetry this analysis also has a complex conjugate of the linearised GP equation [as used in Appendix C], results in the four linearised GP equations

$$\begin{aligned}i\frac{\partial\delta\Psi_1}{\partial t} = &-\frac{\gamma\nabla^2\delta\Psi_1}{2}+2|\Psi_{1,0}|^2\delta\Psi_1+\Psi_{1,0}^2\delta\Psi_1^*+\eta\left[|\Psi_{2,0}|^2\delta\Psi_1+\Psi_{1,0}\Psi_{2,0}^*\delta\Psi_2+\Psi_{1,0}\Psi_{2,0}\delta\Psi_2^*\right]\\&+\alpha\left(|\Psi_{1,0}|^2+z^{3/5}\beta|\Psi_{2,0}|^2\right)^{1/2}\Big\{\frac{3}{2}\big(\left[\Psi_{1,0}^2\delta\Psi_1^*+|\Psi_{1,0}|^2\delta\Psi_1\right]\\&+z^{3/5}\beta\left[\Psi_{1,0}\Psi_{2,0}\delta\Psi_2^*+\Psi_{1,0}\Psi_{2,0}^*\delta\Psi_2\right]\big)\\&+\left(|\Psi_{1,0}|^2+z^{3/5}\beta|\Psi_{2,0}|^2\right)\delta\Psi_1\Big\},\end{aligned}$$

$$\begin{aligned}-i\frac{\partial\delta\Psi_1^*}{\partial t} = &-\frac{\gamma\nabla^2\delta\Psi_1^*}{2}+2|\Psi_{1,0}|^2\delta\Psi_1^*+\left(\Psi_{1,0}^*\right)^2\delta\Psi_1+\eta\left[|\Psi_{2,0}|^2\delta\Psi_1^*+\Psi_{1,0}^*\Psi_{2,0}\delta\Psi_2^*+\Psi_{1,0}^*\Psi_{2,0}^*\delta\Psi_2\right]\\&+\alpha\left(|\Psi_{1,0}|^2+z^{3/5}\beta|\Psi_{2,0}|^2\right)^{1/2}\Big\{\frac{3}{2}\big(\left[\left(\Psi_{1,0}^*\right)^2\delta\Psi_1+|\Psi_{1,0}|^2\delta\Psi_1^*\right]\\&+z^{3/5}\beta\left[\Psi_{1,0}^*\Psi_{2,0}^*\delta\Psi_2+\Psi_{1,0}^*\Psi_{2,0}\delta\Psi_2^*\right]\big)\\&+\left(|\Psi_{1,0}|^2+z^{3/5}\beta|\Psi_{2,0}|^2\right)\delta\Psi_1^*\Big\},\end{aligned}$$

$$\begin{aligned}i\frac{\partial\delta\Psi_2}{\partial t} = &-\frac{\gamma\nabla^2\delta\Psi_2}{2z}+\beta\left[2|\Psi_{2,0}|^2\delta\Psi_2+\Psi_{2,0}^2\delta\Psi_2^*\right]+\eta\beta\left[|\Psi_{1,0}|^2\delta\Psi_2+\Psi_{2,0}\Psi_{1,0}^*\delta\Psi_1+\Psi_{1,0}\Psi_{2,0}\delta\Psi_1^*\right]\\&+\alpha z^{3/5}\beta^2\left(|\Psi_{1,0}|^2+z^{3/5}\beta|\Psi_{2,0}|^2\right)^{1/2}\Big\{\frac{3}{2}\big(\left[\Psi_{1,0}^*\Psi_{2,0}\delta\Psi_1+\Psi_{1,0}\Psi_{2,0}\delta\Psi_1^*\right]\\&+z^{3/5}\beta\left[|\Psi_{2,0}|^2\delta\Psi_2+\Psi_{2,0}^2\delta\Psi_2^*\right]\big)\\&+\left(|\Psi_{1,0}|^2+z^{3/5}\beta|\Psi_{2,0}|^2\right)\delta\Psi_2\Big\},\end{aligned}$$

$$
\begin{aligned}
-i\frac{\partial\delta\Psi_2^*}{\partial t} = &-\frac{\gamma\nabla^2\delta\Psi_2^*}{2z} + \beta\left[2|\Psi_{2,0}|^2\delta\Psi_2^* + \left(\Psi_{2,0}^*\right)^2\delta\Psi_2\right] \\
&+ \eta\beta\left[|\Psi_{1,0}|^2\delta\Psi_2^* + \Psi_{2,0}^*\Psi_{1,0}\delta\Psi_1^* + \Psi_{1,0}^*\Psi_{2,0}^*\delta\Psi_1\right] \\
&+ \alpha z^{3/5}\beta^2\left(|\Psi_{1,0}|^2 + z^{3/5}\beta|\Psi_{2,0}|^2\right)^{1/2}\left\{\frac{3}{2}\Big(\left[\Psi_{1,0}\Psi_{2,0}^*\delta\Psi_1^* + \Psi_{1,0}^*\Psi_{2,0}^*\delta\Psi_1\right]\right. \\
&\qquad\qquad + z^{3/5}\beta\left[|\Psi_{2,0}|^2\delta\Psi_2^* + \left(\Psi_{2,0}^*\right)^2\delta\Psi_2\right]\Big) \\
&\qquad\qquad \left. + \left(|\Psi_{1,0}|^2 + z^{3/5}\beta|\Psi_{2,0}|^2\right)\delta\Psi_2^*\right\}.
\end{aligned}
$$

E.2 Matrix form of Bogoliubov-de Gennes

Writing the ground state wavefunctions as $\Psi_{i,0}(\mathbf{r},t) = \Psi_i e^{-iu_i t}$, and the perturbed wavefunctions in the Bogoliubov form

$$
\begin{aligned}
\delta\Psi_i(\mathbf{r},t) &= e^{-i\mu_i t}\left(u_i(\mathbf{r})e^{-i\omega t} - v_i^*(\mathbf{r})e^{i\omega t}\right), \\
\delta\Psi_i^*(\mathbf{r},t) &= e^{i\mu_i t}\left(u_i^*(\mathbf{r})e^{i\omega t} - v_i(\mathbf{r})e^{-i\omega t}\right),
\end{aligned}
$$

and substituting these and equating terms in powers of $e^{-i\omega t}$ gives the Bogoliubov-de Gennes equations in matrix form,

$$
\begin{pmatrix}
h_1 & -\Omega_{11} & \Omega_{12} & -\Omega_{12} \\
\Omega_{11} & -h_1 & \Omega_{12} & -\Omega_{12} \\
\Omega_{21} & -\Omega_{21} & h_2 & -\Omega_{22} \\
\Omega_{21} & -\Omega_{21} & \Omega_{22} & -h_2
\end{pmatrix}
\begin{pmatrix} u_1 \\ v_1 \\ u_2 \\ v_2 \end{pmatrix}
= \omega
\begin{pmatrix} u_1 \\ v_1 \\ u_2 \\ v_2 \end{pmatrix},
$$

where

$$
\begin{aligned}
h_1 &= -\frac{\gamma}{2}\nabla^2 + 2|\Psi_1|^2 + \eta|\Psi_2|^2 \\
&\quad + \alpha\left[\frac{3}{2}\left(|\Psi_1 + z^{3/5}\beta|\Psi_2|^2\right)^{1/2}|\Psi_1|^2 + \left(|\Psi_1|^2 + z^{3/5}\beta|\Psi_2|^2\right)^{3/2}\right] - \mu_1, \\
h_2 &= -\frac{\gamma}{2z}\nabla^2 + 2\beta|\Psi_2|^2 + \beta\eta|\Psi_1|^2 \\
&\quad + \alpha z^{3/5}\beta^2\left[\frac{3}{2}z^{3/5}\beta\left(|\Psi_1 + z^{3/5}\beta|\Psi_2|^2\right)^{1/2}|\Psi_2|^2 + \left(|\Psi_1|^2 + z^{3/5}\beta|\Psi_2|^2\right)^{3/2}\right] - \mu_2, \\
\Omega_{11} &= |\Psi_1|^2 + \frac{3}{2}\alpha\left(|\Psi_1|^2 + z^{3/5}\beta|\Psi_2|^2\right)^{1/2}|\Psi_1|^2, \\
\Omega_{12} &= \eta|\Psi_1||\Psi_2| + \frac{3}{2}\alpha z^{3/5}\beta\left(|\Psi_1|^2 + z^{3/5}\beta|\Psi_2|^2\right)^{1/2}|\Psi_1||\Psi_2|, \\
\Omega_{21} &= \beta\eta|\Psi_1||\Psi_2| + \frac{3}{2}\alpha z^{3/5}\beta^2\left(|\Psi_1|^2 + z^{3/5}\beta|\Psi_2|^2\right)^{1/2}|\Psi_1||\Psi_2|, \\
\Omega_{22} &= \beta|\Psi_2|^2 + \frac{3}{2}\alpha z^{6/5}\beta^3\left(|\Psi_1|^2 + z^{3/5}\beta|\Psi_2|^2\right)^{1/2}|\Psi_2|^2,
\end{aligned}
$$

which can be solved using the numerical methods presented in Section 2.6.4.

Bibliography

[1] W. D. Phillips, Rev. Mod. Phys. **70**, 721 (1998).

[2] C. N. Cohen-Tannoudji, Rev. Mod. Phys. **70**, 707 (1998).

[3] S. Chu, Rev. Mod. Phys. **70**, 685 (1998).

[4] I. Bloch, J. Dalibard, and W. Zwerger, Rev. Mod. Phys. **80**, 885 (2008).

[5] I. Bloch, J. Dalibard, and S. Nascimbene, Nature Physics **8**, 267 (2012).

[6] T. Hänsch and A. Schawlow, Optics Communications **13**, 68 (1975).

[7] W. D. Phillips and H. Metcalf, Phys. Rev. Lett. **48**, 596 (1982).

[8] S. Chu, L. Hollberg, J. E. Bjorkholm, A. Cable, and A. Ashkin, Phys. Rev. Lett. **55**, 48 (1985).

[9] W. Ertmer, R. Blatt, J. L. Hall, and M. Zhu, Phys. Rev. Lett. **54**, 996 (1985).

[10] J. Prodan, A. Migdall, W. D. Phillips, I. So, H. Metcalf, and J. Dalibard, Phys. Rev. Lett. **54**, 992 (1985).

[11] C. J. Pethick and H. Smith, *Bose-Einstein condensation in dilute gases*, 2nd ed. (Cambridge university press, 2008).

[12] H. F. Hess, Phys. Rev. B **34**, 3476 (1986).

[13] T. Tommila, Europhysics Letters **2**, 789 (1986).

[14] R. Grimm, M. Weidemüller, and Y. B. Ovchinnikov, in *Advances in atomic, molecular, and optical physics*, Vol. 42 (Elsevier, 2000) pp. 95–170.

[15] A. L. Gaunt, T. F. Schmidutz, I. Gotlibovych, R. P. Smith, and Z. Hadzibabic, Phys. Rev. Lett. **110**, 200406 (2013).

[16] I. Bloch, Nature physics **1**, 23 (2005).

[17] M. Lewenstein, A. Sanpera, V. Ahufinger, B. Damski, A. Sen(De), and U. Sen, Advances in Physics **56**, 243 (2007).

[18] M. Greiner, O. Mandel, T. Esslinger, T. W. Hänsch, and I. Bloch, nature **415**, 39 (2002).

[19] W. S. Bakr, J. I. Gillen, A. Peng, S. Fölling, and M. Greiner, Nature **462**, 74 (2009).

[20] A. Görlitz, J. M. Vogels, A. E. Leanhardt, C. Raman, T. L. Gustavson, J. R. Abo-Shaeer, A. P. Chikkatur, S. Gupta, S. Inouye, T. Rosenband, and W. Ketterle, Phys. Rev. Lett. **87**, 130402 (2001).

[21] E. H. Lieb and W. Liniger, Phys. Rev. **130**, 1605 (1963).

[22] L. Tonks, Phys. Rev. **50**, 955 (1936).

[23] M. Girardeau, Journal of Mathematical Physics **1**, 516 (1960).

[24] T. Kinoshita, T. Wenger, and D. S. Weiss, Science **305**, 1125 (2004).

[25] B. Paredes, A. Widera, V. Murg, O. Mandel, S. Fölling, I. Cirac, G. V. Shlyapnikov, T. W. Hänsch, and I. Bloch, Nature **429**, 277 (2004).

[26] M. A. Cazalilla, R. Citro, T. Giamarchi, E. Orignac, and M. Rigol, Rev. Mod. Phys. **83**, 1405 (2011).

[27] S. Inouye, S. Gupta, T. Rosenband, A. P. Chikkatur, A. Görlitz, T. L. Gustavson, A. E. Leanhardt, D. E. Pritchard, and W. Ketterle, Phys. Rev. Lett. **87**, 080402 (2001).

[28] K. W. Madison, F. Chevy, W. Wohlleben, and J. Dalibard, Phys. Rev. Lett. **84**, 806 (2000).

[29] F. Chevy, K. W. Madison, and J. Dalibard, Phys. Rev. Lett. **85**, 2223 (2000).

[30] K. Henderson, C. Ryu, C. MacCormick, and M. G. Boshier, New Journal of Physics **11**, 043030 (2009).

[31] G. Gauthier, I. Lenton, N. M. Parry, M. Baker, M. J. Davis, H. Rubinsztein-Dunlop, and T. W. Neely, Optica **3**, 1136 (2016).

[32] E. Altman, K. R. Brown, G. Carleo, L. D. Carr, E. Demler, C. Chin, B. DeMarco, S. E. Economou, M. A. Eriksson, K.-M. C. Fu, M. Greiner, K. R. Hazzard, R. G. Hulet, A. J. Kollár, B. L. Lev, M. D. Lukin, R. Ma, X. Mi, S. Misra, C. Monroe, K. Murch, Z. Nazario, K.-K. Ni, A. C. Potter, P. Roushan, M. Saffman, M. Schleier-Smith, I. Siddiqi, R. Simmonds, M. Singh, I. Spielman, K. Temme, D. S. Weiss, J. Vučković, V. Vuletić, J. Ye, and M. Zwierlein, PRX Quantum **2**, 017003 (2021).

[33] E. Poli, T. Bland, S. J. M. White, M. J. Mark, F. Ferlaino, S. Trabucco, and M. Mannarelli, Phys. Rev. Lett. **131**, 223401 (2023).

[34] T. Bland, F. Ferlaino, M. Mannarelli, E. Poli, and S. Trabucco, Few-Body Systems **65**, 81 (2024).

[35] T. Roger, C. Maitland, K. Wilson, N. Westerberg, D. Vocke, E. M. Wright, and D. Faccio, Nature communications **7**, 13492 (2016).

[36] S. Eckel, A. Kumar, T. Jacobson, I. B. Spielman, and G. K. Campbell, Phys. Rev. X **8**, 021021 (2018).

[37] N. Proukakis, D. Snoke, and P. Littlewood, *Universal Themes of Bose-Einstein Condensation* (Cambridge University Press, 2017).

[38] M. H. Anderson, J. R. Ensher, M. R. Matthews, C. E. Wieman, and E. A. Cornell, Science **269**, 198 (1995).

[39] K. B. Davis, M. O. Mewes, M. R. Andrews, N. J. van Druten, D. S. Durfee, D. M. Kurn, and W. Ketterle, Phys. Rev. Lett. **75**, 3969 (1995).

[40] W. Ketterle, Rev. Mod. Phys. **74**, 1131 (2002).

[41] E. A. Cornell and C. E. Wieman, Rev. Mod. Phys. **74**, 875 (2002).

[42] S. N. Bose, Z. Phys. **26**, 178 (1924).

[43] A. Einstein, Sitzungsber. Preuss. Akad. Wiss., Phys. Math. Kl. Bericht **1**, 3 (1925).

[44] A. Einstein, Sitzungsber. Preuss. Akad. Wiss., Phys. Math. Kl. Bericht **3**, 18 (1925).

[45] L. Pitaevskii and S. Stringari, *Bose-Einstein condensation and superfluidity*, Vol. 164 (Oxford University Press, 2016).

[46] E. M. Lifshitz, Pitaevskii, J. B. L. P., Sykes, and M. J. Kearsley, *Landau and Lifshitz Course of Theoretical Physics, Statistical Physics, Part 2 - Theory of the Condensed State, Volume 9* (Elsevier, 1980).

[47] O. Penrose, The London, Edinburgh, and Dublin Philosophical Magazine and Journal of Science **42**, 1373 (1951).

[48] O. Penrose and L. Onsager, Phys. Rev. **104**, 576 (1956).

[49] F. London, Nature **141**, 643 (1938).

[50] L. Tisza, Nature **141**, 913 (1938).

[51] L. Landau, Phys. Rev. **60**, 356 (1941).

[52] M. R. Matthews, B. P. Anderson, P. C. Haljan, D. S. Hall, C. E. Wieman, and E. A. Cornell, Phys. Rev. Lett. **83**, 2498 (1999).

[53] J. R. Abo-Shaeer, C. Raman, J. M. Vogels, and W. Ketterle, Science **292**, 476 (2001).

[54] R. J. Donnelly, *Quantized vortices in helium II*, Cambridge studies in low temperature physics (Cambridge University Press, Cambridge [England] ; New York, 1991).

[55] B. P. Anderson, P. C. Haljan, C. A. Regal, D. L. Feder, L. A. Collins, C. W. Clark, and E. A. Cornell, Phys. Rev. Lett. **86**, 2926 (2001).

[56] C. Raman, J. R. Abo-Shaeer, J. M. Vogels, K. Xu, and W. Ketterle, Phys. Rev. Lett. **87**, 210402 (2001).

[57] C. F. Barenghi, R. J. Donnelly, and W. Vinen, *Quantized vortex dynamics and superfluid turbulence*, Vol. 571 (Springer Science & Business Media, 2001).

[58] W. J. Kwon, G. Del Pace, K. Xhani, L. Galantucci, A. Muzi Falconi, M. Inguscio, F. Scazza, and G. Roati, Nature **600**, 64 (2021).

[59] C. Barenghi, H. Middleton-Spencer, L. Galantucci, and N. Parker, AVS Quantum Science **5** (2023).

[60] C. F. Barenghi, L. Skrbek, and K. R. Sreenivasan, *Quantum turbulence* (Cambridge University Press, 2023).

[61] Y. S. Kivshar and B. A. Malomed, Rev. Mod. Phys. **61**, 763 (1989).

[62] L. Khaykovich, F. Schreck, G. Ferrari, T. Bourdel, J. Cubizolles, L. D. Carr, Y. Castin, and C. Salomon, Science **296**, 1290 (2002).

[63] S. Burger, K. Bongs, S. Dettmer, W. Ertmer, K. Sengstock, A. Sanpera, G. V. Shlyapnikov, and M. Lewenstein, Phys. Rev. Lett. **83**, 5198 (1999).

[64] M.-O. Mewes, M. R. Andrews, N. J. van Druten, D. M. Kurn, D. S. Durfee, C. G. Townsend, and W. Ketterle, Phys. Rev. Lett. **77**, 988 (1996).

[65] D. S. Jin, J. R. Ensher, M. R. Matthews, C. E. Wieman, and E. A. Cornell, Phys. Rev. Lett. **77**, 420 (1996).

[66] M. R. Andrews, D. M. Kurn, H.-J. Miesner, D. S. Durfee, C. G. Townsend, S. Inouye, and W. Ketterle, Phys. Rev. Lett. **79**, 553 (1997).

[67] J. L. Roberts, N. R. Claussen, S. L. Cornish, E. A. Donley, E. A. Cornell, and C. E. Wieman, Phys. Rev. Lett. **86**, 4211 (2001).

[68] E. A. Donley, N. R. Claussen, S. L. Cornish, J. L. Roberts, E. A. Cornell, and C. E. Wieman, Nature **412**, 295 (2001).

[69] H. J. Metcalf and P. Van der Straten, The Optics Encyclopedia: Basic Foundations and Practical Applications (2007).

[70] A. Griesmaier, J. Werner, S. Hensler, J. Stuhler, and T. Pfau, Phys. Rev. Lett. **94**, 160401 (2005).

[71] K. Aikawa, A. Frisch, M. Mark, S. Baier, A. Rietzler, R. Grimm, and F. Ferlaino, Phys. Rev. Lett. **108**, 210401 (2012).

[72] M. Lu, N. Q. Burdick, S. H. Youn, and B. L. Lev, Phys. Rev. Lett. **107**, 190401 (2011).

[73] Y. Miyazawa, R. Inoue, H. Matsui, G. Nomura, and M. Kozuma, Phys. Rev. Lett. **129**, 223401 (2022).

[74] M. Greiner, C. A. Regal, and D. S. Jin, Nature **426**, 537 (2003).

[75] M. W. Zwierlein, C. A. Stan, C. H. Schunck, S. M. F. Raupach, S. Gupta, Z. Hadzibabic, and W. Ketterle, Phys. Rev. Lett. **91**, 250401 (2003).

[76] T. Bourdel, J. Cubizolles, L. Khaykovich, K. M. F. Magalhães, S. J. J. M. F. Kokkelmans, G. V. Shlyapnikov, and C. Salomon, Phys. Rev. Lett. **91**, 020402 (2003).

[77] M. Bartenstein, A. Altmeyer, S. Riedl, S. Jochim, C. Chin, J. H. Denschlag, and R. Grimm, Phys. Rev. Lett. **92**, 120401 (2004).

[78] G. B. Partridge, K. E. Strecker, R. I. Kamar, M. W. Jack, and R. G. Hulet, Phys. Rev. Lett. **95**, 020404 (2005).

[79] J. M. McNamara, T. Jeltes, A. S. Tychkov, W. Hogervorst, and W. Vassen, Phys. Rev. Lett. **97**, 080404 (2006).

[80] A. G. Truscott, K. E. Strecker, W. I. McAlexander, G. B. Partridge, and R. G. Hulet, Science **291**, 2570 (2001).

[81] B. DeMarco and D. S. Jin, Science **285**, 1703 (1999).

[82] B. J. DeSalvo, M. Yan, P. G. Mickelson, Y. N. Martinez de Escobar, and T. C. Killian, Phys. Rev. Lett. **105**, 030402 (2010).

[83] B. Naylor, A. Reigue, E. Maréchal, O. Gorceix, B. Laburthe-Tolra, and L. Vernac, Phys. Rev. A **91**, 011603 (2015).

[84] M. Lu, N. Q. Burdick, and B. L. Lev, Phys. Rev. Lett. **108**, 215301 (2012).

[85] K. Aikawa, S. Baier, A. Frisch, M. Mark, C. Ravensbergen, and F. Ferlaino, Science **345**, 1484 (2014).

[86] T. Fukuhara, Y. Takasu, M. Kumakura, and Y. Takahashi, Phys. Rev. Lett. **98**, 030401 (2007).

[87] C. A. Regal, M. Greiner, and D. S. Jin, Phys. Rev. Lett. **92**, 040403 (2004).

[88] M. W. Zwierlein, C. A. Stan, C. H. Schunck, S. M. F. Raupach, A. J. Kerman, and W. Ketterle, Phys. Rev. Lett. **92**, 120403 (2004).

[89] J. Kinast, S. L. Hemmer, M. E. Gehm, A. Turlapov, and J. E. Thomas, Phys. Rev. Lett. **92**, 150402 (2004).

[90] J. Bardeen, L. N. Cooper, and J. R. Schrieffer, Phys. Rev. **106**, 162 (1957).

[91] E. Tiesinga, B. J. Verhaar, and H. T. C. Stoof, Phys. Rev. A **47**, 4114 (1993).

[92] P. Courteille, R. S. Freeland, D. J. Heinzen, F. A. van Abeelen, and B. J. Verhaar, Phys. Rev. Lett. **81**, 69 (1998).

[93] S. Inouye, M. Andrews, J. Stenger, H.-J. Miesner, D. M. Stamper-Kurn, and W. Ketterle, Nature **392**, 151 (1998).

[94] C. Chin, R. Grimm, P. Julienne, and E. Tiesinga, Rev. Mod. Phys. **82**, 1225 (2010).

[95] A. J. Moerdijk, B. J. Verhaar, and A. Axelsson, Phys. Rev. A **51**, 4852 (1995).

[96] J. Stenger, S. Inouye, M. R. Andrews, H.-J. Miesner, D. M. Stamper-Kurn, and W. Ketterle, Phys. Rev. Lett. **82**, 2422 (1999).

[97] T. Weber, J. Herbig, M. Mark, H.-C. Nägerl, and R. Grimm, Phys. Rev. Lett. **91**, 123201 (2003).

[98] C. H. Greene, P. Giannakeas, and J. Pérez-Ríos, Rev. Mod. Phys. **89**, 035006 (2017).

[99] P. Naidon and S. Endo, Reports on Progress in Physics **80**, 056001 (2017).

[100] T. Kraemer, M. Mark, P. Waldburger, J. G. Danzl, C. Chin, B. Engeser, A. D. Lange, K. Pilch, A. Jaakkola, H.-C. Nägerl, *et al.*, Nature **440**, 315 (2006).

[101] M. Zaccanti, B. Deissler, C. D'Errico, M. Fattori, M. Jona-Lasinio, S. Müller, G. Roati, M. Inguscio, and G. Modugno, Nature Physics **5**, 586 (2009).

[102] C. J. Myatt, E. A. Burt, R. W. Ghrist, E. A. Cornell, and C. E. Wieman, Phys. Rev. Lett. **78**, 586 (1997).

[103] S. B. Papp, J. M. Pino, and C. E. Wieman, Phys. Rev. Lett. **101**, 040402 (2008).

[104] G. Modugno, M. Modugno, F. Riboli, G. Roati, and M. Inguscio, Phys. Rev. Lett. **89**, 190404 (2002).

[105] G. Roati, F. Riboli, G. Modugno, and M. Inguscio, Phys. Rev. Lett. **89**, 150403 (2002).

[106] F. Schreck, L. Khaykovich, K. L. Corwin, G. Ferrari, T. Bourdel, J. Cubizolles, and C. Salomon, Phys. Rev. Lett. **87**, 080403 (2001).

[107] Z. Hadzibabic, C. A. Stan, K. Dieckmann, S. Gupta, M. W. Zwierlein, A. Görlitz, and W. Ketterle, Phys. Rev. Lett. **88**, 160401 (2002).

[108] C. A. Stan, M. W. Zwierlein, C. H. Schunck, S. M. F. Raupach, and W. Ketterle, Phys. Rev. Lett. **93**, 143001 (2004).

[109] S. Inouye, J. Goldwin, M. L. Olsen, C. Ticknor, J. L. Bohn, and D. S. Jin, Phys. Rev. Lett. **93**, 183201 (2004).

[110] F. Ferlaino, C. D'Errico, G. Roati, M. Zaccanti, M. Inguscio, G. Modugno, and A. Simoni, Phys. Rev. A **73**, 040702 (2006).

[111] C. D'Errico, M. Zaccanti, M. Fattori, G. Roati, M. Inguscio, G. Modugno, and A. Simoni, New Journal of Physics **9**, 223 (2007).

[112] G. Thalhammer, G. Barontini, L. De Sarlo, J. Catani, F. Minardi, and M. Inguscio, Phys. Rev. Lett. **100**, 210402 (2008).

[113] T. Lahaye, C. Menotti, L. Santos, M. Lewenstein, and T. Pfau, Reports on Progress in Physics **72**, 126401 (2009).

[114] L. Chomaz, I. Ferrier-Barbut, F. Ferlaino, B. Laburthe-Tolra, B. L. Lev, and T. Pfau, Reports on Progress in Physics **86**, 026401 (2022).

[115] A. Trautmann, P. Ilzhöfer, G. Durastante, C. Politi, M. Sohmen, M. J. Mark, and F. Ferlaino, Phys. Rev. Lett. **121**, 213601 (2018).

[116] G. Durastante, C. Politi, M. Sohmen, P. Ilzhöfer, M. J. Mark, M. A. Norcia, and F. Ferlaino, Phys. Rev. A **102**, 033330 (2020).

[117] C. Politi, A. Trautmann, P. Ilzhöfer, G. Durastante, M. J. Mark, M. Modugno, and F. Ferlaino, Phys. Rev. A **105**, 023304 (2022).

[118] T.-L. Ho, Phys. Rev. Lett. **81**, 742 (1998).

[119] D. M. Stamper-Kurn, M. R. Andrews, A. P. Chikkatur, S. Inouye, H.-J. Miesner, J. Stenger, and W. Ketterle, Phys. Rev. Lett. **80**, 2027 (1998).

[120] J. Stenger, S. Inouye, D. Stamper-Kurn, H.-J. Miesner, A. Chikkatur, and W. Ketterle, Nature **396**, 345 (1998).

[121] M.-S. Chang, C. D. Hamley, M. D. Barrett, J. A. Sauer, K. M. Fortier, W. Zhang, L. You, and M. S. Chapman, Phys. Rev. Lett. **92**, 140403 (2004).

[122] T. Kuwamoto, K. Araki, T. Eno, and T. Hirano, Phys. Rev. A **69**, 063604 (2004).

[123] H. Schmaljohann, M. Erhard, J. Kronjäger, M. Kottke, S. van Staa, L. Cacciapuoti, J. J. Arlt, K. Bongs, and K. Sengstock, Phys. Rev. Lett. **92**, 040402 (2004).

[124] B. Pasquiou, E. Maréchal, G. Bismut, P. Pedri, L. Vernac, O. Gorceix, and B. Laburthe-Tolra, Phys. Rev. Lett. **106**, 255303 (2011).

[125] Y. Kawaguchi and M. Ueda, Physics Reports **520**, 253 (2012), spinor Bose–Einstein condensates.

[126] D. M. Stamper-Kurn and M. Ueda, Rev. Mod. Phys. **85**, 1191 (2013).

[127] H. Pu and N. P. Bigelow, Phys. Rev. Lett. **80**, 1130 (1998).

[128] D. S. Hall, M. R. Matthews, J. R. Ensher, C. E. Wieman, and E. A. Cornell, Phys. Rev. Lett. **81**, 1539 (1998).

[129] C. K. Law, C. M. Chan, P. T. Leung, and M.-C. Chu, Phys. Rev. A **63**, 063612 (2001).

[130] C. Hamner, J. J. Chang, P. Engels, and M. A. Hoefer, Phys. Rev. Lett. **106**, 065302 (2011).

[131] M. A. Hoefer, J. J. Chang, C. Hamner, and P. Engels, Phys. Rev. A **84**, 041605 (2011).

[132] A. Richaud, V. Penna, R. Mayol, and M. Guilleumas, Phys. Rev. A **101**, 013630 (2020).

[133] A. Richaud, V. Penna, and A. L. Fetter, Phys. Rev. A **103**, 023311 (2021).

[134] A. Richaud, G. Lamporesi, M. Capone, and A. Recati, Phys. Rev. A **107**, 053317 (2023).

[135] R. Doran, A. W. Baggaley, and N. G. Parker, Phys. Rev. A **109**, 023318 (2024).

[136] K. Sasaki, N. Suzuki, D. Akamatsu, and H. Saito, Phys. Rev. A **80**, 063611 (2009).

[137] S. Gautam and D. Angom, Phys. Rev. A **81**, 053616 (2010).

[138] T. Kadokura, T. Aioi, K. Sasaki, T. Kishimoto, and H. Saito, Phys. Rev. A **85**, 013602 (2012).

[139] D. Kobyakov, A. Bezett, E. Lundh, M. Marklund, and V. Bychkov, Phys. Rev. A **89**, 013631 (2014).

[140] N. Suzuki, H. Takeuchi, K. Kasamatsu, M. Tsubota, and H. Saito, Phys. Rev. A **82**, 063604 (2010).

[141] H. Takeuchi, N. Suzuki, K. Kasamatsu, H. Saito, and M. Tsubota, Phys. Rev. B **81**, 094517 (2010).

[142] H. Kokubo, K. Kasamatsu, and H. Takeuchi, Phys. Rev. A **104**, 023312 (2021).

[143] N. B. Jørgensen, L. Wacker, K. T. Skalmstang, M. M. Parish, J. Levinsen, R. S. Christensen, G. M. Bruun, and J. J. Arlt, Phys. Rev. Lett. **117**, 055302 (2016).

[144] M.-G. Hu, M. J. Van de Graaff, D. Kedar, J. P. Corson, E. A. Cornell, and D. S. Jin, Phys. Rev. Lett. **117**, 055301 (2016).

[145] A. Schirotzek, C.-H. Wu, A. Sommer, and M. W. Zwierlein, Phys. Rev. Lett. **102**, 230402 (2009).

[146] M. Koschorreck, D. Pertot, E. Vogt, B. Fröhlich, M. Feld, and M. Köhl, Nature **485**, 619 (2012).

[147] C. Kohstall, M. Zaccanti, M. Jag, A. Trenkwalder, P. Massignan, G. M. Bruun, F. Schreck, and R. Grimm, Nature **485**, 615 (2012).

[148] M. Cetina, M. Jag, R. S. Lous, I. Fritsche, J. T. M. Walraven, R. Grimm, J. Levinsen, M. M. Parish, R. Schmidt, M. Knap, and E. Demler, Science **354**, 96 (2016).

[149] A. Bulgac, Phys. Rev. Lett. **89**, 050402 (2002).

[150] P. F. Bedaque, A. Bulgac, and G. Rupak, Phys. Rev. A **68**, 033606 (2003).

[151] A. Bulgac, Physics Today **73**, 10 (2020).

[152] I. Ferrier-Barbut, Physics Today **73**, 11 (2020).

[153] D. S. Petrov, Phys. Rev. Lett. **115**, 155302 (2015).

[154] N. B. Jørgensen, G. M. Bruun, and J. J. Arlt, Phys. Rev. Lett. **121**, 173403 (2018).

[155] T. G. Skov, M. G. Skou, N. B. Jørgensen, and J. J. Arlt, Phys. Rev. Lett. **126**, 230404 (2021).

[156] D. S. Petrov, Nature Physics **14**, 211 (2018).

[157] Y. Castin and R. Dum, Phys. Rev. Lett. **77**, 5315 (1996).

[158] F. Ancilotto, M. Barranco, M. Guilleumas, and M. Pi, Phys. Rev. A **98**, 053623 (2018).

[159] V. Cikojević, E. Poli, F. Ancilotto, L. Vranješ-Markić, and J. Boronat, Physical Review A **104**, 033319 (2021).

[160] D. Baillie, R. M. Wilson, and P. B. Blakie, Phys. Rev. Lett. **119**, 255302 (2017).

[161] G. Ferioli, G. Semeghini, L. Masi, G. Giusti, G. Modugno, M. Inguscio, A. Gallemí, A. Recati, and M. Fattori, Phys. Rev. Lett. **122**, 090401 (2019).

[162] F. Böttcher, J.-N. Schmidt, J. Hertkorn, K. S. Ng, S. D. Graham, M. Guo, T. Langen, and T. Pfau, Reports on Progress in Physics **84**, 012403 (2020).

[163] Z.-H. Luo, W. Pang, B. Liu, Y.-Y. Li, and B. A. Malomed, Frontiers of physics **16**, 32201 (2021).

[164] H. Kadau, M. Schmitt, M. Wenzel, C. Wink, T. Maier, I. Ferrier-Barbut, and T. Pfau, Nature. **530**, 194 (2016).

[165] I. Ferrier-Barbut, H. Kadau, M. Schmitt, M. Wenzel, and T. Pfau, Phys. Rev. Lett. **116**, 215301 (2016).

[166] M. Schmitt, M. Wenzel, F. Böttcher, I. Ferrier-Barbut, and T. Pfau, Nature. **539**, 259 (2016).

[167] L. Chomaz, S. Baier, D. Petter, M. J. Mark, F. Wächtler, L. Santos, and F. Ferlaino, Phys. Rev. X **6**, 041039 (2016).

[168] C. R. Cabrera, L. Tanzi, J. Sanz, B. Naylor, P. Thomas, P. Cheiney, and L. Tarruell, Science **359**, 301 (2018).

[169] G. Semeghini, G. Ferioli, L. Masi, C. Mazzinghi, L. Wolswijk, F. Minardi, M. Modugno, G. Modugno, M. Inguscio, and M. Fattori, Phys. Rev. Lett. **120**, 235301 (2018).

[170] P. Cheiney, C. R. Cabrera, J. Sanz, B. Naylor, L. Tanzi, and L. Tarruell, Phys. Rev. Lett. **120**, 135301 (2018).

[171] C. D'Errico, A. Burchianti, M. Prevedelli, L. Salasnich, F. Ancilotto, M. Modugno, F. Minardi, and C. Fort, Phys. Rev. Res. **1**, 033155 (2019).

[172] L. Cavicchioli, C. Fort, F. Ancilotto, M. Modugno, F. Minardi, and A. Burchianti, Dynamical formation of multiple quantum droplets in a bose-bose mixture (2024), arXiv:2409.16017 [cond-mat.quant-gas] .

[173] Z. Guo, F. Jia, L. Li, Y. Ma, J. M. Hutson, X. Cui, and D. Wang, Phys. Rev. Research **3**, 033247 (2021).

[174] F. Wächtler and L. Santos, Phys. Rev. A **93**, 061603(R) (2016).

[175] R. N. Bisset, R. M. Wilson, D. Baillie, and P. B. Blakie, Phys. Rev. A **94**, 033619 (2016).

[176] S. Pal, D. Baillie, and P. B. Blakie, Phys. Rev. A **102**, 043306 (2020).

[177] A.-C. Lee, D. Baillie, and P. B. Blakie, Phys. Rev. Research **3**, 013283 (2021).

[178] S. Pal, D. Baillie, and P. B. Blakie, Phys. Rev. A **105**, 023308 (2022).

[179] L. Santos, G. V. Shlyapnikov, and M. Lewenstein, Phys. Rev. Lett. **90**, 250403 (2003).

[180] D. H. J. O'Dell, S. Giovanazzi, and G. Kurizki, Phys. Rev. Lett. **90**, 110402 (2003).

[181] L. Landau, J. Phys. Ussr **5**, 71 (1941).

[182] J. L. Bohn, R. M. Wilson, and S. Ronen, Laser Physics **19**, 547 (2009).

[183] N. Parker, C. Ticknor, A. Martin, and D. O'Dell, Physical Review A—Atomic, Molecular, and Optical Physics **79**, 013617 (2009).

[184] L. Chomaz, R. M. van Bijnen, D. Petter, G. Faraoni, S. Baier, J. H. Becher, M. J. Mark, F. Waechtler, L. Santos, and F. Ferlaino, Nature physics **14**, 442 (2018).

[185] T. Bland, E. Poli, C. Politi, L. Klaus, M. A. Norcia, F. Ferlaino, L. Santos, and R. N. Bisset, Phys. Rev. Lett. **128**, 195302 (2022).

[186] A. Andreev and I. Lifshits, Zhur Eksper Teoret Fiziki **56**, 2057 (1969).

[187] G. V. Chester, Phys. Rev. A **2**, 256 (1970).

[188] A. J. Leggett, Phys. Rev. Lett. **25**, 1543 (1970).

[189] L. Chomaz, D. Petter, P. Ilzhöfer, G. Natale, A. Trautmann, C. Politi, G. Durastante, R. M. W. van Bijnen, A. Patscheider, M. Sohmen, M. J. Mark, and F. Ferlaino, Phys. Rev. X **9**, 021012 (2019).

[190] L. Tanzi, E. Lucioni, F. Famà, J. Catani, A. Fioretti, C. Gabbanini, R. N. Bisset, L. Santos, and G. Modugno, Phys. Rev. Lett. **122**, 130405 (2019).

[191] F. Böttcher, J.-N. Schmidt, M. Wenzel, J. Hertkorn, M. Guo, T. Langen, and T. Pfau, Phys. Rev. X **9**, 011051 (2019).

[192] M. A. Norcia, C. Politi, L. Klaus, E. Poli, M. Sohmen, M. J. Mark, R. N. Bisset, L. Santos, and F. Ferlaino, Nature **596**, 357 (2021).

[193] E. Poli, T. Bland, C. Politi, L. Klaus, M. A. Norcia, F. Ferlaino, R. N. Bisset, and L. Santos, Phys. Rev. A **104**, 063307 (2021).

[194] T. Bland, E. Poli, L. A. Peña Ardila, L. Santos, F. Ferlaino, and R. N. Bisset, Phys. Rev. A **106**, 053322 (2022).

[195] D. Baillie and P. B. Blakie, Phys. Rev. Lett. **121**, 195301 (2018).

[196] Y.-C. Zhang, F. Maucher, and T. Pohl, Phys. Rev. Lett. **123**, 015301 (2019).

[197] A. Gallemí and L. Santos, Phys. Rev. A **106**, 063301 (2022).

[198] Y.-C. Zhang, T. Pohl, and F. Maucher, Phys. Rev. A **104**, 013310 (2021).

[199] J. Hertkorn, J.-N. Schmidt, M. Guo, F. Böttcher, K. S. H. Ng, S. D. Graham, P. Uerlings, T. Langen, M. Zwierlein, and T. Pfau, Phys. Rev. Res. **3**, 033125 (2021).

[200] F. Ancilotto, M. Barranco, and M. Pi, Phys. Rev. A **107**, 063312 (2023).

[201] C. Fort and M. Modugno, Applied Sciences **11** (2021).

[202] M. Tylutki, G. E. Astrakharchik, B. A. Malomed, and D. S. Petrov, Phys. Rev. A **101**, 051601(R) (2020).

[203] T. Bienaimé, E. Fava, G. Colzi, C. Mordini, S. Serafini, C. Qu, S. Stringari, G. Lamporesi, and G. Ferrari, Phys. Rev. A **94**, 063652 (2016).

[204] A. Cappellaro, T. Macrì, and L. Salasnich, Phys. Rev. A **97**, 053623 (2018).

[205] A.-C. Lee, D. Baillie, P. B. Blakie, and R. N. Bisset, Phys. Rev. A **103**, 063301 (2021).

[206] A.-C. Lee, D. Baillie, and P. B. Blakie, Phys. Rev. Res. **4**, 033153 (2022).

[207] J. C. Smith, D. Baillie, and P. B. Blakie, Phys. Rev. Lett. **126**, 025302 (2021).

[208] R. N. Bisset, L. A. Peña Ardila, and L. Santos, Phys. Rev. Lett. **126**, 025301 (2021).

[209] J. C. Smith, P. B. Blakie, and D. Baillie, Phys. Rev. A **104**, 053316 (2021).

[210] D. Scheiermann, L. A. Peña Ardila, T. Bland, R. N. Bisset, and L. Santos, Phys. Rev. A **107**, L021302 (2023).

[211] S. Li, U. N. Le, and H. Saito, Phys. Rev. A **105**, L061302 (2022).

[212] W. Kirkby, A.-C. Lee, D. Baillie, T. Bland, F. Ferlaino, P. B. Blakie, and R. N. Bisset, Phys. Rev. Lett. **133**, 103401 (2024).

[213] A.-C. Lee, D. Baillie, and P. B. Blakie, Phys. Rev. A **109**, 023323 (2024).

[214] K. E. Wilson, A. Guttridge, J. Segal, and S. L. Cornish, Phys. Rev. A **103**, 033306 (2021).

[215] S. Tassy, N. Nemitz, F. Baumer, C. Höhl, A. Batär, and A. Görlitz, Journal of Physics B: Atomic, Molecular and Optical Physics **43**, 205309 (2010).

[216] A. Guttridge, S. A. Hopkins, S. L. Kemp, M. D. Frye, J. M. Hutson, and S. L. Cornish, Phys. Rev. A **96**, 012704 (2017).

[217] V. D. Vaidya, J. Tiamsuphat, S. L. Rolston, and J. V. Porto, Phys. Rev. A **92**, 043604 (2015).

[218] D. A. Brue and J. M. Hutson, Phys. Rev. A **87**, 052709 (2013).

[219] K. E. Wilson, A. Guttridge, I.-K. Liu, J. Segal, T. P. Billam, N. G. Parker, N. P. Proukakis, and S. L. Cornish, Phys. Rev. Research **3**, 033096 (2021).

[220] C. Chin, V. Vuletić, A. J. Kerman, and S. Chu, Phys. Rev. Lett. **85**, 2717 (2000).

[221] T. A. Flynn, L. Parisi, T. P. Billam, and N. G. Parker, Phys. Rev. Res. **5**, 033167 (2023).

[222] T. A. Flynn, N. A. Keepfer, N. G. Parker, and T. P. Billam, Phys. Rev. Res. **6**, 013209 (2024).

[223] J. McMillan, T. A. Flynn, and R. Doran, Phys. Rev. Lett. **133**, 093403 (2024).

[224] N. Keepfer, T. Flynn, N. Parker, and T. Billam, Supervortexnet: Reconstructing superfluid vortex filaments using deep learning (2023), arXiv:2312.14815 [cond-mat.quant-gas] .

[225] T. D. Lee and C. N. Yang, Phys. Rev. **105**, 1119 (1957).

[226] K. Huang and C. N. Yang, Phys. Rev. **105**, 767 (1957).

[227] T. D. Lee, K. Huang, and C. N. Yang, Phys. Rev. **106**, 1135 (1957).

[228] T. T. Wu, Phys. Rev. **115**, 1390 (1959).

[229] N. M. Hugenholtz and D. Pines, Phys. Rev. **116**, 489 (1959).

[230] K. Sawada, Phys. Rev. **116**, 1344 (1959).

[231] N. Navon, S. Piatecki, K. Günter, B. Rem, T. C. Nguyen, F. Chevy, W. Krauth, and C. Salomon, Phys. Rev. Lett. **107**, 135301 (2011).

[232] N. Bogoliubov, J. Phys **11**, 23 (1947).

[233] F. Dalfovo, A. Lastri, L. Pricaupenko, S. Stringari, and J. Treiner, Phys. Rev. B **52**, 1193 (1995).

[234] E. P. Gross, Il Nuovo Cimento (1955-1965) **20**, 454 (1961).

[235] L. P. Pitaevskii, Sov. Phys. JETP **13**, 451 (1961).

[236] N. P. Proukakis and B. Jackson, Journal of Physics B: Atomic, Molecular and Optical Physics **41**, 203002 (2008).

[237] J. Steinhauer, R. Ozeri, N. Katz, and N. Davidson, Phys. Rev. Lett. **88**, 120407 (2002).

[238] K. E. Strecker, G. B. Partridge, A. G. Truscott, and R. G. Hulet, Nature **417**, 150 (2002).

[239] S. L. Cornish, S. T. Thompson, and C. E. Wieman, Phys. Rev. Lett. **96**, 170401 (2006).

[240] D. S. Petrov, Beyond-mean-field effects in mixtures: few-body and many-body aspects (2023), arXiv:2312.05336 [cond-mat.quant-gas] .

[241] F. Minardi, F. Ancilotto, A. Burchianti, C. D'Errico, C. Fort, and M. Modugno, Phys. Rev. A **100**, 063636 (2019).

[242] E. Fava, T. Bienaimé, C. Mordini, G. Colzi, C. Qu, S. Stringari, G. Lamporesi, and G. Ferrari, Phys. Rev. Lett. **120**, 170401 (2018).

[243] L. Cavicchioli, C. Fort, M. Modugno, F. Minardi, and A. Burchianti, Phys. Rev. Res. **4**, 043068 (2022).

[244] J. H. Kim, D. Hong, and Y. Shin, Phys. Rev. A **101**, 061601 (2020).

[245] M. Ota and G. E. Astrakharchik, SciPost Phys. **9**, 020 (2020).

[246] V. Cikojević, L. Vranješ-Markić, G. E. Astrakharchik, and J. Boronat, Phys. Rev. A **99**, 023618 (2019).

[247] H. Hu and X.-J. Liu, Phys. Rev. A **102**, 043302 (2020).

[248] H. Hu and X.-J. Liu, Phys. Rev. Lett. **125**, 195302 (2020).

[249] H. Hu, J. Wang, and X.-J. Liu, Phys. Rev. A **102**, 043301 (2020).

[250] T. Bourdel, L. Khaykovich, J. Cubizolles, J. Zhang, F. Chevy, M. Teichmann, L. Tarruell, S. J. J. M. F. Kokkelmans, and C. Salomon, Phys. Rev. Lett. **93**, 050401 (2004).

[251] Q. Gu and L. Yin, Phys. Rev. B **102**, 220503(R) (2020).

[252] Y. Xiong and L. Yin, Phys. Rev. A **105**, 053305 (2022).

[253] H. Hu and X.-J. Liu, Phys. Rev. A **102**, 053303 (2020).

[254] D. S. Petrov and G. E. Astrakharchik, Phys. Rev. Lett. **117**, 100401 (2016).

[255] P. Naidon and D. S. Petrov, Phys. Rev. Lett. **126**, 115301 (2021).

[256] R. Ozeri, N. Katz, J. Steinhauer, and N. Davidson, Rev. Mod. Phys. **77**, 187 (2005).

[257] S. Stringari, Phys. Rev. Lett. **77**, 2360 (1996).

[258] D. M. Stamper-Kurn, H.-J. Miesner, S. Inouye, M. R. Andrews, and W. Ketterle, Phys. Rev. Lett. **81**, 500 (1998).

[259] M. L. Chiofalo, S. Succi, and M. P. Tosi, Phys. Rev. E **62**, 7438 (2000).

[260] R. Courant, K. Friedrichs, and H. Lewy, IBM Journal of Research and Development **11**, 215 (1967).

[261] R. B. Lehoucq, D. C. Sorensen, and C. Yang, *ARPACK users' guide: solution of large-scale eigenvalue problems with implicitly restarted Arnoldi methods* (SIAM, 1998).

[262] P. Virtanen, R. Gommers, T. E. Oliphant, M. Haberland, T. Reddy, D. Cournapeau, E. Burovski, P. Peterson, W. Weckesser, J. Bright, S. J. van der Walt, M. Brett, J. Wilson, K. J. Millman, N. Mayorov, A. R. J. Nelson, E. Jones, R. Kern, E. Larson, C. J. Carey, İ. Polat, Y. Feng, E. W. Moore, J. VanderPlas, D. Laxalde, J. Perktold, R. Cimrman, I. Henriksen, E. A. Quintero, C. R. Harris, A. M. Archibald, A. H. Ribeiro, F. Pedregosa, P. van Mulbregt, and SciPy 1.0 Contributors, Nature Methods **17**, 261 (2020).

[263] L. Li, L. Shen, G. D. Nguyen, A. El-Zein, and F. Maggi, Computational mechanics **62**, 1071 (2018).

[264] G. Ferioli, G. Semeghini, S. Terradas-Briansó, L. Masi, M. Fattori, and M. Modugno, Phys. Rev. Res. **2**, 013269 (2020).

[265] M. Edwards, P. A. Ruprecht, K. Burnett, R. J. Dodd, and C. W. Clark, Phys. Rev. Lett. **77**, 1671 (1996).

[266] B. D. Esry, Phys. Rev. A **55**, 1147 (1997).

[267] L. You, W. Hoston, and M. Lewenstein, Phys. Rev. A **55**, R1581 (1997).

[268] T. Mithun, A. Maluckov, K. Kasamatsu, B. A. Malomed, and A. Khare, Symmetry **12** (2020).

[269] M. N. Tengstrand and S. M. Reimann, Phys. Rev. A **105**, 033319 (2022).

[270] J. Vallès-Muns, I. Morera, G. E. Astrakharchik, and B. Juliá-Díaz, SciPost Phys. **16**, 074 (2024).

[271] F. Dalfovo, S. Giorgini, L. P. Pitaevskii, and S. Stringari, Rev. Mod. Phys. **71**, 463 (1999).

[272] N. Navon, R. P. Smith, and Z. Hadzibabic, Nature Physics **17**, 1334 (2021).

[273] F. Wang, X. Li, D. Xiong, and D. Wang, Journal of physics. B, Atomic, molecular, and optical physics **49** (2015).

[274] A. Burchianti, C. D'Errico, M. Prevedelli, L. Salasnich, F. Ancilotto, M. Modugno, F. Minardi, and C. Fort, Condensed Matter **5** (2020).

[275] W. Kohn, Physical review **123**, 1242 (1961).

[276] T. A. Yoğurt, U. Tanyeri, A. Keleş, and M. O. Oktel, Phys. Rev. A **108**, 033315 (2023).

[277] K. W. Vugrin, L. P. Swiler, R. M. Roberts, N. J. Stucky-Mack, and S. P. Sullivan, Water Resources Research **43** (2007).

[278] J. R. Ensher, D. S. Jin, M. R. Matthews, C. E. Wieman, and E. A. Cornell, Phys. Rev. Lett. **77**, 4984 (1996).

[279] D. M. Stamper-Kurn, H.-J. Miesner, A. P. Chikkatur, S. Inouye, J. Stenger, and W. Ketterle, Phys. Rev. Lett. **81**, 2194 (1998).

[280] G. R. Dennis, J. J. Hope, and M. T. Johnsson, Computer Physics Communications **184**, 201 (2013).

[281] J. L. Roberts, N. R. Claussen, S. L. Cornish, and C. E. Wieman, Phys. Rev. Lett. **85**, 728 (2000).

[282] A. Marte, T. Volz, J. Schuster, S. Dürr, G. Rempe, E. G. M. van Kempen, and B. J. Verhaar, Phys. Rev. Lett. **89**, 283202 (2002).

[283] T. Weber, J. Herbig, M. Mark, H.-C. Nägerl, and R. Grimm, Science **299**, 232 (2003).

[284] G. Smirne, R. M. Godun, D. Cassettari, V. Boyer, C. J. Foot, T. Volz, N. Syassen, S. Dürr, G. Rempe, M. D. Lee, K. Góral, and T. Köhler, Phys. Rev. A **75**, 020702 (2007).

[285] Y. Kagan, B. Svistunov, and G. Shlyapnikov, JETP Lett **42** (1985).

[286] E. A. Burt, R. W. Ghrist, C. J. Myatt, M. J. Holland, E. A. Cornell, and C. E. Wieman, Phys. Rev. Lett. **79**, 337 (1997).

[287] L. Lavoine and T. Bourdel, Phys. Rev. A **103**, 033312 (2021).

[288] G. E. Astrakharchik and B. A. Malomed, Phys. Rev. A **98**, 013631 (2018).

[289] P. Zin, M. Pylak, T. Wasak, M. Gajda, and Z. Idziaszek, Phys. Rev. A **98**, 051603 (2018).

[290] G. Delannoy, S. G. Murdoch, V. Boyer, V. Josse, P. Bouyer, and A. Aspect, Phys. Rev. A **63**, 051602 (2001).

[291] F. Schreck, G. Ferrari, K. L. Corwin, J. Cubizolles, L. Khaykovich, M.-O. Mewes, and C. Salomon, Phys. Rev. A **64**, 011402 (2001).

[292] I. Bloch, M. Greiner, O. Mandel, T. W. Hänsch, and T. Esslinger, Phys. Rev. A **64**, 021402 (2001).

[293] G. Modugno, G. Ferrari, G. Roati, R. J. Brecha, A. Simoni, and M. Inguscio, Science **294**, 1320 (2001).

[294] M. Mudrich, S. Kraft, K. Singer, R. Grimm, A. Mosk, and M. Weidemüller, Phys. Rev. Lett. **88**, 253001 (2002).

[295] P. Stürmer, M. N. Tengstrand, R. Sachdeva, and S. M. Reimann, Phys. Rev. A **103**, 053302 (2021).

[296] I. A. Englezos, S. I. Mistakidis, and P. Schmelcher, Phys. Rev. A **107**, 023320 (2023).

[297] Y. Fei, X. Du, X.-L. Chen, and Y. Zhang, Phys. Rev. A **109**, 053309 (2024).

[298] Y. Li, Z. Chen, Z. Luo, C. Huang, H. Tan, W. Pang, and B. A. Malomed, Phys. Rev. A **98**, 063602 (2018).

[299] Y. V. Kartashov, B. A. Malomed, L. Tarruell, and L. Torner, Phys. Rev. A **98**, 013612 (2018).

[300] M. N. Tengstrand, P. Stürmer, E. O. Karabulut, and S. M. Reimann, Phys. Rev. Lett. **123**, 160405 (2019).

[301] Y. V. Kartashov, B. A. Malomed, and L. Torner, Phys. Rev. Lett. **122**, 193902 (2019).

[302] P. Examilioti and G. M. Kavoulakis, Journal of Physics B: Atomic, Molecular and Optical Physics **53**, 175301 (2020).

[303] Y. V. Kartashov, B. A. Malomed, and L. Torner, Phys. Rev. Res. **2**, 033522 (2020).

[304] S. R. Otajonov, E. N. Tsoy, and F. K. Abdullaev, Phys. Rev. E **102**, 062217 (2020).

[305] L. Dong and Y. V. Kartashov, Phys. Rev. Lett. **126**, 244101 (2021).

[306] Z. Lin, X. Xu, Z. Chen, Z. Yan, Z. Mai, and B. Liu, Communications in Nonlinear Science and Numerical Simulation **93**, 105536 (2021).

[307] M. Caldara and F. Ancilotto, Phys. Rev. A **105**, 063328 (2022).

[308] W. F. Vinen, Proceedings of the Royal Society of London. Series A. Mathematical and Physical Sciences **240**, 114 (1957).

[309] W. F. Vinen, Proceedings of the Royal Society of London. Series A. Mathematical and Physical Sciences **240**, 128 (1957).

[310] W. F. Vinen, Proceedings of the Royal Society of London. Series A. Mathematical and Physical Sciences **242**, 493 (1957).

[311] W. F. Vinen, Proceedings of the Royal Society of London. Series A. Mathematical and Physical Sciences **243**, 400 (1958).

[312] S. Ishino, H. Takeuchi, and M. Tsubota, Journal of Low Temperature Physics **162**, 361 (2011).

[313] S. Ishino, M. Tsubota, and H. Takeuchi, Phys. Rev. A **83**, 063602 (2011).

[314] M. Delehaye, S. Laurent, I. Ferrier-Barbut, S. Jin, F. Chevy, and C. Salomon, Phys. Rev. Lett. **115**, 265303 (2015).

[315] K. Fujimoto and M. Tsubota, Phys. Rev. A **85**, 033642 (2012).

[316] V. Zakharov and A. Rubenchik, Zh. Eksp. Teor. Fiz **65**, 997 (1973).

[317] Y. S. Kivshar and B. Luther-Davies, Physics Reports **298**, 81 (1998).

[318] D. L. Feder, M. S. Pindzola, L. A. Collins, B. I. Schneider, and C. W. Clark, Phys. Rev. A **62**, 053606 (2000).

[319] S. K. Adhikari, Journal of Physics B: Atomic, Molecular and Optical Physics **36**, 1109 (2003).

[320] F. K. Abdullaev and J. Garnier, Phys. Rev. A **70**, 053604 (2004).

[321] B. Li, X.-F. Zhang, Y.-Q. Li, Y. Chen, and W. M. Liu, Phys. Rev. A **78**, 023608 (2008).

[322] W. Bragg, in *Proceedings of the Cambridge Philosophical Society*, Vol. 17 (1912) p. 43.

[323] P. J. Martin, B. G. Oldaker, A. H. Miklich, and D. E. Pritchard, Phys. Rev. Lett. **60**, 515 (1988).

[324] P. B. Blakie and R. J. Ballagh, Journal of Physics B: Atomic, Molecular and Optical Physics **33**, 3961 (2000).

[325] A. Brunello, F. Dalfovo, L. Pitaevskii, S. Stringari, and F. Zambelli, Phys. Rev. A **64**, 063614 (2001).

[326] P. B. Blakie, R. J. Ballagh, and C. W. Gardiner, Phys. Rev. A **65**, 033602 (2002).

[327] J. Stenger, S. Inouye, A. P. Chikkatur, D. M. Stamper-Kurn, D. E. Pritchard, and W. Ketterle, Phys. Rev. Lett. **82**, 4569 (1999).

[328] D. M. Stamper-Kurn, A. P. Chikkatur, A. Görlitz, S. Inouye, S. Gupta, D. E. Pritchard, and W. Ketterle, Phys. Rev. Lett. **83**, 2876 (1999).

[329] M. Kozuma, L. Deng, E. W. Hagley, J. Wen, R. Lutwak, K. Helmerson, S. L. Rolston, and W. D. Phillips, Phys. Rev. Lett. **82**, 871 (1999).

[330] R. Ozeri, N. Katz, J. Steinhauer, and N. Davidson, Rev. Mod. Phys. **77**, 187 (2005).

[331] D. Petter, G. Natale, R. M. W. van Bijnen, A. Patscheider, M. J. Mark, L. Chomaz, and F. Ferlaino, Phys. Rev. Lett. **122**, 183401 (2019).

[332] J. J. A. Houwman, D. Baillie, P. B. Blakie, G. Natale, F. Ferlaino, and M. J. Mark, Phys. Rev. Lett. **132**, 103401 (2024).